THE UNIVERSITY OF NOTTINGHAM

DEPARTMENT OF ELECTRICAL AND

ELECTRONIC ENGINEERING

COMPUTATIONAL STUDIES OF THE ELECTROMAGNETIC PROPERTIES OF METAMATERIALS AND APPLICATIONS

By

HIROKI WAKATSUCHI, MEng.

Thesis submitted to the University of Nottingham

for the degree of Doctor of Philosophy

JULY 2011

Abstract

In this thesis computational studies on electromagnetic properties of metamaterials and applications are introduced. The studies include an introduction to the time–domain transmission line modelling (TLM) method and the fundamental scattering properties of metamaterials. The first major objective of the thesis is directed to predicting the resonant frequencies of some forms of cut–wire (CW) metamaterials by using approximate equivalent circuits. The second objective is the improvement of metamaterial simulation efficiency based on two approaches: a simulation method based on retrieved metamaterial electromagnetic properties and one based on digital filtering (DF) techniques. By using the DF techniques, metamaterials are effectively modelled and the simulation times are significantly reduced. The third objective is focused on studying CW metamaterial as potential absorbers by deliberately including conductive losses. The proposed CW metamaterials are found to exhibit customisable absorptance characteristics with arbitrary polarisation. This metamaterial absorber study includes an experimental validation.

Publications related to this thesis[1]

Journals

[1] Hiroki Wakatsuchi, John Paul, Stephen Greedy, and Christos Christopoulos, "Use of effective equivalent circuits for the prediction of resonant and absorbing behaviour of cut–wire–based metamaterials," *IEEE Trans. Microw. Theory Tech.* (submitted).

[2] Hiroki Wakatsuchi and Christos Christopoulos, "Generalized scattering control using cut–wire–based metamaterials," *Appl. Phys. Lett.*, vol. 98, no. 22, **221105**, 2011.

[3] Hiroki Wakatsuchi, Stephen Greedy, Christos Christopoulos, and John Paul, "Customised Broadband metamaterial absorbers for arbitrary polarisation," *Opt. Express*, vol. 18, issue 21, pp. 22187–22198, 2010.

[4] Hiroki Wakatsuchi, Stephen Greedy, John Paul, and Christos Christopoulos, "Efficient modelling method for artificial materials using digital filtering techniques and EMC applications," *IEICE Trans. Commun.*, vol. E93–B, no. 7, pp. 1760–1767, 2010.

Conferences

In English

[1] H. Wakatsuchi, J. Paul, S. Greedy, and C. Christopoulos, "Performance enhancement of cut–wire–based metamaterial absorbers," *Metamateri-*

[1] Other publications by the author may be found in appendix E.

als'2011 Fifth International Congress on Advanced Electromagnetic Materials in Microwave and Optics, Barcelona, Spain (accepted).

[2] John Paul, Steve Greedy, Hiroki Wakatsuchi, and Christos Christopoulos, "Measurements and Simulations of Enclosure Damping Using Loaded Antenna Elements," *EMC Europe 2011*, York, U.K. (accepted).

[3] H. Wakatsuchi, J. Paul, S. Greedy, and C. Christopoulos, "Contribution of Conductive loss to Cut–Wire Metamaterial Absorbers," *AP–RASC'10 2010 Asia–Pacific Radio Science Conference*, pp. DC1–7, Toyama, Japan, Sep. 2010.

[4] H. Wakatsuchi and J. Paul, "Predictions of Resonant Frequency Shifts in Asymmetrical Cut–Wire Metamaterials," *Metamaterials'2010 Fourth International Congress on Advanced Electromagnetic Materials in Microwave and Optics*, pp. 881–883, Karlsruhe, Germany, Sep. 2010.

[5] C. Christopoulos, J. D. Paul, D. W. P. Thomas, S. Greedy, H. Wakatsuchi, and M. H. Alsadi, "Characterisation and modelling of materials for electromagnetic shielding," *UK Magnetic Society Electromagnetic Field Protection*, Abingdon, U.K., Apr. 2010.

[6] H. Wakatsuchi, S. Greedy, J. Paul, and C. Christopoulos, "Implementation of Digital Filtering Techniques to EBG structures and Metamaterials for Efficient Numerical Simulations," *UK URSI Festival of Radio Science*, Birmingham, U.K., Dec. 2009.

[7] H. Wakatsuchi, S. Greedy, J. Paul, and C. Christopoulos, "Efficient Modelling of Band–gap and Metamaterial Structures in EMC," *2009 International Symposium Electromagnetic Compatibility Kyoto*, pp. 745–748, Kyoto, Japan, July 2009.

Awards

[1] AP–RASC'10 Student Paper Competition, Second Prize, *AP–RASC'10 2010 Asia–Pacific Radio Science Conference*, 22nd to 26th Sep. 2010.

[2] York EMC Services Ltd Best Paper Prize, Festival of Radio Science URSI, 15th Dec. 2009.

Acknowledgements

Firstly, I would like to express the greatest appreciation to my main supervisor Professor Christos Christopoulos. No doubt without his great supervision and sincere support, this research would not have been completed and I could not have derived as much fun from my life and research in Nottingham. I also appreciate the other supervisors Dr John Paul for his technical supervision and experimental support and Dr Stephen Greedy for his support to set up the environment of my computational studies in the University. I express my appreciation to Dr Chris Smartt for his advice on the development of the programme code for oblique wave excitation with periodic boundary. Also, I would like to thank Ms Kathryn Sanderson for her daily support in a working environment unfamiliar for me.

I also express my appreciation to the other staff and students of the George Green Institute for Electromagnetics Research (GGIEMR) for their support and encouragement to pursue my research and degree. I would like to express my appreciation to other friends and University staff I got to know through my PhD course.

Also, I would like to thank friends and researchers who were involved in my life in Japan and kept encouraging the study outside the U.K. Their support was essential and precious to me. Finally, I sincerely appreciate my family who supported me mentally and financially all through the three–year study. Without their support I could not have even stepped on the land of the U.K.

List of Symbols

Symbol	Description	First use
A	absorptance	eq. (7.3.1)
A_x, A_y, A_z	periodicity of periodic structure	Fig. 3.2
c_0	speed of light in vacuum (= 299,792,458)	eq. (2.1.13)
c	speed of light	page 28
C	capacitance	Fig. 2.1
C_m	mutual capacitance	page 81
C_s	self capacitance	page 81
E	magnitude of electric field	eq. (2.1.3)
$\mathbf{E}$	vector of electric field	Fig. 2.10
E_x, E_y, E_z	x, y, z axis components of electric field	eq. (2.1.3)
f	frequency	page 27
f_e	electric resonance frequency	page 174
f_m	magnetic resonance frequency	Fig. 5.13
G	magnetic loss	Fig. 2.1
H	magnitude of magnetic field	eq. (2.1.4)
$\mathbf{H}$	vector of magnetic field	Fig. 2.10
H_x, H_y, H_z	x, y, z axis components of magnetic field	eq. (2.1.4)
I	current	page 20
j	$\sqrt{-1}$	Table 3.1
$\mathbf{J}$	electric current source	page 32
k	wave number	eq. (5.2.15)
$\mathbf{k}$	vector of incident wave	Fig. 2.10
k_0	wave number in vacuum (= ω/c_0)	eq. (5.2.1)
L	inductance	Fig. 2.1
L_m	mutual inductance	page 81

L_s	self inductance	page 81
m, n	integer	Fig. 2.9
$\mathbf{M}$	magnetic current source	page 32
n	refractive index	page 9
$\mathbf{n}$	unit vector normal to surface	page 37
N	time step number	page 42
n'	real part of refractive index	page 9
n''	imaginary part of refractive index	page 9
P	power	page 167
r	radius	eq. (2.2.3)
R	electric loss	Fig. 2.1
R	sheet resistance	page 44
s	complex frequency (= $j\omega$)	eq. (4.4.1)
S_{11}	reflection coefficient at port 1	page 112
$\lvert S_{11}\rvert$	magnitude of S_{11}	page 83
S_{21}	transmission coefficient from port 1 to port 2	page 112
$\lvert S_{21}\rvert$	magnitude of S_{21}	eq. (7.3.1)
t	time	eq. (2.2.1)
^{t}	transposed matrix	eq. (6.2.7)
T	transmission coefficient	page 44
V	voltage	Fig. 2.2
V^i	incident voltage	Fig. 2.2
V^r	reflected voltage	Fig. 2.2
x, y, z	spacial coordinates	Fig. 2.3
Y	admittance	eq. (2.1.11)
Z	impedance	eq. (2.1.12)
Z_0	wave impedance in vacuum (= $\sqrt{\mu_0/\varepsilon_0}$)	page 20
z	normalised wave impedance	page 10
z'	real part of normalised wave impedance	eq. (5.2.9)

z''	imaginary part of normalised wave impedance	page 122
$\mathcal{Z}$	bilinear $\mathcal{Z}$ transform operator	page 145
Γ	reflection coefficient	page 44
Δl	edge length of cubic TLM unit cell	page 20
Δt	time step	page 27
$\Delta x,\ \Delta y,\ \Delta z$	lengths of TLM unit cell along $x,\ y,\ z$ axes	page 20
ε_0	permittivity of vacuum (= $1/\mu_0 c_0^2$)	eq. (2.1.26)
ε	permittivity	page 24
ε_r	relative permittivity	page 10
ε_r'	real part of relative permittivity	page 113
θ	incident angle of wave	Fig. 2.10
λ	wavelength	page 9
μ_0	permeability of vacuum (= $4\pi \times 10^{-7}$)	eq. (2.1.27)
μ	permeability	page 24
μ_r	relative permeability	page 10
μ_r'	real part of relative permeability	page 113
π	circular constant (= $3.141592\cdots$)	page 24
ω	angular frequency (= $2\pi f$)	eq. (2.1.26)

List of Abbreviations

Word	Description	First use
AMC	artificial magnetic conductor	page 7
CLL	capacitively–loaded loop	page 59
CPU	central processing unit	page 140
CW	cut–wire	page 4
D	dimension	Fig. 1.1
DF	digital filtering	page 12
DNG	double negative	page 135
DPS	double positive	page 135
E	electric	page 20
EBG	electromagnetic bandgap	page 45
EM	electromagnetic	page 16
EMC	electromagnetic compatibility	page 7
FDTD	electromagnetic compatibility	page 229
FFT	fast Fourier transform	page 49
G	giga	page 151
GHz	gigahertz	page 10
GND	ground	Fig. 2.7
H	magnetic	page 20
LHM	left–handed material	page 116
M	matched condition	Fig. 6.8
MUT	material under test	page 47
NP	number of poles	eq. (6.2.1)
NRI	negative refractive index	page 1
SCN	symmetrical condensed node	page 131
SRR	split–ring resonator	page 1

TE	transverse electric field	eq. (D.2.2)
THz	terahertz	page 4
TL	transmission line	Fig. 2.4
TLM	transmission line modelling	page 11
TM	transverse magnetic field	eq. (D.2.2)
PEC	perfect electric conductor	page 70
PMC	perfect magnetic conductor	page 49
PML	perfectly matched layer	page 235
RAM	random–access memory	page 151

Contents

1 Introduction **1**

1.1 First Metamaterial Measurements 1

1.2 Extension to the Optical Region 3

1.3 Metamaterial Applications 5

1.4 Current Prominent Problems 7

1.4.1 Conductive Loss 8

1.4.2 Metamaterial Modelling 9

1.5 Focus of the Thesis 12

1.6 Contents of the Thesis 13

2 Simulation Techniques **16**

2.1 TLM Method 16

2.1.1 Introduction to the TLM Method 16

2.1.2 Modelling of Propagation in Vacuum 19

2.1.3 Modelling of Lossless Materials 21

2.1.4 Modelling of Lossy Materials 25

2.2 Wire Modelling 27

2.3 Huygen's Surface Implementation 32

2.3.1 Introduction 32

2.3.2 Implementation of Huygen's Surface in the TLM Method . 33
2.4 Other Aspect of the Simulation 42
2.4.1 Wave Forms of Excited Waves 42
2.4.2 Boundary Conditions 43
2.4.3 Reflection and Transmission from Infinitesimally Thin Metal 44
2.5 Conclusion 44

3 Fundamental Scattering Properties **45**
3.1 Introduction 45
3.2 Electric Resonance 47
3.3 Magnetic Resonance 59
3.4 EBG Structure 68
3.4.1 Introduction 68
3.4.2 Simulation Results 70
3.5 Conclusion 79

4 Predictions of Resonant Frequencies **80**
4.1 Introduction 80
4.1.1 Predictions of Resonant Frequencies by Equivalent Circuits 80
4.1.2 CW Metamaterials 81
4.1.3 Focus 86
4.2 Calculation Models 86
4.3 Calculation Results 87
4.3.1 Equivalent Circuit for Single CW 87
4.3.2 Equivalent Circuit for Symmetrically Paired CW 93

4.3.3 Equivalent Circuit for Asymmetrically Paired CW 97
4.4 Discussion 103
4.4.1 Previous Equivalent Circuit for Symmetrically Paired CW 103
4.4.2 Calculation Errors for Asymmetrically Paired CW 103
4.4.3 Mutual Inductances 105
4.4.4 Resonant Frequency Shifts from Single CW 106
4.5 Conclusion 110

5 Characterisation by Retrieval Methods 111

5.1 Introduction 111
5.2 Retrieval Methods 112
5.2.1 Smith's Method 112
5.2.2 Ziolkowski's Method 114
5.3 Applications of Retrieval Methods 116
5.3.1 Calculation Conditions 117
5.3.2 Straight Wires 120
5.3.3 SRRs 122
5.3.4 LHM 125
5.3.5 Discussion 128
5.4 Metamaterial Simulations Based on Retrieved Metamaterial Properties 131
5.4.1 Theory 131
5.4.2 Calculation Conditions 133
5.4.3 Calculation Results 134
5.4.4 Discussion 140
5.5 Conclusion 140

6 Characterisation by DF Techniques **141**

6.1 Introduction . . . 141

6.2 Theory . . . 143

6.3 Calculation Results . . . 147

6.3.1 Calculation Models . . . 147

6.3.2 Calculation Results . . . 149

6.4 Large–Scale Metamaterial Simulation Based on DF Techniques . . 155

6.5 Discussion . . . 158

6.6 Conclusion . . . 160

7 Metamaterial Absorbers **162**

7.1 Introduction . . . 162

7.1.1 Past Achievements and Outstanding Issues . . . 162

7.1.2 Focus . . . 163

7.2 Calculation Models and Conditions . . . 164

7.3 Single CW Metamaterial Absorbers . . . 166

7.4 Paired CW Metamaterial Absorbers . . . 173

7.5 Single CW Metamaterial Absorbers on PEC Wall . . . 178

7.6 Customisation of Absorptances . . . 180

7.7 Experimental Validation . . . 184

7.7.1 Models . . . 184

7.7.2 Results . . . 188

7.8 Discussion . . . 190

7.9 Conclusion . . . 193

8 Conclusions **194**

9 Discussion and Further Work **196**

References **201**

Appendices **219**

A Use of Sheet Resistance Unit in the TLM Method **219**

B Scattering Matrices Used for Representation of Metamaterial Properties **221**

C Solution for n' in Retrieval Method **224**

C.1 Method 224

C.2 Limitation 227

D Oblique Wave Excitation with Periodicity **229**

D.1 Calculation Methods 229

D.1.1 Overview 229

D.1.2 Implementation in the TLM Algorithm 233

D.2 Impedance Boundary 235

E Other Publications by the Author **240**

List of Figures

1.1 Thin wire structures (left) [5, 6] and SRRs (right) [7] proposed by Pendry et al. to artificially obtain negative permittivity and negative permeability, respectively. 2

1.2 The first metamaterials proposed by Smith et al. The left and right figures show the 1D and 2D metamaterials reported in 2000 [1] and 2001 [3]. 3

1.3 Periodic units of CW metamaterial (left) and fish–net structure (right). 5

1.4 Transformation to CW metamaterial. The resonant frequency of the SRR illustrated in the left can be reproduced in the CW metamaterial in the right. 5

1.5 Cloaking method proposed by Pendry et al. 6

1.6 Enhancement of directivity (or gain) of antenna by metamaterials. The red arrows indicate the forward wave and the blue arrows represent the wave reflected at the back metamaterials. Both waves have a same phase so that the antenna directivity (gain) is improved. 8

1.7 Use of gain media for realisation of lossless metamaterials. $n'' = 0$ cannot be obtained at more than two frequency points, since further increase of gain leads to $n'' < 0$ which results in unstable metamaterials due to the over–accumulation of the energy. . . . 10

2.1 Analysis space (left) expressed by TLM method (right). 17

2.2 Procedure of general TLM calculation algorithm illustrated for simplicity in 2D. 18

2.3 Unit cell of TLM (for vacuum). 19

2.4 Implementation example of lossless electric property for z axis component (left) and magnetic property for x axis component (right) into TLM unit cell. The subscripts TL and s respectively indicate values of the transmission line (i.e. the impedance without the inserted electric and magnetic properties) and the extra stubs (to describe the electromagnetic properties), and Y_s and Z_s are calculated as eqs. (2.1.11) and (2.1.12) [85]. 21

2.5 Implementation example of lossy electric property for z axis component (left) and magnetic property for x axis component (right) into TLM unit cell. The subscripts TL and s respectively indicate values of the transmission line (i.e. the impedance without the inserted electric and magnetic properties) and the extra stubs (to describe the electromagnetic properties), and Y_s, Z_s, G_s and R_s are calculated as eqs. (2.1.11), (2.1.12), (2.1.20) and (2.1.21) [85]. 25

2.6 Round wire modelled in centre of TLM unit cell. 28

2.7 Equivalent circuit of round wire. 29

2.8 Incident wave (left) represented by Huygen's sources (right). . . 33

2.9 Excitation of electromagnetic wave by Huygen's surface. An impulse propagating in the analysis space at different time step t is drawn. The situation to be assumed (left) is simulated by using the Huygen's surface (right). If the tangential fields produced by the Huygen's sources are correct everywhere on the boundary in the right figure, then the same situation as the left figure can be realised in the right figure. 34

2.10 Oblique wave expressed by Huygen's sources and time delay on each boundary. 35

2.11 Time delay calculations. 36

2.12 Magnetic current sources **M** and electric current sources **J** on Huygen's surface. 38

2.13 Magnetic current source **M** and electric current source **J** for the boundary at the negative direction of z axis. 39

2.14 Positions of each voltage port with added Huygen's source. . . . 41

3.1 Electric resonance (left) and magnetic resonance (right). 46

3.2 Calculation model for **y**–shaped metamaterial. This structure was used in the analysis space of Fig. 3.3 as the MUT so that the periodic boundaries were deployed for yz and zx boundaries. 48

3.3 Simulation space for scattering parameter calculations. 49

3.4 Magnitude and phase of reflection coefficient of **y**–shaped metamaterial. 50

3.5 Magnitude and phase of transmission coefficient of **y**–shaped metamaterial. 50

3.6 Current distribution calculated on the front surface of **y**–shaped metamaterial at 16.29 (top left), 31.75 (top right) and 55.17 GHz (bottom left). 52

3.7 Decomposed and numbered **y**–shaped metamaterial parts. . . . 53

3.8 Reflection coefficient magnitudes (top) and phases (bottom) of decomposed **y**–shaped metamaterial models 1, 2 and 3. 54

3.9 Reflection coefficient magnitudes (top) and phases (bottom) of decomposed **y**–shaped metamaterial models 1, 4 and 5. 55

3.10 Reflection coefficient magnitudes (top) and phases (bottom) of decomposed **y**–shaped metamaterial models 1, 6 and 7. 56

3.11 Reflection coefficient magnitudes (top) and phases (bottom) of decomposed **y**–shaped metamaterial models 1, 8 and 9. 57

3.12 Reflection coefficient magnitudes (top) and phases (bottom) of decomposed **y**–shaped metamaterial models 1, 10 and 11. 57

3.13 Reflection coefficient magnitudes (top) and phases (bottom) of decomposed **y**–shaped metamaterial models 8 and 12 and **y**–shaped metamaterial. 58

3.14 Calculation model for CLL–based metamaterial. This structure was used in the analysis space of Fig. 3.3 as the MUT so that the periodic boundaries were deployed for yz and zx boundaries. . . 59

3.15 Magnitude and phase of reflection coefficient of CLL–based metamaterial. 61

3.16 Magnitude and phase of transmission coefficient of CLL–based metamaterial. 61

3.17 Profile of CLL–based metamaterial at 9.789 GHz. The top left figure shows the current distribution at zx plane, while the top right and bottom left represent the electric field (E_x and E_z) and magnetic field (H_y) distributions, respectively. 63

3.18 Profile of CLL–based metamaterial at 4.026 GHz. The top left figure shows the current distribution at zx plane, while the top right and bottom left represent the electric field (E_x and E_z) and magnetic field (H_y) distributions, respectively. 64

3.19 Reflection coefficient dependence of CLL–based metamaterial on component L. 65

3.20 Reflection coefficient dependence of CLL–based metamaterial on component S. 65

3.21 Reflection coefficient dependence of CLL–based metamaterial on component U. 66

3.22 Reflection coefficient dependence of CLL–based metamaterial on relative permittivity of substrate. 66

3.23 Reflection coefficient dependence of CLL–based metamaterial on relative permeability of substrate. 67

3.24 EBG structure (left) and its resonance behaviour (right). 68

3.25 Simulated EBG structure. This structure was used in the analysis space of Fig. 3.3 as the MUT so that the periodic boundaries were deployed for yz and zx boundaries. 70

3.26 Reflection coefficient of EBG structure. The top figure shows the magnitude and phase, while the bottom figure represents the real part and imaginary part. 71

3.27 Current distributions of EBG structure at 11.89 GHz. The top figure shows the distribution at zx plane, and the bottom left and right figures respectively represent the distributions at the bottom surface of the top patch and the surface of the ground plate. 72

3.28 Electric field (E_x and E_z) distribution (top) and magnetic field (H_y) distribution (bottom) of EBG structure at 11.89 GHz. 73

3.29 Reflection coefficient phase dependence of EBG structure on via height. The top figure shows the reflection coefficient phase as a function of frequency up to 40 GHz. The bottom figure shows the in–phase reflection bandwidth (grey bars) and its ratio to the centre frequency (crosses). 75

3.30 Reflection coefficient phase dependence of EBG structure on top patch gap. The top figure shows the reflection coefficient phase as a function of frequency up to 40 GHz. The bottom figure shows the in–phase reflection bandwidth (grey bars) and its ratio to the centre frequency (crosses). 76

3.31 Reflection coefficient phase dependence of EBG structure on relative permittivity of substrate. The top figure shows the reflection coefficient phase as a function of frequency up to 40 GHz. The bottom figure shows the in–phase reflection bandwidth (grey bars) and its ratio to the centre frequency (crosses). 77

3.32 Reflection coefficient phase dependence of EBG structure on relative permeability of substrate. The top figure shows the reflection coefficient phase as a function of frequency up to 20 GHz. The bottom figure shows the in–phase reflection bandwidth (grey bars) and its ratio to the centre frequency (crosses). 78

4.1 Scattering parameters of single CW metamaterial (top) and symmetrically paired CW metamaterial (bottom). 82

4.2 Electric field (top) and the conduction current in time domain (bottom) at 24.89 GHz (magnetic resonance). 84

4.3 Electric field (top) and the conduction current in time domain (bottom) at 26.71 GHz (electric resonance). 85

4.4 Calculated default CW metamaterial model. The illustrated structure represents the asymmetrically paired CW metamaterial. For the symmetrically paired CW metamaterial the offset d_x was set to zero. For the single CW metamaterial the bottom CW was removed. The details of each components are summarised in Table 4.1. 87

4.5 Parameters used for self inductance and mutual inductance calculations (eq. (4.3.2)). 89

4.6 Parameters used for fringing effect calculations (eq. (4.3.6)). w and g represent the plate widths and the gap between the plates. 90

4.7 Mutual inductances and mutual capacitances used for equivalent circuit of single CW array. The subscripts s and m represent self and mutual values. The subscripts following m indicate main directions along which the mutual effects work. The directions of the conduction currents are described by the black arrows. . . 91

4.8 Equivalent circuit for predicting electric resonant frequencies of single CW arrays. The equivalent circuit is based on eq. (4.3.8). . 91

4.9 Resonant frequencies for single CW arrays. The resonant frequencies were derived by equivalent circuit (see Fig. 4.8 and eq. (4.3.8)) and numerical simulations. 92

4.10 Normalised E_z in substrate of paired CW. This result was numerically obtained. 93

4.11 Calculation method for mutual capacitance C of two parallel plates having linearly changing potential difference. 94

4.12 Mutual inductances and mutual capacitances used for equivalent circuit of symmetrically paired CW array. The subscripts s and m represent self and mutual values. The subscripts following m indicate main directions along which the mutual effects work. The directions of the conduction currents are described by the black arrows. 96

4.13 Equivalent circuit for predicting magnetic resonant frequencies of symmetrically paired CW arrays. The equivalent circuit is based on eq. (4.3.17). 96

4.14 Magnetic resonant frequencies for symmetrically paired CW arrays. The resonant frequencies were derived by equivalent circuit (see Fig. 4.13 and eq. (4.3.17)) and numerical simulations. . . 97

4.15 Calculation processes for mutual inductance between different lengths of two wires [110]. 98

4.16 Calculation processes for mutual inductance between geometrically asymmetric but same lengths of two wires. 99

4.17 Mutual inductances and mutual capacitances used for equivalent circuit of asymmetrically paired CW array. The subscripts s and m represent self and mutual values. The subscripts following m indicate main directions along which the mutual effects work. The directions of the conduction currents are described by the black arrows. 101

4.18 Equivalent circuit for predicting magnetic resonant frequencies of asymmetrically paired CW arrays. The equivalent circuit is based on eq. (4.3.24). This equivalent circuit is same with that for symmetrically paired CW arrays (illustrated in Fig. 4.13), although some mutual parameters are modified to take account of the geometrical asymmetry. 102

4.19 Magnetic resonant frequencies for asymmetrically paired CW arrays. The resonant frequencies were derived by equivalent circuit (see Fig. 4.13 and eq. (4.3.17)) and numerical simulations. . . 102

4.20 All inductance values used for equivalent circuit of asymmetrically paired CW arrays. 104

4.21 All capacitance values used for equivalent circuit of asymmetrically paired CW arrays. 104

4.22 Electric field of asymmetrically paired CW at the magnetic resonant frequency of d_x = 1.2 mm. 105

4.23 Magnetic resonant frequencies for asymmetrically paired CW arrays with various y axis periodicities. 106

4.24 Equivalent circuit to predict resonant frequency shift of symmetrically paired CW from single CW. 107

4.25 Equivalent circuit to predict resonant frequency shift of three CW pair from single CW. 109

5.1 Analysis space and calculation condition for retrieval. 118

5.2 Retrieved periodic structures. The left and right figures respectively illustrate a wire structure unit and LHM unit. For a SRR unit the wire part was removed from the LHM unit. 118

5.3 n' retrieved by Smith's method using wire units. 120

5.4 n' retrieved by Ziolkowski's method using wire units. The finer scale of the result is described in the inset. 121

5.5 ε'_r retrieved by Smith's method and Ziolkowski's method using wire units. The wider range of the result is described in the inset. 121

5.6 z retrieved by Smith's method (top) and Ziolkowski's method (bottom) using four wire units. 123

5.7 n' retrieved by Smith's method using SRR units. 124

5.8 Real part of relative permeability retrieved by Ziolkowski's method using SRR units. 124

5.9 n' retrieved by Smith's method using LHM units. 125

5.10 n' retrieved by Ziolkowski's method using LHM units. 126

5.11 ε'_r retrieved by Ziolkowski's method using LHM units. The wider range of the result is illustrated in the inset. 126

5.12 μ'_r retrieved by Ziolkowski's method using LHM units. The narrower range of the result is illustrated in the inset. 127

5.13 Expected anti–resonance behaviour in ε'_r of LHM. f_m stands for the magnetic resonance frequency. 128

5.14 Real part of relative permittivity retrieved by Ziolkowski's method using SRR units. The inset describes the retrieved n'. . . 129

5.15 Inter–cell network between regular SCNs. RHM and LHM respectively stand for right–handed material and left–handed material here. 132

5.16 Notations of voltage nodes used for inter–cell network between regular SCNs. 132

5.17 Analysis space of numerical simulations based on retrieved electromagnetic properties. Each parameter is given on Table 5.2. . . 134

5.18 Calculation results of E_x at centre of y axis with various numbers of times step. A plane wave was excited at z = 19 mm. 136

5.19 Calculation result of E_x at centre of xy plane with various numbers of time step. A plane wave was excited at z = 19 mm. 137

5.20 Calculation results of E_x at centre of y axis with various numbers of time step. The excitation point was $(x,\ y,\ z)$ = (49, 49, 19) mm. 138

5.21 Finer time step resolutions of Fig. 5.20. 139

6.1 Use of DF techniques in the TLM. The scattering properties obtained with the fine mesh can be incorporated in the digital filter deployed on the surface of the coarse TLM unit cell. 142

6.2 Signal–flow diagram to calculate new incident voltages for cells with embedded digital filter. 146

6.3 EBG structure unit simulated for DF technique implementation. 147

6.4 CLL–based metamaterial unit simulated for DF technique implementation. 148

6.5 Scattering parameter comparison of EBG structure between fine mesh simulation and Padé form. 150

6.6 Scattering parameter comparison of EBG structure between fine mesh and coarse mesh simulations. 151

6.7 Scattering parameter comparisons in x polarisation (top) and y polarisation (bottom) of CLL–based metamaterial between fine mesh and coarse mesh simulations. 154

6.8 Calculation conditions of antenna simulation to show practical application example of DF techniques in EMC field. 155

6.9 Comparisons of electric fields obtained with DF and matched boundaries (top) or PEC boundaries (bottom) having various gaps between dipole antenna and the DF boundary. The electric field when the DF boundary was deployed behind the antenna was divided by that obtained in the matched boundary case or PEC case. 157

7.1 Simulated CW metamaterials. The default parameters are summarised on Table 7.1. 165

7.2 Absorptance of the single CW composed of only lossy metal. In the inset the absorptance dependence on R at 26.59 GHz is illustrated. 167

7.3 Conduction current I and dissipated power P ($= IR^2$) in CW with various values of R. The inset describes an equivalent circuit for the single CW, where R, L and C represent the sheet resistance, the total inductance and the total capacitance, respectively. 167

7.4 Absorptances of single CW composed of both lossless metal part and lossy metal part. The lossy metal parts were restricted to both edges (0.9 mm per each edge and 1.8 mm in total). 168

7.5 Absorptances of single CW composed of both lossless metal part and lossy metal part. The lossy metal parts were restricted to one edge (1.8 mm). 169

7.6 Absorptances of single CW composed of both lossless metal part and lossy metal part. The lossy metal parts were restricted to one edge (1.2 mm). 169

7.7 Absorptance of single CW with various loss distributions. The distributions used here are illustrated in the top figure. The calculation results are summarised in the bottom figure. The resistance values in the legend of the bottom figure are used as maximum resistance R in the top figure. 171

7.8 Absorptance of different lengths of single CWs (top) and absorptance of structure composed of part or all of the CWs (bottom). The lengths and the resistances in the legends represent the CW length and R, respectively. 172

7.9 Configurations of simulated asymmetrically paired CW metamaterial. 173

7.10 $|S_{11}|$ of lossless paired CW having various geometrical offset length d_x. The inset shows $|S_{21}|$ of each structure. d_x is expressed in each legend. In this figure same values of R described in the brackets of the legends were used for the front CW and the back CW. 174

7.11 Absorptance of the symmetrically paired CW with various R. In this figure same values of R described in the brackets of the legends were used for the front CW and the back CW. 175

7.12 Absorptances of the paired CW with various d_x. d_x is expressed in each legend. In this figure same values of R described in the brackets of the legends were used for the front CW and the back CW. 175

7.13 Various combinations of R applied for paired CW. The top left, top right and bottom left figures show the absorptances of no offset at 26.35 GHz, 1.2 mm offset at 26.23 GHz and 2.4 mm offset at 27.20 GHz, respectively. The dots in the figures represent the calculated sheet resistance patterns and the intermediate values were estimated by using spline interpolation. 177

7.14 Absorptances of different lengths of CWs placed near to PEC wall. The inset describes the simulated situation. 179

7.15 Influence of another pair of CW used in Fig. 7.14. The pair of each CW was placed orthogonally, as is illustrated in the inset. . 179

7.16 Absorptance of combinations of CW pairs used in Fig. 7.15. In this figure part or all of the CW pairs used in Fig. 7.15 were combined as one metamaterial unit. The inset shows the structure having all the CW pairs. 180

7.17 Demonstration of double absorptance peak. 5.1 and 3.3 mm CW pairs were combined as one metamaterial unit here. 181

7.18 Demonstration of triple absorptance peak. 5.1, 3.9 and 3.3 mm CW pairs were combined as one metamaterial unit here. Modification of the resistance value used for the 3.3 mm CW leads to the triple absorptance peak. The resistance values used for the 3.3 mm CW are shown in the legend. The other resistance values are the same as those of Fig. 7.15. 182

7.19 Absorptance of two CW pairs of 5.1 and 3.3 mm is improved by use of adjusted resistance values. In addition, the use of a lossless 4.5 mm CW pair exhibits a strong reduction of the absorptance at about 30 GHz. 183

7.20 Resonances of CW metamaterial (left) and I–shaped metamaterial (right). The red arrows represent the movements of the induced electric charges. 184

7.21 Experimental setup and metal box. 186

7.22 Simulation model of metal box. 187

7.23 Experiment model (left) and calculation model (right) of I–shaped strip. 188

7.24 Measurement and simulation results of shielding effectiveness of metal box and its improvement by I–shaped strip. The resistance part of the I–shaped strip was composed of 1.5 $\Omega\square^{-1}$ of sprayed resistor. 189

7.25 Measurement and simulation results of shielding effectiveness of metal box and its improvement by I–shaped strip. The top figure shows the I-shaped strip used. 50 Ω of a lumped resistor was used for this structure. The other part of the structure was composed of copper tape. The measurement and simulation results using the lumped resistor type of the I–shaped strip in the metal box are shown in the bottom figure. 191

9.1 Image of metamaterial system. The scattered field is dynamically adjusted depending on the state of the incident field according to user defined criteria. This control is performed either locally or on a large scale. 197

9.2 Example of metamaterial absorbers sharing metal geometry for double absorptance peak [77]. The metal geometry is placed close to a PEC wall. The middle part of the metal geometry is used for both first and second absorptance peaks (resonances). . 198

9.3 L–shaped metamaterial (top) and its reflection coefficients (bottom). A_x, A_y, l, w, t_m and t_s were modelled to be 6.3, 6.3, 5.7, 0.3, 0.0 and 1.2 mm by cubical unit cells of $\Delta l = 0.075$ mm. The electromagnetic properties of the substrate were $\varepsilon_r = 1.0$ and $\mu_r = 1.0$. No loss factor was implemented. The reflection coefficients were calculated along x axis which was the same as the incident electric field direction (Γ_{xx}) and y axis (Γ_{yx}). The polarisation of the electric field was changed by 90 degrees at around 22 GHz. 200

A.1 Dimension of metal (top) and infinitesimally thin metal modelled in the TLM (bottom). 220

C.1 Comparison between magnitudes of $n''z'$ and $2\pi z''/k_0 d$ of one paired CW metamaterial unit. 228

D.1 Calculation space for oblique incidence with periodicity. 230

D.2 Voltage copy process. In each time the left and right spaces represent the sub periodic unit and main periodic unit. 232

D.3 Use of impedance boundary to reduce reflection of incident wave. The boundary is connected to Z_x of the characteristic impedance so that the reflection of the oblique wave is reduced. . 236

D.4 Performance of impedance boundary and matched boundary for 15 degrees of TE wave. Electric field along x axis was calculated at a sampling plane next to Huygen's surface. 237

D.5 Performance of impedance boundary and matched boundary for 45 degrees of TE wave. Electric field along x axis was calculated at a sampling plane next to Huygen's surface. 238

D.6 Performance of impedance boundary and matched boundary for 45 degrees of TM wave. Electric field along x axis was calculated at a sampling plane next to Huygen's surface. 239

List of Tables

3.1 Default parameters of **y**–shaped metamaterial. 48

3.2 Summary of decomposed **y**–shaped metamaterial models. The numbers written in the right column indicates the used part(s) corresponding to that (those) of Fig. 3.7. 53

3.3 Default values of CLL–based metamaterial. 60

3.4 Default values of EBG structure. 70

4.1 Details of calculation parameters used for resonant frequency prediction of CW metamaterial (Fig. 4.4). 88

5.1 Details of retrieval simulation space. 119

5.2 Parameters used in numerical simulations based on retrieved electromagnetic properties. The analysis space is illustrated in Fig. 5.17. 135

6.1 Details of EBG structure simulated for DF technique implementation. 147

6.2 Details of CLL–based metamaterial simulated for DF technique implementation. 148

6.3 Coefficients of Padé form (eq. (6.2.1)) used for EBG structure. . . 149

6.4 Comparison between fine and coarse mesh simulations. Details of calculation machine used for both calculations are as are followed: CPU is AMD Athlon (tm) 64 Processor 2.00 GHz; memory is 2.00 GB RAM. 152

6.5 Coefficients of Padé form (eq. (6.2.1)) used for x polarisation of CLL–based metamaterial. 153

6.6 Coefficients of Padé form (eq. (6.2.1)) used for y polarisation of CLL–based metamaterial. 153

6.7 Details of calculation conditions of antenna simulation illustrated in Fig. 6.8. 156

7.1 Default parameters of single CW metamaterial absorber illustrated in Fig. 7.1. 165

7.2 Absorptance peaks of paired CW with various x axis offset d_x. . . 176

CHAPTER 1

Introduction

1.1 First Metamaterial Measurements

For the first time in the history of science, negative values of refractive indices have been experimentally demonstrated by using metamaterials by Smith et al. [1–3]. Since these first experiments, metamaterial research has spread among many researchers primarily due to the potential for exploitation.

The existence of metamaterials was first predicted in the Soviet Union by physicist Veselago in 1968 [4]. Although at this point details on how to produce metamaterials had not been specifically mentioned, he indicated possibilities of many unusual but physically new behaviours achievable due to the negative refractive index (NRI). His discoveries include reversal of Snell's law. In the NRI media the phase velocity becomes anti–parallel (i.e. the opposite direction) to the group velocity so that the waves behave as they propagate backward, though the energy still propagates forward.

From 1996 to 1999 Pendry et al. of Imperial College London theoretically demonstrated that thin–wire structures [5, 6] and split–ring resonators (SRRs) [7] can respectively have negative permittivity and negative permeability (see Fig. 1.1 for the structures). The resonant behaviour of these artificially

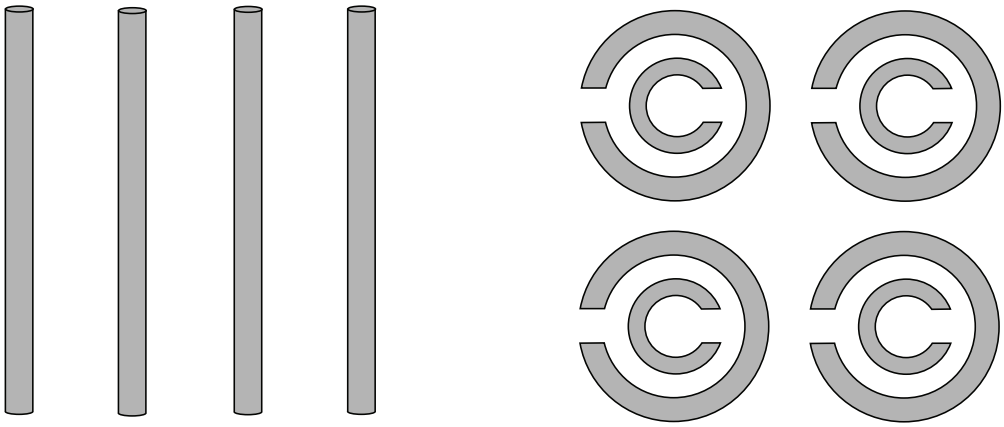

Figure 1.1: Thin wire structures (left) [5, 6] and SRRs (right) [7] proposed by Pendry et al. to artificially obtain negative permittivity and negative permeability, respectively.

composed structures are different from that of conventional materials available in nature. Specifically, the non–artificial materials are composed of atoms or molecules, and their resonant frequencies depend on the polarisations of the molecules, whose structural size is extremely small compared to the wavelength of the incident waves. However, in the artificial materials (e.g. those suggested by Pendry et al.) the structures consist of not only the naturally available materials, but also periodic metal units. These metal units are much larger than the molecule sizes, but still small enough compared to the wavelength of the incident waves. In this case, the resonant frequency is also affected by the polarisation of the metal composites which are artificially embedded in the host medium. In other words, the resonance can be artificially manipulated by changing the geometries of the sub–wavelength components.

In 2000 the two types of the artificial structures proposed by Pendry et al., i.e. the thin–wire structures and the SRRs, were combined as a one periodic structure by a research group of Smith et al. in University of California at San Diego [1] (see the left of Fig. 1.2). By using the one–dimensional periodic structure, they reported that a stop band of the SRRs can be changed to a pass band due to NRIs produced by the interaction with the added thin–wires. In the following year this structure was extended to a two–dimensional

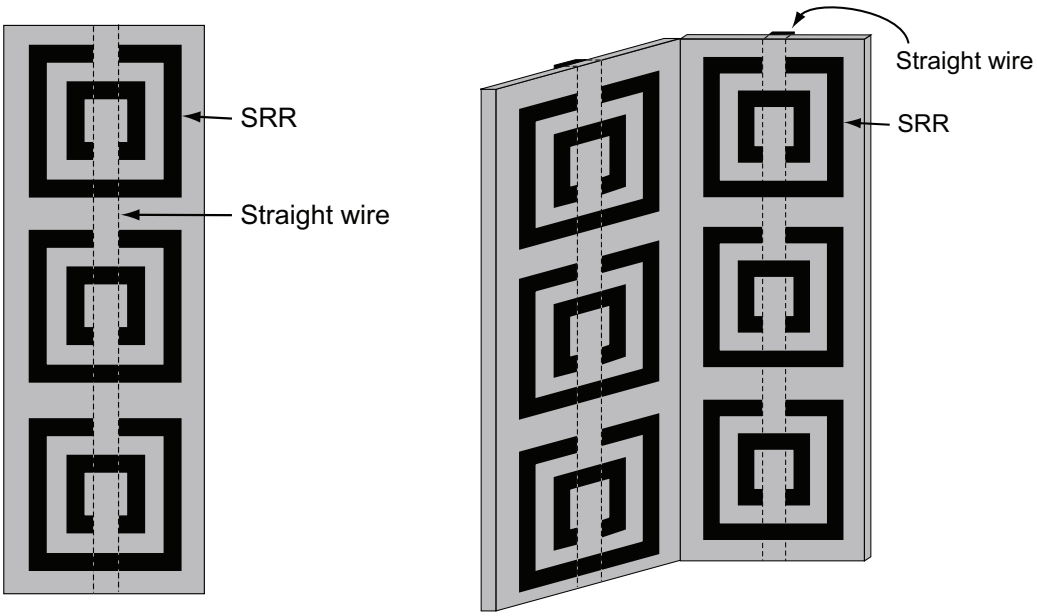

Figure 1.2: The first metamaterials proposed by Smith et al. The left and right figures show the 1D and 2D metamaterials reported in 2000 [1] and 2001 [3].

metamaterial (see the right of Fig. 1.2), in which two metamaterial slabs were arranged vertically to each other to take account of two axis components [2], and in [3] NRIs were experimentally demonstrated for the first time by using the 2D structure.

1.2 Extension to the Optical Region

Since the first series of experimental demonstrations by Smith et al. many metamaterial studies have been performed. For example, various metal geometries or new combinations of them were proposed as alternative forms of the SRRs and the thin metal strips to improve the properties of metamaterials [8–12]. In addition, the metamaterial studies were also focused on substrates to satisfy the wide demands for metamaterials. For instance, some metamaterial geometries are drawn on thin films or flexible substrates, which makes it possible, due to their flexibility, to use them on uneven surfaces [13, 14].

Although many studies have been performed so far, one of the main streams of fundamental metamaterial property research was directed toward the extension of the applicable frequency region to higher frequencies, such as the THz, the infrared and the optical regions. As is explained in the next section, many metamaterial applications have been proposed for the high frequency regions. Hence, the interest of many researchers was attracted to increasing the operating frequency of the metamaterials.

However, as the application frequency increases, the geometries of the metal components needed to be transformed. First of all, since metamaterials are composed of sub–wavelength structures, the metal geometries need to be smaller (inversely proportional to frequency). Therefore, the resulting complicated geometries of metamaterial composites are difficult to fabricate in practice.

Another important reason lies in the conductive loss of the metal composites. Although in comparative low frequencies (e.g. the microwave band) the conductive loss of the metal can be negligibly small (lossless metal), in the very high frequency regions (e.g. the THz band, the infrared and optical regions) most types of metals exhibit nonnegligible level of the ohmic losses, which leads to larger imaginary part of refractive index. The large imaginary part can be further increased by using bent metal forms. Therefore, bending metal forms, such as SRRs, can result in lossier behaviour.

For these reasons, in actual experimental reports metamaterials in high frequency regions tend to be composed of straight wires or their simple combinations, e.g. the so–called cut–wire (CW) metamaterials [15–17] (the left of Fig. 1.3) and fish–net structures [18–21] (the right of Fig. 1.3). The relationship between metamaterial geometries and operational frequency is discussed in [11]. Although the two types of the metamaterials mentioned are similar to each other from the viewpoint of the resonant behaviour and equivalent

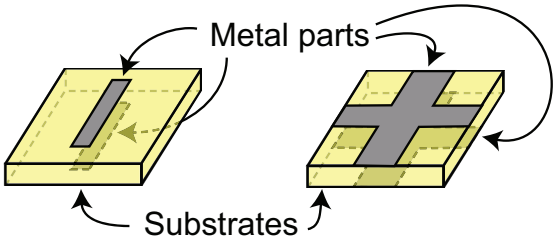

Figure 1.3: Periodic units of CW metamaterial (left) and fish–net structure (right).

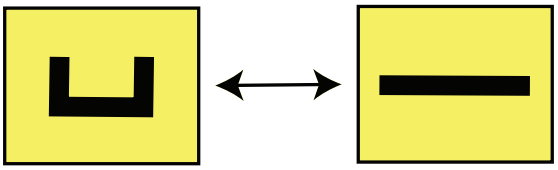

Figure 1.4: Transformation to CW metamaterial. The resonant frequency of the SRR illustrated in the left can be reproduced in the CW metamaterial in the right.

circuits, it is known that the fish–net structures are lower loss structures than the CW metamaterials [11]. Due to the simple geometries of CW metamaterials other metamaterials can be transformed to the CW metamaterials, while keeping the original resonant frequency [22, 23] (see Fig. 1.4).

1.3 Metamaterial Applications

Alongside fundamental metamaterial studies, a wide range of metamaterial applications have been proposed. One of the most famous examples is metamaterial cloaking. Basically the cloaking methods can be categorised into one of two types: ones relying on optical transformations [24]; those on scattering cancellations [25]. In the former case, which was first suggested by Pendry et al. [24], the cloaked object is covered by metamaterials as illustrated in Fig. 1.5. The refractive indices of the metamaterials are carefully designed so that incident wave is bent inside the metamaterial cover without reaching the concealed object. After penetrating the metamaterials the phase of the incident wave is restored as there is no structure. As a result, the object covered by the

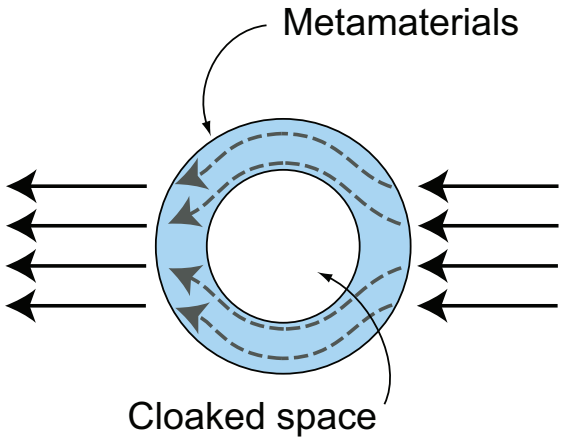

Figure 1.5: Cloaking method proposed by Pendry et al.

metamaterials cannot be detected from the outside.

In the later case, cloaking is achieved by cancelling out the total scattering instead of bending incident wave. This method was first proposed by Alù and Engheta of University of Pennsylvania [25]. In contrast to the cloaking method by optical transformations, in this case the incident wave impinges the object covered by metamaterials and scatters from there. However, the scattering is cancelled out by that from the metamaterials, resulting in no scattering as a whole. Later Alù and Engheta extended this idea, suggesting a useful application named an invisible sensor which does not interfere with the surrounding fields but can still measure the electromagnetic fields [26]. Moreover, it became unnecessary to fully cover the cloaked object which also played an important role in markedly reducing the cloaking device thickness [27].

Both types of the cloaking methods were further studied and sometimes combined. In [28] a research group of the Hong Kong University of Science and Technology proposed a cloaking method which does not require a cloaked material to be surrounded by cloaking devices (or metamaterials). In addition, the research group reported it is possible to convert scattering from an object to that from an arbitrary designed form [29]. As a result, the original object can

look different from the outside.

Other popular metamaterial applications include metamaterial lenses known as perfect lenses, superlenses and hyperlenses [30–35]. The application, theoretically proposed by Pendry [30] in 2000, has overcome some problems including a propagation loss issue [36] and been experimentally realised to resolve gratings of 145 nm [31] and 75 nm [32] in 2005. The point of the metamaterial lenses lies in their resolution. Specifically, conventional lenses have a limitation on their minimum resolution, i.e. wavelength of the operating frequencies. However, this limitation can be overcome by using the negative properties of the metamaterials. The metamaterial lenses may be useful in many other fields, e.g. medical field, to observe fine features.

Metamaterial applications were proposed not only for high frequency regions, but also for low frequency regions, such as the microwave band. For example, metamaterials are applied to antennas at radio wave frequencies [37–39]. One of the advantages of metamaterials lies in miniaturising the physical sizes of the antennas [40, 41]. In addition, metamaterials, when placed behind an antenna, can play a role of an artificial magnetic conductor (AMC) [42]. In this way the phase of the scattering from the AMC can be same with the phase of the front wave so that the directivity (or the gain) of the antenna can be concentrated forward (see Fig. 1.6). Another well known application is in designing absorbers (see section 1.5), used in EMC (electromagnetic compatibility) and radar problems.

1.4 Current Prominent Problems

Despite the wide range of the past metamaterial studies there are still important issues which have not been fully addressed. The thesis addresses two such problems as discussed below.

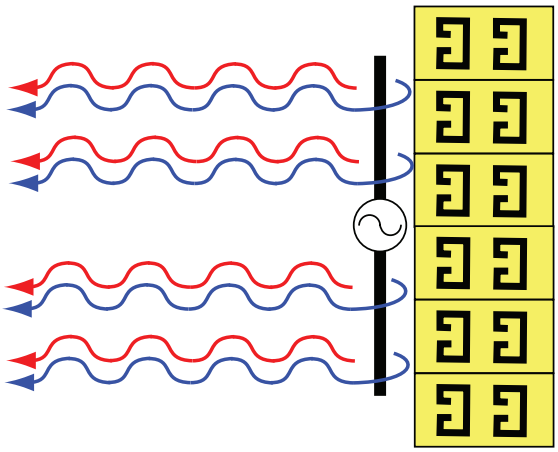

Figure 1.6: Enhancement of directivity (or gain) of antenna by metamaterials. The red arrows indicate the forward wave and the blue arrows represent the wave reflected at the back metamaterials. Both waves have a same phase so that the antenna directivity (gain) is improved.

1.4.1 Conductive Loss

The first important issue is, as mentioned in section 1.2, the conductive losses of metal composites [43]. Most metamaterial applications rely on the negative properties, such as a NRI, negative permittivity and negative permeability, which can be obtained when the metal composites strongly resonate. However, the conductive loss becomes larger as the frequency increases and affects the resonance making it difficult to obtain negative values. Therefore, the negative properties are difficult to obtain in the high frequency regions due to the ohmic loss.

This issue can be addressed by several approaches in addition to the geometry changes already mentioned. For example, magnetodielectric metamaterials (or all–dielectric metamaterials) [44–49] can be one of the solutions. The magnetodielectric metamaterials are composed only of two types of dielectric, i.e. a main dielectric host medium having relatively low permittivity and dielectric spheres having high values of permittivity. In these structures the dielectric spheres are periodically deployed in the host medium. Since these

metamaterials are free of any metallic component, the ohmic loss issue does not arise. However, some limitations of the magnetodielectric metamaterials are reported in [50]. For example, these structures tend to show relatively narrow frequency band characteristics. In addition, the material costs become high in this case.

Another major approach is the use of gain media [51]. In fact, many recent metamaterials tend to use the gain media, especially for high frequency regions. By using the gain media the energy loss caused by the conductive loss can be compensated so that low overall loss properties can be obtained. So far various gain media have been used, e.g. quantum dots [52, 53] and dye solutions [54–57]. In one of recent reports [57] rhodamine 800 (Rh800) dye was doped to an epoxy substrate of fish–net structures, resulting in $n' \approx -1.6$ with a small value of imaginary part ($n'' \approx 0.039$) at λ = 737 nm, where the $'$ and $''$ signs of the refractive index n represent the real part and imaginary part, respectively, and λ is the wavelength at the operating frequency. However, to maintain a sustainable metamaterial system, the imaginary part of refractive index needs to be equal to or higher than zero for every single frequency. Otherwise the energy is over–accumulated and results in an unstable metamaterial system. This means lossless properties are difficult to obtain at more than two frequency points in this way (see Fig. 1.7). This fact can be also confirmed from results of [57], where the small values of n'' calculated at $\lambda = 737$ nm increases with an increase or decrease of frequency.

1.4.2 Metamaterial Modelling

Another important problem is associated with numerical simulations for metamaterials. In general most electromagnetic simulations only require a tenth of a wavelength resolution but this resolution level is insufficient in resolving the fine geometrical details of metamaterials. For example, the first metamaterial introduced by Smith et al. [1] used SRRs, and their ring widths were designed

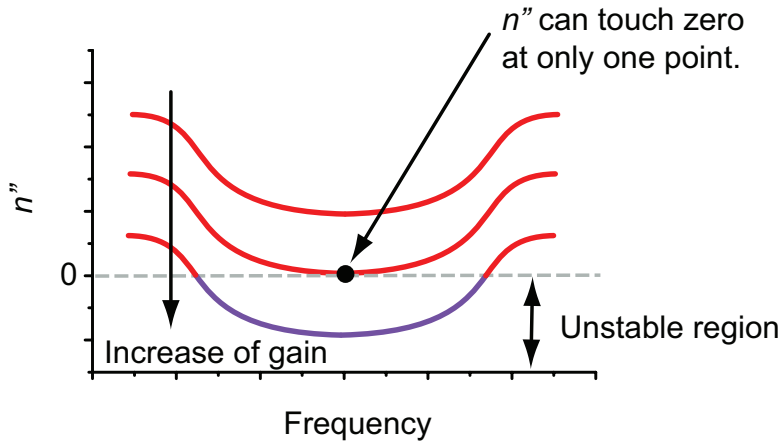

Figure 1.7: Use of gain media for realisation of lossless metamaterials. $n'' = 0$ cannot be obtained at more than two frequency points, since further increase of gain leads to $n'' < 0$ which results in unstable metamaterials due to the over–accumulation of the energy.

to be 0.8 mm. Since the metamaterial had an operation frequency at around 5 GHz, the ring widths are about $0.01\lambda_{5GHz}$, where λ_{5GHz} represents the wavelength at 5 GHz. Therefore, direct application of the numerical models would require enormous computational resources and very long simulation times. Without efficient simulation technique it is very difficult to explore the exploitation of metamaterials in challenging large scale practical problems.

The computational inefficiency problem can be solved by using retrieval methods [58–61]. These methods average the electromagnetic properties of metamaterials from the macroscopic viewpoint. In these methods the reflection and transmission coefficients calculated from the metamaterial unit(s) are applied in the equations of Nicolson–Ross–Weir [62–66], in which the scattering parameters are associated with refractive index n and wave impedance normalised by the value of vacuum z. Since these parameters are expressed in terms of relative permittivity ε_r and relative permeability μ_r (i.e. $n^2 = \sqrt{\varepsilon_r \mu_r}$ and $z^2 = \mu_r/\varepsilon_r$), inverting n and z can lead to ε_r and μ_r which represent the homogenised electromagnetic properties of the metamaterials. Using the homogenised ε_r and μ_r for electromagnetic calculation simulations, details

of sub–wavelength structures no longer need to be modelled and the use of coarse mesh (e.g. $\lambda/10$) becomes possible. Therefore, computational effort can be significantly reduced in this way.

Several kinds of retrieval methods have been proposed and the proper choice is essential when incorporate *appropriate* values in numerical simulations. For example, some metamaterials have bianisotropic [67] or chiral properties [68, 69], and some extra factors involved in interactions occurring inside the metamaterial units need to be taken into account. These properties are not included in the first retrieval method proposed by Smith et al. [58], although this is one of the most widely used methods so far. For this reason, numerical simulation results based on some of the available retrieval methods may give results far from those calculated using a fine mesh metamaterial model.

Another important issue when using retrieval methods is related to some metamaterials designed for high frequency regions, e.g. CW metamaterials and fish–net structures. These structures have metal composites drawn on both sides of the substrate surfaces, and the substrate thicknesses, compared to distances between the metamaterial units, are relatively thin. Therefore, interactions within each unit become strong. In this case the number of metamaterial units used for the retrieval methods can affect the calculation results, indicating these structures have a dependence on the metamaterial unit number used, which is physically unreasonable [70, 71]. Although it may be possible to extract the refractive index from many metamaterial units stacked together, no widely agreed method is yet available.

Numerical simulations based on retrieved properties may still demand heavy computational resources. For example, in [72] where such homogenised electromagnetic properties are embedded in unit cells of the Transmission Line Modelling (TLM) time–domain method, each voltage port needs to have

additional components to express the negative parameters of metamaterials. This means that the calculations for each TLM unit cell, which has twelve ports for calculations of vacuum, require an extra twelve calculations (though exactly speaking six, since the calculations with neighbouring cells are combined), resulting in much slower computation speed.

1.5 Focus of the Thesis

Taking account of the two issues introduced above, this thesis focuses primarily on three topics described below. Whilst in many metamaterial applications conductive losses are undesirable, for the design of absorbers it is essential to maximise losses [73–80]. This is the application which is described in the thesis as the first topic. The practical use of metamaterials as wave absorbers is becoming popular for applications in areas such as EMC, crosstalk reduction etc. For this reason, this thesis studies metamaterial absorbers with losses for general applications.

Secondly, the metamaterial modelling issue is addressed by using digital filtering (DF) techniques [81–83]. As mentioned in the last section, difficult choices are necessary when using retrieval methods and their numerical simulations require huge computation resources. Hence, a different approach is introduced in this thesis.

Thirdly, one of the objectives of the thesis is predicting resonant frequencies of CW structures by using equivalent circuits. As was described in section 1.2, CW metamaterials can be transformed from other types of metamaterials, while maintaining the resonant frequencies. Therefore, the CW metamaterials play an important role in fundamental metamaterial research. In addition, approximately predicting resonant frequencies by equivalent circuit is helpful in designing metamaterials. The availability of equivalent circuit models for

metamaterial absorbers makes it possible to predict quickly and easily the resonant frequency and thus provides a first design which then may be further optimised using the full–technique desired in other parts of the thesis. For these reasons, this thesis studies CW metamaterials, using equivalent circuits.

1.6 Contents of the Thesis

The thesis is composed as follows:

In chapter 2 simulation techniques used in the thesis are explained. Most of results introduced in the thesis are based on computational simulations which are performed using the TLM method [84–86]. The simulation method is detailed in chapter 2, including additional procedures necessary for the metamaterial studies performed here.

Chapter 3 shows the basic properties of metamaterials. More specifically this chapter introduces the scattering parameters of different resonance types, i.e. electrically induced resonances or magnetically induced resonances. These scattering parameters are investigated in more detail by decomposing the simulated structures into smaller components or by changing each component size. In this way important factors contributing to resonances are clarified.

Chapter 4 addresses the first major objective of the thesis and predicts the resonant frequencies of some forms of CW metamaterials by using approximated equivalent circuits. The resonant frequencies are calculated from the equivalent circuits composed of self and mutual capacitive and inductive parameters. Comparison results with detailed numerical simulations show good agreement. Some equivalent circuits have been reported to predict resonant frequencies of CW metamaterials. This chapter discusses differences between results obtained in this thesis and results from one of the most cited

equivalent circuits.

Chapter 5 describes details of retrieval methods and shows calculation results of retrieved electromagnetic properties. Then, a numerical simulation method based on retrieved properties is introduced and some numerical simulation results are shown. It is shown in this chapter that retrieval methods can be problematic and therefore a more direct and efficient method is needed. Such a method is developed in chapter 6 of this thesis.

Chapter 6 addresses the second objective of the thesis, which is the application of DF techniques for improving metamaterial simulation efficiency. First of all, the principle of DF techniques is explained in detail and this technique is illustrated by some examples. Furthermore, a large scale simulation is performed to demonstrate the applicability of the DF techniques to realistic situations. In this simulation metamaterial properties characterised by the DF techniques are used to improve a directivity of an antenna.

Chapter 7 shows a study of metamaterial absorbers, which is the third objective of the thesis. The chapter explores a possibility of using metamaterials in realistic application as absorbers. In this study the metal geometries are based on a simple CW or their combinations. The important finding of this chapter is that the CW metamaterial absorbers make it possible to realise customisable absorptance characteristics for arbitrary polarisation[1] in a relatively simple way. These structures show not only customised enhancement of absorptance but also, if required, reduction of absorptance. The chapter concludes with an experimental validation of the numerical results.

In chapter 8 conclusions are presented and future possibilities for meta-

[1] Although the CW metamaterial absorbers have been directly tested for two orthogonal polarisations, a wave incident at another angle can be decomposed into these two polarisations and thus efficiently absorbed.

material studies are discussed in chapter 9.

CHAPTER 2

Simulation Techniques

2.1 TLM Method

2.1.1 Introduction to the TLM Method

In the thesis one of numerical simulation methods in time domain, the TLM method, is used to calculate the electromagnetic (EM) fields and study EM properties of metamaterials. This method was originally developed in 3D by Johns of the University of Nottingham in 1987 [84]. The TLM method [84–86] reduces the simulation space to lumped circuit models, composed of capacitors and inductors (see Fig. 2.1). The lumped circuit models effectively spatially discretise the problem into nodes or cells that may be replaced by their transmission line equivalents (time discretisation). Since the details of the basic TLM method have been fully discussed in many publications [84–86], this thesis shows only the general ideas sufficient to understand the calculation algorithms and adaptations made to model metamaterials. Although commercial TLM software is available, all the programme codes required for the TLM simulations and other simulation techniques explained in this thesis were built up by the author from the beginning to make it easier to modify and customise the details.

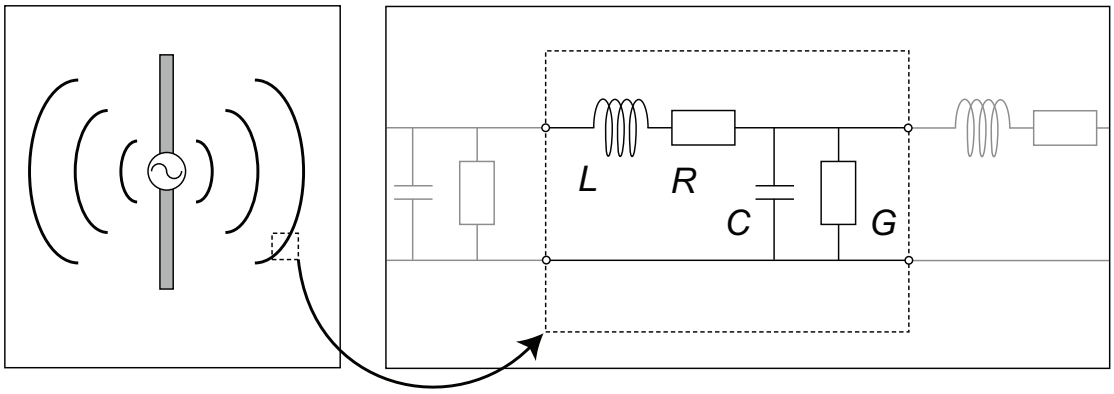

Figure 2.1: Analysis space (left) expressed by TLM method (right).

In TLM the procedure to obtain the EM fields is composed of four steps: input of the initial condition, the scattering and connecting (or swapping) processes, and the EM field calculations. This is summarised in Fig. 2.2.

For the initial condition in the thesis all the voltage values are set to zero except for those of an excitation source. At the excitation cell(s) a Gaussian pulse or a sinusoidal constant wave (both of which are explained in section 2.4) is used as the wave form.

Secondly, the scattering process, i.e. the calculations of the voltages scattered from the centre of each cell, is performed by using the next equation:

$$\mathbf{V}^r = \mathbf{S} \cdot \mathbf{V}^i, \tag{2.1.1}$$

where $\mathbf{V}$ and $\mathbf{S}$ represent vectors with the voltage components at each node and the scattering matrix, respectively, and the superscripts of $\mathbf{V}$ r and i express the reflected and incident voltages, respectively.

Thirdly, the connecting process is performed by exchanging the voltage values with those of the neighbour unit cells so that the new incident voltages are obtained from the reflected voltages entering from the neighbouring cells. The second and third processes (scatter and connect) are repeated for as long as required. Finally, the EM fields are derived from the incident voltages [85].

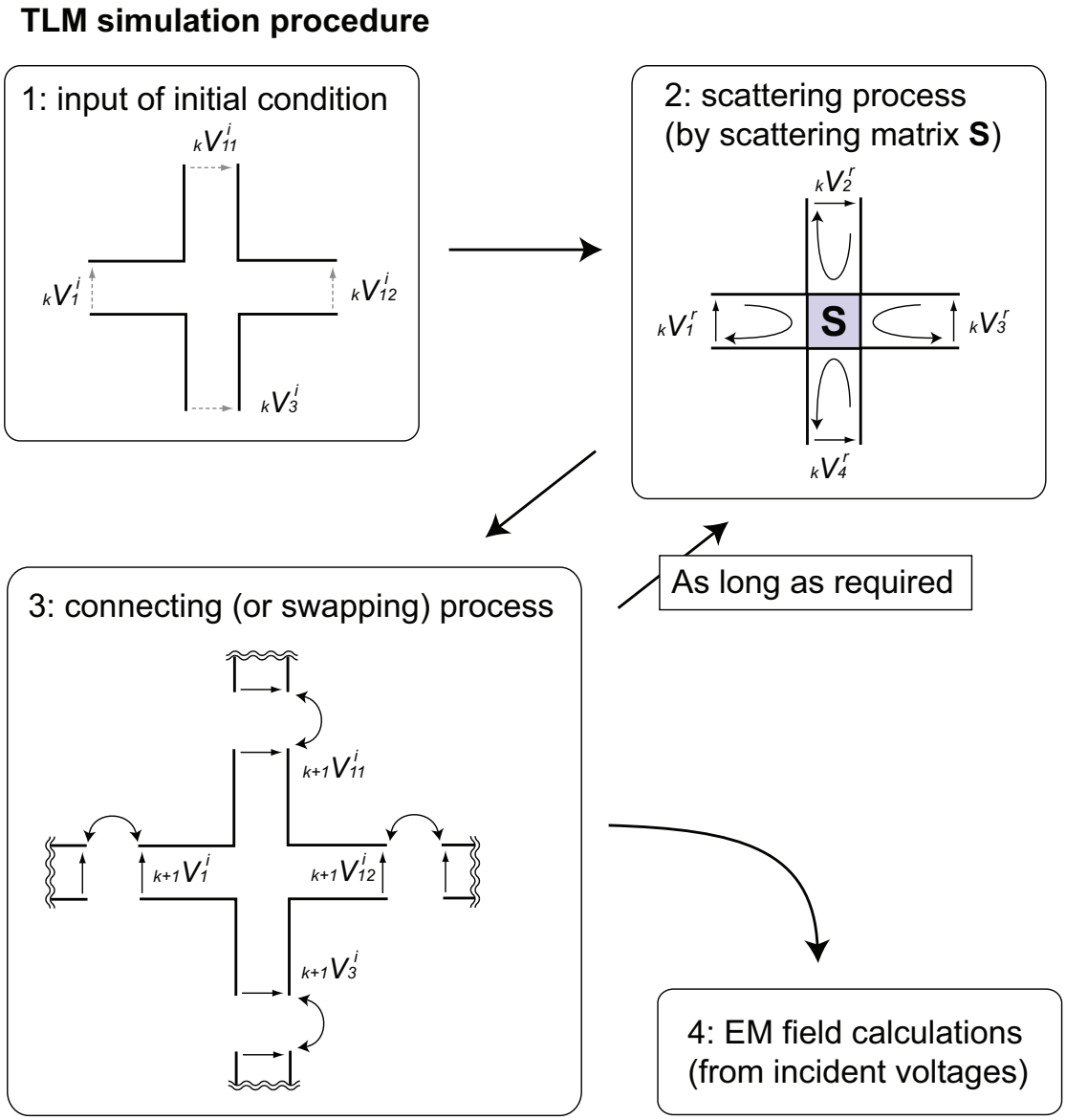

Figure 2.2: Procedure of general TLM calculation algorithm illustrated for simplicity in 2D.

The details for the scattering process to the electromagnetic field calculations differ, depending on what types of materials are modelled, e.g. vacuum, lossless material, or lossy material, and different scattering matrices apply in each case. They are explained in the following subsections.

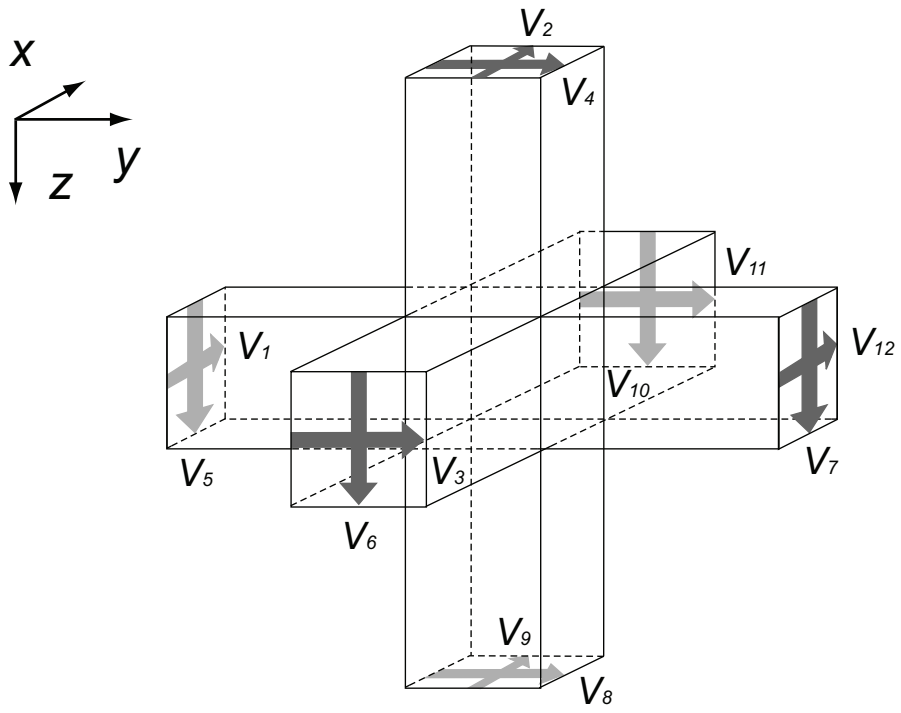

Figure 2.3: Unit cell of TLM (for vacuum).

2.1.2 Modelling of Propagation in Vacuum

For the free space (vacuum) modelling each cell has twelve port voltages, as is illustrated in Fig. 2.3, i.e. $\mathbf{V} = [V_1\ V_2\ \cdots\ V_{12}]^t$. The subscript numbers correspond to those of Fig. 2.3.

The scattering matrix for the free space is given in the next expression

[85]:

$$\mathbf{S} = 0.5 \begin{bmatrix} 0 & 1 & 1 & 0 & 0 & 0 & 0 & 0 & 1 & 0 & -1 & 0 \\ 1 & 0 & 0 & 0 & 0 & 1 & 0 & 0 & 0 & -1 & 0 & 1 \\ 1 & 0 & 0 & 1 & 0 & 0 & 0 & 1 & 0 & 0 & 0 & -1 \\ 0 & 0 & 1 & 0 & 1 & 0 & -1 & 0 & 0 & 0 & 1 & 0 \\ 0 & 0 & 0 & 1 & 0 & 1 & 0 & -1 & 0 & 1 & 0 & 0 \\ 0 & 1 & 0 & 0 & 1 & 0 & 1 & 0 & -1 & 0 & 0 & 0 \\ 0 & 0 & 0 & -1 & 0 & 1 & 0 & 1 & 0 & 1 & 0 & 0 \\ 0 & 0 & 1 & 0 & -1 & 0 & 1 & 0 & 0 & 0 & 1 & 0 \\ 1 & 0 & 0 & 0 & 0 & -1 & 0 & 0 & 0 & 1 & 0 & 1 \\ 0 & -1 & 0 & 0 & 1 & 0 & 1 & 0 & 1 & 0 & 0 & 0 \\ -1 & 0 & 0 & 1 & 0 & 0 & 0 & 1 & 0 & 0 & 0 & 1 \\ 0 & 1 & -1 & 0 & 0 & 0 & 0 & 0 & 1 & 0 & 1 & 0 \end{bmatrix}. \tag{2.1.2}$$

For the EM field calculation of the square unit cell (i.e. $\Delta l = \Delta x = \Delta y = \Delta z$, where Δx, Δy and Δz are the lengths of the unit cell along x, y and z axes) the next equations apply:

$$\begin{aligned} E_{(x,\,y,\,z)} &= -\frac{V_{(x,\,y,\,z)}}{\Delta l} \\ &= -\frac{V^i_{(1,\,3,\,5)} + V^i_{(2,\,4,\,6)} + V^i_{(9,\,11,\,7)} + V^i_{(12,\,8,\,10)}}{2\Delta l} \end{aligned} \tag{2.1.3}$$

$$\begin{aligned} H_{(x,\,y,\,z)} &= \frac{I_{(x,\,y,\,z)}}{\Delta l} \\ &= \frac{V^i_{(4,\,6,\,1)} + V^i_{(7,\,9,\,11)} - V^i_{(5,\,2,\,3)} - V^i_{(8,\,10,\,12)}}{2Z_0\Delta l}. \end{aligned} \tag{2.1.4}$$

In these equations E, H, I and Z_0 denote the electric field, the magnetic field, the current and the free–space impedance, respectively. For the three sets of the numbers or letters in the small brackets, same positions apply. For example, for E_x

$$E_x = -\frac{V_x}{\Delta l} = -\frac{V^i_1 + V^i_2 + V^i_9 + V^i_{12}}{2\Delta l}.$$

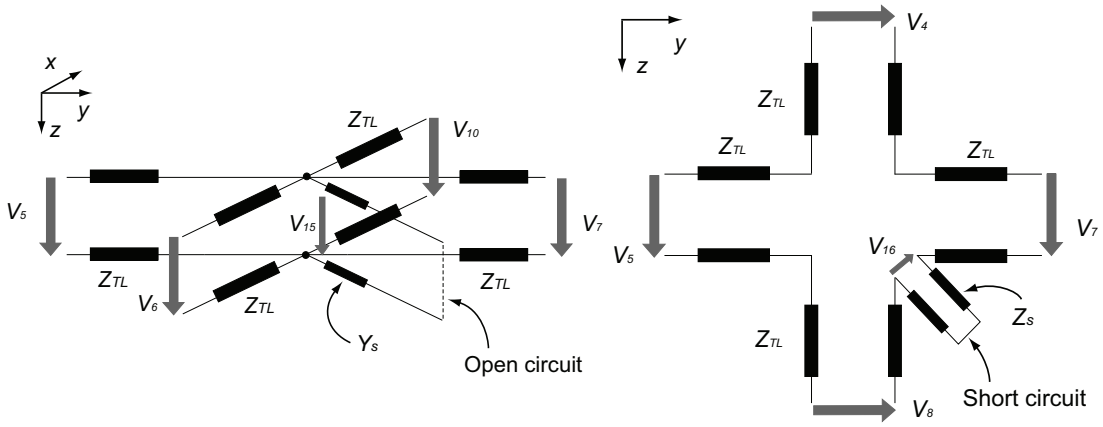

Figure 2.4: Implementation example of lossless electric property for z axis component (left) and magnetic property for x axis component (right) into TLM unit cell. The subscripts TL and s respectively indicate values of the transmission line (i.e. the impedance without the inserted electric and magnetic properties) and the extra stubs (to describe the electromagnetic properties), and Y_s and Z_s are calculated as eqs. (2.1.11) and (2.1.12) [85].

2.1.3 Modelling of Lossless Materials

The inclusion of dielectric and/or magnetic materials is accomplished through the addition of six extra ports (stubs) (see Fig. 2.4), i.e. $\mathbf{V}$ of eq. (2.1.1) becomes $\mathbf{V} = [V_1\ V_2\ \cdots\ V_{18}]^t$. V_{13} to V_{15} are used for expressing the dielectric property, while V_{16} to V_{18} for the magnetic property. V_{13} and V_{16} are used for x axis components; V_{14} and V_{17} for y axis components; V_{15} and V_{18} for z axis components. Also the scattering matrix is changed to the next form [85]:

$$\mathbf{S} = \begin{bmatrix} \mathbf{A} & \mathbf{B} \\ \mathbf{C} & \mathbf{D} \end{bmatrix}, \tag{2.1.5}$$

where

$$\mathbf{A} = \begin{bmatrix} a & b & d & 0 & 0 & 0 & 0 & 0 & b & 0 & -d & c \\ b & a & 0 & 0 & 0 & d & 0 & 0 & c & -d & 0 & b \\ d & 0 & a & b & 0 & 0 & 0 & b & 0 & 0 & c & -d \\ 0 & 0 & b & a & d & 0 & -d & c & 0 & 0 & b & 0 \\ 0 & 0 & 0 & d & a & b & c & -d & 0 & b & 0 & 0 \\ 0 & d & 0 & 0 & b & a & b & 0 & -d & c & 0 & 0 \\ 0 & 0 & 0 & -d & c & b & a & d & 0 & b & 0 & 0 \\ 0 & 0 & b & c & -d & 0 & d & a & 0 & 0 & b & 0 \\ b & c & 0 & 0 & 0 & -d & 0 & 0 & a & d & 0 & b \\ 0 & -d & 0 & 0 & b & c & b & 0 & d & a & 0 & 0 \\ -d & 0 & c & b & 0 & 0 & 0 & b & 0 & 0 & a & d \\ c & b & -d & 0 & 0 & 0 & 0 & 0 & b & 0 & d & a \end{bmatrix}, \tag{2.1.6}$$

$$\mathbf{B} = \begin{bmatrix} g & 0 & 0 & 0 & 0 & i \\ g & 0 & 0 & 0 & -i & 0 \\ 0 & g & 0 & 0 & 0 & -i \\ 0 & g & 0 & i & 0 & 0 \\ 0 & 0 & g & -i & 0 & 0 \\ 0 & 0 & g & 0 & i & 0 \\ 0 & 0 & g & -i & 0 & 0 \\ 0 & g & 0 & -i & 0 & 0 \\ g & 0 & 0 & 0 & i & 0 \\ 0 & 0 & g & 0 & -i & 0 \\ 0 & g & 0 & 0 & 0 & i \\ g & 0 & 0 & 0 & 0 & -i \end{bmatrix}, \tag{2.1.7}$$

$$\mathbf{C} = \begin{bmatrix} e & e & 0 & 0 & 0 & 0 & 0 & 0 & e & 0 & 0 & e \\ 0 & 0 & e & e & 0 & 0 & 0 & e & 0 & 0 & e & 0 \\ 0 & 0 & 0 & 0 & e & e & e & 0 & 0 & e & 0 & 0 \\ 0 & 0 & 0 & f & -f & 0 & f & -f & 0 & 0 & 0 & 0 \\ 0 & -f & 0 & 0 & 0 & f & 0 & 0 & f & -f & 0 & 0 \\ f & 0 & -f & 0 & 0 & 0 & 0 & 0 & 0 & 0 & f & -f \end{bmatrix}, \tag{2.1.8}$$

$$\mathbf{D} = \begin{bmatrix} h & 0 & 0 & 0 & 0 & 0 \\ 0 & h & 0 & 0 & 0 & 0 \\ 0 & 0 & h & 0 & 0 & 0 \\ 0 & 0 & 0 & j & 0 & 0 \\ 0 & 0 & 0 & 0 & j & 0 \\ 0 & 0 & 0 & 0 & 0 & j \end{bmatrix}. \tag{2.1.9}$$

Each coefficient can be calculated from

$$\begin{aligned} a &= \frac{-\hat{Y}}{2(4+\hat{Y})} + \frac{\hat{Z}}{2(4+\hat{Z})} \\ b &= \frac{4}{2(4+\hat{Y})} \\ c &= \frac{-\hat{Y}}{2(4+\hat{Y})} - \frac{\hat{Z}}{2(4+\hat{Z})} \\ d &= \frac{4}{2(4+\hat{Z})} \\ e &= b \\ f &= \hat{Z}d \\ g &= \hat{Y}b \\ h &= \frac{\hat{Y}-4}{\hat{Y}+4} \\ i &= d \\ j &= \frac{4-\hat{Z}}{4+\hat{Z}}. \end{aligned} \tag{2.1.10}$$

The coefficients need to take account which axis component is calculated. For example,

$$d_{(6,\,9)} = \frac{4}{2(4+\hat{Z}_y)},$$

where the subscript numbers of d represent the voltage ports and correspond to the orders of the row and column of eq. (2.1.5). Y and Z are respectively the admittance and impedance describing the dielectric property and magnetic property, and $\hat{}$ denotes normalising the values by those of vacuum, e.g.

$$Y_x = 2\varepsilon\frac{\Delta y\Delta z}{\Delta x\Delta t} - \frac{4}{Z_0} \tag{2.1.11}$$

$$Z_x = 2\mu\frac{\Delta y\Delta z}{\Delta x\Delta t} - 4Z_0 \tag{2.1.12}$$

$$\hat{Y}_x = 2\varepsilon_r\frac{\Delta y\Delta z}{\Delta x\Delta t c_0} - 4 \tag{2.1.13}$$

$$\hat{Z}_x = 2\mu_r\frac{\Delta y\Delta z}{\Delta x\Delta t c_0} - 4, \tag{2.1.14}$$

where $\varepsilon_r = \varepsilon/\varepsilon_0$ and $\mu_r = \mu/\mu_0$. ε and μ represent the permittivity and the permeability, and the subscripts 0 and r indicate the values of vacuum ($\mu_0 = 4\pi \times 10^{-7}$ [H/m] and $\varepsilon_0 = 1/\mu_0 c_0^2$ [F/m] where c_0 is the speed of light $c_0 = 299792458$ [m/s]) and the relative values to those of the vacuum. For cube unit cells ($\Delta l = \Delta x = \Delta y = \Delta z$) the normalised Y and Z become

$$\hat{Y}_x = 2\varepsilon_r\frac{\Delta l}{\Delta t c_0} - 4 \tag{2.1.15}$$

$$\hat{Z}_x = 2\mu_r\frac{\Delta l}{\Delta t c_0} - 4. \tag{2.1.16}$$

Electromagnetic fields for the lossless materials can be calculated from:

$$\begin{aligned} & E_{(x,\,y,\,z)} = -\frac{V_{(x,\,y,\,z)}}{\Delta l} \\ = & -\frac{2\left(V^i_{(1,\,3,\,5)} + V^i_{(2,\,4,\,6)} + V^i_{(9,\,11,\,7)} + V^i_{(12,\,8,\,10)} + \hat{Y}_{(x,\,y,\,z)}V^i_{(13,\,14,\,15)}\right)}{\Delta l\left(4 + \hat{Y}_{(x,\,y,\,z)}\right)} \end{aligned} \tag{2.1.17}$$

$$\begin{aligned} & H_{(x,\,y,\,z)} = \frac{I_{(x,\,y,\,z)}}{\Delta l} \\ = & \frac{2\left(V^i_{(4,\,6,\,1)} + V^i_{(7,\,9,\,11)} - V^i_{(5,\,2,\,3)} - V^i_{(8,\,10,\,12)}\right)}{\Delta l\left(4Z_0 + Z_0\hat{Z}_{(x,\,y,\,z)}\right)}. \end{aligned} \tag{2.1.18}$$

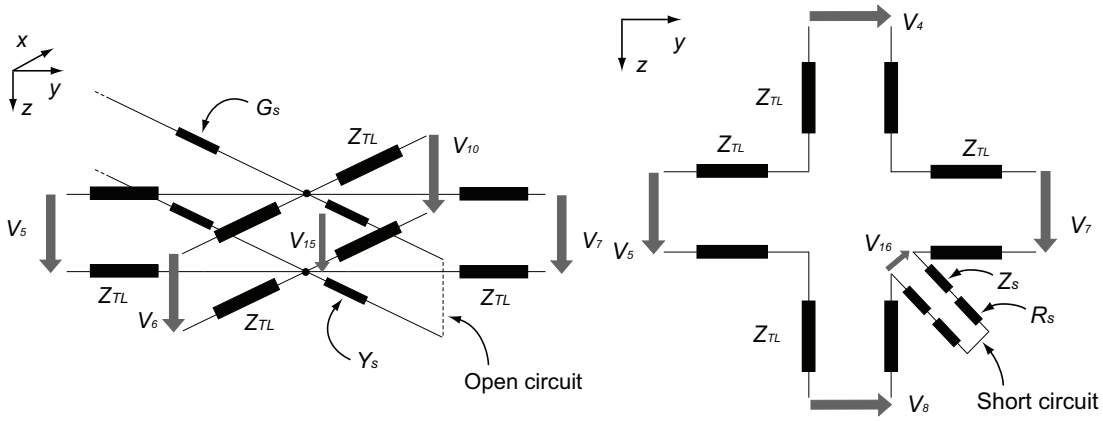

Figure 2.5: Implementation example of lossy electric property for z axis component (left) and magnetic property for x axis component (right) into TLM unit cell. The subscripts TL and s respectively indicate values of the transmission line (i.e. the impedance without the inserted electric and magnetic properties) and the extra stubs (to describe the electromagnetic properties), and Y_s, Z_s, G_s and R_s are calculated as eqs. (2.1.11), (2.1.12), (2.1.20) and (2.1.21) [85].

Again, as with eqs. (2.1.3) and (2.1.4), same positions of factors are extracted from the small brackets, i.e. to obtain the x–component magnetic field we need port voltages 4, 7, 5 and 8.

2.1.4 Modelling of Lossy Materials

For the scattering process of lossy dielectric or/and magnetic materials whose lossy behaviour is described in the TLM unit cells as shown in Fig. 2.5, the same scattering matrices as those of lossless materials (i.e. eqs. (2.1.5) to (2.1.9))

are applicable, but eq. (2.1.10) is modified as below [85]:

$$\begin{aligned}
a &= -\frac{\hat{Y}+\hat{G}}{2(\hat{Y}+\hat{G}+4)}+\frac{\hat{Z}+\hat{R}}{2(\hat{Z}+\hat{R}+4)} \\
b &= \frac{4}{2(\hat{Y}+\hat{G}+4)} \\
c &= -\frac{\hat{Y}+\hat{G}}{2(\hat{Y}+\hat{G}+4)}-\frac{\hat{Z}+\hat{R}}{2(\hat{Z}+\hat{R}+4)} \\
d &= \frac{4}{2(\hat{Z}+\hat{R}+4)} \\
e &= b \\
f &= \hat{Z}d \\
g &= \hat{Y}b \\
h &= \frac{\hat{Y}-\hat{G}-4}{\hat{Y}+\hat{G}+4} \\
i &= d \\
j &= \frac{4-\hat{R}-\hat{Z}}{4+\hat{R}+\hat{Z}}.
\end{aligned} \tag{2.1.19}$$

Analogous to the lossless cases, each coefficient calculation is dependent on which voltage port pair and which axis are considered. Also, G and R represent the electric loss and magnetic loss, and again $\hat{}$ denotes normalising G and R to the admittance and impedance of vacuum, i.e.

$$G_x = \sigma_{ex}\frac{\Delta y \Delta z}{\Delta x} \tag{2.1.20}$$

$$R_x = \sigma_{mx}\frac{\Delta y \Delta z}{\Delta x} \tag{2.1.21}$$

$$\hat{G}_x = \sigma_{ex}\frac{\Delta y \Delta z}{\Delta x Y_0} \tag{2.1.22}$$

$$\hat{R}_x = \sigma_{mx}\frac{\Delta y \Delta z}{\Delta x Z_0} \tag{2.1.23}$$

for $\Delta x = \Delta y = \Delta z = \Delta l$,

$$\hat{G}_x = \frac{\sigma_{ex}\Delta l}{Y_0} \tag{2.1.24}$$

$$\hat{R}_x = \frac{\sigma_{mx}\Delta l}{Z_0}, \tag{2.1.25}$$

where the conductivities associated with the electric loss and magnetic loss along x axis, σ_{ex} and σ_{mx}, are calculated from

$$\sigma_{ex} = \omega\varepsilon_r\varepsilon_0 \tan\delta_{ex} \tag{2.1.26}$$

$$\sigma_{mx} = \omega\mu_r\mu_0 \tan\delta_{mx}, \tag{2.1.27}$$

where ω is the angular frequency $\omega = 2\pi f$. Therefore, the electric loss and magnetic loss are determined depending on the ratio of the imaginary part to the real part of the electromagnetic properties at a frequency f:

$$\tan\delta_{ex} = \frac{\sigma_{ex}}{2\pi f\varepsilon_r\varepsilon_0} \tag{2.1.28}$$

$$\tan\delta_{mx} = \frac{\sigma_{mx}}{2\pi f\mu_r\mu_0}. \tag{2.1.29}$$

2.2 Wire Modelling

Round straight wires are modelled in the thesis, based on the technique described in [87, 88]. In this method, as is illustrated in Fig. 2.6, the round wires are deployed in the centre of TLM unit cells and their interaction with the EM field is modelled by the equivalent circuit shown in Fig. 2.7. This equivalent circuit is interfaced to the relevant voltage ports of the TLM unit cells (see Fig. 2.6).

First of all, assuming that the wire modelled is aligned along x axis, the telegrapher's equations for the wire can be described by [87, 88]

$$-\frac{\partial V_w}{\partial x} = \frac{L_w - L_0}{\Delta l}\frac{\partial I_w}{\partial t} + \frac{R_w}{\Delta l}I_w - \frac{V_x}{\Delta l} \tag{2.2.1}$$

$$-\frac{\partial I_w}{\partial x} = \frac{C_w}{\Delta l}\frac{\partial V_w}{\partial t}, \tag{2.2.2}$$

where V_w is the wire potential, I_w is the wire current, $(L_w - L_0)/\Delta l$ is the wire inductance per length, L_0 is the inductance associated with the external electric field and calculated from $L_0 = \Delta t Z_0/8$, and Δt is the time step in the TLM simulation. Also, $R_w/\Delta l$ and $C_w/\Delta l$ are the wire resistance and capaci-

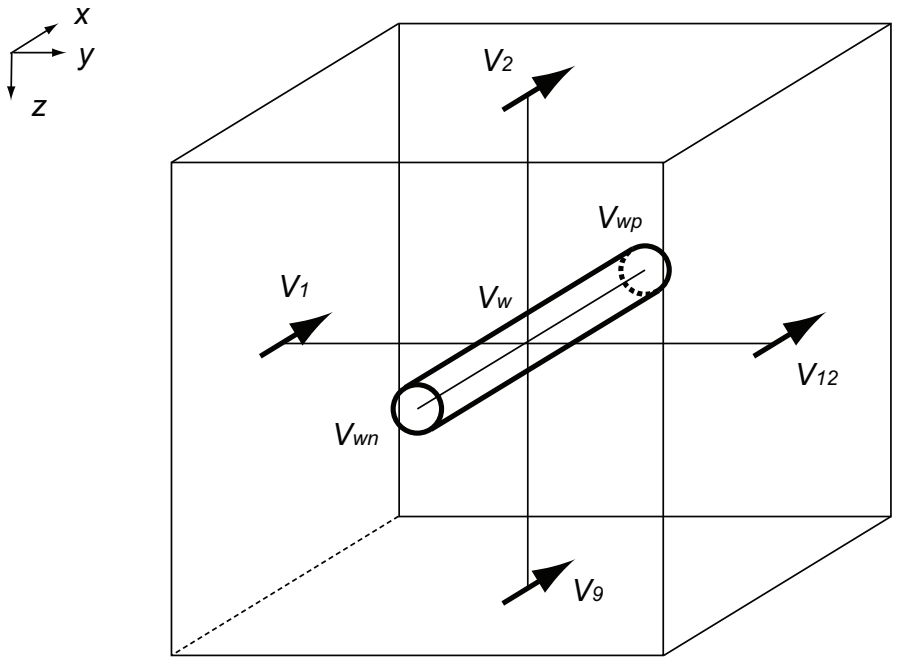

Figure 2.6: Round wire modelled in centre of TLM unit cell.

tance per length. The wire inductance and capacitance per length are respectively expressed by $L_w/\Delta l = \mu_0 k_w$ and $C_w/\Delta l = \varepsilon_0 k_w$, and k_w is a frequency–independent dimensionless geometrical factor. Since the velocity of propagation of charge density variations along the wire is the speed of light (i.e. $c = \Delta l/\sqrt{L_w C_w}$), the characteristic impedance of the wire becomes

$$Z_w = \sqrt{\frac{L_w}{C_w}} = Z_0 k_w = \frac{Z_0}{2\pi} \ln \frac{1.08\Delta l}{2r}, \tag{2.2.3}$$

where r is the radius of the wire. Normalising the wire current, the time derivative and space derivative as below:

$$I_w = \frac{i_w}{Z_0} \tag{2.2.4}$$

$$\frac{\partial}{\partial x} = \frac{1}{\Delta l}\frac{\partial}{\partial X} \tag{2.2.5}$$

$$\frac{\partial}{\partial t} = \frac{1}{\Delta t}\frac{\partial}{\partial T}, \tag{2.2.6}$$

since the maximum time step in the three–dimensional TLM calculations is $\Delta t = \Delta l/(2c)$ [85], the telegrapher's equations (eqs. (2.2.1) and (2.2.2)) can be

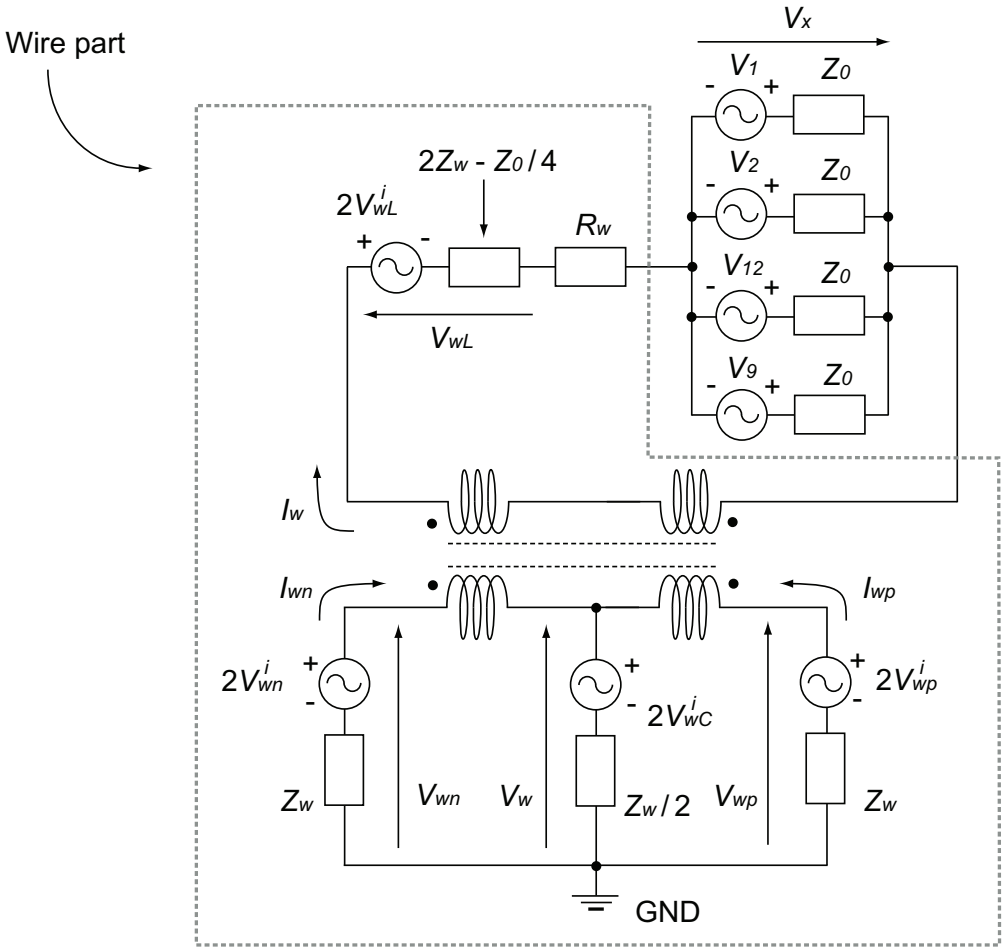

Figure 2.7: Equivalent circuit of round wire.

modified as the next forms:

$$-\frac{\partial V_w}{\partial X} = \left(2 - \frac{y_{0w}}{8}\right)\frac{\partial i_w}{\partial T} + r_w i_w - V_x \tag{2.2.7}$$

$$-\frac{\partial i_w}{\partial X} = 2\frac{\partial V_w}{\partial T}, \tag{2.2.8}$$

where r_w is the normalised wire resistance ($r_w = R_w / Z_w$). These equations can be converted to the travelling wave format using the equivalences [89]

$$\begin{aligned} -\frac{\partial V_w}{\partial X} - \frac{\partial i_w}{\partial T} &= 2V^i_{w4} - 2V^i_{w5} - 2i_w \\ -\frac{\partial i_w}{\partial X} - \frac{\partial V_w}{\partial T} &= 2V^i_{w4} + 2V^i_{w5} - 2V_w, \end{aligned} \tag{2.2.9}$$

resulting in

$$\begin{aligned} 2V^i_{w4} - 2V^i_{w5} &= \frac{\partial i_w}{\partial T} + (2 + r_w) i_w - V_x \\ 2V^i_{w4} + 2V^i_{w5} &= \frac{\partial V_w}{\partial T} + 2V_w. \end{aligned} \tag{2.2.10}$$

The derivatives of the equations are converted to a stub format [85, 90] using

$$\begin{aligned} \left(1 - \frac{y_{0w}}{8}\right) \frac{\partial i_w}{\partial T} &= 2V^i_{wL} + \left(2 - \frac{y_{0w}}{4}\right) i_w \\ \frac{\partial V_w}{\partial T} &= 2V_w - 4V^i_{wC}, \end{aligned} \tag{2.2.11}$$

where V^i_{wL} is the incident voltage on the inductive stub and V^i_{wC} is the incident voltage on the capacitive stub. Here the normalised conduction current i_w can be used for x axis of the total voltage V_x, i.e.

$$V_x = \frac{V^i_1 + V^i_2 + V^i_9 + V^i_{12}}{2} - \frac{i_e}{4}, \tag{2.2.12}$$

where $i_e = y_{0w} i_w$ and $y_{0w} = Z_0 / Z_w$. Assuming $V^r_x = V^i_1 + V^i_2 + V^i_9 + V^i_{12}$ gives

$$V_x = \frac{V^r_x}{2} - \frac{y_{0w}}{4} i_w. \tag{2.2.13}$$

Substituting eqs. (2.2.11) and (2.2.13) into eq. (2.2.10) leads to

$$\begin{aligned} i_w &= T_w \left(2V^i_{w4} - 2V^i_{w5} - 2V^i_{wL} + \frac{V^r_x}{2}\right) \\ V_w &= \frac{2V^i_{w4} + 2V^i_{w5} + 4V^i_{wC}}{4}, \end{aligned} \tag{2.2.14}$$

where $T_w = (4 + r_w)^{-1}$. Also, the transformers used to couple the field and wire are assumed to be ideal and have a 1:1 turn ratio, i.e.

$$i_w = \frac{i_{w4} - i_{w5}}{2}. \tag{2.2.15}$$

The stub incident voltages at the next time step are calculated from

$$\begin{aligned} {}_{k+1}V^i_{wL} &= -\,{}_kV^r_{wL} = -\left[{}_kV^i_{wL} + \left(2 - \frac{y_{0w}}{4}\right) i_w\right] \\ {}_{k+1}V^i_{wC} &= {}_kV^r_{wC} = {}_kV_w - {}_kV^i_{wC}, \end{aligned} \tag{2.2.16}$$

and the reflected wire voltage pulses are given by

$$\begin{aligned} V_{w4}^{r} &= V_w - i_w - V_{w5}^{i} \\ V_{w5}^{r} &= V_w + i_w - V_{w4}^{i}. \end{aligned} \tag{2.2.17}$$

For the actual TLM programming, the calculation steps consist of scattering and swapping (including the connection with the external field) processes, which are similar to the TLM calculation processes of vacuum. The scattering step is carried out by using eq. (2.2.17), and then the voltages are swapped with those of the neighbour cells. If the swapped cell is an edge of the wire, then the new incident voltage becomes equal to the scattered voltage (open circuit boundary condition). If the wire is connected to metal plate, then the new incident voltage is same as the scattered voltage but with the opposite sign (short circuit boundary condition). Finally, for the coupling process with the external field (i.e. the connection with the associated voltage ports of the TLM unit cells), i_w and V_w renewed by eq. (2.2.14) are used for the calculation of the total voltage of the unit cell, i.e. eq. (2.2.13). This calculation result is applied in the next equation, where Maxwell's equations are expressed as a form directly applicable to the TLM calculations [87]:

$$\begin{bmatrix} V_x \\ V_y \\ V_z \\ i_x \\ i_y \\ i_z \end{bmatrix} = \frac{1}{2} \begin{bmatrix} V_1^i + V_2^i + V_{12}^i + V_9^i \\ V_3^i + V_4^i + V_{11}^i + V_8^i \\ V_6^i + V_5^i + V_{10}^i + V_7^i \\ -(V_4^i - V_8^i - V_5^i + V_7^i) \\ -(V_6^i - V_{10}^i - V_2^i + V_9^i) \\ -(V_1^i - V_{12}^i - V_3^i + V_{11}^i) \end{bmatrix}. \tag{2.2.18}$$

The reflected voltages are calculated by the next equation together with eq. (2.2.18)

$$\begin{bmatrix} V_2^r \\ V_9^r \\ V_1^r \\ V_{12}^r \\ V_3^r \\ V_{11}^r \\ V_4^r \\ V_8^r \\ V_5^r \\ V_7^r \\ V_6^r \\ V_{10}^r \end{bmatrix} = \begin{bmatrix} V_x - i_y - V_9^r \\ V_x + i_y - V_2^r \\ V_x + i_z - V_{12}^r \\ V_x - i_z - V_1^r \\ V_y - i_z - V_{11}^r \\ V_y + i_z - V_3^r \\ V_y + i_x - V_8^r \\ V_y - i_x - V_4^r \\ V_z - i_x - V_7^r \\ V_z + i_x - V_5^r \\ V_z + i_y - V_{10}^r \\ V_z - i_y - V_6^r \end{bmatrix}. \tag{2.2.19}$$

These reflected voltages are used for the swapping processes of the main TLM calculations explained in subsection 2.1.1. In addition to these, the incident voltages of the inductor and capacitor parts of the wire need to be renewed by eq. (2.2.16) after eq. (2.2.14).

2.3 Huygen's Surface Implementation

2.3.1 Introduction

This thesis uses Huygen's surface, based on the equivalence theorem [91, 92]. The basic idea for the implementation of the Huygen's surface into the TLM method can be found from [92]. Huygen's surface makes it possible to launch waves at an arbitrary direction as an option which is very useful for testing the performance of absorbing boundaries to waves incident at an angle. In this scheme the incident electric field and magnetic field are expressed by tangential magnetic current source **M** and electric current source **J**, which are imple-

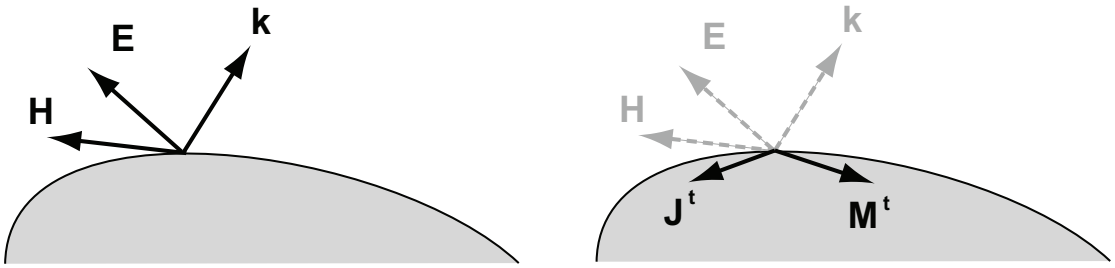

Figure 2.8: Incident wave (left) represented by Huygen's sources (right).

mented on the Huygen's surface (see Fig. 2.8). As is mentioned in [91], if the tangential fields produced by the Huygen's sources are correct everywhere on the boundary, then they are correct everywhere in the confined region. This idea is visualised in Fig. 2.9, where the situation to be simulated (the left of Fig. 2.9) is realised by using the Huygen's surface. In this case only the inside of the calculation space has the incident wave, while the scattering wave appears in the whole space. In the TLM calculation algorithms the Huygen's sources are incorporated in the new incident voltage calculations (i.e. the swapping processes), so that using the Huygen's surface can be equivalent with exciting the arbitrary angles of the incident waves.

2.3.2 Implementation of Huygen's Surface in the TLM Method

The implementation of the Huygen's surface scheme into the TLM calculation algorithms can be achieved by addressing the next three points. First, the Huygen's sources represent the incident electric field and magnetic field, which differs in accordance with the time delay and voltage port position at each TLM unit cell. Hence, the Huygen's sources **M** and **J** need to take account of the time–and–position–dependent fields at every time step. For the second and third points **M** and **J** need to be expressed by the excited electromagnetic fields and the incident voltages. In this way the assumed incident electromagnetic fields are converted into **M** and **J**, and these Huygen's sources are incorporated into the analysis space through the voltage ports.

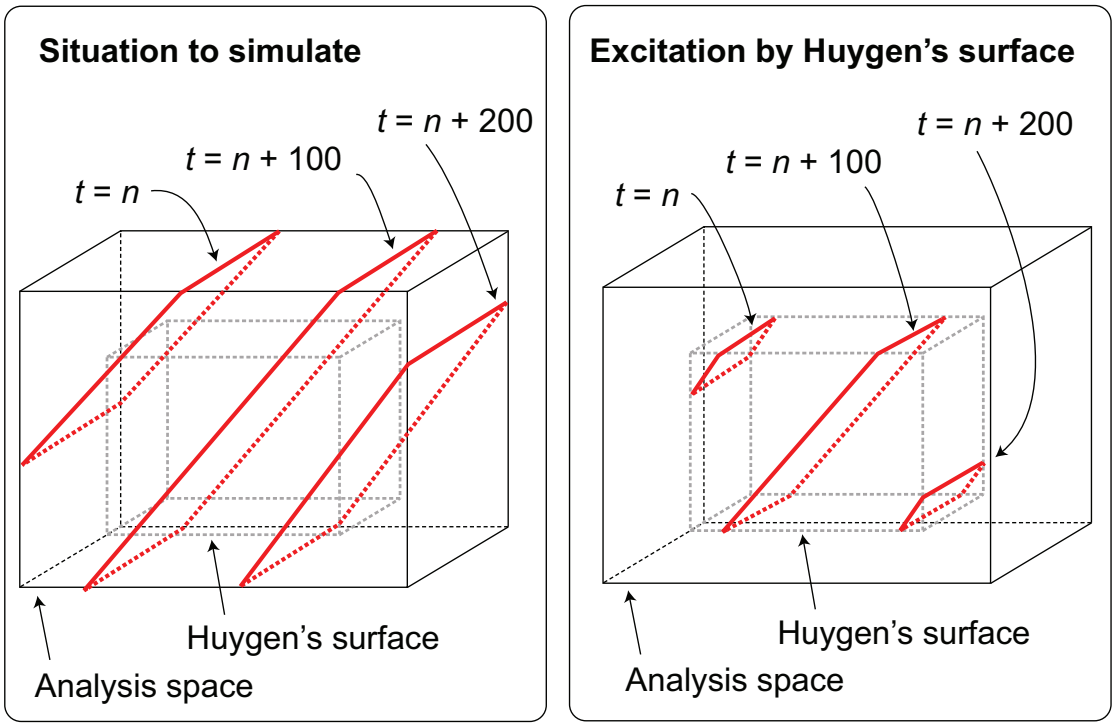

Figure 2.9: Excitation of electromagnetic wave by Huygen's surface. An impulse propagating in the analysis space at different time step t is drawn. The situation to be assumed (left) is simulated by using the Huygen's surface (right). If the tangential fields produced by the Huygen's sources are correct everywhere on the boundary in the right figure, then the same situation as the left figure can be realised in the right figure.

To exemplify the procedure, an oblique impulse illustrated in Fig. 2.10 is considered here. In this figure one of the incident field components (i.e. **E** or **H**) is vertical to yz plane and the wave front has an incident angle θ toward the positive direction of y axis measured anticlockwise. The region surrounded by the Huygen's surface has the dimension of $(i_x \times i_y \times i_z)$ cells, respectively, for x, y and z axes where i_x, i_y and i_z are positive integers, and the cells aligned along x, y and z axes begin at x_0, y_0 and z_0 and end at x_{i_x-1}, y_{i_y-1} and z_{i_z-1}. The time delay at each unit cell on the Huygen's surface is expressed by τ. For example, superscripts of the time delays $\tau^{yn}(z)$ and $\tau^{yp}(z)$ represent the time delays of the Huygen's surface at negative (n) and positive (p) direction sides

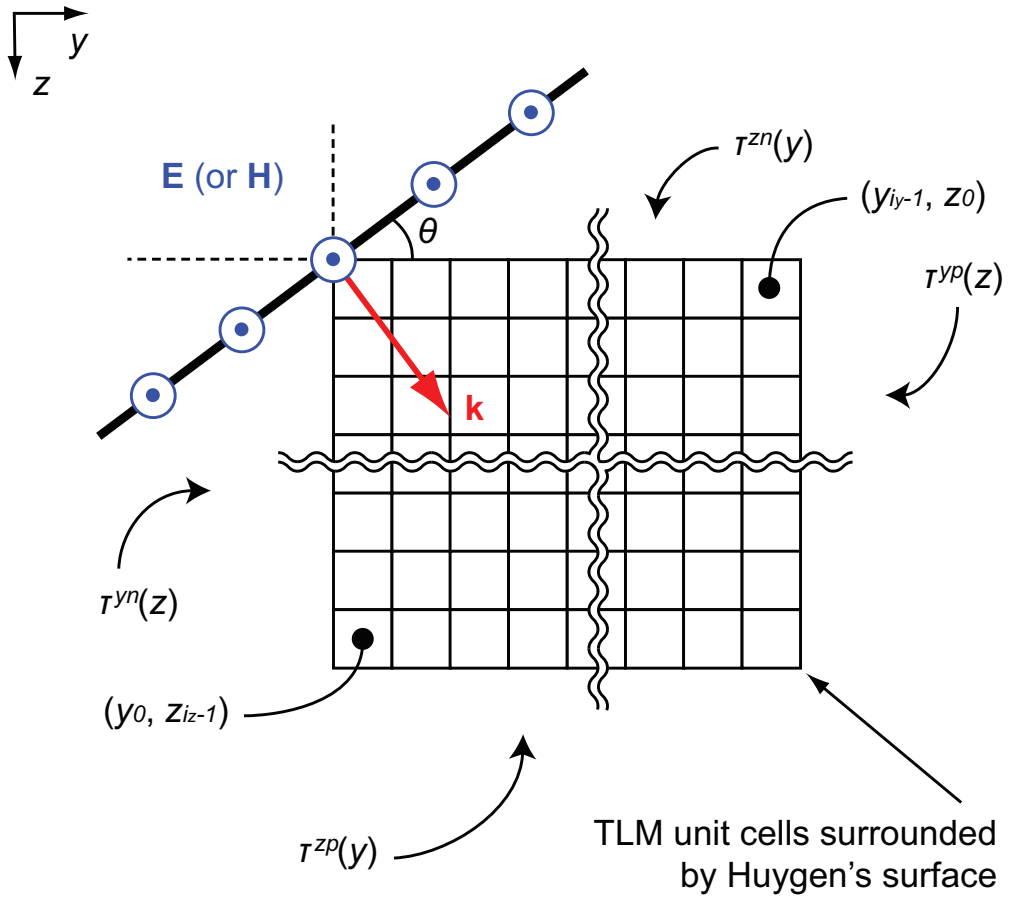

Figure 2.10: Oblique wave expressed by Huygen's sources and time delay on each boundary.

of y axis, respectively. z in the bracket denotes that the delays are functions of z axis position. The same manner is applied for the other parts of the surface so that the time delays at negative and positive directions of x, y and z axes are expressed by $\tau^{xn}(y,\, z)$, $\tau^{yn}(z)$, $\tau^{zn}(y)$, $\tau^{xp}(y,\, z)$, $\tau^{yp}(z)$, and $\tau^{zp}(y)$, respectively.

For the first step of the Huygen's surface implementation, the time delays at each voltage port of the TLM unit cells are calculated. These calculations are made by taking account of the distance between each voltage port and the wave front, as described in Fig. 2.11. For example, $\tau^{yn}(z)$ is calculated from

$$\tau^{yn}(z) \;=\; \frac{(0.5 + z - z_0)\Delta l \cos\theta}{c}. \tag{2.3.1}$$

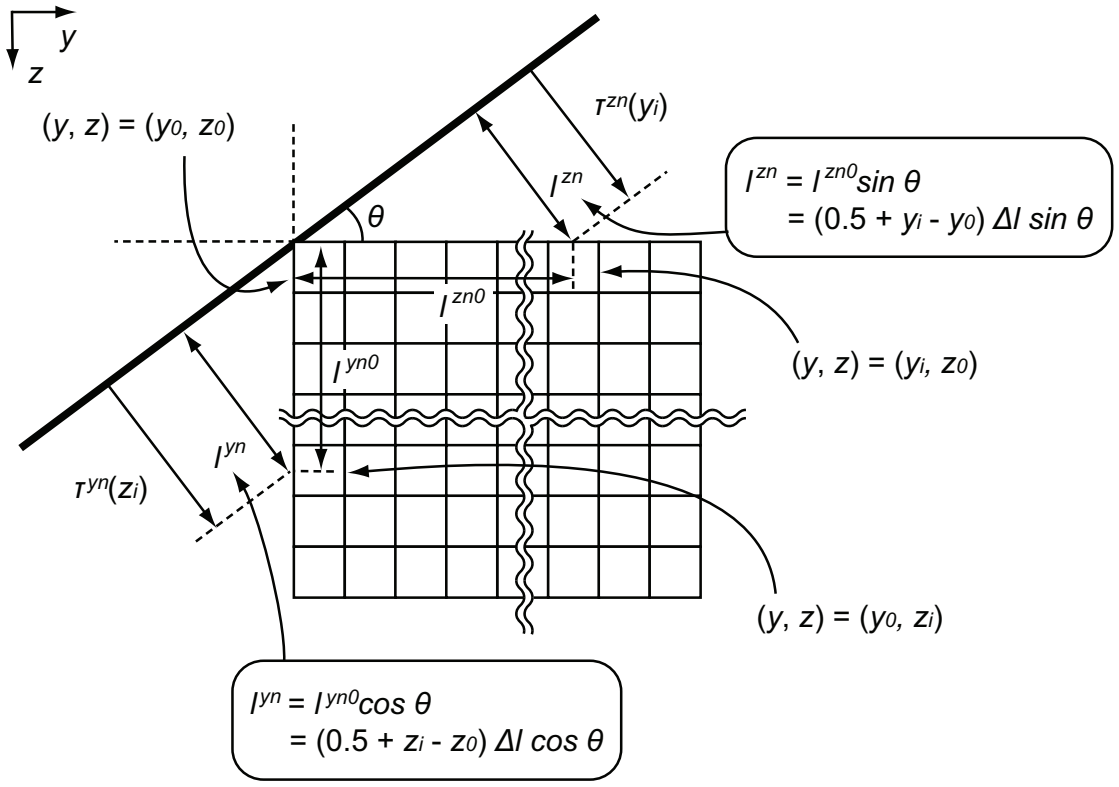

Figure 2.11: Time delay calculations.

The other delays are obtained from

$$\tau^{yp}(z) = \frac{(0.5 + z - z_0 + (y_{i_y - 1} - y_0 + 1)\tan\theta)\Delta l \cos\theta}{c} \quad (2.3.2)$$

$$\tau^{zn}(y) = \frac{(0.5 + y - y_0)\Delta l \sin\theta}{c} \quad (2.3.3)$$

$$\tau^{zp}(y) = \frac{((z_{i_z - 1} - z_0 + 1) + (0.5 + y - y_0)\tan\theta)\Delta l \cos\theta}{c} \quad (2.3.4)$$

$$\tau^{xn}(y,\, z) = \frac{((0.5 + z - z_0 + 1) + (0.5 + y - y_0)\tan\theta)\Delta l \cos\theta}{c} \quad (2.3.5)$$

$$\tau^{xp}(y,\, z) = \tau^{xn}(y,\, z). \quad (2.3.6)$$

Secondly, the Huygen's sources are defined by the incident electric field and magnetic field. From the generalised current concept derived from Maxwell's equations [93], electromagnetic fields associated with a magnetic current source

and electric current source can be expressed by

$$\begin{aligned} \nabla \times \mathbf{E} &= -\mathbf{M}^t \\ \nabla \times \mathbf{H} &= \mathbf{J}^t, \end{aligned} \tag{2.3.7}$$

where t denotes the tangential components. This equation can be applied for the surface of the TLM unit cells by taking rotations of, respectively, the electric field and magnetic field around the unit vector $\mathbf{n}$ normal to the surface and directed to the internal region, i.e.

$$\mathbf{M}^t = ({}^{\mathbf{in}}\mathbf{E} - {}^{\mathbf{out}}\mathbf{E}) \times \mathbf{n} \tag{2.3.8}$$

$$\mathbf{J}^t = \mathbf{n} \times ({}^{\mathbf{in}}\mathbf{H} - {}^{\mathbf{out}}\mathbf{H}), \tag{2.3.9}$$

where **in** and **out** represent the inside and the outside of the region surrounded by the Huygen's surface. If the fields of the outside are set to 0 (i.e. ${}^{\mathbf{out}}\mathbf{E} = \mathbf{0}$ and ${}^{\mathbf{out}}\mathbf{H} = \mathbf{0}$), then

$$\mathbf{M} = \mathbf{E} \times \mathbf{n} \tag{2.3.10}$$

$$\mathbf{J} = \mathbf{n} \times \mathbf{H}, \tag{2.3.11}$$

where t and **in** are suppressed. From simple vector calculations the Huygen's sources on each boundary are expressed by the electric field and magnetic field as below:

$$\mathbf{M}^{\mathbf{yn}} = -\mathbf{M}^{\mathbf{yp}} = (-E_z,\ 0,\ E_x) \tag{2.3.12}$$

$$\mathbf{J}^{\mathbf{yn}} = -\mathbf{J}^{\mathbf{yp}} = (H_z,\ 0,\ -H_x) \tag{2.3.13}$$

$$\mathbf{M}^{\mathbf{zn}} = -\mathbf{M}^{\mathbf{zp}} = (E_y,\ -E_x,\ 0) \tag{2.3.14}$$

$$\mathbf{J}^{\mathbf{zn}} = -\mathbf{J}^{\mathbf{zp}} = (-H_y,\ H_x,\ 0) \tag{2.3.15}$$

$$\mathbf{M}^{\mathbf{xn}} = -\mathbf{M}^{\mathbf{xp}} = (0,\ E_z,\ -E_y) \tag{2.3.16}$$

$$\mathbf{J}^{\mathbf{xn}} = -\mathbf{J}^{\mathbf{xp}} = (0,\ -H_z,\ H_y), \tag{2.3.17}$$

where the superscripts (e.g. yn) are used in the same manner with those of eqs. (2.3.1) to (2.3.6). The subscripts x, y and z represent the components of the incident fields along x, y and z axes. Eqs. (2.3.12) to (2.3.17) are summarised in

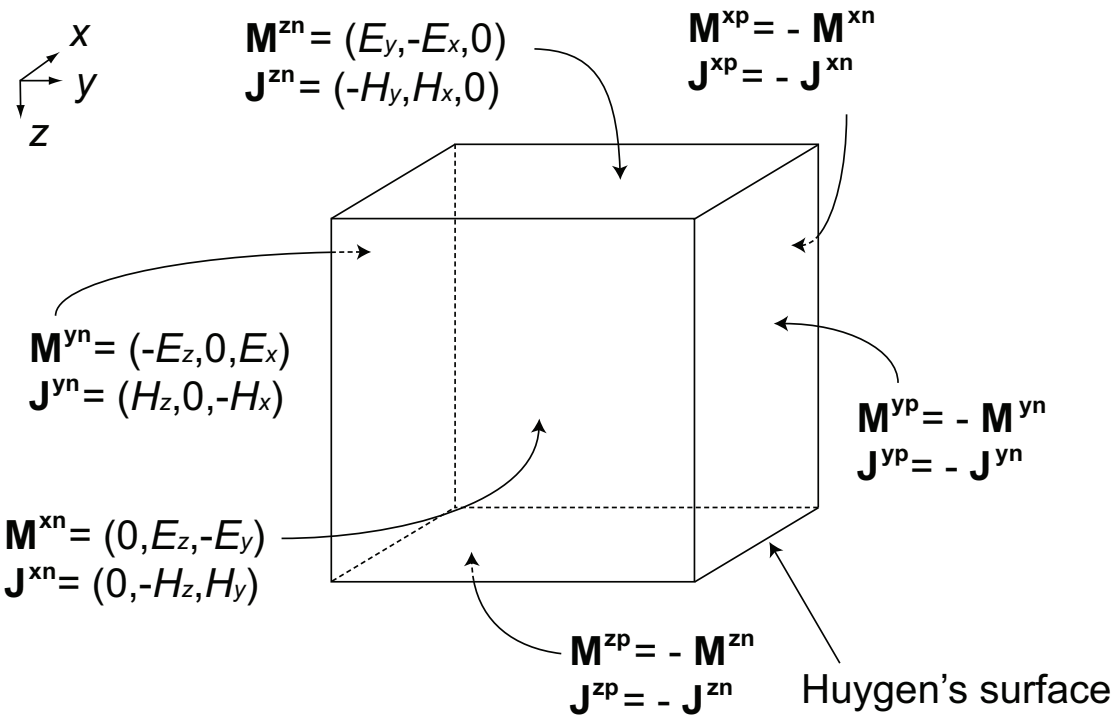

Figure 2.12: Magnetic current sources **M** and electric current sources **J** on Huygen's surface.

Fig. 2.12.

Finally, the Huygen's sources are expressed by the incident voltages of the ports facing the Huygen's surface. This can be achieved by considering how each field is expressed by the voltage ports. For example, for the boundary at the negative direction of z axis (see Fig. 2.13),

$$M_x^{zn} = {}^{in}E_y - {}^{out}E_y \equiv ({}^{in}V_4^i + {}^{in}V_4^r) - ({}^{out}V_8^i + {}^{out}V_8^r) \quad (2.3.18)$$

$$J_y^{zn} = {}^{in}H_x - {}^{out}H_x \equiv \frac{({}^{in}V_4^i - {}^{in}V_4^r) - ({}^{out}V_8^r - {}^{out}V_8^i)}{Z_0} \quad (2.3.19)$$

and

$$-M_y^{zn} = {}^{in}E_x - {}^{out}E_x \equiv ({}^{in}V_2^i + {}^{in}V_2^r) - ({}^{out}V_9^i + {}^{out}V_9^r) \quad (2.3.20)$$

$$-J_x^{zn} = {}^{in}H_y - {}^{out}H_y \equiv \frac{({}^{in}V_2^r - {}^{in}V_2^i) - ({}^{out}V_9^i - {}^{out}V_9^r)}{Z_0}, \quad (2.3.21)$$

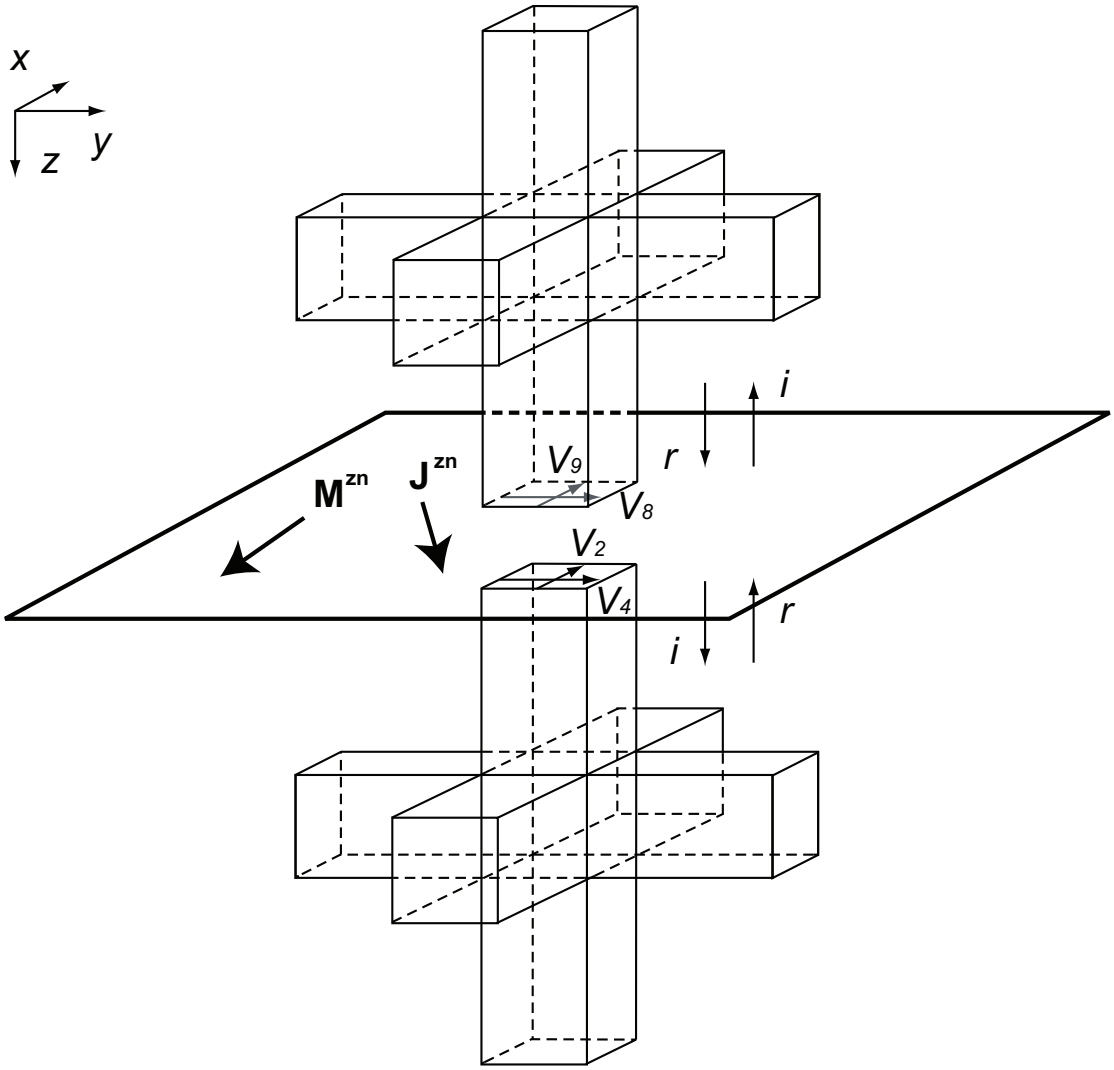

Figure 2.13: Magnetic current source **M** and electric current source **J** for the boundary at the negative direction of z axis.

where the subscripts x and y represent x and y axis components of each current source. Solving these equations for ${}^{in}V_4$, ${}^{out}V_8$, ${}^{in}V_2$ and ${}^{out}V_9$ leads to

$$\begin{aligned}
{}^{in}V_4^i &= \frac{1}{2}(M_x^{zn} + Z_0 J_y^{zn}) + {}^{out}V_8^r \\
{}^{out}V_8^i &= -\frac{1}{2}(M_x^{zn} - Z_0 J_y^{zn}) + {}^{in}V_4^r \\
{}^{in}V_2^i &= -\frac{1}{2}(M_y^{zn} - Z_0 J_x^{zn}) + {}^{out}V_9^r \\
{}^{out}V_9^i &= \frac{1}{2}(M_x^{zn} + Z_0 J_y^{zn}) + {}^{in}V_2^r. \qquad (2.3.22)
\end{aligned}$$

The same procedure can be applied for the other boundaries. To sum up these,

for the internal voltage ports

$$ {}^{in}V^{i}_{(4,\,6,\,1)} = \frac{1}{2}\left(M^{(zn,\,xn,\,yn)}_{(x,\,y,\,z)} + Z_0 J^{(zn,\,xn,\,yn)}_{(y,\,z,\,x)} \right) + {}^{out}V^{r}_{(8,\,10,\,12)} \tag{2.3.23} $$

$$ {}^{in}V^{i}_{(8,\,10,\,12)} = -\frac{1}{2}\left(M^{(zp,\,xp,\,yp)}_{(x,\,y,\,z)} - Z_0 J^{(zp,\,xp,\,yp)}_{(y,\,z,\,x)} \right) + {}^{out}V^{r}_{(4,\,6,\,1)} \tag{2.3.24} $$

$$ {}^{in}V^{i}_{(2,\,3,\,5)} = -\frac{1}{2}\left(M^{(zn,\,xn,\,yn)}_{(y,\,z,\,x)} - Z_0 J^{(zn,\,xn,\,yn)}_{(x,\,y,\,z)} \right) + {}^{out}V^{r}_{(9,\,11,\,7)} \tag{2.3.25} $$

$$ {}^{in}V^{i}_{(9,\,11,\,7)} = \frac{1}{2}\left(M^{(zp,\,xp,\,yp)}_{(y,\,z,\,x)} + Z_0 J^{(zp,\,xp,\,yp)}_{(x,\,y,\,z)} \right) + {}^{out}V^{r}_{(2,\,3,\,5)}. \tag{2.3.26} $$

For the voltage ports of the external region

$$ {}^{out}V^{i}_{(4,\,6,\,1)} = \frac{1}{2}\left(M^{(zp,\,xp,\,yp)}_{(x,\,y,\,z)} + Z_0 J^{(zp,\,xp,\,yp)}_{(y,\,z,\,x)} \right) + {}^{in}V^{r}_{(8,\,10,\,12)} \tag{2.3.27} $$

$$ {}^{out}V^{i}_{(8,\,10,\,12)} = -\frac{1}{2}\left(M^{(zn,\,xn,\,yn)}_{(x,\,y,\,z)} - Z_0 J^{(zn,\,xn,\,yn)}_{(y,\,z,\,x)} \right) + {}^{in}V^{r}_{(4,\,6,\,1)} \tag{2.3.28} $$

$$ {}^{out}V^{i}_{(2,\,3,\,5)} = -\frac{1}{2}\left(M^{(zp,\,xp,\,yp)}_{(y,\,z,\,x)} - Z_0 J^{(zp,\,xp,\,yp)}_{(x,\,y,\,z)} \right) + {}^{in}V^{r}_{(9,\,11,\,7)} \tag{2.3.29} $$

$$ {}^{out}V^{i}_{(9,\,11,\,7)} = \frac{1}{2}\left(M^{(zn,\,xn,\,yn)}_{(y,\,z,\,x)} + Z_0 J^{(zn,\,xn,\,yn)}_{(x,\,y,\,z)} \right) + {}^{in}V^{r}_{(2,\,3,\,5)}. \tag{2.3.30} $$

This is summarised in Fig. 2.14.

For the calculation processes in the TLM simulations, first of all, after reflecting the time delay at each voltage port position (eqs. (2.3.1) to (2.3.6)), excited electromagnetic fields are calculated. Secondly, the excited fields are converted to the Huygen's sources using eqs. (2.3.12) to (2.3.17). Finally, the Huygen's sources are incorporated in the voltage ports through eqs. (2.3.23) to (2.3.30) so that inside the Huygen's surface the excitation of the arbitrary angles of the incident wave can be realised.

It may be also useful to mention that these calculations can be simplified for specific situations to improve the calculation efficiencies. For example, if a TE wave is simulated, the electric field **E** and magnetic field **H** become **E**=(E_x,

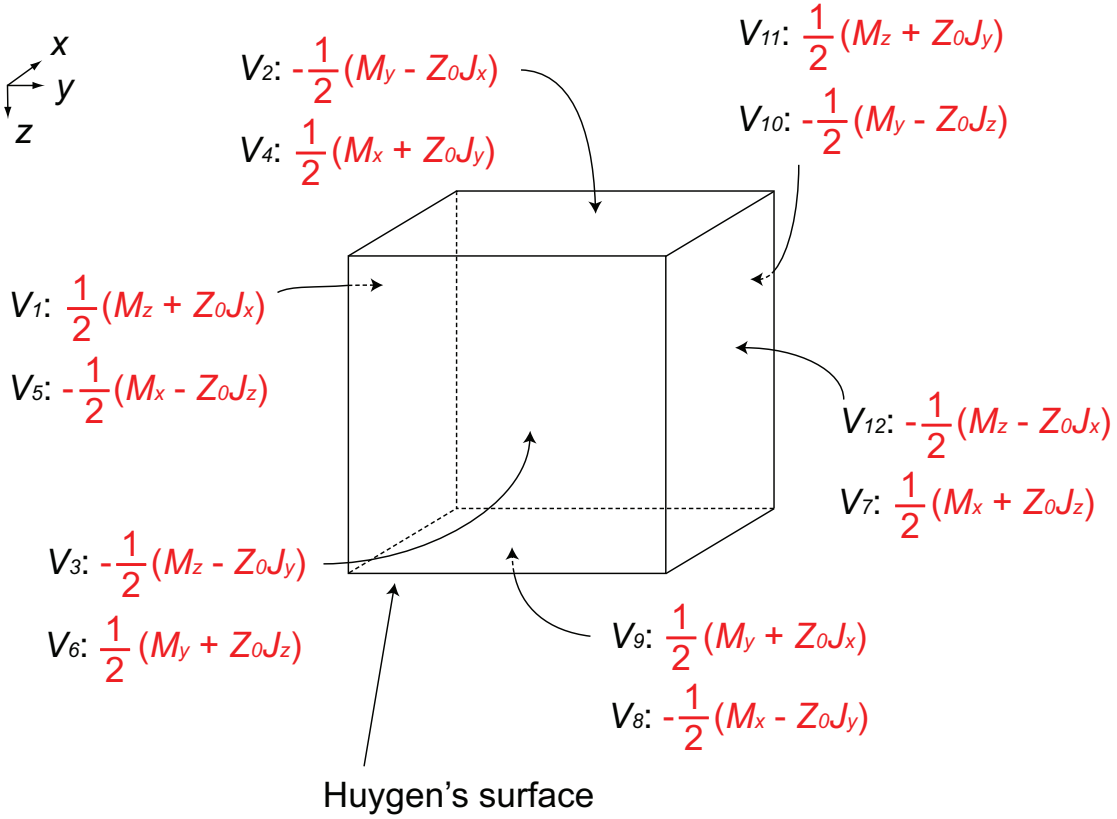

Figure 2.14: Positions of each voltage port with added Huygen's source.

$E_y,\ E_z) = (E_0,\ 0,\ 0)$ and $\mathbf{H}$=$(H_x,\ H_y,\ H_z)$=$(0,\ H_0\cos\theta,\ -H_0\sin\theta)$, respectively, where E_0 and H_0 are the magnitudes of the excited electric and magnetic fields. The incident angle θ is same with Fig. 2.10. In this case applying the electromagnetic field components to eqs. (2.3.12) to (2.3.17) leads to

$$\mathbf{M_{yn}} = -\mathbf{M_{yp}} = (0,\ 0,\ E_0) \tag{2.3.31}$$

$$\mathbf{J_{yn}} = -\mathbf{J_{yp}} = (-H_0\sin\theta,\ 0,\ 0) \tag{2.3.32}$$

$$\mathbf{M_{zn}} = -\mathbf{M_{zp}} = (0,\ -E_0,\ 0) \tag{2.3.33}$$

$$\mathbf{J_{zn}} = -\mathbf{J_{zp}} = (-H_0\cos\theta,\ 0,\ 0) \tag{2.3.34}$$

$$\mathbf{M_{xn}} = -\mathbf{M_{xp}} = \mathbf{0} \tag{2.3.35}$$

$$\mathbf{J_{xn}} = -\mathbf{J_{xp}} = (0,\ H_0\sin\theta,\ H_0\cos\theta). \tag{2.3.36}$$

Compared to eqs. (2.3.12) to (2.3.17), the above equations are found to have smaller numbers of components. This means the reduction of the calculation amount, resulting in the improvement of the calculation speed. Also, substitut-

ing these equations to eqs. (2.3.23) to (2.3.30) and removing the zero Huygen's sources can further economise the computational effort.

Although this section showed an example of free space, it is also possible to use the Huygen's surface placed in dielectric or/and magnetic material(s). In this case some modifications are necessary, such as revisions on electromagnetic fields entering and leaving the internal region (i.e. revisions on eqs. (2.3.18) to (2.3.21)) as well as the delay time.

2.4 Other Aspect of the Simulation

2.4.1 Wave Forms of Excited Waves

For wave forms of excited waves a Gaussian pulse or constant sinusoidal wave is used. The Gaussian pulse programmed in numerical simulations is expressed by the next equation as a function of the time step number N:

$$f[N] = A \exp\left[\frac{\ln[r](N\Delta t - t_0)^2}{h^2}\right], \tag{2.4.1}$$

where Δt and t_0 are respectively the time step and the time delay. For analysis spaces composed of cube unit cells in the thesis, Δt is generally set to $\Delta l/2c$. A, r and h are the amplitude, truncation amplitude (fixed at 0.001 in this thesis) and half width, respectively.

For the sinusoidal wave of a constant frequency f_s, the following expression is applied:

$$f[N] = A(1 - \exp[-\alpha(N\Delta t - t_0)])\sin[2\pi f_s N\Delta t + \phi]u[N\Delta t - t_0], \tag{2.4.2}$$

where ϕ is the phase shift and α is the exponential soft-start coefficient:

$$\alpha = -\frac{2\pi f_s \ln(0.01)}{10\pi}. \tag{2.4.3}$$

2.4.2 Boundary Conditions

This thesis uses matched, short–circuit and open–circuit boundaries for boundary conditions. In these cases voltages reflected from each type of the boundaries (i.e. new incident voltages in the next time step ${}_{k+1}V^i$) become

$$
\begin{aligned}
{}_{k+1}V^i = 0 \qquad & \text{(for matched boundary)} && (2.4.4)\\
{}_{k+1}V^i = {}_kV^r \qquad & \text{(for open circuit boundary)} && (2.4.5)\\
{}_{k+1}V^i = -{}_kV^r \qquad & \text{(for short circuit circuit).} && (2.4.6)
\end{aligned}
$$

In addition, periodic boundary is used for expressing periodicities of metamaterials. In this case the reflected voltages going out from the boundaries re–enter the exactly same position of the opposite boundaries, i.e.

$$
\begin{aligned}
V_1^i(x,\, y_0,\, z) &= V_{12}^r(x,\, y_{i_{y-1}},\, z)\\
V_2^i(x,\, y,\, z_0) &= V_9^r(x,\, y,\, z_{i_{z-1}})\\
V_3^i(x_0,\, y,\, z) &= V_{11}^r(x_{i_{x-1}},\, y,\, z)\\
V_4^i(x,\, y,\, z_0) &= V_8^r(x,\, y,\, z_{i_{z-1}})\\
V_5^i(x,\, y_0,\, z) &= V_7^r(x,\, y_{i_{y-1}},\, z)\\
V_6^i(x_0,\, y,\, z) &= V_{10}^r(x_{i_{x-1}},\, y,\, z)\\
V_7^i(x,\, y_{i_{y-1}},\, z) &= V_5^r(x,\, y_0,\, z)\\
V_8^i(x,\, y,\, z_{i_{z-1}}) &= V_4^r(x,\, y,\, z_0)\\
V_9^i(x,\, y,\, z_{i_{z-1}}) &= V_2^r(x,\, y,\, z_0)\\
V_{10}^i(x_{i_{x-1}},\, y,\, z) &= V_6^r(x_0,\, y,\, z)\\
V_{11}^i(x_{i_{x-1}},\, y,\, z) &= V_3^r(x_0,\, y,\, z)\\
V_{12}^i(x,\, y_{i_{y-1}},\, z) &= V_1^r(x,\, y_0,\, z), \qquad (2.4.7)
\end{aligned}
$$

where it is assumed that the calculation space has the dimension of $(i_x \times i_y \times i_z)$ cells, respectively, for x, y and z axes, and the cell positions along x, y and z axes begin at x_0, y_0 and z_0 and end at x_{i_x-1}, y_{i_y-1} and z_{i_z-1}.

2.4.3 Reflection and Transmission from Infinitesimally Thin Metal

Reflection and transmission from infinitesimally thin metal (including lossless metal and lossy metal) are determined in the way that the reflection coefficient Γ and transmission coefficient T are calculated from

$$\begin{aligned} \Gamma &= \frac{R_0 - Z_0}{R_0 + Z_0} \\ T &= \frac{2R_0}{R_0 + Z_0}, \end{aligned} \tag{2.4.8}$$

where Z_0 is the characteristic impedance in vacuum. R_0 is calculated from

$$R_0 = \frac{RZ_0}{R + Z_0}, \tag{2.4.9}$$

where R is the sheet resistance (in the unit of $[\Omega\square^{-1}]$). For lossless metal $R = 0$, resulting in $T = 0$. The conversion from resistance to sheet resistance is found from appendix A.

2.5 Conclusion

In this chapter, simulation techniques used in the thesis have been explained. This chapter covered a basic algorithm of the time–domain TLM method, wire-modelling, Huygen's surface implementation and some other techniques necessary for the metamaterial research introduced later. All the programme codes used in the thesis were built up by the author from the beginning to allow for easy modification and the introduction of new capabilities.

CHAPTER 3

Fundamental Scattering Properties

3.1 Introduction

This chapter introduces the fundamental characteristics of metamaterials by showing the scattering properties of some metamaterials. First of all, two types of resonances, i.e. electric resonance and magnetic resonance, are explained with two specific structures and then investigated in more detail to clarify the relationships between the resonant frequencies of the scatterers and the physical structure of the components. As mentioned in the next chapter, the resonant frequencies f can be generally predicted by the effective inductances L and effective capacitances C through the equation of $f = 1/2\pi\sqrt{LC}$. Thus, in some simulation results introduced here, the resonant frequencies are associated with these parameters L and C. Thirdly, this chapter describes scattering characteristics of another type of artificial structures called electromagnetic band gap (EBG) structures [94, 95]. No studies of scattering parameters at oblique incidence are shown in this chapter, but the capability of launching oblique waves was developed in appendix D. There was insufficient time for a full study to be included in the thesis and this part is therefore left as future investigations.

So far, many patterns of metamaterial geometries have been proposed to

satisfy a range of applications, such as low frequency or high frequency shifts, improvement in the scattering properties and realisation of multi–band characteristics. Specifically, axially symmetric SRRs have better transmission characteristics and the properties of **S**–shaped metamaterials becomes broadband, compared to the first metamaterials proposed by Smith et al. [8, 96].

Metamaterials can generally exhibit electric resonance or/and magnetic resonance, as shown in Fig. 3.1 where the two types of the resonances are explained using simple metamaterials. As shown in the left of Fig. 3.1, for the electric resonance the periodic metal geometry interacts with the incident wave, and a conduction current flows parallel to the incident electric field. As a result, the structure behaves as an electric dipole. Since the induced conduction current is in the opposite direction to the incident electric field, the artificial electric dipole can lead to a negative value of permittivity. On the other hand, at the magnetic resonance shown in the right figure of Fig. 3.1, the periodic metal geometry interacts with the incident wave so as to produce the conduction current circulating around the direction of the incident magnetic field. Similarly with the electric resonance, the metal components behave as an magnetic dipole and can lead to a negative values of permeability.

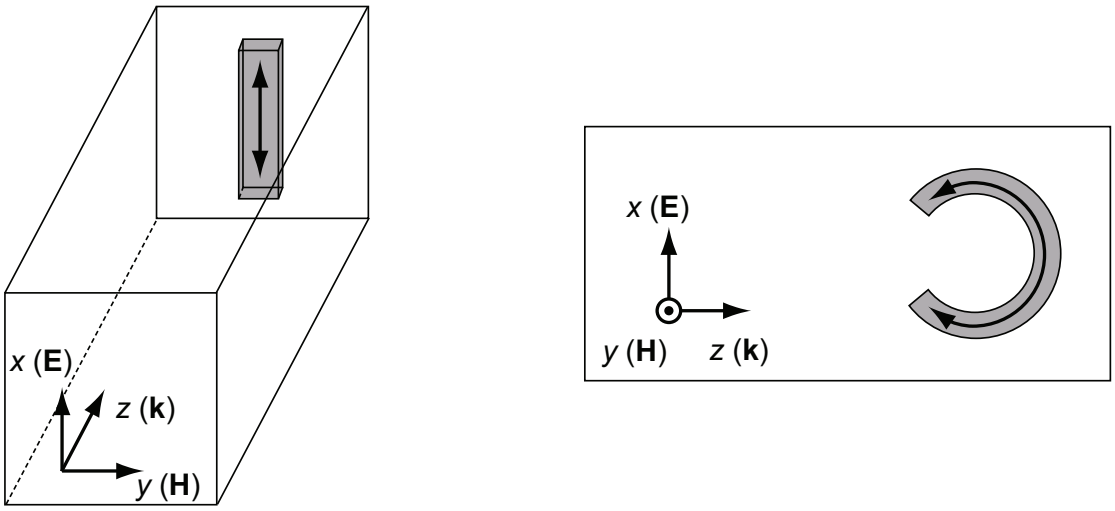

Figure 3.1: Electric resonance (left) and magnetic resonance (right).

3.2 Electric Resonance

In this section electric resonances are studied numerically using a **y**–shaped metamaterial [97, 98]. This structure is decomposed into several parts to examine the relationship between each part and the resonance frequencies. The decomposed parts become simple straight strips parallel or orthogonal to the incident electric field, which enable us to intuitively understand the resonance mechanism. For this reason, the **y**–shaped metamaterial is chosen here. In this section, calculation results of the conduction current are also used to confirm the resonant behaviour of the **y**–shaped metamaterial. Although this structure is not used directly in the absorber designs in chapter 7, it is nevertheless generic enough to warrant a full study.

The simulated structure and calculation conditions are summarised in Figs. 3.2 and 3.3, respectively. The default parameters are displayed on Table 3.1. As is described in Fig. 3.2 and Table 3.1, the **y**–shaped metal was composed of 2 cell width of lossless metal (i.e. $R = 0[\Omega\square^{-1}]$), where the edge lengths of the cubical TLM cells, Δl, was 0.1 mm. The dimension of the analysis space was composed of $(38 \times 26 \times 108)$ cells, respectively, for x, y and z axes. At the boundary periodic boundary conditions were deployed for the xz and yz planes so that the metamaterial simulated was assumed to spread infinitely on the xy plane. The observation planes were placed far enough from the front surface of the metamaterial (in this case $D_z = 50$ cells where D_z is the distance between the front surface of the material under test (MUT) and the observation planes). This configuration can be confirmed from Fig. 3.3.

The scattering parameters were calculated by the following procedure. At first, a Gaussian pulse was excited one cell above the observation plane of the reflection coefficient. The reflected voltages and transmitted voltages were sampled using the voltage ports of each observation plane at the MUT sides (i.e. in Fig. 2.3 the incident voltages at the port 9 and port 2 for the reflection

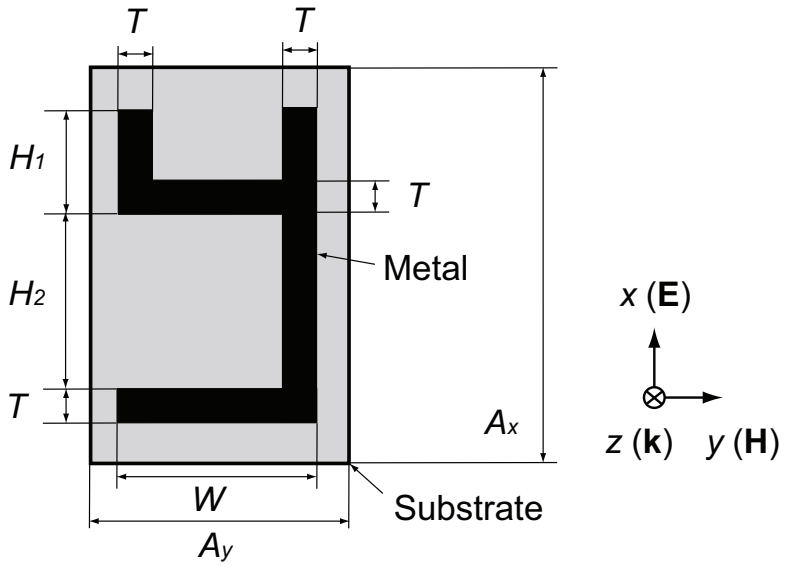

Figure 3.2: Calculation model for **y**–shaped metamaterial. This structure was used in the analysis space of Fig. 3.3 as the MUT so that the periodic boundaries were deployed for yz and zx boundaries.

Table 3.1: Default parameters of **y**–shaped metamaterial.

A_x	3.8 [mm]
A_y	2.6 [mm]
H_1	1.4 [mm]
H_2	1.8 [mm]
T	0.2 [mm]
W	2.4 [mm]
Substrate thickness	0.3 [mm]
Metal thickness	0.0 [mm]
Sheet resistance of metal	0.0 $\Omega\square^{-1}$
Relative permittivity of substrate	$2.2 \cdot (1.0 + j0.0)$
Relative permeability of substrate	$1.0 \cdot (1.0 + j0.0)$
TLM unit cell size	$0.1 \times 0.1 \times 0.1$ [mm^3]

and transmission, respectively). The sampled voltages were averaged in the time domain and then this process was repeated until the end of the iteration

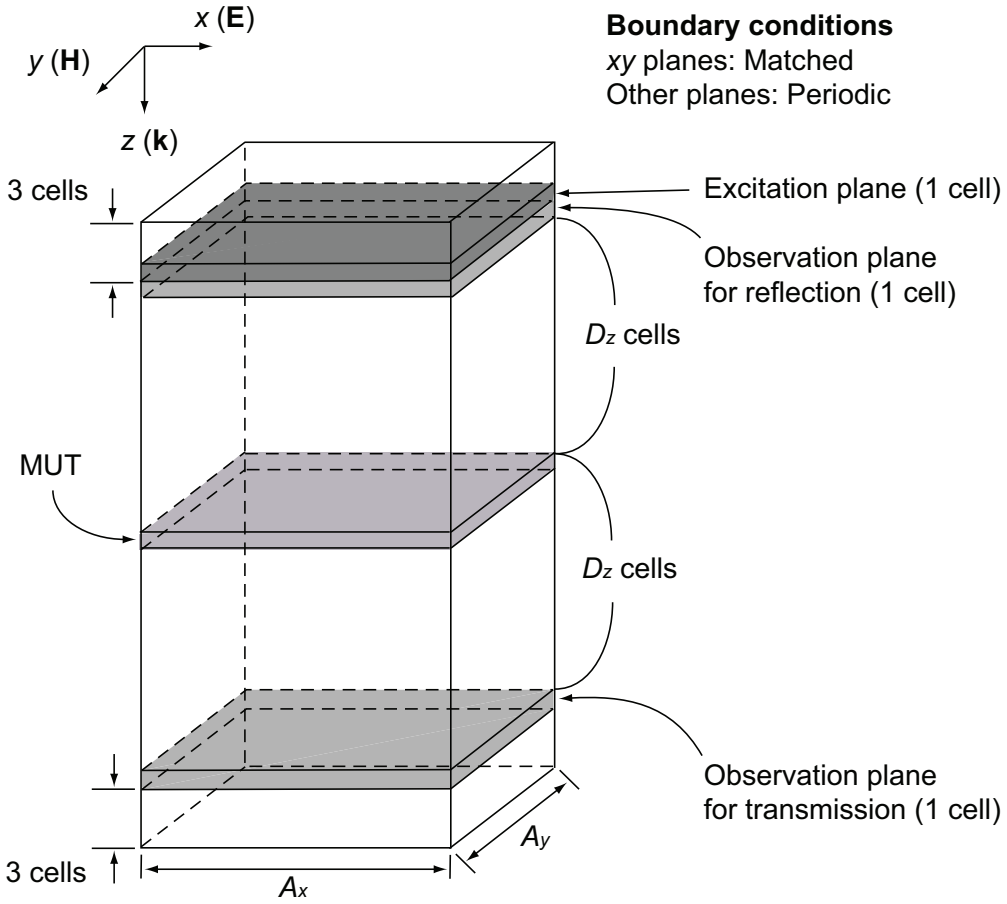

Figure 3.3: Simulation space for scattering parameter calculations.

(here 2^{16} = 65,536). Finally, a Fast Fourier Transform (FFT) was performed to calculate the magnitudes in the frequency domain. These values were divided by magnitudes of reflected voltages obtained from the pre–simulation where a perfect magnetic wall (PMC) was placed on the front surface of the MUT.

The calculated scattering parameters of the **y**–shaped metamaterial are shown in Figs. 3.4 and 3.5, where the reflection and transmission coefficients are respectively shown as a function of frequency up to 60 GHz. Within the frequency range shown here the **y**–shaped metamaterial exhibited three peaks for the reflection coefficient magnitude. Around the three peaks the reflection coefficient phase became $\pm$ 180 degrees. On the other hand, the magnitude of the transmission coefficient showed minima at the same frequencies.

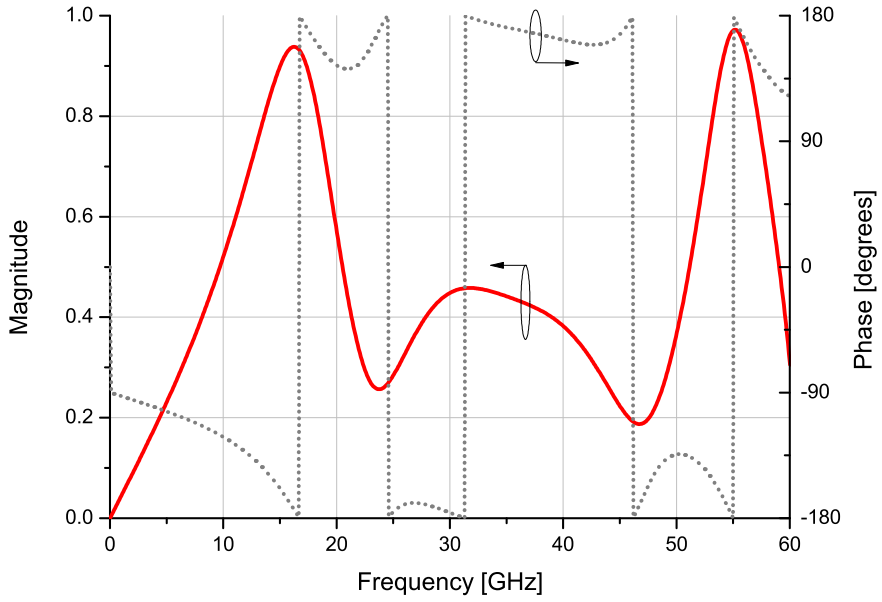

Figure 3.4: Magnitude and phase of reflection coefficient of **y**–shaped metamaterial.

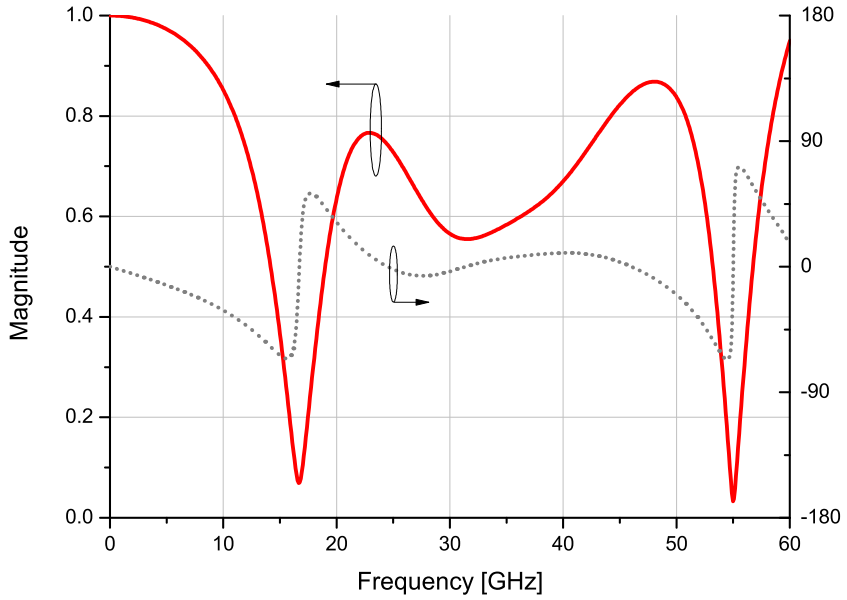

Figure 3.5: Magnitude and phase of transmission coefficient of **y**–shaped metamaterial.

To clarify the resonance mechanism at each frequency the surface current distributions of the **y**–shaped metamaterial at 16.29, 31.75 and 55.17 GHz (corresponding to the peaks of the reflection coefficient) are shown in Fig. 3.6. One of the most important points for the electric resonances is that the structure exhibits the strong conduction current distributions along the incident electric field direction, as explained in section 3.1.

As is found from Fig. 3.6, at the first resonant frequency one strong conduction current curve appeared in the structure. In the second resonant frequency, where the magnitude of the reflection coefficient was relatively smaller than the other two, a similar vertical conduction current path was found. However, in this case the calculation result showed another path going out from the main vertical path, and this became parallel to it along x axis. The opposite direction of the conduction current may be attributed to the reason for the weak resonance magnitude. In the third resonant frequency two current lines appeared. Although the conduction current paths are the opposite directions around the centre of the structure, along x axis (i.e. the direction of the incident electric field) the current directions became the same, which is assumed to contribute to the large magnitude of the reflection coefficient.

Next, the **y**–shaped metamaterial was decomposed into smaller parts, and each part is numbered as in Fig. 3.7. The reflection coefficients calculated from each part or several combined parts were calculated in Figs. 3.8 to 3.13, where the simulated models are illustrated together and the used part(s) is/are summarised on Table 3.2.

The simplest calculation results are found in Fig. 3.8 where the metal geometries of the simulated structures were composed of only one straight strip parallel to the incident electric field. This figure shows a very simple relationship between the strip length and the resonant frequency, i.e. as the strip length decreases, the resonant frequency increases as expected. In the shortest length

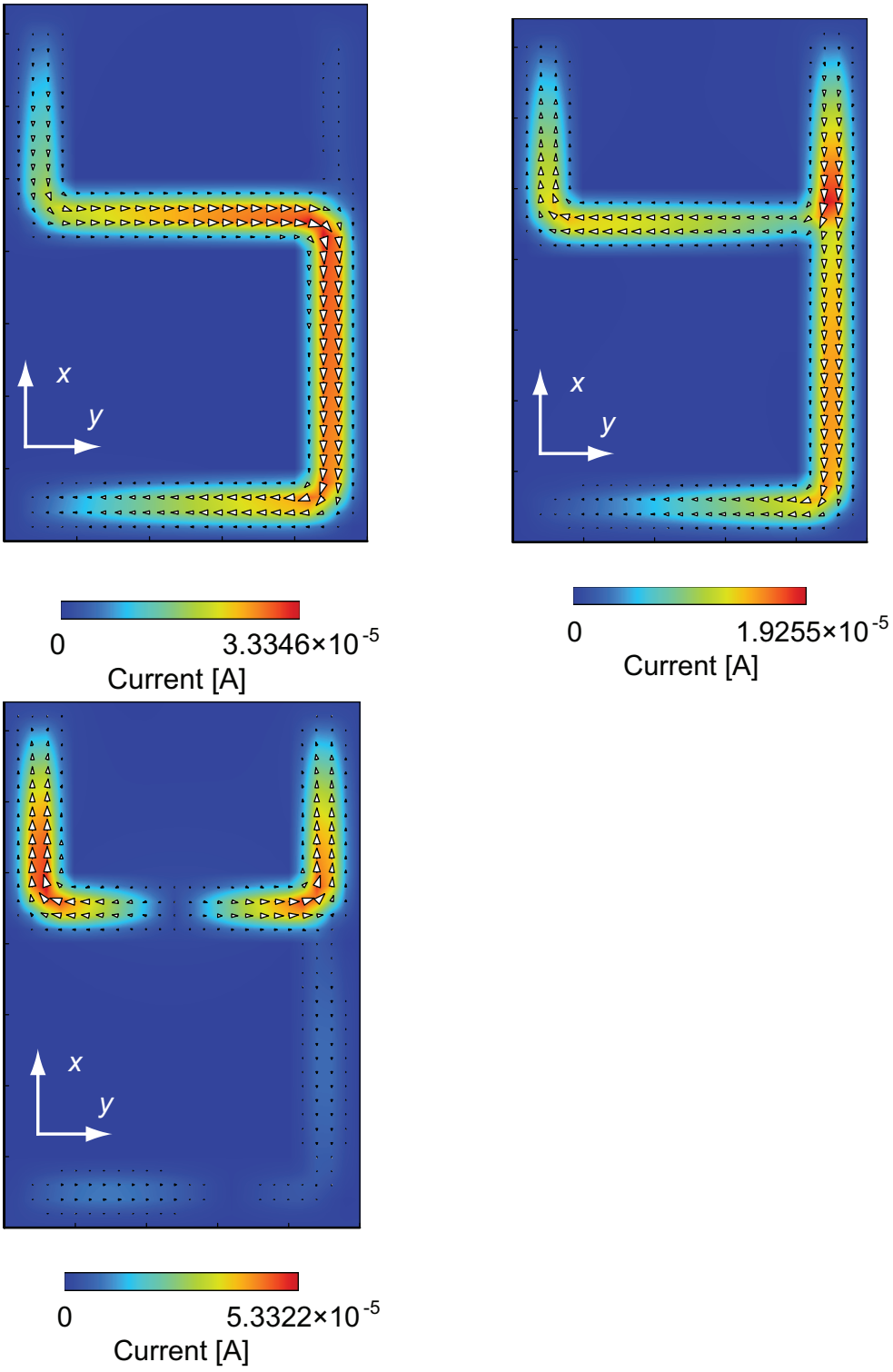

Figure 3.6: Current distribution calculated on the front surface of **y**–shaped metamaterial at 16.29 (top left), 31.75 (top right) and 55.17 GHz (bottom left).

Table 3.2: Summary of decomposed **y**–shaped metamaterial models. The numbers written in the right column indicates the used part(s) corresponding to that (those) of Fig. 3.7.

Model 1	2, 5, 6 and 8
Model 2	5, 6 and 8
Model 3	1
Model 4	3 to 5
Model 5	3, 4, 5, 7 and 8
Model 6	1, 2, 5, 6 and 8
Model 7	1 and 2
Model 8	1 to 5
Model 9	3 to 8
Model 10	2, 5, 6, 7 and 8
Model 11	2, 3, 4, 5, 6 and 8
Model 12	1, 3, 4, 5, 6, 7 and 8

case (i.e. model 3) the resonant frequency exceeded the frequency range shown here.

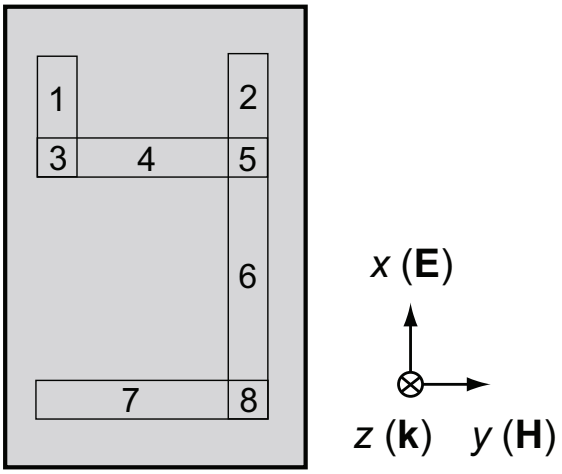

Figure 3.7: Decomposed and numbered **y**–shaped metamaterial parts.

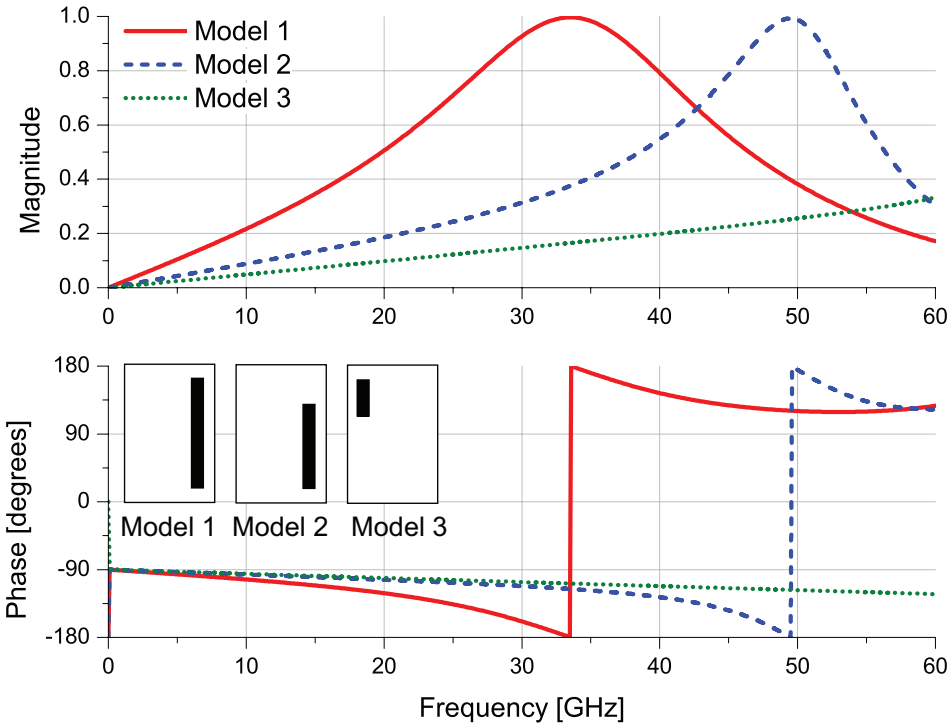

Figure 3.8: Reflection coefficient magnitudes (top) and phases (bottom) of decomposed **y**–shaped metamaterial models 1, 2 and 3.

Similar results are found in Fig. 3.9 where one straight strip or two was/were deployed along y axis (i.e. orthogonal to the incident electric field). In this case the lengths along x axis are too short, resulting in no resonance up to 60 GHz.

Fig. 3.10 shows results of two strips parallel to x axis. For the model 6 whose one of the strip lengths was same with model 1, the resonant frequency remained almost same with that of model 1. This means that in this case the shorter strip did not affect the resonant behaviour. For model 7 the resonant frequency was out of the range, as found in the result of model 3 whose strip length was same with those of model 7.

The two parallel strip pairs used for model 5 and 7 were connected by another strips in Fig. 3.11. Compared to model 7, model 8 exhibited a resonant frequency within the calculated frequency range. In part this is assumed to be because the conduction current path became longer enough. In addition,

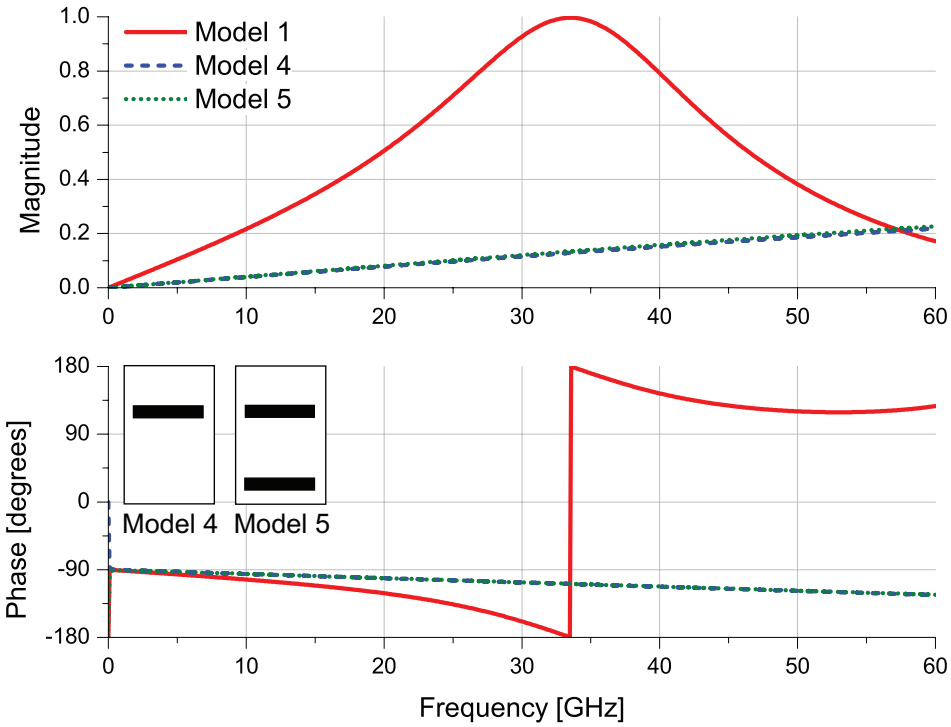

Figure 3.9: Reflection coefficient magnitudes (top) and phases (bottom) of decomposed **y**–shaped metamaterial models 1, 4 and 5.

mutual inductances and mutual capacitances might reduce the resonant frequency position. The same explanations can be applied for model 9 which showed two resonances up to 60 GHz.

Fig. 3.12 shows structures composed of a long straight wire (same with model 1) and another strip connected to it along y axis. Each structure exhibited two resonant frequencies. In model 10 the first resonance was found at frequency lower than that of model 1. It is expected that in the resonance the conduction current path appears at the whole part of the metal strip, which contributed to the increase of the inductance and thus decrease of the resonant frequency. In the second resonant frequency the structure might exhibit a high order mode of the first resonance, since the resonant frequency is almost double of the first resonant frequency. In model 11, associating the resonant frequencies with the current path lengths, the conduction current is expected to appear at the horizontal strip in addition to the bottom part of the vertical strip

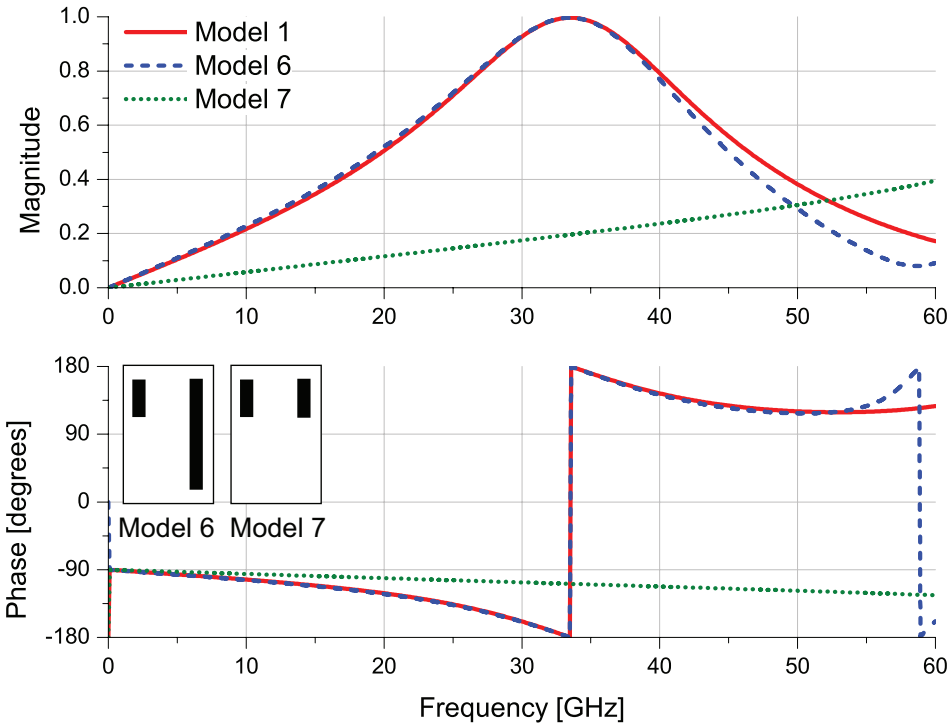

Figure 3.10: Reflection coefficient magnitudes (top) and phases (bottom) of decomposed **y**–shaped metamaterial models 1, 6 and 7.

for the lower resonance frequency, while for the higher resonant frequency only at the vertical strip.

In Fig. 3.13 the parts resonated at the first resonant frequency of the **y**–shaped metamaterial (i.e. the top left of Fig. 3.6) were extracted. The calculation result is compared to the **y**–shaped metamaterial, and as a reference the result of model 8 (which corresponds to the current path of the third resonance of the **y**–shaped metamaterial) is also shown. It turns out from this figure that the resonant frequencies of the decomposed models are almost same with those of the original structure.

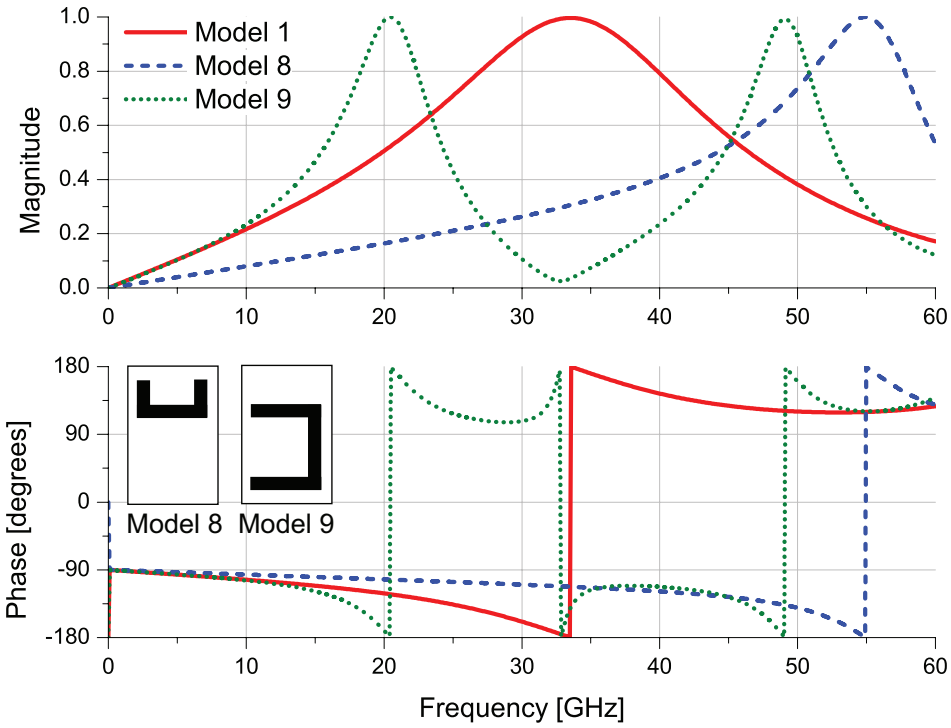

Figure 3.11: Reflection coefficient magnitudes (top) and phases (bottom) of decomposed **y**–shaped metamaterial models 1, 8 and 9.

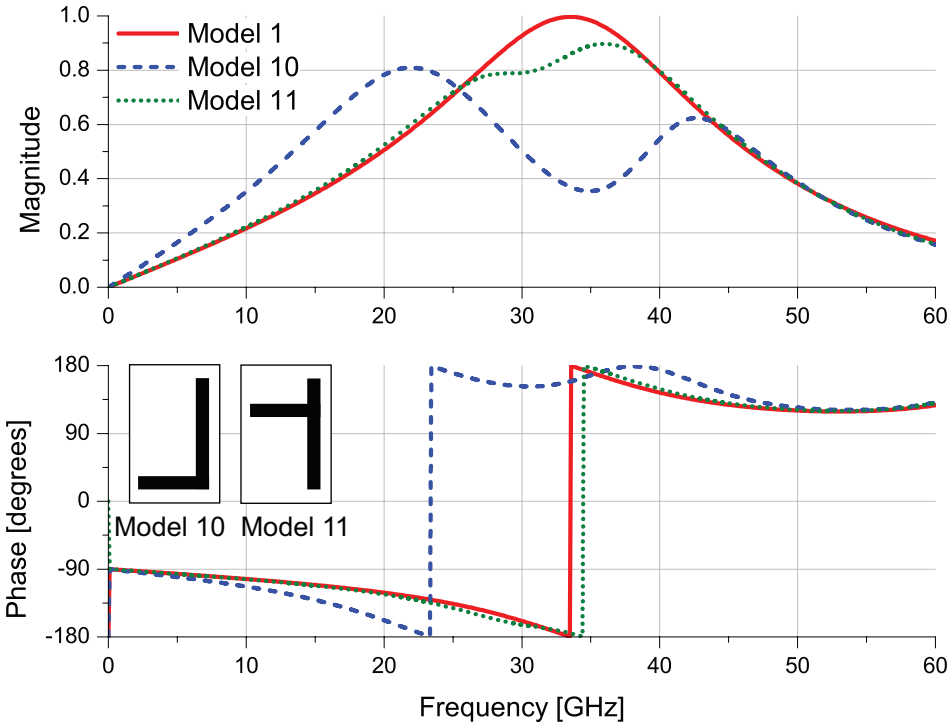

Figure 3.12: Reflection coefficient magnitudes (top) and phases (bottom) of decomposed **y**–shaped metamaterial models 1, 10 and 11.

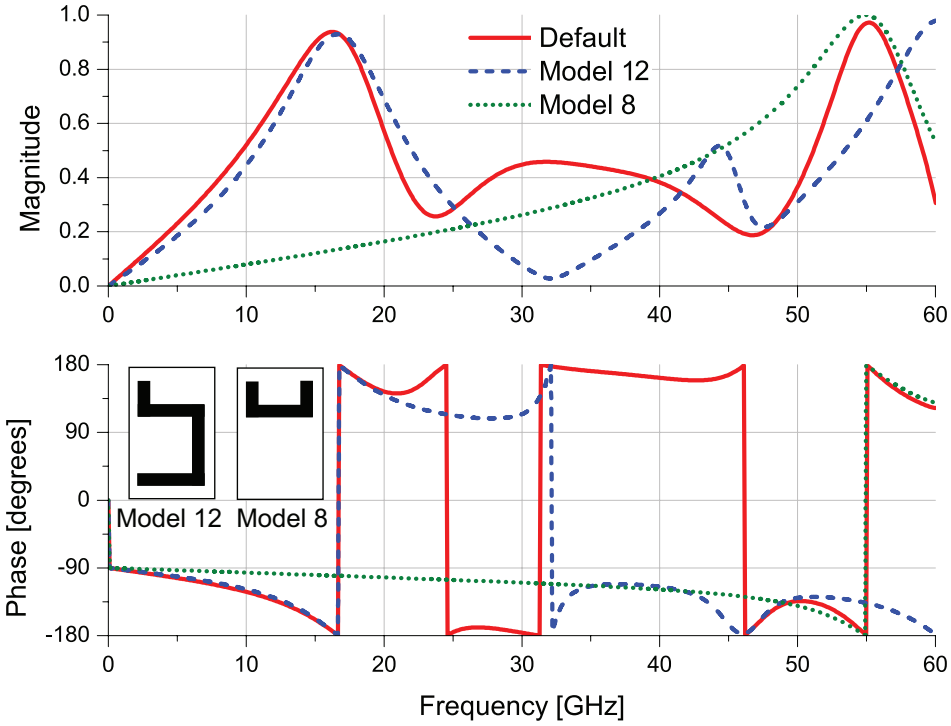

Figure 3.13: Reflection coefficient magnitudes (top) and phases (bottom) of decomposed **y**–shaped metamaterial models 8 and 12 and **y**–shaped metamaterial.

3.3 Magnetic Resonance

This section addresses magnetic resonances with the capacitively–loaded loop (CLL) based metamaterial [42] illustrated in Fig. 3.14. The default parameters of the structure are provided on Table 3.3. The substrate of this structure had a complex relative permittivity of $\varepsilon_r = 2.2$ and $\tan\delta_e = 0.00090$ where $\tan\delta_e = \sigma_e/\omega_0\varepsilon_r\varepsilon_0$ and $\omega_0 = 2\pi \cdot 10 \cdot 10^9$.

The scattering parameters of the default CLL–based metamaterial are shown in Figs. 3.15 and 3.16. Similarly to the **y**–shaped metamaterial simulated in the last section, the CLL–based metamaterial exhibited some reflection coefficient peaks from 0 to 20 GHz, while the same number of dips was found in the transmission coefficient curve. However, in contrast to the **y**–shaped metamaterial, the phase of the reflection coefficients of the CLL–based metamaterial became

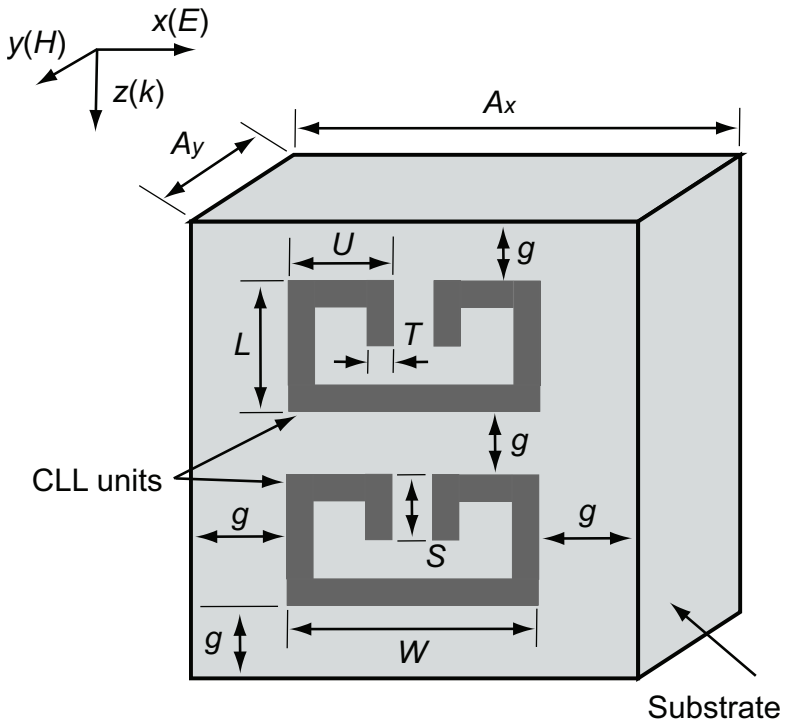

Figure 3.14: Calculation model for CLL–based metamaterial. This structure was used in the analysis space of Fig. 3.3 as the MUT so that the periodic boundaries were deployed for yz and zx boundaries.

Table 3.3: Default values of CLL–based metamaterial.

L	2.5 [mm]
S	1.2 [mm]
T	0.5 [mm]
U	1.7 [mm]
W	4.1 [mm]
t_m (thickness of CLL metal)	0.1 [mm]
g	0.5 [mm]
A_x	5.1 [mm]
A_y	0.8 [mm]
Resistance of metal block	0.0 Ω
Relative permittivity of substrate	$2.2 \cdot (1.0+j0.00090)$
Relative permeability of substrate	$1.0 \cdot (1.0+j0.0)$
TLM unit cell size	$0.1 \times 0.1 \times 0.1$ [mm^3]

0 degrees around the resonance of 9.789 GHz, which is known as magnetic resonance. Also, this result indicates that this structure behaves as an artificial magnetic conductor around this frequency.

Fig. 3.17 shows electric field (E_x and E_y), magnetic field (H_y) and current distributions at 9.789 GHz. It reveals that the induced conduction current circulated along the whole part of the only top CLL unit. As a result, an artificial magnetic dipole appeared inside the CLL unit. As a comparison to the magnetic resonance, Fig. 3.18 shows the profile of the electric resonance at 4.026 GHz. In this case both CLL units interacted with the external fields. However, in contrast to the magnetic resonant frequency which showed strong electric field inside the top CLL unit, electric field appeared around the yz boundaries (see the top right of Fig. 3.18). Although magnetic field appeared inside the CLL units in the electric resonance as well, was an order of magnitude smaller than of the magnetic resonance (c.f. the bottom left of Fig. 3.17). As a result, the

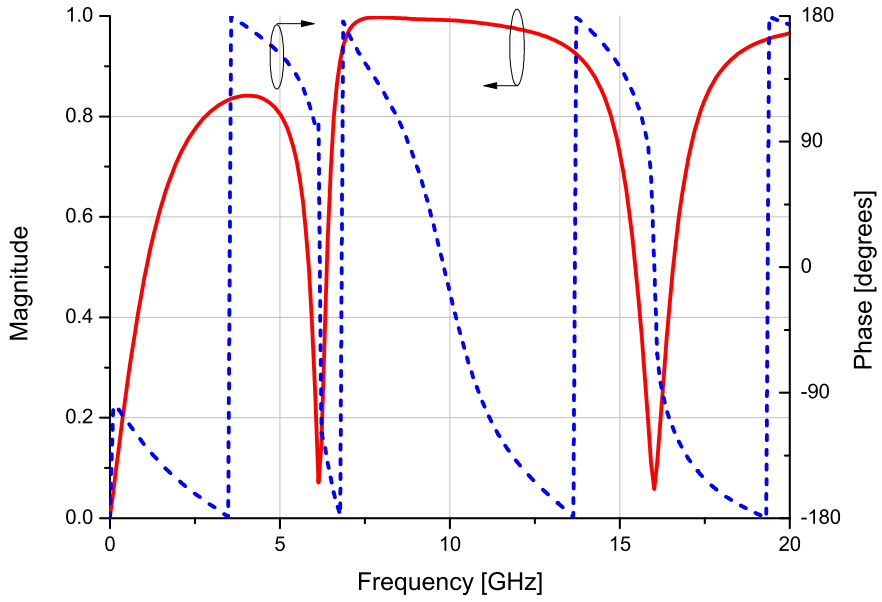

Figure 3.15: Magnitude and phase of reflection coefficient of CLL–based metamaterial.

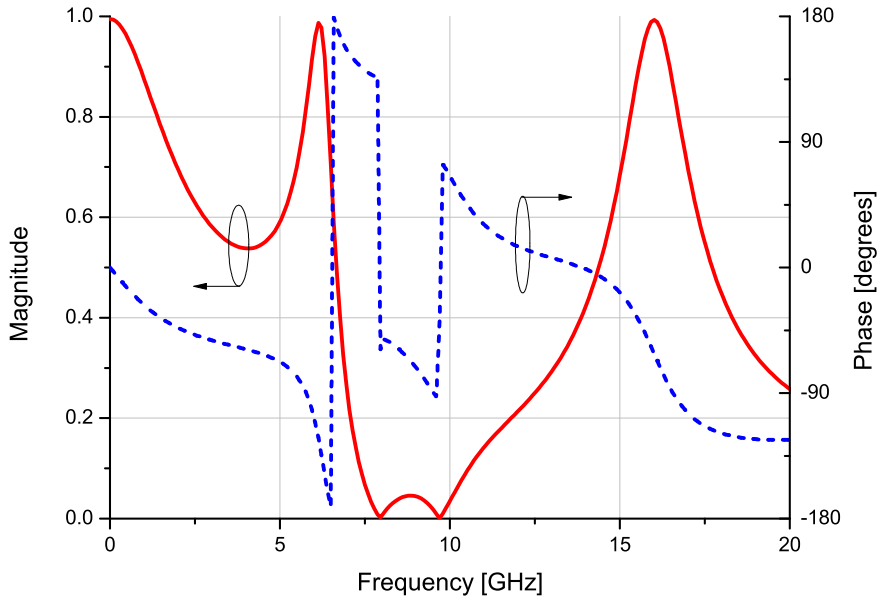

Figure 3.16: Magnitude and phase of transmission coefficient of CLL–based metamaterial.

resonance around 4.026 GHz became analogous to the structures simulated in the last section.

To further study the magnetic resonance some components of the CLL–based metamaterials were changed, while the dimension of the substrate was fixed. The calculation results are displayed in Figs. 3.19 to 3.23. In Figs. 3.19 the length L was varied (see Fig. 3.14 for the dimension L). It turns out from these figures that as the length L increases, the magnetic resonance shifts to lower frequency. This is assumed to be because this dimension relates with the length of the current path.

In Figs. 3.20 and 3.21 the lengths of S and U were changed. In this case increasing these lengths led to the decrease of the magnetic resonant frequency. Similarly to Fig. 3.19 the current path is expected to be longer as these parameters increase. However, these changes affect not only the length of the current path but also the capacitance of this resonance mechanism. As shown in the top right of Fig. 3.17, strong electric field is concentrated between the gap part of the CLL units, indicating this part plays a role of the capacitor. Therefore, the increases of the S and U lengths lead to the increase of the capacitance, resulting in the decrease of the magnetic resonant frequency.

Figs. 3.22 and 3.23 show the reflection coefficient dependence on the relative permittivity and permeability of the substrate, respectively. Although in these simulations no metal component lengths were changed, the increases of these electromagnetic properties (i.e. ε_r and μ_r) affected the total capacitance and total inductance, resulting in the decrease of the magnetic resonant frequency.

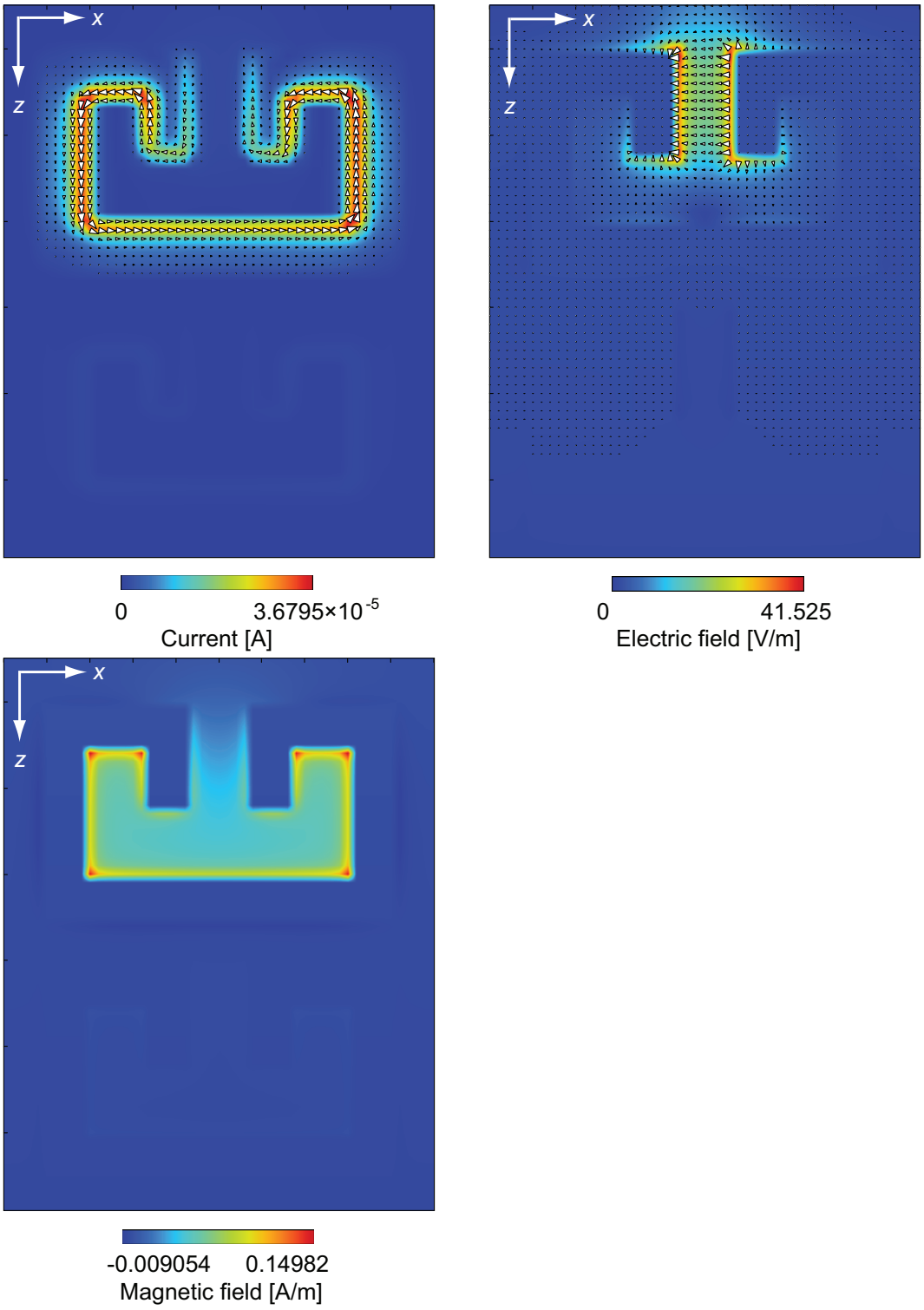

Figure 3.17: Profile of CLL–based metamaterial at 9.789 GHz. The top left figure shows the current distribution at zx plane, while the top right and bottom left represent the electric field (E_x and E_z) and magnetic field (H_y) distributions, respectively.

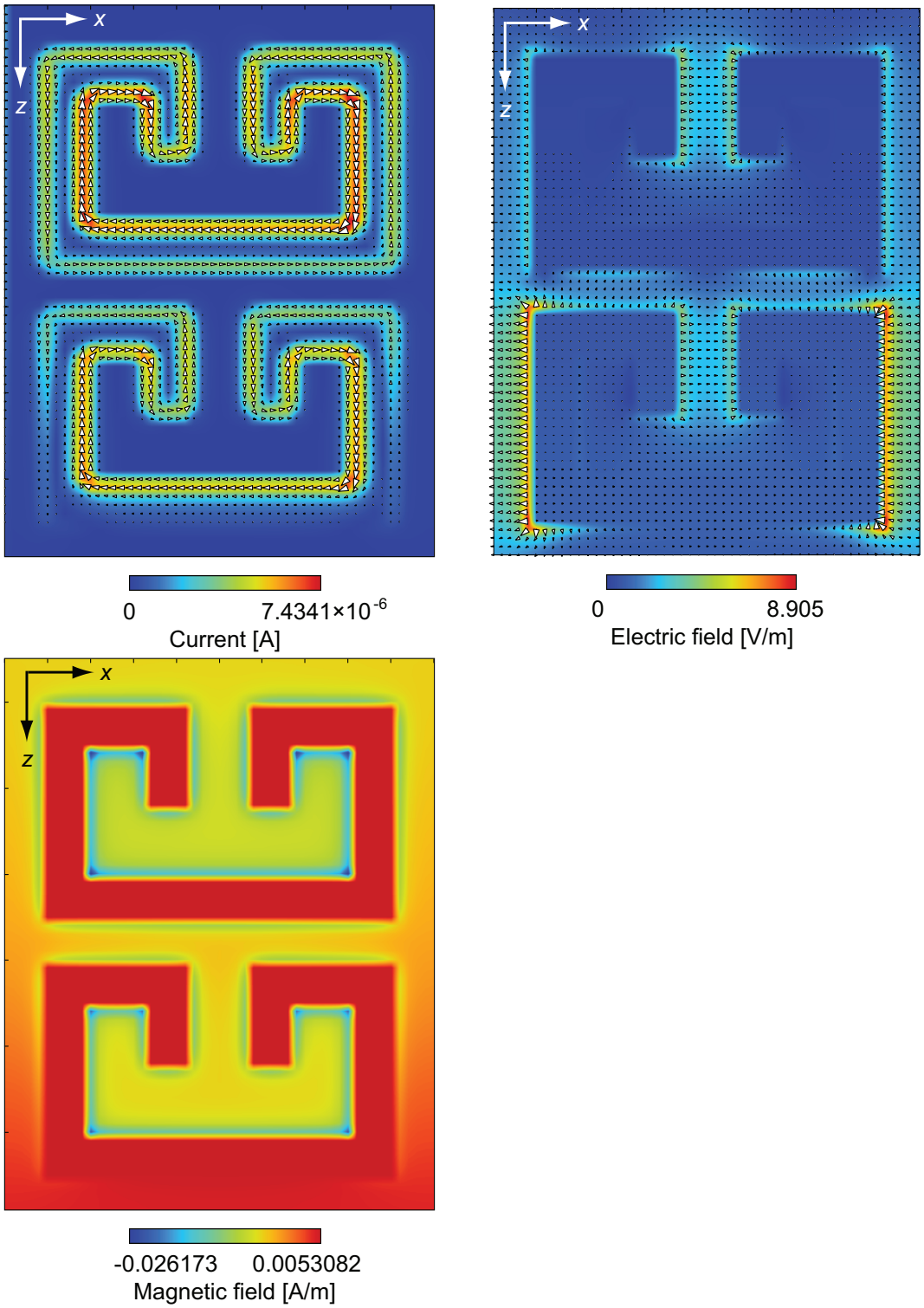

Figure 3.18: Profile of CLL–based metamaterial at 4.026 GHz. The top left figure shows the current distribution at zx plane, while the top right and bottom left represent the electric field (E_x and E_z) and magnetic field (H_y) distributions, respectively.

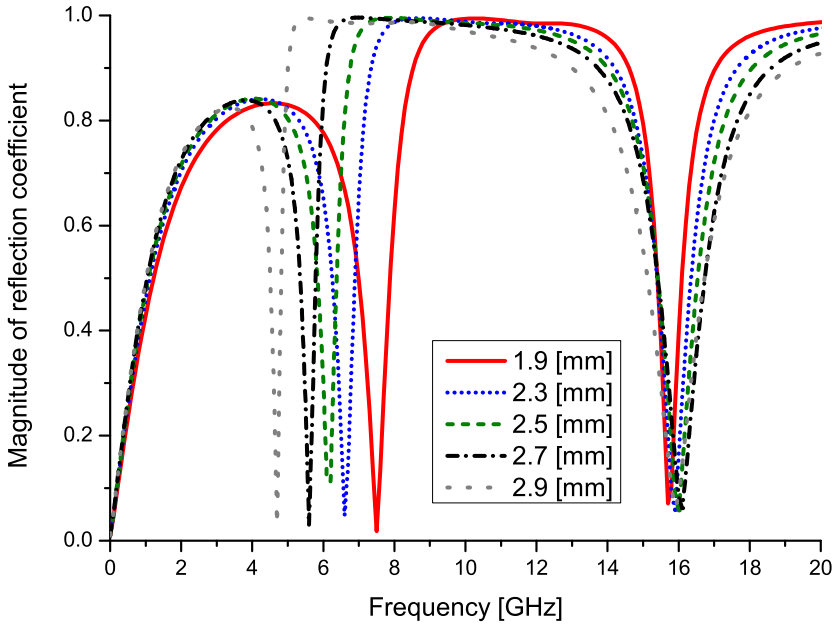

Figure 3.19: Reflection coefficient dependence of CLL–based metamaterial on component *L*.

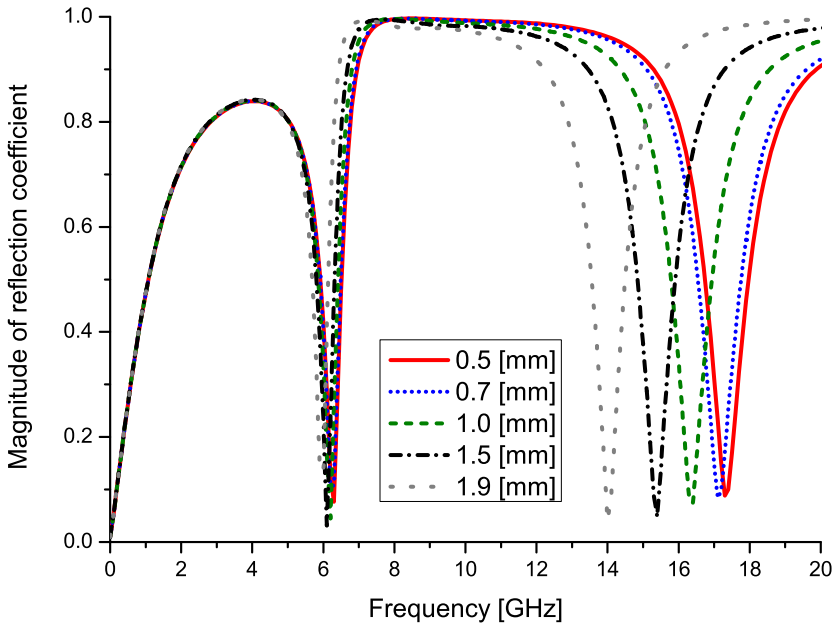

Figure 3.20: Reflection coefficient dependence of CLL–based metamaterial on component *S*.

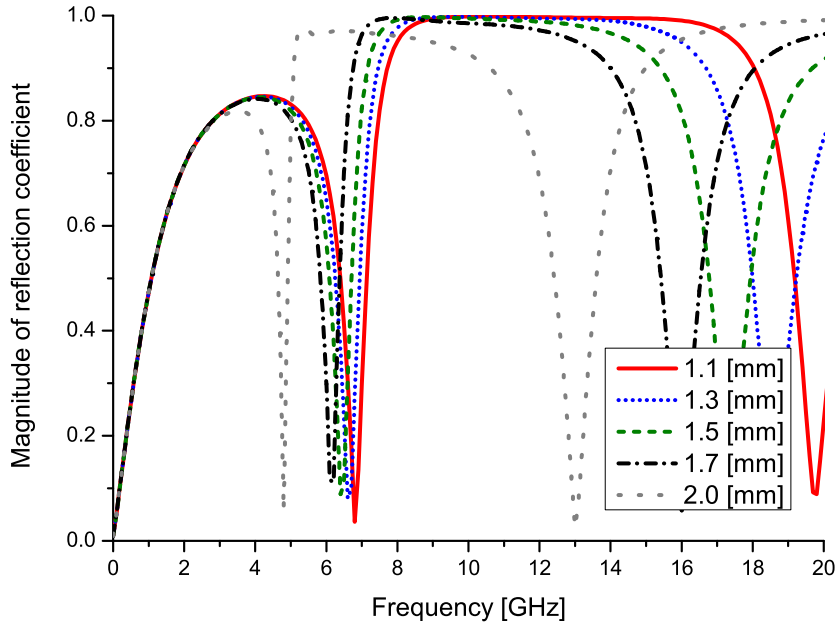

Figure 3.21: Reflection coefficient dependence of CLL–based metamaterial on component U.

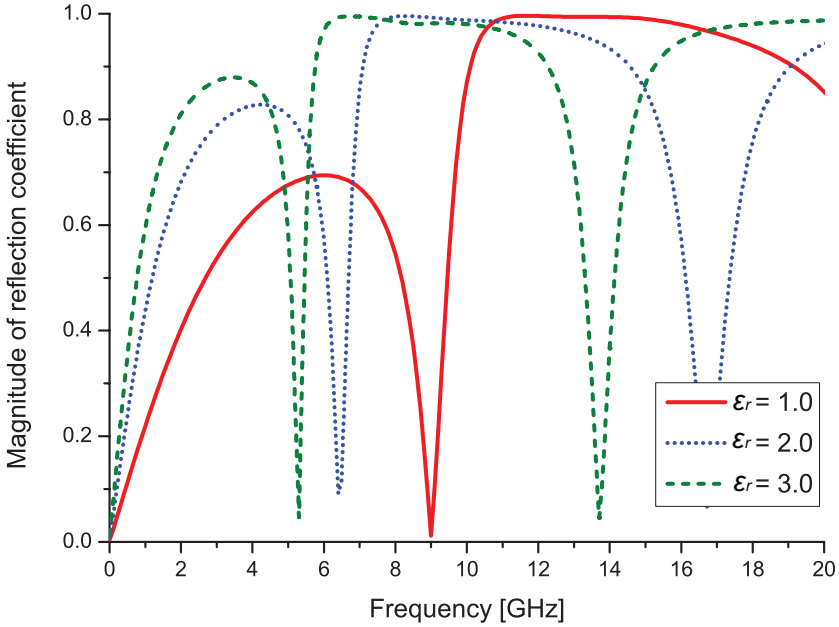

Figure 3.22: Reflection coefficient dependence of CLL–based metamaterial on relative permittivity of substrate.

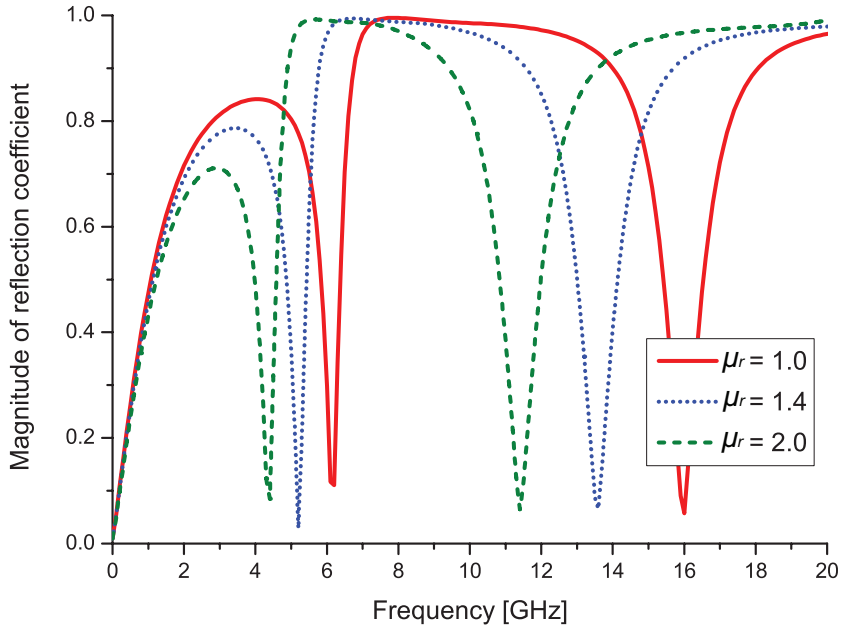

Figure 3.23: Reflection coefficient dependence of CLL–based metamaterial on relative permeability of substrate.

3.4 EBG Structure

3.4.1 Introduction

In this section the EBG structure is described. This structure was originally suggested by Sievenpiper et al. of University of California at Los Angeles in 1999 [94, 95]. The EBG structure unit is generally composed of a metal patch, ground plate and via connecting them (see the left of Fig. 3.24). When a radio wave impinges on the surface of the metal patch as shown in the right of Fig. 3.24, electric charges circulate in the EBG structure units. At the resonant frequencies the electric charges are concentrated at the edges of the top patches. In this case the patch edges and the other parts of the structure play the roles of a capacitor and inductor, respectively. Also, conduction current is induced, when radio wave propagates along the ground plate surface, and in this case the structure presents a stop band to the radio wave [99]. Therefore, the EBG structure is useful to mitigate propagation of unnecessary surface current and can be deployed, for example, on print circuit board (PCB) to prevent interference from other signal sources.

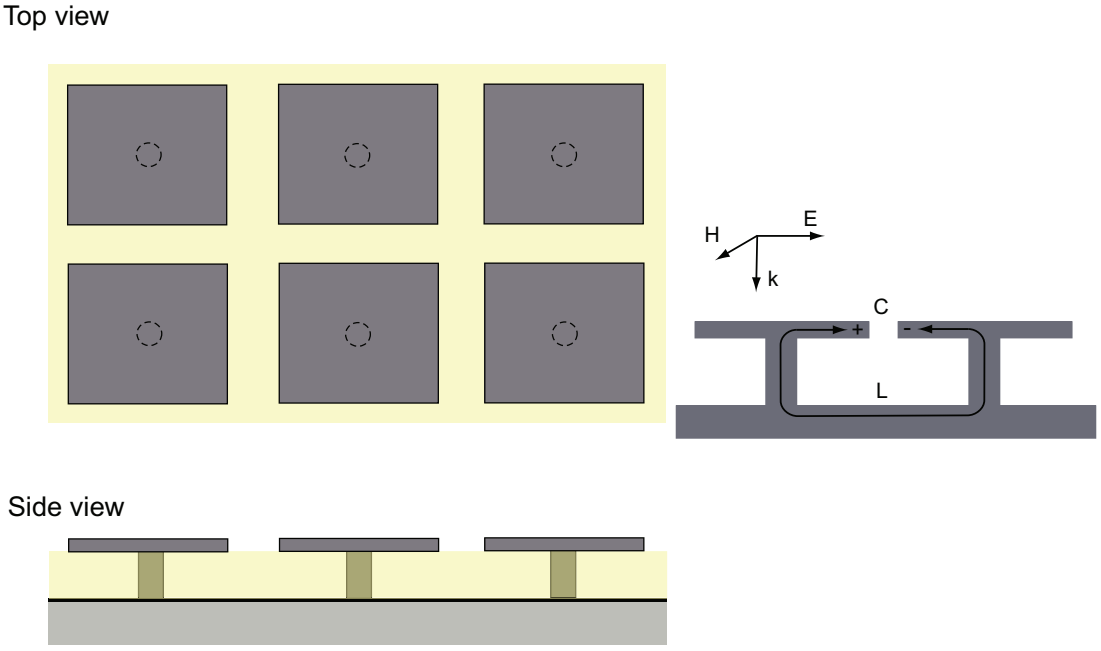

Figure 3.24: EBG structure (left) and its resonance behaviour (right).

EBG structures have some analogies with metamaterials from the viewpoint that they can change scattering characteristics in *artificial* ways. For example, in the right of Fig. 3.24 artificial magnetic dipoles appear inside the structures, which is similar to the CLL–based metamaterial introduced in the last section. Moreover, the scattering properties can be changed even on a large scale by using a large number of EBG structure units covering a surface. In [100, 101] scattering from a metal plane and cylinder was manipulated by modifying the surface impedance of each unit independently. This idea was extended in [102] where a slit was made in each top patch with various angles so that the scattering properties from the large–scale EBG structure units became different depending on whether the incident wave has left hand or right hand circular polarisation.

One point distinguishing EBG structures from metamaterials is the scale of the periodicity p. It is generally known that metamaterial units are much smaller than the EBG structure units. For instance, reference [9] states that the metamaterial periodicity is "$p/\lambda \approx 10^{-1}$ to 10^{-2}" where λ is the wavelength of the incident wave, and as long as $p/\lambda < 1/4$, the difference between the metamaterials and naturally available materials is just the sizes of the resonating structures (i.e. metal composites in metamaterials; molecules in naturally available structures). In contrast, the periodicities of the EBG structures are multiples of the half–wavelength ($p = n\lambda/2$ where n is an integer), and in this case Bragg's law is applicable for the diffraction angles, which is not the case of the metamaterials. In addition, resonances of metamaterials are basically fundamental modes, while those of the EBG structures include high order modes as well [9].

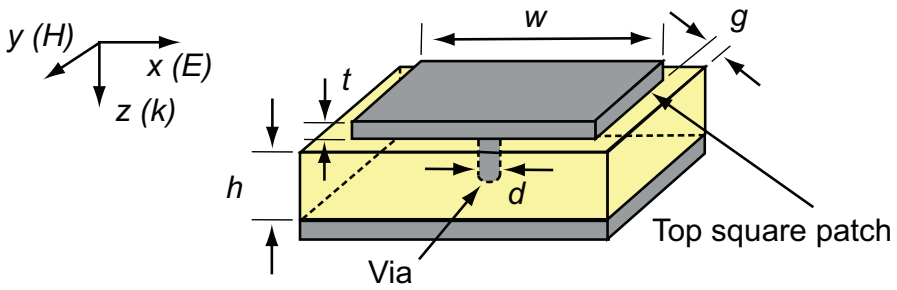

Figure 3.25: Simulated EBG structure. This structure was used in the analysis space of Fig. 3.3 as the MUT so that the periodic boundaries were deployed for yz and zx boundaries.

Table 3.4: Default values of EBG structure.

w	4.0 [mm]
d	0.8 [mm]
t	0.1 [mm]
h	1.5 [mm]
g	0.2 [mm]
Relative permittivity of substrate	$2.2 \cdot (1.0+j0.0)$
Relative permeability of substrate	$1.0 \cdot (1.0+j0.0)$
TLM unit cell size	$0.1 \times 0.1 \times 0.1$ [mm^3]

3.4.2 Simulation Results

The EBG structure described in Fig. 3.25 and Table 6.1 is simulated to study its scattering parameters. Since in this case all of the structure components were lossless and the bottom of the structure is fully covered by a perfect electric conductor (PEC) wall, the magnitudes of the reflection coefficient and transmission coefficient became a unity and zero. Hence, most results show only the phases of the reflection coefficients.

Fig. 3.26 shows the calculation result for the EBG structure. Within the frequency range from 0 to 20 GHz the reflection coefficient phase gradually

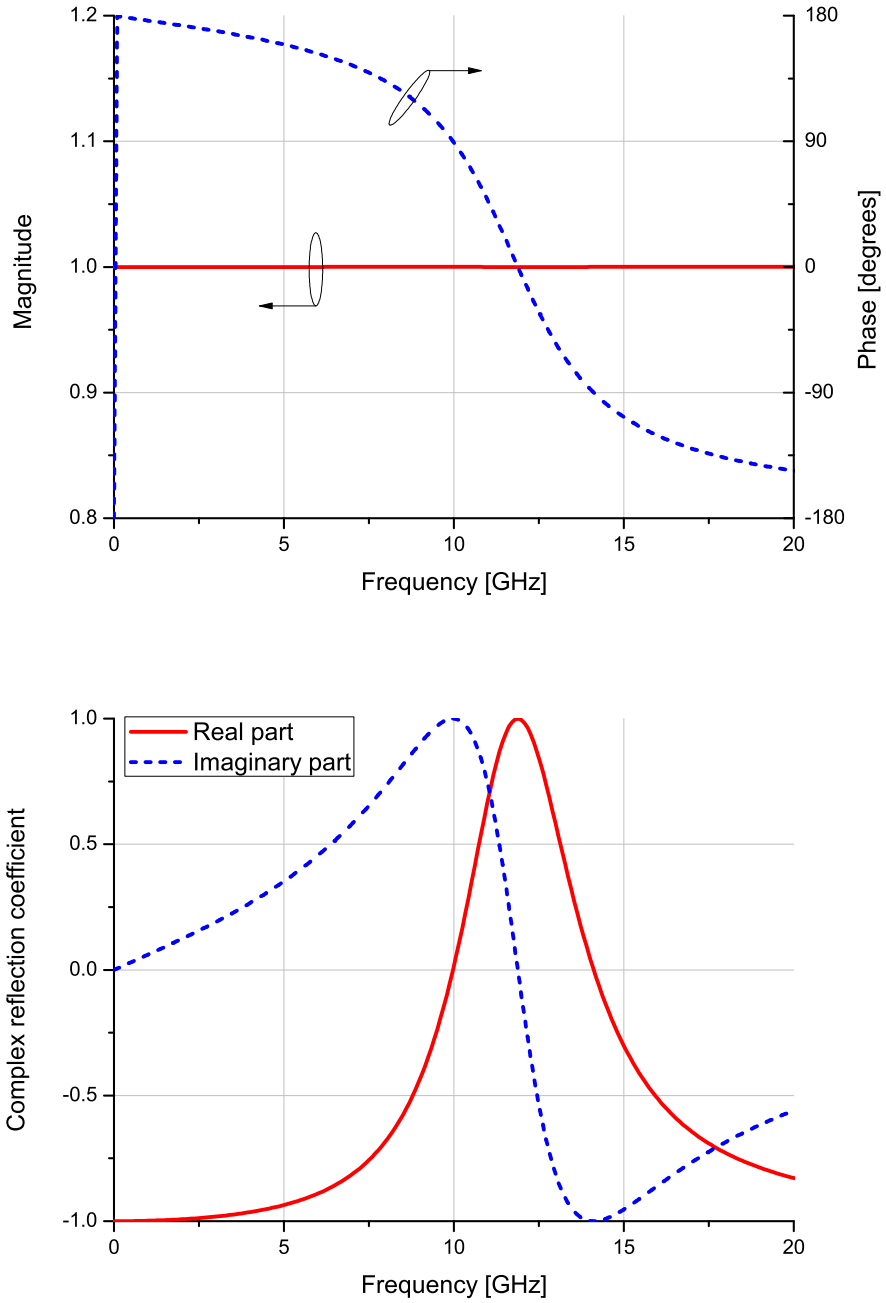

Figure 3.26: Reflection coefficient of EBG structure. The top figure shows the magnitude and phase, while the bottom figure represents the real part and imaginary part.

reduced from 180 to -180 degrees. At around 11.89 GHz the phase approached 0 degrees. As a result, at this frequency the EBG structure behaved as an artifi-

cial perfect magnetic wall, which is similar to the CLL–based metamaterial (c.f. Fig. 3.15).

Figs. 3.27 and 3.28 show the current distributions and electromagnetic field distributions respectively of the simulated EBG structure at 11.89 GHz. Fig. 3.27 proves that the conduction current flowed inside the EBG structures and was concentrated around the edges of the top patch. This conduction current concentration caused the strong electric field around the top patch

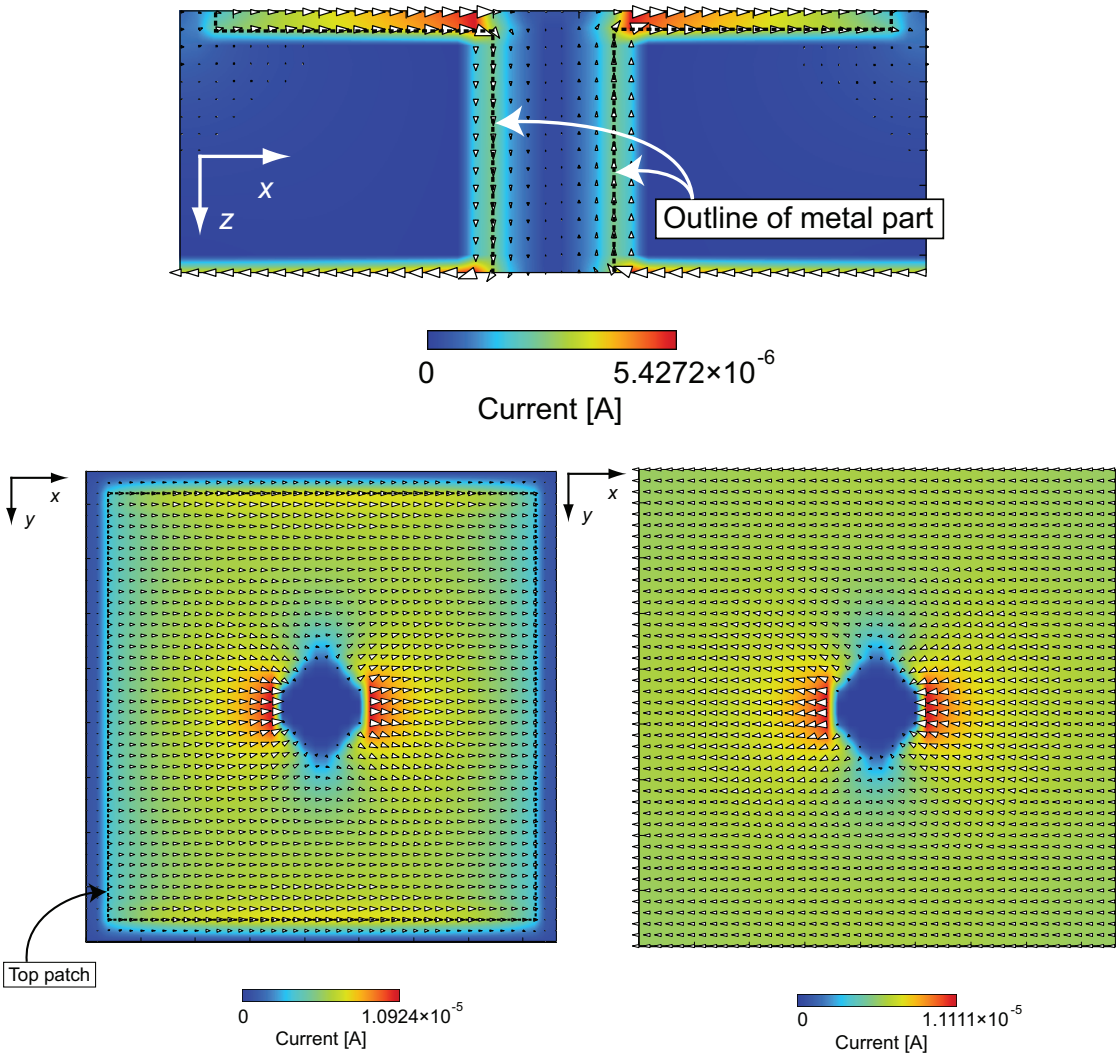

Figure 3.27: Current distributions of EBG structure at 11.89 GHz. The top figure shows the distribution at zx plane, and the bottom left and right figures respectively represent the distributions at the bottom surface of the top patch and the surface of the ground plate.

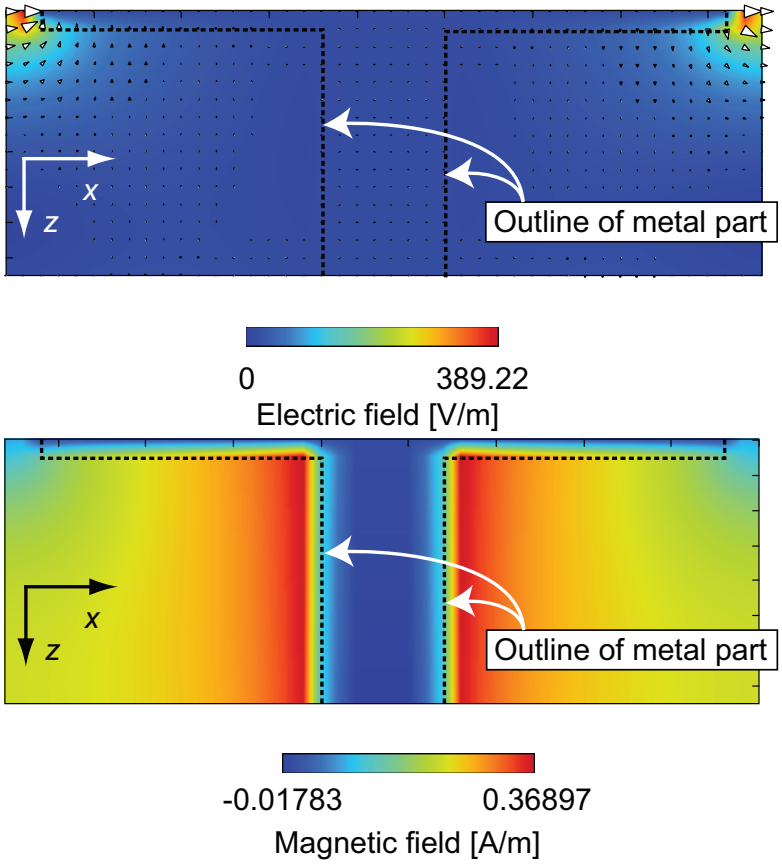

Figure 3.28: Electric field (E_x and E_z) distribution (top) and magnetic field (H_y) distribution (bottom) of EBG structure at 11.89 GHz.

edges and also generated the magnetic field inside the EBG structure substrate, as demonstrated in Fig. 3.28. As a result of the enhanced magnetic field, the EBG structure behaved as an magnetic conductor so that the reflection coefficient phase became 0 degrees.

Similarly to the CLL–based metamaterial, some parameters of the EBG structure were changed to further study the magnetic resonance response. In addition, these simulations show in–phase reflection bandwidth (defined by frequency region in which the phase is from -$\pi/4$ to +$\pi/4$ [103]) and its ratio to the centre frequency of each magnetic resonance. In Fig. 3.29 the via height was increased from 0.5 to 1.5 mm so that the magnetic resonance frequency shifted to lower frequency. This dependence may be attributed for the increase of the current path, which resulted in the increase of the total inductance and

thus the decrease of the resonant frequency.

Fig. 3.30 represents the dependence on the gaps between the top patches. As the gap width increases, the magnetic resonance frequency was found to increase. This shift is assumed to be due to the decrease of not only the total inductance but also total capacitance, leading to the relatively large shift of the resonant frequency, compared to the result of Fig. 3.29.

In Fig. 3.31 and 3.32 the relative permittivity and permeability of the substrate were respectively changed. As found in the results of the CLL–based metamaterial (c.f. Figs. 3.22 and 3.23) the increase of the electromagnetic properties of the substrate shifted the magnetic resonance to lower frequency.

It is found from Figs. 3.29 to 3.32 that the in–phase reflection bandwidth and the ratio to the centre frequency change differently depending on the parameter being changed. For example, the increase of the top patch gap led to the "increase" of the magnetic resonant frequency and the increase of the in–phase reflection coefficient bandwidth ratio. In contrast, the increase of the permeability of the substrate resulted in the "decrease" of the resonant frequency, while still increasing the in–phase reflection coefficient bandwidth ratio. These trends may be useful in designing broadband artificial magnetic conductors in high frequency and low frequency regions, respectively.

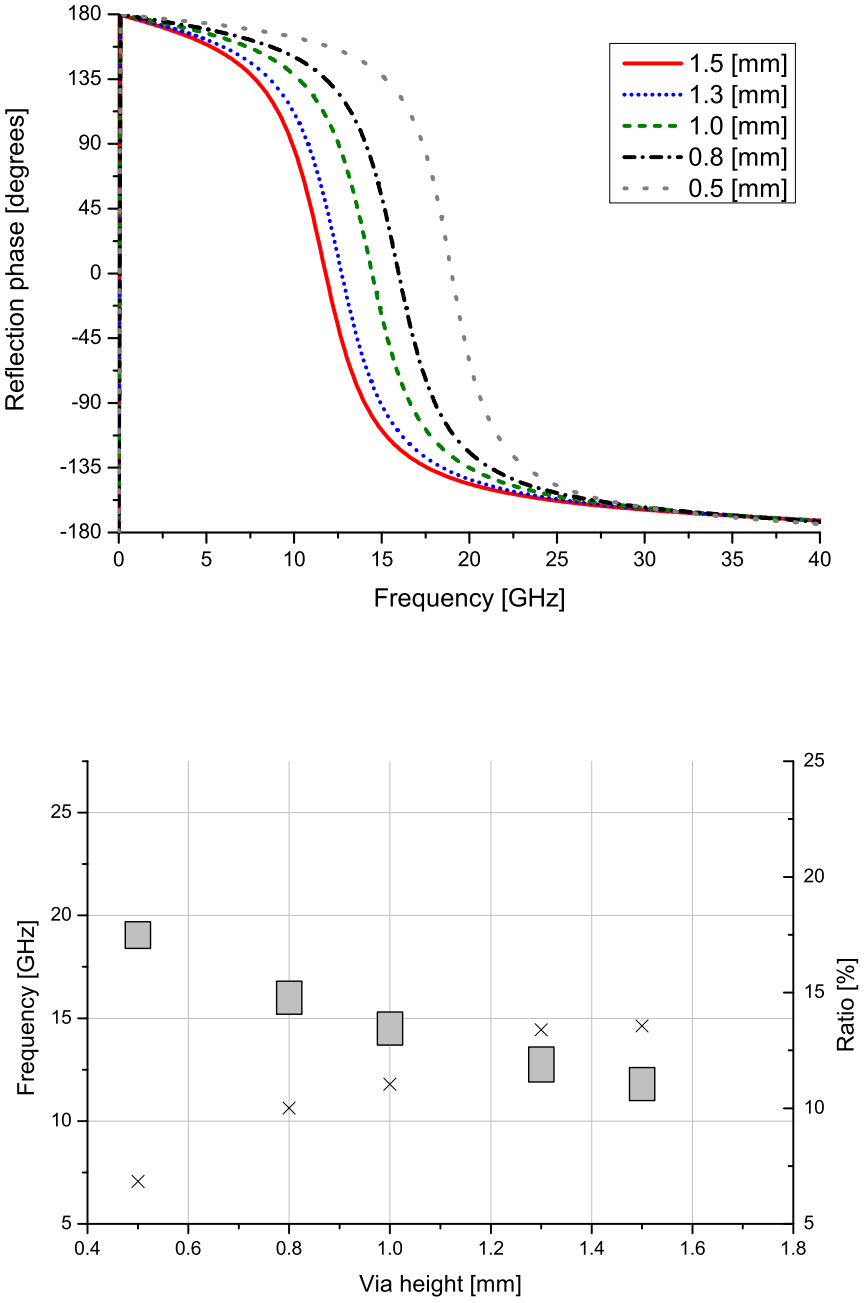

Figure 3.29: Reflection coefficient phase dependence of EBG structure on via height. The top figure shows the reflection coefficient phase as a function of frequency up to 40 GHz. The bottom figure shows the in–phase reflection bandwidth (grey bars) and its ratio to the centre frequency (crosses).

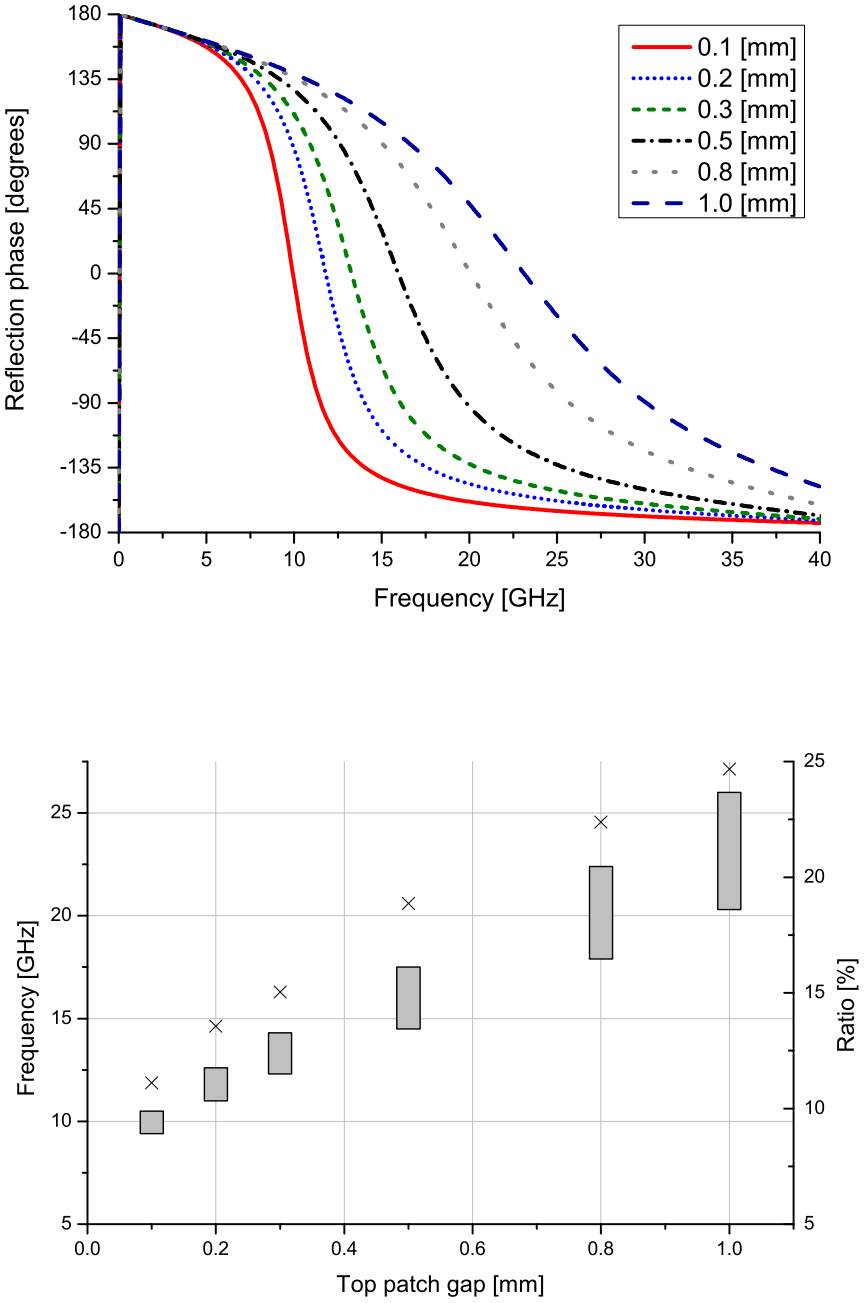

Figure 3.30: Reflection coefficient phase dependence of EBG structure on top patch gap. The top figure shows the reflection coefficient phase as a function of frequency up to 40 GHz. The bottom figure shows the in–phase reflection bandwidth (grey bars) and its ratio to the centre frequency (crosses).

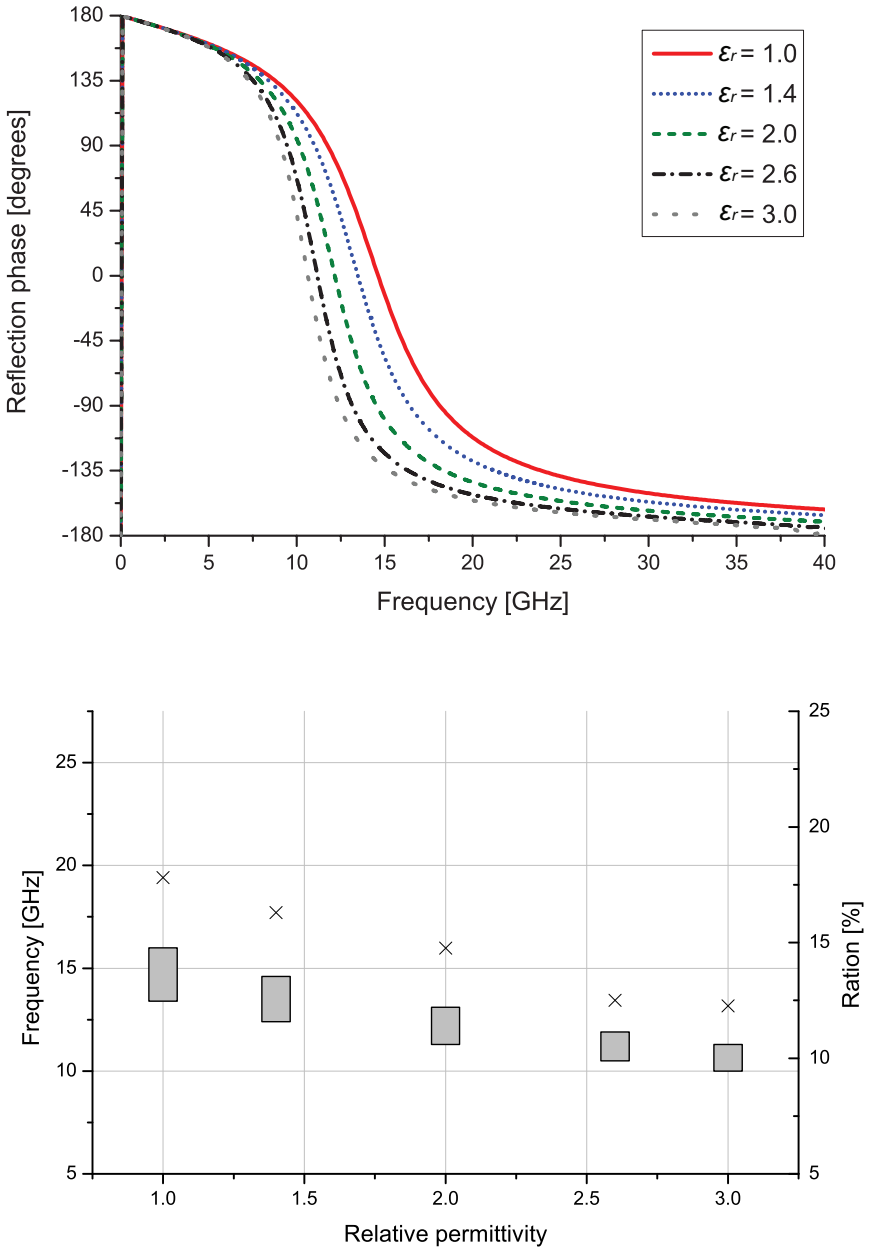

Figure 3.31: Reflection coefficient phase dependence of EBG structure on relative permittivity of substrate. The top figure shows the reflection coefficient phase as a function of frequency up to 40 GHz. The bottom figure shows the in–phase reflection bandwidth (grey bars) and its ratio to the centre frequency (crosses).

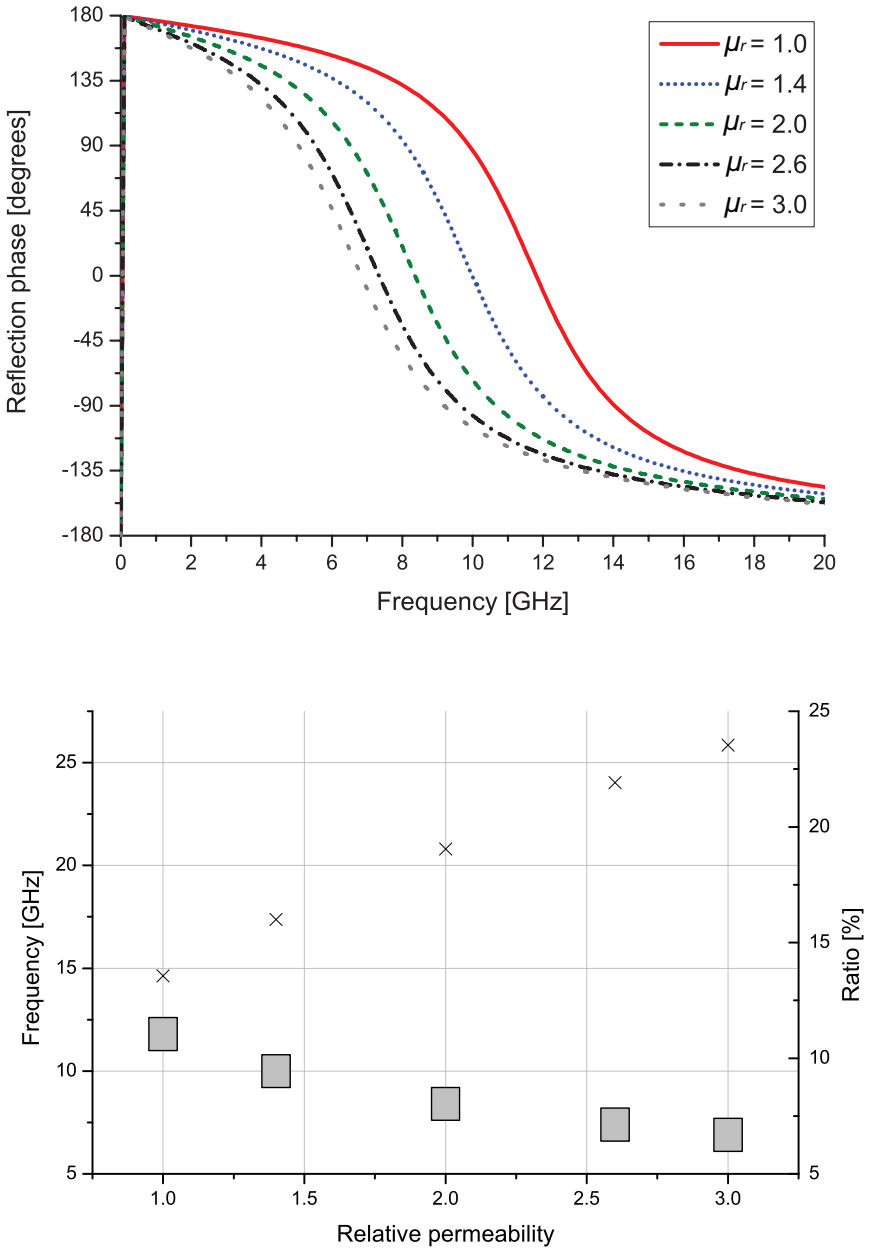

Figure 3.32: Reflection coefficient phase dependence of EBG structure on relative permeability of substrate. The top figure shows the reflection coefficient phase as a function of frequency up to 20 GHz. The bottom figure shows the in–phase reflection bandwidth (grey bars) and its ratio to the centre frequency (crosses).

3.5 Conclusion

In this chapter electric resonance of **y**–shaped metamaterial and magnetic resonance of CLL–based metamaterial were studied with the scattering properties. It was shown that for the electric resonance, electric field was induced due to the resonance of the metal composite along the direction of the external electric field, while for the magnetic resonance magnetic field was induced along the external magnetic field. In addition to these structures, an EBG structure was also simulated to study its resonance mechanisms. The properties of these three structures were investigated in more detail by decomposing the metal geometry or changing the component values. As a result, the trends and relationships between various design parameters and resonant frequencies were clarified.

CHAPTER 4

Predictions of Resonant Frequencies

4.1 Introduction

4.1.1 Predictions of Resonant Frequencies by Equivalent Circuits

Based on the results of chapter 3, in this chapter equivalent circuits applicable to predictions of resonant frequencies of CW metamaterials are studied. The use of equivalent circuits is useful for a systematic metamaterial design and enables us to obtain a first estimate of the dimensions needed for resonances at particular frequencies.

Equivalent circuits are composed of the total (or effective) inductance L and total capacitance C. If a loss mechanism is involved in the resonance behaviour, then the total resistance R is inserted in the circuit. For a series circuit the total impedance Z of the circuit becomes

$$Z = R + j \cdot \left(\omega L - \frac{1}{\omega C} \right). \tag{4.1.1}$$

The current flowing in the circuit can be calculated from

$$I = \frac{V_{in}}{R + j \cdot \left(\omega L - \frac{1}{\omega C} \right)}, \tag{4.1.2}$$

where V_{in} is the applied voltage. I and V_{in} are phasors. Taking the magnitude of the current,

$$|I| = \frac{|V_{in}|}{\sqrt{R^2 + \left(\omega L - \frac{1}{\omega C}\right)^2}}. \tag{4.1.3}$$

At the resonant frequency $|I|$ reaches the maximum value, i.e. $(\omega L - 1/\omega C) = 0$. Therefore, the general condition of the resonant frequencies is

$$\omega = \frac{1}{\sqrt{LC}} \tag{4.1.4}$$

or

$$f = \frac{1}{2\pi\sqrt{LC}}. \tag{4.1.5}$$

Note that in more complex cases the total inductance L and total capacitance C may consist not only of self inductance L_s and self capacitance C_s, but also of mutual inductance(s) L_m and mutual capacitance(s) C_m etc.

4.1.2 CW Metamaterials

In this chapter equivalent circuits for CW metamaterials (see the insets of Fig. 4.1 for the structures of a single CW and symmetrically paired CW) are designed for the following reasons. Firstly, the CW metamaterials are very simple structures and the periodic unit is composed of only a dielectric substrate and a single or paired CW. Due to their simplicity, CW metamaterials can be the basic elements of other more complex types of metamaterials [22, 23], so they play an important role in fundamental metamaterial research. Secondly, the CW metamaterials are readily scalable to higher frequency regions, compared to most other metamaterials. This is due to relatively simple manufacturing processes in fabrication and the absence of bent metal geometry, which leads to strong loss mechanisms in the high frequency region [11]. Thirdly, the CW metamaterials do not require any extra metal components to produce a NRI. For example, the first metamaterial developed [1–3] is composed of

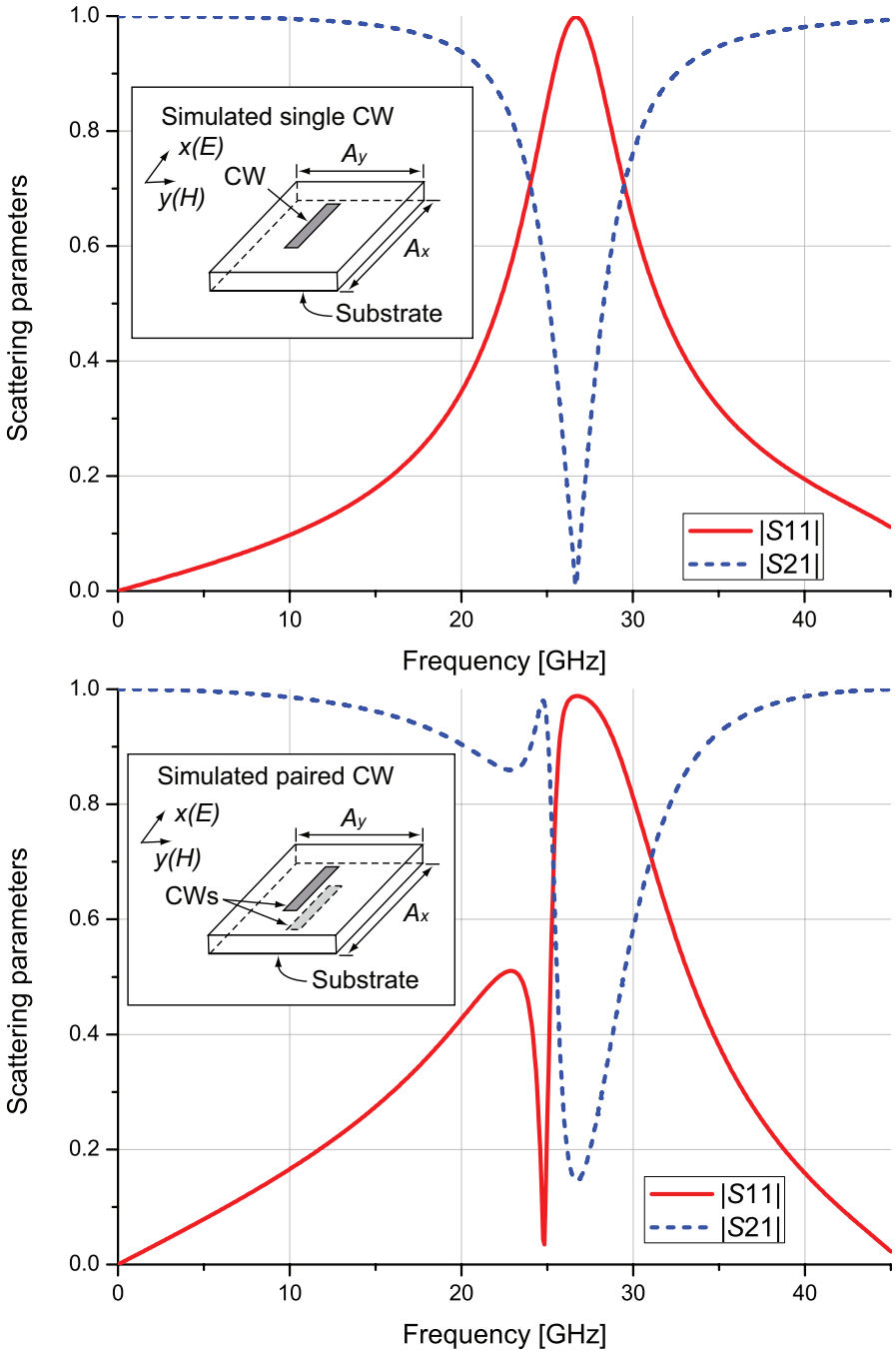

Figure 4.1: Scattering parameters of single CW metamaterial (top) and symmetrically paired CW metamaterial (bottom).

split–ring resonators, yielding a negative value of permeability, and long metal strips, yielding a negative value of permittivity, and hence two types of metal structures are necessary to produce a NRI. However, the CW metamaterials can exhibit both negative permittivity and permeability through a simply paired CW.

As a brief introduction to CW metamaterials, the fundamental scattering characteristics are shown in Fig. 4.1. The top of Fig. 4.1 shows the calculation results of a single CW metamaterial whose periodic unit is composed of one metal strip, while the bottom of Fig. 4.1 represents the results of a symmetrically paired CW metamaterial whose periodic unit is composed of two metal strips on either side of the substrate. To simplify the situation, the relative permittivity ε_r of the substrate was set $\varepsilon_r = 1.0 \cdot (1.0 + j0.0)$. The CW structure had a width of 0.3 mm along the y axis (H–field) and a length of 5.1 mm along the x axis (E–field). The thickness of the CWs was set to be infinitesimally thin thickness, and the sheet resistance was 0.0 $\Omega\square^{-1}$. The dimension of the periodic unit was $A_x = A_y = 6.3$ mm where A_x and A_y represent the periodicities along x and y axes, respectively. This structure was modelled using cubical TLM unit cells having the edge lengths of $\Delta l = 0.075$ mm. The scattering parameters were calculated using observation planes 15 mm away from the top surface of the CW metamaterial, and a Gaussian pulse was excited on a plane one cell above the observation plane for the calculation of the reflection coefficient. Since periodic boundaries were applied for the xz and yz plane boundaries, the CW metamaterial unit modelled was assumed to belong to infinite array on xy plane.

As shown in Fig. 4.1, the simulated single CW and paired CW metamaterials exhibited reflection coefficient peaks at around 26.65 and 26.71 GHz, respectively. In addition, the paired CW metamaterial showed a dip in the $|S_{11}|$ at around 24.89 GHz. The former peaks and latter dip are respectively known as electric resonance and magnetic resonance [22].

More details of the resonance behaviour of the paired CW metamaterial are clarified with Figs. 4.2 and 4.3 where the electric field and the conduction current in time domain and at the resonant frequencies are summarised. As seen in the top of Fig. 4.2, when an incident wave is excited with the electric

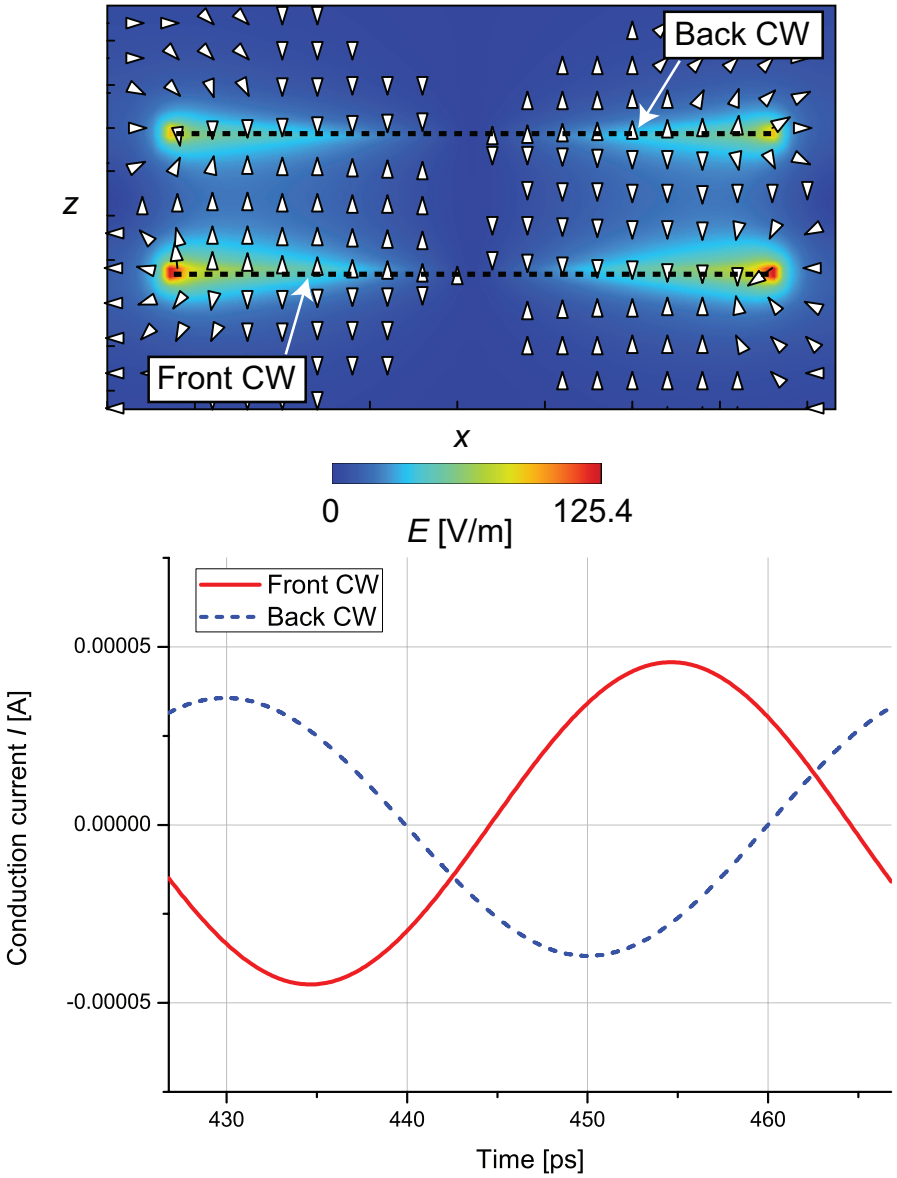

Figure 4.2: Electric field (top) and the conduction current in time domain (bottom) at 24.89 GHz (magnetic resonance).

field parallel to the direction of the CW metals, the conduction currents flow in opposite directions in each CW at the magnetic resonance. In this case the electric field is anti–parallel at the two edges of the CW metamaterial, and a magnetic field (not shown here) concentrated within the area bounded by the paired CW is generated. This magnetic field plays the role of an artificial magnetic dipole and can lead to a negative value of permeability. On the other hand, at the electric resonance shown in Fig. 4.3 conduction currents in the CWs become dominant, resulting in a strong unidirectional electric field at the

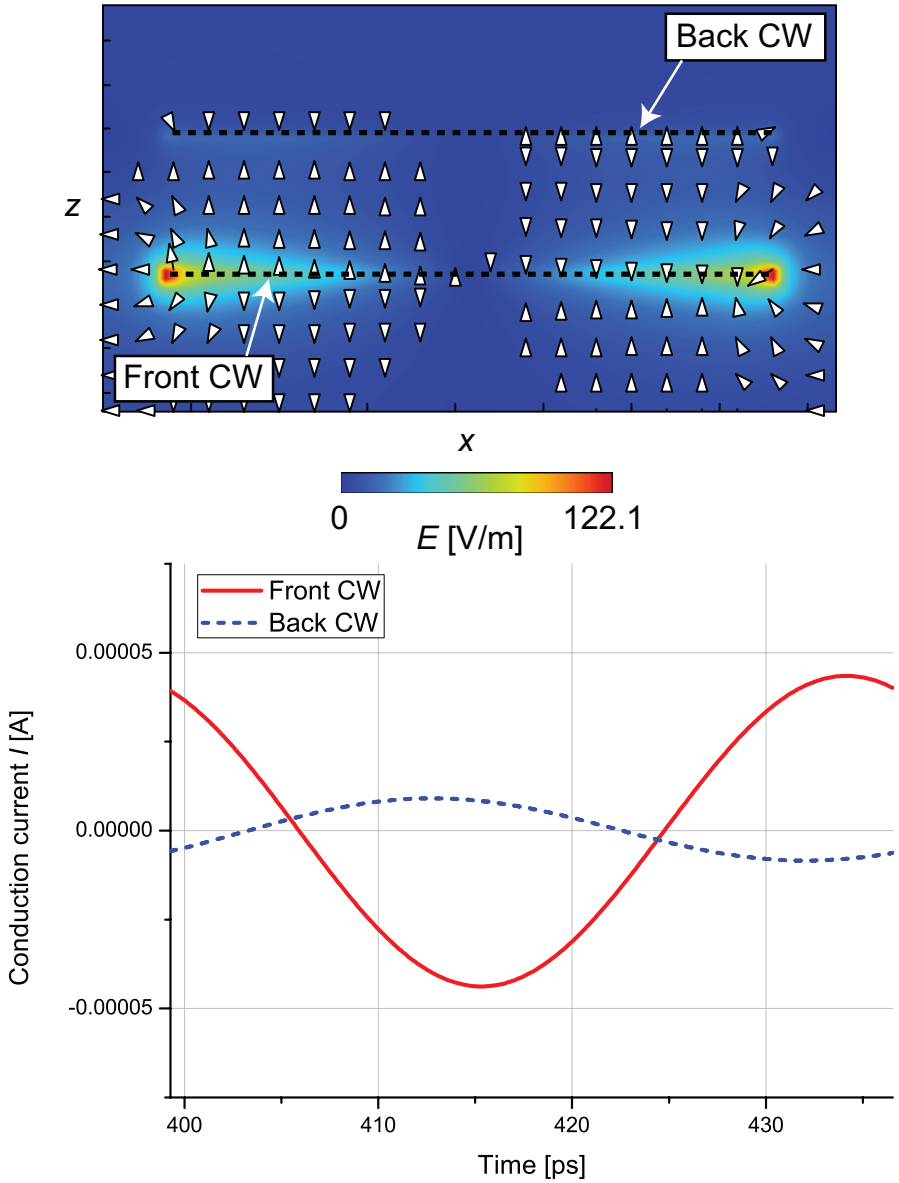

Figure 4.3: Electric field (top) and the conduction current in time domain (bottom) at 26.71 GHz (electric resonance).

edges of the CWs. Similarly with the magnetic resonance this electric field behaves as an artificial electric dipole so as to produce a negative value of permittivity. A similar unidirectional electric field is found in the $|S_{11}|$ peak of the single CW metamaterial.

4.1.3 Focus

So far equivalent circuits for geometrically symmetric paired CW metamaterials have been reported to calculate the resonant frequencies [22]. However, geometrically asymmetric cases in which the CW positions are shifted parallel to the incident E field have not been fully discussed using equivalent circuits, despite the fact that introducing asymmetry is one of the easiest ways to realise NRI [104]. For this reason this chapter aims at the realisation of equivalent circuits to predict the resonant frequencies of the asymmetrical CW metamaterials. The equivalent circuit is designed to predict magnetic resonances (i.e. Fig. 4.2), since this resonance mechanism is similar to that of CW metamaterial absorbers introduced in chapter 7. In this chapter, firstly, an equivalent circuit for a single CW in a periodic array is introduced and then extended to that for a symmetrically paired CW. Finally, an equivalent circuit for an asymmetrically paired CW is proposed. The calculated results are compared to those obtained by numerical simulations. In [105] the equivalent circuits introduced here for the single CW and symmetrically paired CW have been reported. The equivalent circuit models introduced in this thesis are extended to the prediction of absorptance peak frequencies of CW metamaterial absorbers in [106].

4.2 Calculation Models

Based on reference [104] for the basic structure, the CW metamaterial illustrated in Fig. 4.4 (also see Table 4.1 for the details of each component) was modelled and analyzed. For simplicity, however, the substrate was set $\varepsilon_r = 1$, no dielectric or conductive loss. The CW length l_t along E field of an incident wave was varied from 9.6 to 15.6 mm except for the asymmetrically paired CW which used the fixed value of $l_t = 9.6$ mm. Instead, for the asymmetrically paired CW the offset length d_x was changed from 0 to 9.6 mm. Both the metal width w and metal thickness t_m were set to be 0.3 mm. The basic metamaterial unit had the dimension of 19.2×9.6 mm^2, respectively, for x axis (parallel to E field) and y

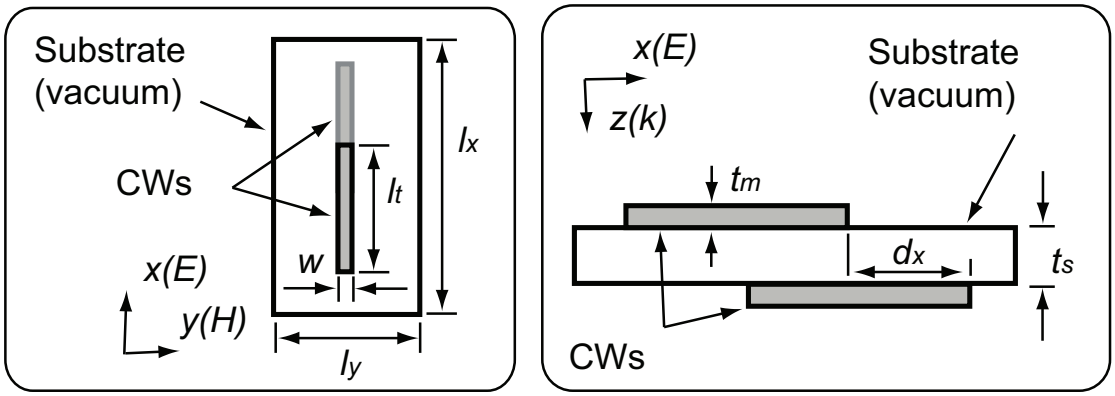

Figure 4.4: Calculated default CW metamaterial model. The illustrated structure represents the asymmetrically paired CW metamaterial. For the symmetrically paired CW metamaterial the offset d_x was set to zero. For the single CW metamaterial the bottom CW was removed. The details of each components are summarised in Table 4.1.

axis (parallel to H field). The analysis space was composed of $(N_x \times N_y \times N_z)$ = $(128 \times 64 \times 408)$ cells and the cube unit cells had the edge lengths of 0.15 mm.

4.3 Calculation Results

4.3.1 Equivalent Circuit for Single CW

First of all, a resonant frequency of a single CW in a periodic array is considered based on an equivalent circuit. In this calculation the back metal was removed and the front metal was approximated by a round wire, where the wire radius r was set to be [107]

$$r = \frac{w}{4}. \tag{4.3.1}$$

Table 4.1: Details of calculation parameters used for resonant frequency prediction of CW metamaterial (Fig. 4.4).

l_x	19.2 [mm]
l_y	9.6 [mm]
l_t	9.6 [mm]
	(for asymmetrically paired CW)
	9.6 to 15.6 [mm]
	(for the other CWs)
w	0.3 [mm]
t_m	0.3 [mm]
t_s	1.2 [mm]
d_x	0.0 to 9.6 [mm]
	(for asymmetrically paired CW)
	0.0 [mm]
	(for the other CWs)
Relative permittivity of substrate	$1.0 \cdot (1.0 + j\,0.0)$
Relative permeability of substrate	$1.0 \cdot (1.0 + j\,0.0)$
TLM unit cell size	$0.15 \times 0.15 \times 0.15$ [mm^3]
(for numerical simulations)	

This approximation facilitates analytical calculations. All inductances used in this chapter were calculated from the next equation [108]:

$$L(a_1,\, a_2) \;=\; \frac{\mu_0 a_2 \left(\ln \left[\frac{a_2}{a_1} + \sqrt{\left(\frac{a_2}{a_1}\right)^2 + 1} \right] + \frac{a_1}{a_2} - \sqrt{\left(\frac{a_1}{a_2}\right)^2 + 1} \right)}{2\pi} \;\; [\mathrm{H/m}] \tag{4.3.2}$$

where μ_0 is the permeability of vacuum and, as illustrated in Fig. 4.5, a_1 is the radius for self inductance L_s and the distance vertical to next wire for mutual inductance L_m. In terms of a_2 the wire length l_t is substituted. Therefore, the total inductance L_1 became

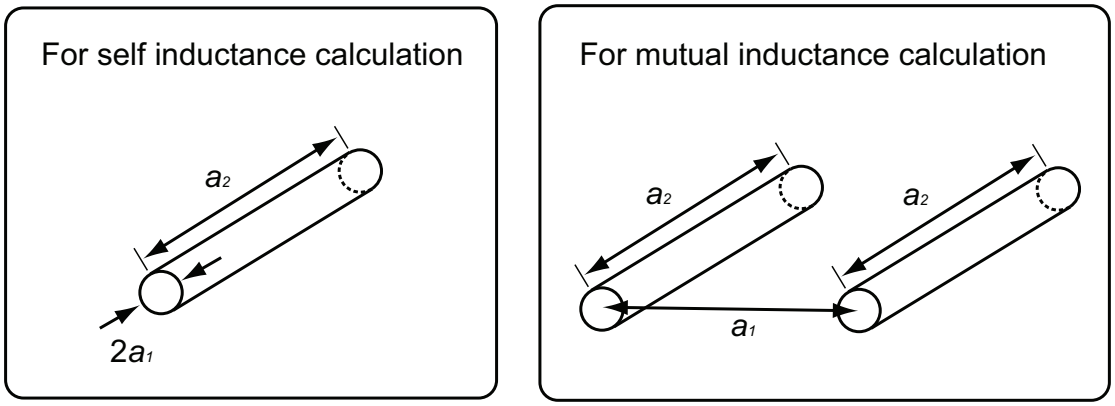

Figure 4.5: Parameters used for self inductance and mutual inductance calculations (eq. (4.3.2)).

$$L_1 = L_s(r,\ l_t) - 2L_{my}(l_y,\ l_t) \tag{4.3.3}$$

where the subscript y of L_{my} represents the mutual inductance with the neighbour CW metamaterial units along y axis and the sign was determined by numerical simulations in which the substrate dimensions (l_y in this case) were varied. Regarding the total capacitance C_1 the self capacitance C_s and mutual capacitances C_{mx} with CWs neighbour along x axis were incorporated. C_s was estimated from the relationship between the self resonance frequency f_s and the metal length l_t, i.e.

$$f_s = \frac{c_0}{2l_t} = \frac{1}{2\pi\sqrt{L_s(r,\ l_t)C_s}} \tag{4.3.4}$$

where c_0 is the speed of light in vacuum. C_{mx} was calculated from the capacitance C'_{mx} of a parallel plate capacitor, i.e.

$$C'_{mx} = \frac{\varepsilon_0 w t_m}{l_x - l_t}\ \ [\mathrm{F/m}], \tag{4.3.5}$$

and the fringing effect, which was taken into account by using a coefficient $C_n(a_3)$ obtained from [109]

$$C_n(a_3) = \frac{\pi\dfrac{(1+\varepsilon_r)}{\varepsilon_r}}{\ln(8a_3) + \dfrac{1}{16a_3^2(1+\varepsilon_r)} + \dfrac{\varepsilon_r - 1}{\varepsilon_r}\left[\dfrac{0.041}{a_3^2} - 0.454\right]}, \tag{4.3.6}$$

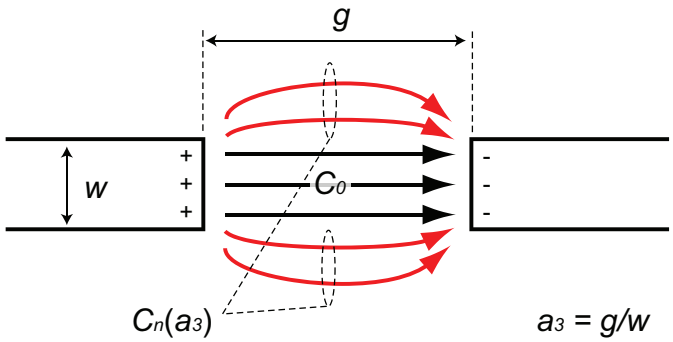

Figure 4.6: Parameters used for fringing effect calculations (eq. (4.3.6)). w and g represent the plate widths and the gap between the plates.

where a_3 represents a ratio of the gap between the parallel plates to the width, as illustrated in Fig. 4.6. ε_r is the relative permittivity and here set to $\varepsilon_r = 1$. Therefore, C_{mx} was estimated from

$$C_{mx} = C'_{mx}\left[C_n\left(\frac{l_x - l_t}{w}\right) + C_n\left(\frac{l_x - l_t}{t_m}\right) - 1\right] \quad [\mathrm{F/m}] \tag{4.3.7}$$

and the resultant resonance frequency f_1 became

$$\begin{aligned} f_1 &= \frac{1}{2\pi\sqrt{L_1 C_1}} \\ &= \frac{1}{2\pi\sqrt{\left[L_s(r,\, l_t) - 2L_{my}(l_y,\, l_t)\right]\left(C_s + \dfrac{C_{mx}}{2}\right)}} \quad [\mathrm{Hz}], \end{aligned} \tag{4.3.8}$$

where C_1 is the total capacitance. The mutual inductances and mutual capacitances used here are visualised in Fig. 4.7, and in Fig. 4.8 the equivalent circuit is drawn. As is found from Fig. 4.9, the resonant frequencies calculated by the equivalent circuit were close to those by numerical simulations, the average difference being about 4 %. Note that by the use of L_{my} and C_{mx} this equivalent circuit takes account of the mutual coupling between array elements.

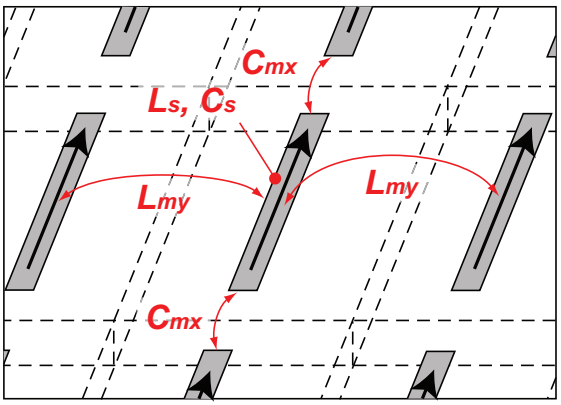

Figure 4.7: Mutual inductances and mutual capacitances used for equivalent circuit of single CW array. The subscripts *s* and *m* represent self and mutual values. The subscripts following *m* indicate main directions along which the mutual effects work. The directions of the conduction currents are described by the black arrows.

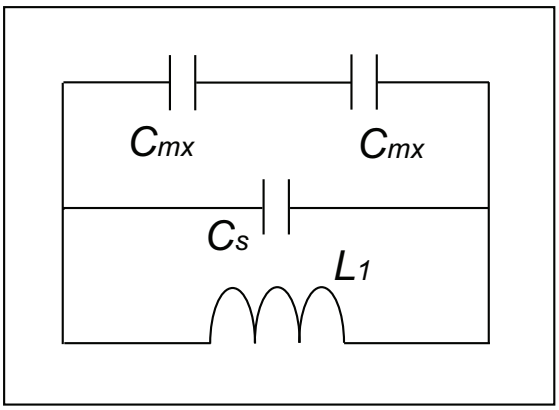

Figure 4.8: Equivalent circuit for predicting electric resonant frequencies of single CW arrays. The equivalent circuit is based on eq. (4.3.8).

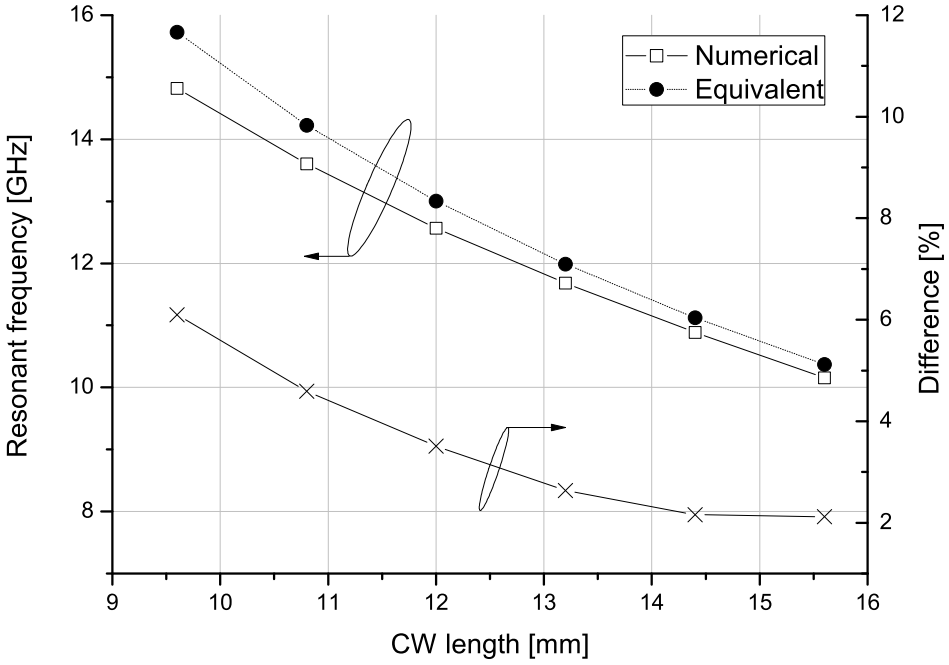

Figure 4.9: Resonant frequencies for single CW arrays. The resonant frequencies were derived by equivalent circuit (see Fig. 4.8 and eq. (4.3.8)) and numerical simulations.

4.3.2 Equivalent Circuit for Symmetrically Paired CW

Regarding the magnetic resonance frequency f_2 of the symmetrical paired CW metamaterial, mutual capacitances C_{mz} and a mutual inductance between the pair of the CWs were also incorporated in addition to the parameters used above. As is seen from Fig. 4.10 where E field along z axis was calculated in the paired CW at f_2, the E field is not evenly distributed and varies almost linearly in the CWs.

To estimate this mutual capacitance, the electrostatic energy W stored in the parallel plate structure illustrated in Fig. 4.11, where the potential difference linearly decreases to zero, was firstly calculated and its mutual capacitance C was then obtained from

$$W = \frac{CV_{in}^2}{2} \tag{4.3.9}$$

where all the symbols used here correspond to those in Fig. 4.11 (e.g. V_{in} is the potential difference at one edge of the parallel plates).

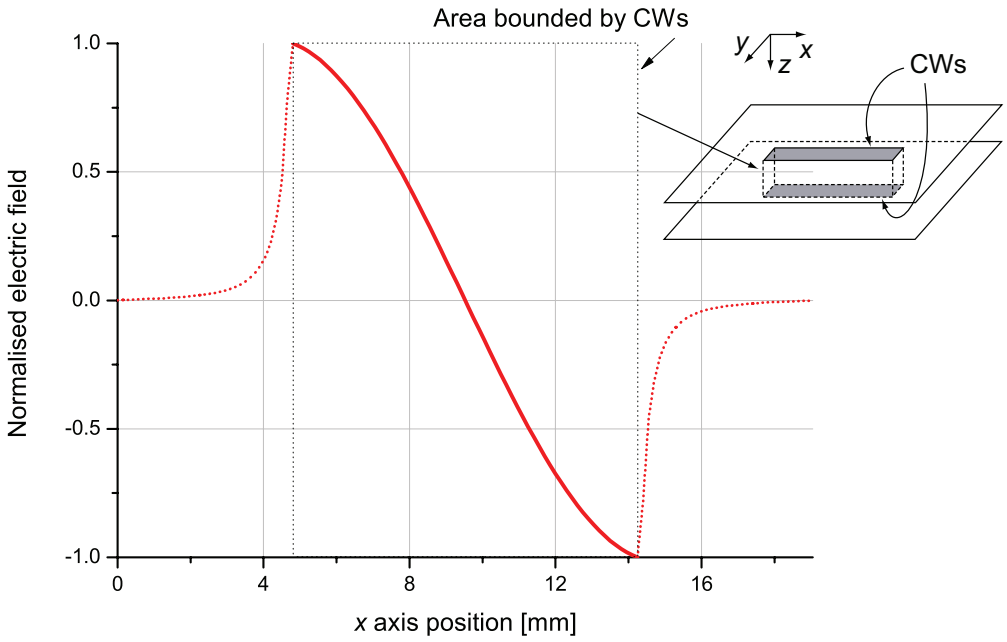

Figure 4.10: Normalised E_z in substrate of paired CW. This result was numerically obtained.

First of all, potential difference V_0 at position x illustrated in Fig. 4.11 is

$$V_0 = V_{in}\frac{x}{l_c}, \tag{4.3.10}$$

where l_c is the parallel plate length. Hence, the electric field E_0 at x is

$$E_0 = \frac{V_0}{d_c} = \frac{V_{in}}{l_c d_c}x, \tag{4.3.11}$$

where d_c is the gap between the plates. Next the stored energy W can be obtained from

$$\begin{aligned} W &= \int_0^{l_c} \frac{1}{2}\varepsilon_0 E_0^2 \cdot w_c d_c \cdot dx = \frac{1}{2}\varepsilon \frac{V_{in}^2 w_c d_c}{l_c^2 d_c^2}\left[\frac{x^3}{3}\right]_0^{l_c} \\ &= \frac{\varepsilon_0 w_c l_c V_{in}^2}{6 d_c}, \end{aligned} \tag{4.3.12}$$

where w_c is the CW width. From eq. (4.3.9),

$$C = \varepsilon_0 \frac{w_c l_c}{3 d_c}. \tag{4.3.13}$$

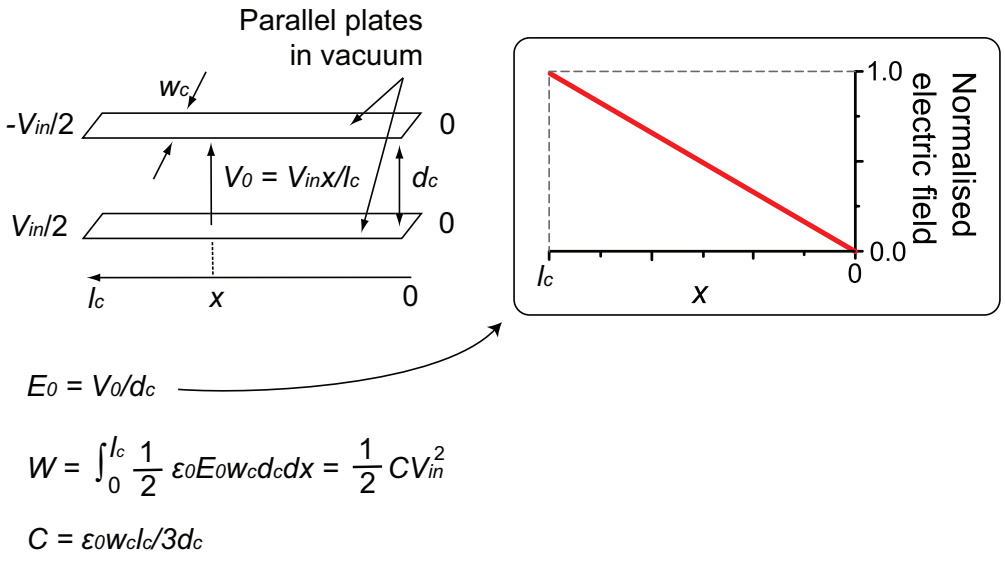

Figure 4.11: Calculation method for mutual capacitance C of two parallel plates having linearly changing potential difference.

In the constant potential difference case, since $E_0 = V_0/d_c = V_{in}/d_c$, the energy W becomes

$$\begin{aligned} W &= \int_0^{l_c} \frac{1}{2}\varepsilon_0 E_0^2 \cdot w_c d_c \cdot dx = \frac{1}{2}\varepsilon_0 \frac{V_{in}^2 w_c d_c}{d_c^2}[x]_0^{l_c} \\ &= \frac{\varepsilon_0 w_c l_c V_{in}^2}{2d_c}. \end{aligned} \tag{4.3.14}$$

Hence, equalising this equation to eq. (4.3.9) gives

$$C = \varepsilon_0 \frac{w_c l_c}{d_c}. \tag{4.3.15}$$

Compared to eq. (4.3.15), it is found that the capacitance of the linearly changing case (i.e. eq. (4.3.13)) is one third of that of the constant potential difference case (i.e. eq. (4.3.15)). Therefore, this coefficient 1/3 was applied to the mutual capacitance between the CW pair, and the resultant C_{mz} became

$$C_{mz} = \frac{\varepsilon_0 l_t w C_n \left(\dfrac{t_s}{w}\right)}{6t_s} \quad [\mathrm{F/m}], \tag{4.3.16}$$

where C_{mz} was additionally divided by two and multiplied by C_n to consider $l_t/2$ and the fringing effect, respectively. Regarding the mutual inductances, L_{mz} was similarly calculated from eq. (4.3.2) and L_{my} was set to zero due to cancellations from the pairs of the CWs. As a result, the magnetic resonant frequency f_2 became

$$\begin{aligned} f_2 &= \frac{1}{2\pi\sqrt{L_2 C_2}} \\ &= \frac{1}{2\pi\sqrt{\left[L_s - L_{mz}(t_s,\, l_t)\right]\left(C_s + \dfrac{C_{mx}}{2} + \dfrac{C_{mz}}{2}\right)}} \quad [\mathrm{Hz}], \end{aligned} \tag{4.3.17}$$

where L_2 and C_2 represent the total inductance and the total capacitance, respectively. The mutual inductances and mutual capacitances used here are visualised in Fig. 4.12, and in Fig. 4.13 the equivalent circuit is drawn. Fig. 4.14 shows the calculation results of the resonant frequencies. It is found from this figure that the calculation results were close to numerically derived values, the difference being only about 6 %. Note that this equation also takes account of the mutual coupling between the array elements by the use of C_{mx}.

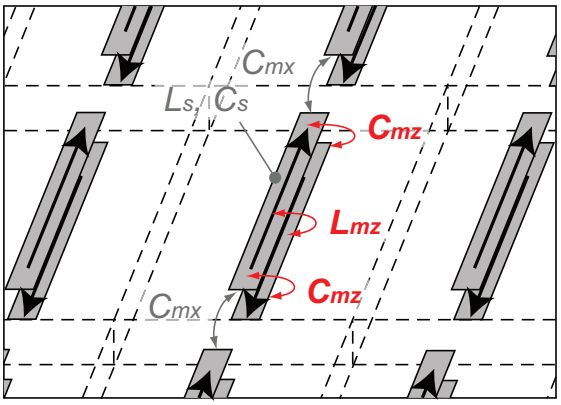

Figure 4.12: Mutual inductances and mutual capacitances used for equivalent circuit of symmetrically paired CW array. The subscripts s and m represent self and mutual values. The subscripts following m indicate main directions along which the mutual effects work. The directions of the conduction currents are described by the black arrows.

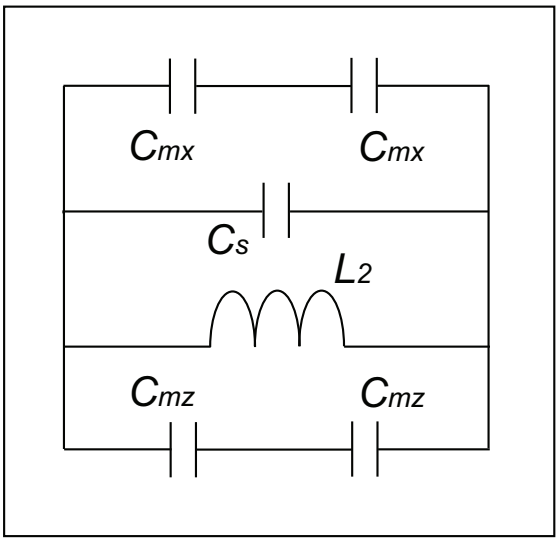

Figure 4.13: Equivalent circuit for predicting magnetic resonant frequencies of symmetrically paired CW arrays. The equivalent circuit is based on eq. (4.3.17).

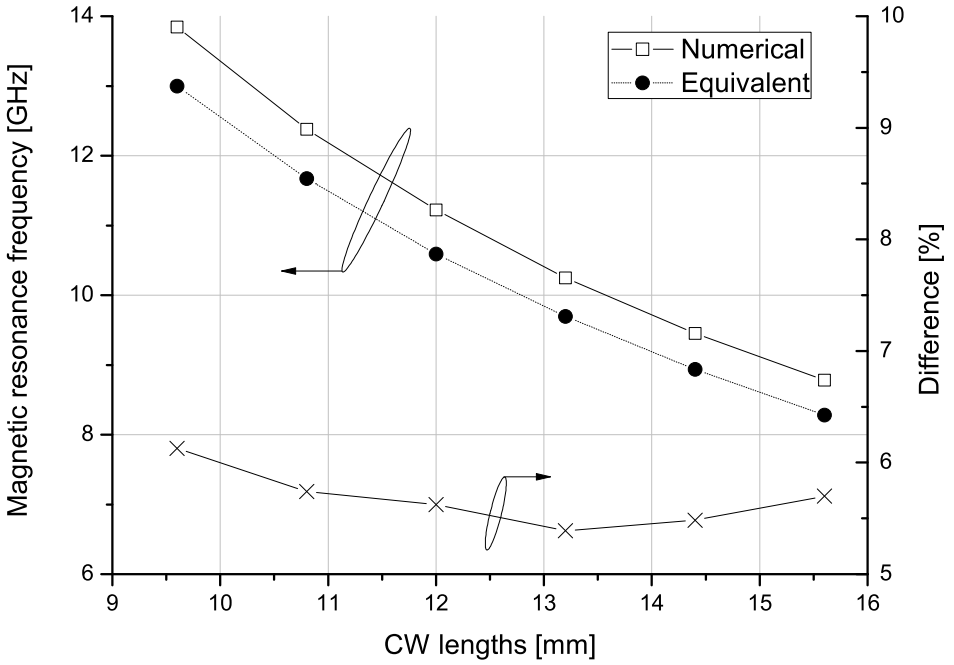

Figure 4.14: Magnetic resonant frequencies for symmetrically paired CW arrays. The resonant frequencies were derived by equivalent circuit (see Fig. 4.13 and eq. (4.3.17)) and numerical simulations.

4.3.3 Equivalent Circuit for Asymmetrically Paired CW

For the asymmetrically paired CW the same equivalent circuit as that used for the symmetrical case (Fig. 4.13) was applied, but some mutual parameters were modified. First of all, for the mutual capacitances between the pair of the CWs (i.e. C_{mz}) it was assumed that as the geometrical offset (asymmetry) d_x increases, the mutual capacitance decreases linearly and reaches zero at $d_x = l_t/2$, i.e.

$$C'_{mz} = \begin{cases} \frac{l_t - 2d_x}{l_t} C_{mz} & (\text{for } 2d_x < l_t) \\ 0 & (\text{for } 2d_x \geq l_t) \end{cases} . \tag{4.3.18}$$

In addition, L_{my} was incorporated again as the geometrical symmetry is broken.

Before the calculation procedure for L_{my} is explained, a simpler case is considered first in Fig. 4.15 where a mutual inductance between different

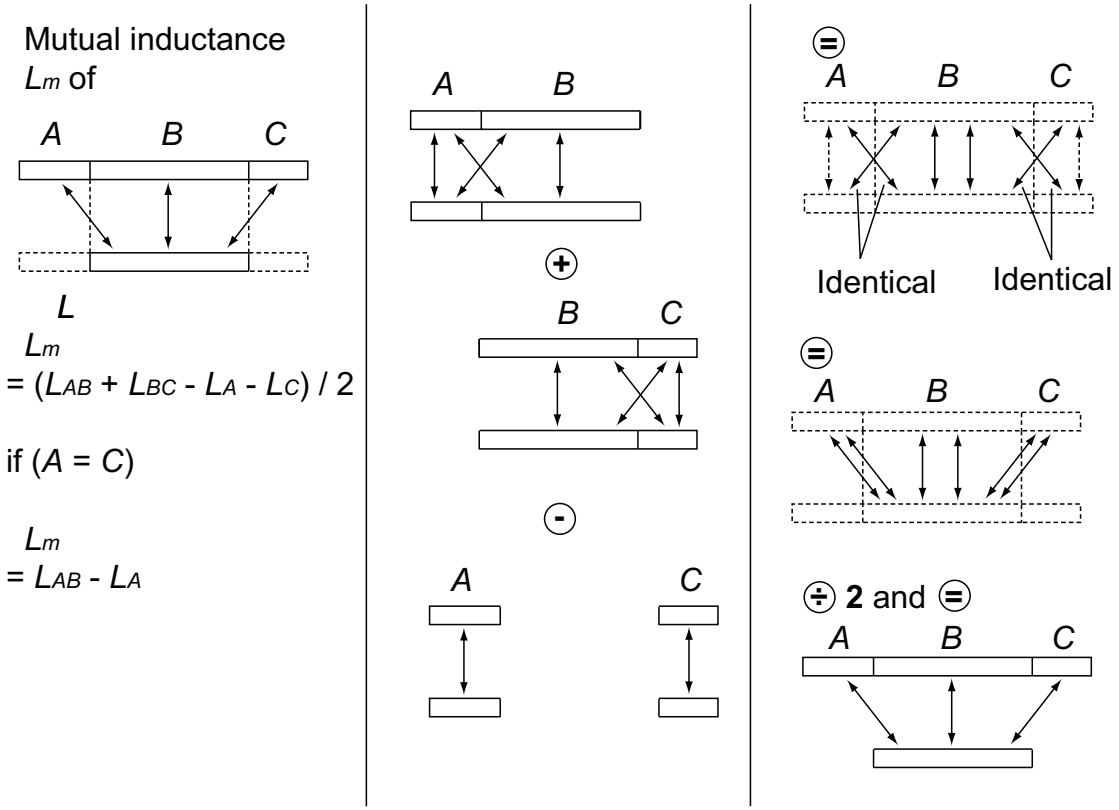

Figure 4.15: Calculation processes for mutual inductance between different lengths of two wires [110].

lengths of two wires is calculated. These calculation processes are described in [110]. In this figure the longer wire (the top wire in Fig. 4.15) is decomposed into the three parts: the centre part B which is geometrically symmetric to the bottom wire; the left part A; the right part C. Also, the corresponding parts of another wire are used in some calculations (i.e. the A and C parts of the shorter wire and those surrounded by the dashed lines in the left column of Fig. 4.15).

To begin with, the mutual inductance between the two wires whose lengths correspond to the AB parts is calculated (the top of the centre column in Fig. 4.15). The same calculation is performed for the BC parts (the middle of the centre column in Fig. 4.15). If the summation of these values is subtracted from the mutual inductances of the A part and C part (the bottom of the centre column in Fig. 4.15), then it is found that the calculation result becomes double of the mutual inductance of the original structure (the top and middle of the

right column in Fig. 4.15). Hence, dividing the value by two leads to the mutual inductance of the initial two wires (the bottom right in Fig. 4.15)).

A similar idea is applied for the geometrically asymmetric case whose calculation processes are summarised in Fig. 4.16. For this case too the wire is divided into three parts, and the centre part *B* corresponds to the geometrically symmetry part. The other two parts *A* and *C* are the left and right parts of the rest.

First, the calculation processes used for the simpler case (i.e. Fig. 4.15) are applied to this case so that the mutual inductances between *A* and *B*, *B* and *B* and *B* and *C* are obtained, and only the mutual inductance between *A* and *C* is left (the centre column in Fig. 4.16). When the mutual inductance between the *ABC* parts is subtracted from those between the *AB* and *BC* parts and

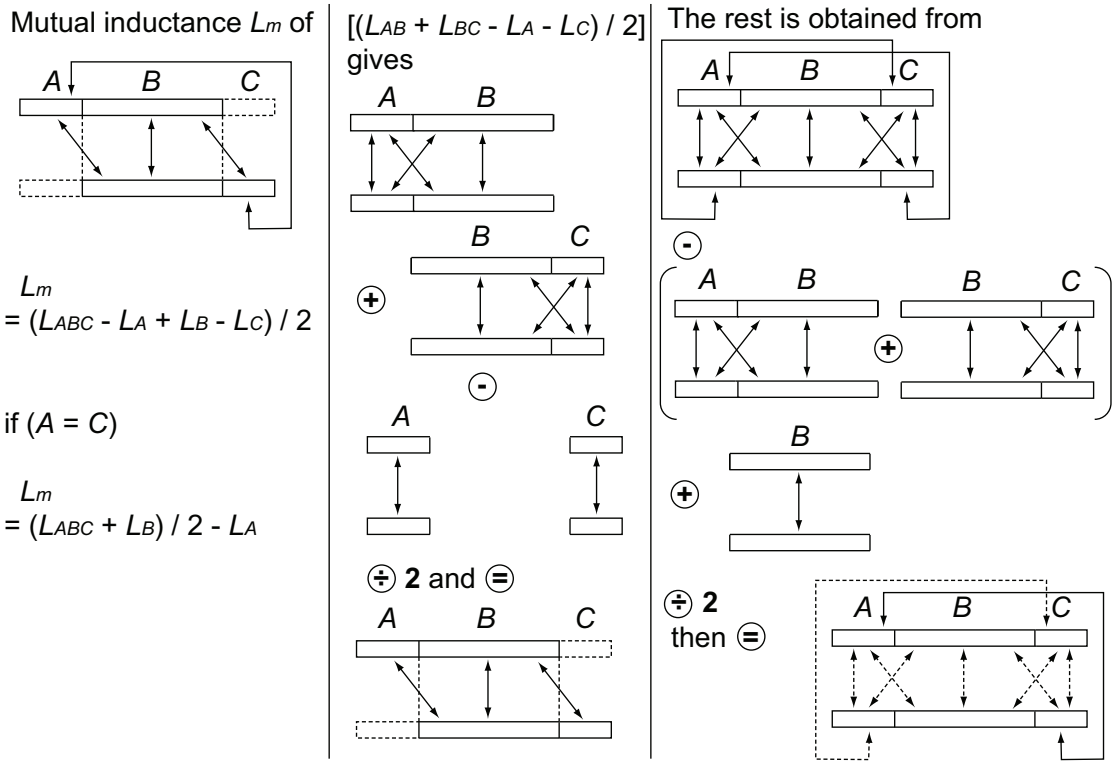

Figure 4.16: Calculation processes for mutual inductance between geometrically asymmetric but same lengths of two wires.

added to that between the B part (the centre of the right column in Fig. 4.16), the calculated value becomes double of the mutual inductance between the AC parts. Therefore, dividing it by two and adding this to the previous calculation result lead to the mutual inductance between geometrically asymmetric wires ${}_{asm}L_m$ (the bottom of the right column in Fig. 4.16), i.e.

$$\begin{aligned} {}_{asm}L_m &= \frac{(L_{AB} + L_{BC} - L_A - L_C) + (L_{ABC} - L_{AB} - L_{BC} + L_B)}{2} \\ &= \frac{L_{ABC} - L_A + L_B - L_C}{2}, \end{aligned} \tag{4.3.19}$$

where the subscripts A, B and C represent the corresponding parts of the wires. If the A and C parts are a same length as the asymmetrically paired CW used in this subsection,

$${}_{asm}L_m = \frac{L_{ABC} + L_B}{2} - L_A. \tag{4.3.20}$$

Therefore, the mutual inductances with the bottom CWs in the neighbouring units, L_{my_btm}, can be calculated from

$$\begin{aligned} L_{my\_btm} &= \frac{L\left(l_y + d_x,\ \sqrt{l_t^2 + t_s^2}\right) + L\left(l_y - d_x,\ \sqrt{l_t^2 + t_s^2}\right)}{2} \\ &\quad - L\left(d_x,\ \sqrt{l_t^2 + t_s^2}\right). \end{aligned} \tag{4.3.21}$$

Because of the symmetric geometry a straightforward calculation is applied for the mutual inductances with the top CWs in the neighbour units

$$L_{my\_top} = L(l_y,\ l_t). \tag{4.3.22}$$

Due to the asymmetry the L_{mz} calculation uses the same calculation processes with L_{my_btm}, i.e.

$$L_{mz} = \frac{L(l_y + d_x,\ t_s) + L(l_y - d_x,\ t_s)}{2} - L(d_x,\ t_s). \tag{4.3.23}$$

Adding these modified parameters to the equivalent circuit for the asymmetrically paired CW metamaterials, the resonant frequency of the asymmetrically

paired CW metamaterials, f_{2_asm}, is given from the next equation:

$$\begin{aligned} f_{2\_asm} &= \frac{1}{2\pi\sqrt{L_{2\_asm}C_{2\_asm}}} \\ &= \frac{1}{2\pi\sqrt{\left[L_s - L_{mz} + 2\left(L_{my\_top} - L_{my\_btm}\right)\right]\left[C_s + \frac{C_{mx}}{2} + \frac{C'_{mz}}{2}\right]}} \quad [\mathrm{Hz}], \end{aligned} \tag{4.3.24}$$

where L_{2_asm} and C_{2_asm} represent the total inductance and total capacitance, respectively. The mutual inductances and mutual capacitances used here are visualised in Fig. 4.17, and the equivalent circuit is drawn in Fig. 4.18. The comparison results between the magnetic resonant frequencies calculated by eq. (4.3.24) and those by numerical simulations are shown in Fig. 4.19. This figure demonstrates close agreement between them, the difference being only about 4 %.

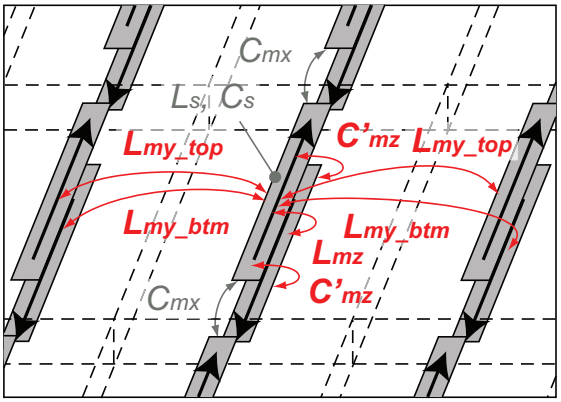

Figure 4.17: Mutual inductances and mutual capacitances used for equivalent circuit of asymmetrically paired CW array. The subscripts s and m represent self and mutual values. The subscripts following m indicate main directions along which the mutual effects work. The directions of the conduction currents are described by the black arrows.

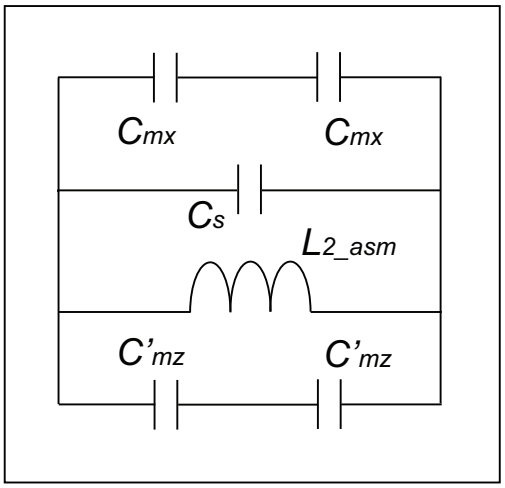

Figure 4.18: Equivalent circuit for predicting magnetic resonant frequencies of asymmetrically paired CW arrays. The equivalent circuit is based on eq. (4.3.24). This equivalent circuit is same with that for symmetrically paired CW arrays (illustrated in Fig. 4.13), although some mutual parameters are modified to take account of the geometrical asymmetry.

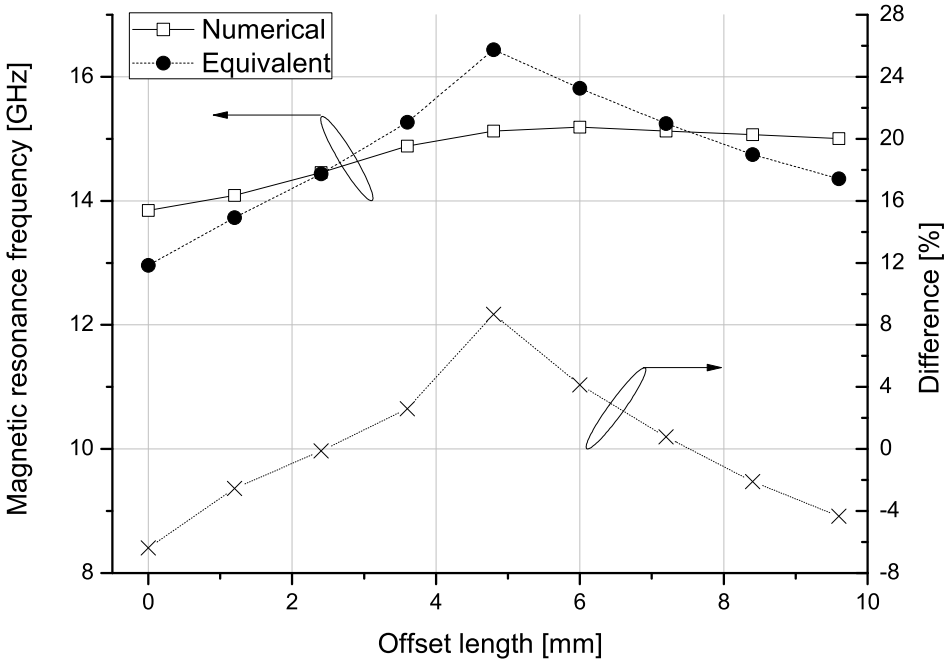

Figure 4.19: Magnetic resonant frequencies for asymmetrically paired CW arrays. The resonant frequencies were derived by equivalent circuit (see Fig. 4.13 and eq. (4.3.17)) and numerical simulations.

4.4 Discussion

In this section comparisons with a previous equivalent circuit, improvements in the proposed equivalent circuits and another explanation for resonant frequency shift of paired CW compared to those of single CW, are discussed.

4.4.1 Previous Equivalent Circuit for Symmetrically Paired CW

In reference [22] a different equation for the magnetic resonance frequency of a symmetrically paired CW is provided. However, one of the most important differences with [22] is that, while [22] uses a numerical factor having a certain range to obtain the resonant frequency, the equivalent circuit offered in this chapter avoided the use of such a factor. Other merits of the proposed equivalent circuit include that it enables us to consider some small influences of the substrate thickness t_s (and width l_y if L_{my} is included) and other characteristics. Furthermore, [22] did not study the asymmetric case, which is considered here.

4.4.2 Calculation Errors for Asymmetrically Paired CW

Although generally good agreement was obtained for the asymmetrically paired CW, the difference with numerical simulation exceeded 8 % around d_x = 4.8 mm. This is assumed to be due to some factors which were not incorporated in the equivalent circuit.

Figs. 4.20 and 4.21 respectively summarise all the inductances and capacitances used here as a function of the offset length. Referring to the resonant frequencies calculated in Fig. 4.19, it is found that the sharp increase of the resonant frequencies from 0.0 to 4.8 mm offset can be attributed to the sharp decrease of the total capacitance, which was dominated by C_{mz}. The formulae used here do not take into account edge effects, thus explaining the observed

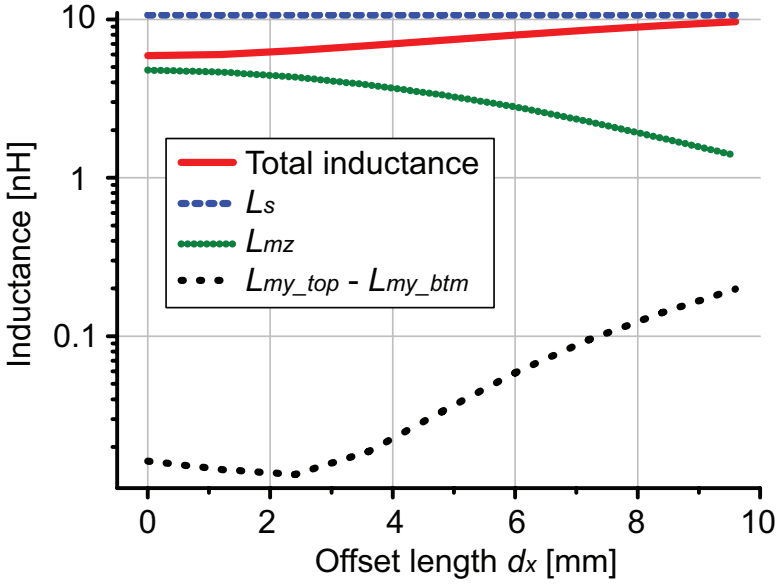

Figure 4.20: All inductance values used for equivalent circuit of asymmetrically paired CW arrays.

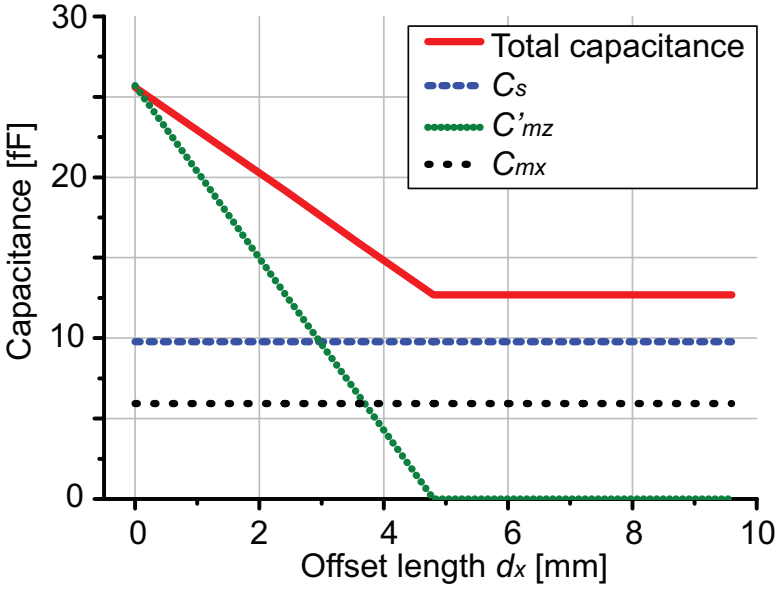

Figure 4.21: All capacitance values used for equivalent circuit of asymmetrically paired CW arrays.

discrepancies. In Fig. 4.22 the electric field at the zx plane of the CW positions is shown for d_x = 1.2 mm, and these effects are highlighted by the two black dashed circles.

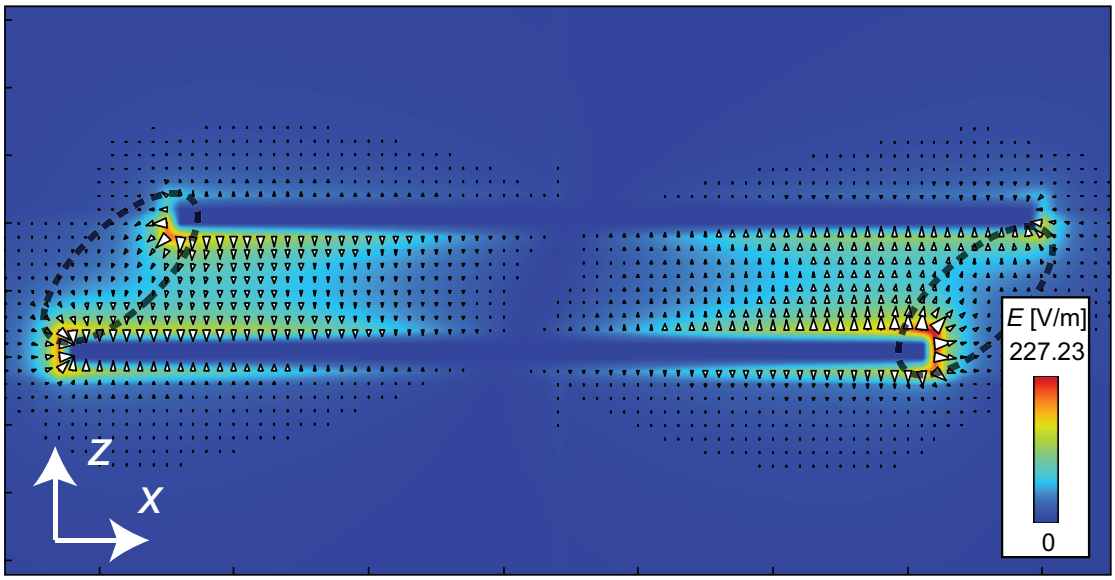

Figure 4.22: Electric field of asymmetrically paired CW at the magnetic resonant frequency of d_x = 1.2 mm.

4.4.3 Mutual Inductances

As mentioned in the subsection 4.3.1 the impact of the mutual inductances was determined by numerical simulations. In these simulations the dimension of the substrate (periodicity) of the CW metamaterials was changed so that it was confirmed whether the mutual inductances have influence over the total inductance positively or negatively.

Although straightforward trends were confirmed in the single CW and symmetrically paired CW, for the L_{my} (which is calculated from the difference between L_{my_top} and L_{my_btm}) of the asymmetrically paired CW, a complicated situation was found as shown in Fig. 4.23. In this figure the magnetic resonant frequencies are shown as a function of y axis dimension. It turns out from these results that for the shorter offset length the magnetic resonance decreases as the y axis dimension decreases. Since the influence of L_{my_top} becomes relatively stronger than that of L_{my_btm} due to the shorter distance, these results indicate that L_{my_top} and L_{my_btm} respectively have positive and negative influences on the total inductance here. However, the opposite phenomenon is confirmed for

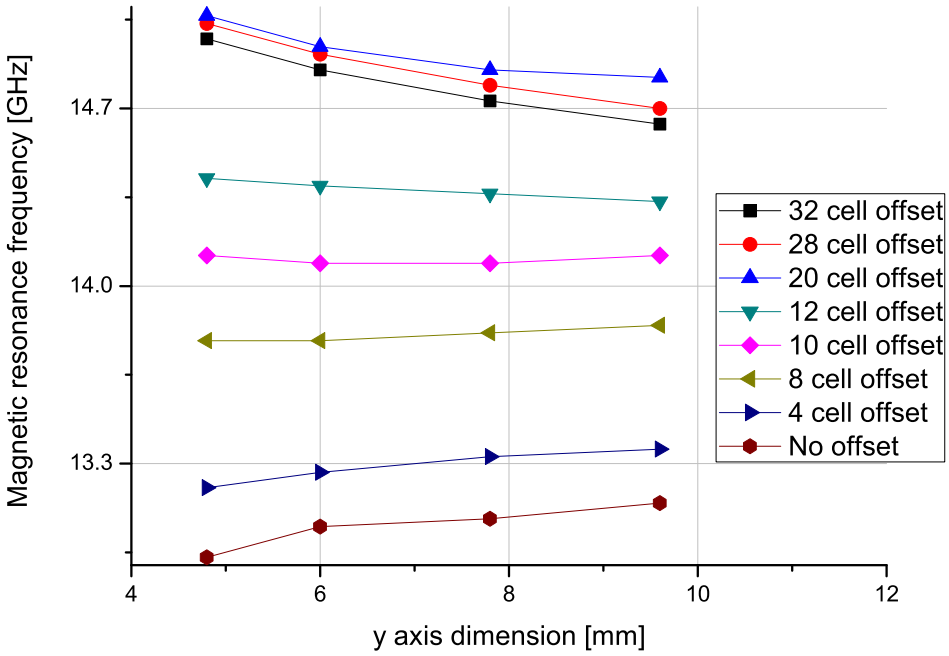

Figure 4.23: Magnetic resonant frequencies for asymmetrically paired CW arrays with various y axis periodicities.

the longer offset case and, for example, for $d_x = 9.6$ mm L_{my_top} and L_{my_btm} respectively have negative and positive influences. Though the contribution of L_{my} to the total inductance is relatively limited as found from Fig. 4.20, clarifying these trends may be useful to further understand the resonance mechanism of the asymmetrically paired CW.

4.4.4 Resonant Frequency Shifts from Single CW

In electric and magnetic resonances of symmetrically paired CW metamaterials, the resonant frequencies tend to shift from that of the single CW metamaterial to lower and higher frequencies, respectively (see Fig. 4.1). As found from Fig. 4.1, the induced magnetic field and electric field appear between the CW pair in each case, which indicates that the pair of the CWs is coupled by capacitors and inductor, respectively. These resonant shifts can

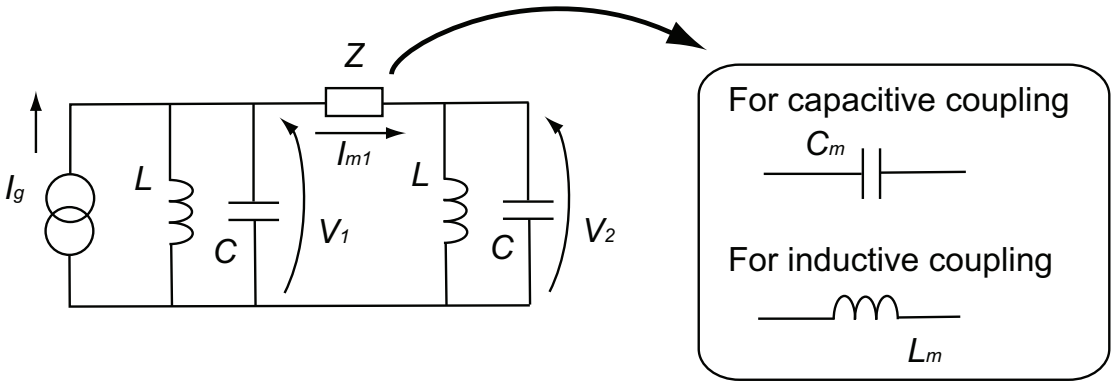

Figure 4.24: Equivalent circuit to predict resonant frequency shift of symmetrically paired CW from single CW.

be explained by a circuit illustrated in Fig. 4.24. In this circuit each CW is described by the total capacitance C and total inductance L, and the capacitive coupling and inductive coupling are described by C_m and L_m located in the position of the impedance Z.

As an example, the inductive coupling (i.e. $Z = j\omega L$) is considered below. In this case the following equations are obtained from this circuit (Fig. 4.24):

$$\begin{cases} I_g - I_{m1} &= \frac{1}{sL}V_1 + sCV_1 \\ I_{m1} &= \frac{1}{sL}V_2 + sCV_2 \end{cases}, \tag{4.4.1}$$

where $j\omega$ and $1/j\omega$ are respectively replaced with s and $1/s$, V_1 and V_2 are the voltages of the two CWs, I_g is the applied voltage and I_{m1} is the current flowing in Z. Also, from the voltage differences,

$$\begin{cases} V_1 - V_2 &= sL_mI_{m1} \\ \frac{1}{sL_m}(V_1 - V_2) &= I_{m1} \end{cases}. \tag{4.4.2}$$

Substituting eq. (4.4.2) into eq. (4.4.1) gives

$$\begin{bmatrix} \frac{1}{sL} + sC + \frac{1}{sL_m} & -\frac{1}{sL_m} \\ -\frac{1}{sL_m} & \frac{1}{sL} + sC + \frac{1}{sL_m} \end{bmatrix} \begin{bmatrix} V_1 \\ V_2 \end{bmatrix} = \begin{bmatrix} I_g \\ 0 \end{bmatrix} \tag{4.4.3}$$

$$\mathbf{Y} \begin{bmatrix} V_1 \\ V_2 \end{bmatrix} = \begin{bmatrix} I_g \\ 0 \end{bmatrix}, \tag{4.4.4}$$

where

$$\mathbf{Y} = \begin{bmatrix} \frac{1}{sL} + sC + \frac{1}{sL_m} & -\frac{1}{sL_m} \\ -\frac{1}{sL_m} & \frac{1}{sL} + sC + \frac{1}{sL_m} \end{bmatrix}. \tag{4.4.5}$$

At resonant frequency $\det \mathbf{Y} = 0$. Therefore,

$$LCs^4 + \left(2 + \frac{2L}{L_m}\right)s^2 + \frac{1}{LC} + \frac{2}{L_m C} = 0. \tag{4.4.6}$$

Solving this equation for s^2 leads

$$s^2 = \frac{-\left(1 + \frac{L}{L_m}\right) \pm \frac{L}{L_m}}{LC}. \tag{4.4.7}$$

Substituting $s = j\omega$ and $\omega_0 = 1/\sqrt{LC}$ where ω_0 is the angular resonant frequency of the single CW,

$$\begin{aligned} \omega^2 &= \omega_0^2\left(1 + \frac{L}{L_m} \pm \frac{L}{L_m}\right) \\ \omega &= \omega_0, \quad \omega_0\sqrt{1 + \frac{2L}{L_m}}. \end{aligned} \tag{4.4.8}$$

This equation indicates that the electric resonance frequency of the paired CW is shifted from that of the single CW to higher frequency.

Similarly the resonance frequency shift of the capacitive coupling can be predicted by using the mutual capacitance C_m instead of the mutual inductance L_m. The resultant resonance frequency becomes

$$\omega = \omega_0, \quad \frac{\omega_0}{\sqrt{1 + \frac{2C_m}{C}}}. \tag{4.4.9}$$

Hence, the magnetic resonant frequency of the paired CW is found to shift to lower frequency region, compared to that of the single CW.

This notion can be applied to the coupling of some other structures. For example, in [111] where the authors study metamaterial units composed of

more than two SRRs, capacitive and inductive coupling are found between the SRR units. Although they explained the resonant frequency shifts in a different way, the explanations introduced here are also applicable to this case and consistent with the results shown in [111].

In addition to the two CW pair case, the three CW pair case can be also derived in a similar manner by using the circuit sketched in Fig. 4.25. Similar calculation processes can be applied for this case as well and the result of the magnetic resonant frequency becomes

$$\omega = \omega_0, \quad \frac{\omega_0}{\sqrt{1 + \frac{3C_m}{C}}}. \tag{4.4.10}$$

This indicates a further shift from the magnetic resonance frequency of the two CW pair to lower frequency. Numerical simulations showed that the electric resonance frequency of a single CW (l_t = 9.6 mm) and the magnetic resonance frequencies of the two and three CW pairs appear around 14.70, 13.85 and 13.11 GHz, respectively, and supported the resonant frequency shifts predicted by eqs. (4.4.9) and (4.4.10).

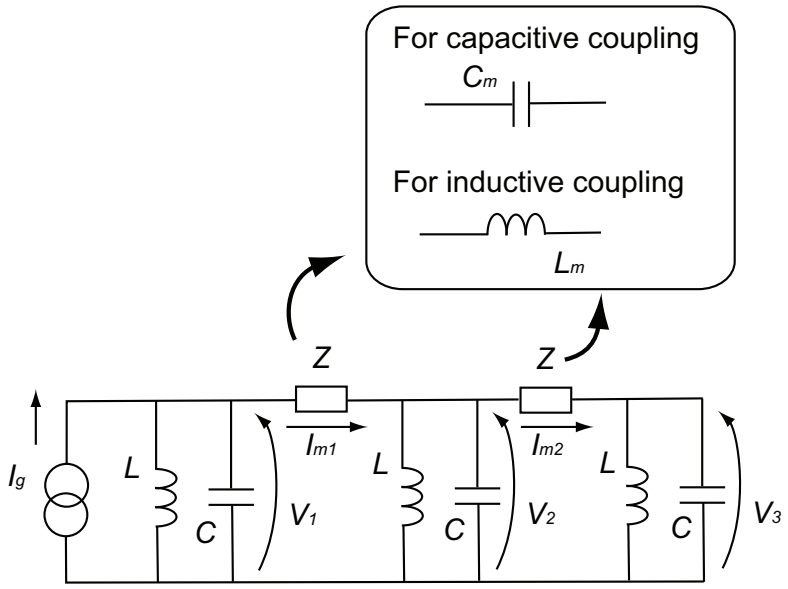

Figure 4.25: Equivalent circuit to predict resonant frequency shift of three CW pair from single CW.

4.5 Conclusion

Equivalent circuits for three types of CW metamaterials have been proposed in this chapter. Close agreement with numerically derived values was obtained, the difference being approximately 4, 6, and 4 % for single CW, symmetrically paired CW and asymmetrically paired CW, respectively. In reference [22] a different equation for the magnetic resonance frequency of the symmetrically paired CW is provided. However, one of the most important differences with [22] is that, while [22] uses a numerical factor having a certain range to obtain the resonant frequency, the equivalent circuit offered here avoided the use of such a factor. Other merits of eq. (4.3.17) include that it enables us to consider some small influences of the substrate thickness t_s (and width if L_{my} is included) and other characteristics. Furthermore, the equivalent circuit introduced here was extended to asymmetric cases which are useful when a negative refractive index is desired. In the asymmetrically paired CW the differences between estimates from the equivalent circuit and numerical simulations became relatively large at around d_x = 4.8 mm. This discrepancy may be reduced by accounting for edge effects.

CHAPTER 5

Characterisation by Retrieval Methods

5.1 Introduction

This chapter introduces a calculation method to effectively perform large–scale metamaterial simulations [72]. This is possible by using retrieved (homogenised and extracted) metamaterial properties. In the first part of this chapter some retrieval methods [58, 59] are introduced and applied to basic metamaterial structures. Then a numerical simulation method based on such retrieved properties is explained and used to confirm fundamental metamaterial behaviour in the TLM. This is one of the ways introduced in this thesis to reduce computational effort of metamaterial modelling, since the original fine features of metamaterials can be described by coarse cells with bulk properties. This chapter shows calculation results obtained by the simulation techniques already reported in past research works [58, 59, 72]. However, these results are still necessary to clarify differences between these techniques and DF techniques introduced in the next chapter.

5.2 Retrieval Methods

So far many retrieval methods have been suggested based on the type of the retrieving processes and what metamaterial is considered. In reference [112], for example, the existing methods are categorised into groups depending on the techniques used, e.g. retrieval using scattering parameters [58, 59, 61], averaged fields [113, 114], quasi–mode theory [115] and wave propagations [112, 116]. In addition to these, the classical Snell's law can be simply applied for exact metamaterial structures to solve for the refractive index, e.g. [3, 117, 118] (note this is a solution to derive only refractive indices). This chapter utilises the retrieval method proposed by Smith et al. in 2002 [58] (termed Smith's method here) and the one by Ziolkowski in 2005 [59] (termed Ziolkowski's method here), both of which solve for the effective electromagnetic parameters, based on scattering parameters. Since these techniques are well known and the details can be found from [58, 59], only brief introductions are given below.

5.2.1 Smith's Method

Smith's method derives relative permittivities ε_r and relative permeabilities μ_r of metamaterials from the following classical transmission line equations including the reflection coefficient S_{11} and transmission coefficient S_{21} [58]:

$$\frac{1}{S_{21}} = \left(\cos\left(nk_0d\right) - \frac{1}{2}j\left(z + \frac{1}{z}\right)\sin\left(nk_0d\right)\right)\exp\left(jk_0d\right), \tag{5.2.1}$$

$$\frac{S_{11}}{\hat{S}_{21}} = -\frac{1}{2}j\left(z - \frac{1}{z}\right)\sin\left(nk_0d\right), \tag{5.2.2}$$

where

$$\hat{S}_{21} = S_{21}\exp\left(jk_0d\right), \tag{5.2.3}$$

k_0 is a wavenumber of the incident wave (i.e. $k_0 = \omega/c_0$) and d is the total thickness of the metamaterial structure considered. n and z represent the refractive

index and normalised wave impedance calculated from

$$n = \pm\sqrt{\varepsilon_r \mu_r} \tag{5.2.4}$$

$$z = \sqrt{\frac{\mu_r}{\varepsilon_r}}, \tag{5.2.5}$$

where ε_r and μ_r represent the relative permittivity and relative permeability, respectively. The negative sign is added to n in the above expression to take account of $n' < 0$, when $\varepsilon_r' < 0$ and $\mu_r' < 0$, where $'$ indicates the real part of the complex number [4, 9].

Solving eqs. (5.2.1) and (5.2.2) for n and z leads to [58]

$$z = \pm\sqrt{\frac{(1+S_{11})^2 - \hat{S}_{21}^2}{(1-S_{11})^2 - \hat{S}_{21}^2}}, \tag{5.2.6}$$

$$n'' = \pm\mathbf{Im}\left[\frac{\arccos\dfrac{1-(S_{11}^2 - \hat{S}_{21}^2)}{2\hat{S}_{21}}}{k_0 d}\right], \tag{5.2.7}$$

$$n' = \pm\mathbf{Re}\left[\frac{\arccos\dfrac{1-(S_{11}^2 - \hat{S}_{21}^2)}{2\hat{S}_{21}}}{k_0 d}\right] + \frac{2\pi m}{k_0 d}, \tag{5.2.8}$$

where $''$ represents the imaginary part of the complex number, **Re** and **Im** denote taking the real part and imaginary part and m is an integer. As seen from these equations, each parameter has at least two candidates for the answer, since n and z in eqs. (5.2.1) and (5.2.2) are associated with the trigonometrical functions. Also, since n was inverted from the cosine function (see eqs. (5.2.7) and (5.2.8)), n' has multiple candidate answers.

For retrieval methods based on scattering parameters, overcoming these ambiguities is an issue and some approaches to this problem have been suggested (e.g. [61]. This method is introduced in appendix C). In Smith's method the double sign issue is simply solved by imposing the following requirements:

$$z' > 0, \tag{5.2.9}$$

$$n'' > 0. \tag{5.2.10}$$

These conditions are expected to be valid, unless metamaterials include gain media, which may lower n'' below zero (this is not a stable condition as explained in subsection 1.4.1).

Also, as a solution for n', Smith's method proposed to retrieve different numbers of metamaterial units and compare the answers to each other. In this way, although there may be interaction(s) between the metamaterial units, which can slightly affect the retrieved results, n' is basically independent of the number of the metamaterial units. Therefore, the result closest to that of other metamaterial unit numbers can be the right answer for n'.

Although this is not mentioned in [58], to maintain the consistency of following the Maxwell's equations for negative refractive index media as well [4], the next expressions were used in this chapter:

$$\mu_r = \pm nz \tag{5.2.11}$$

$$\varepsilon_r = \pm \frac{n}{z}. \tag{5.2.12}$$

These signs are normally set to $+$ signs. If $n' < 0$ which indicates that μ_r' and ε_r' are expected to be both negative (see eq. (5.2.4)), the $\pm$ signs were manipulated so that $\mu_r' < 0$ and $\varepsilon_r' < 0$ are obtained.

5.2.2 Ziolkowski's Method

Similarly to Smith's method, Ziolkowski's method [59] retrieves relative permittivity and permeability of metamaterials from the scattering parameters, but different equations are applied to avoid the ambiguous signs and branch issue in n' (i.e. the m term in eq. (5.2.8)). This method is essentially based on the conditions

$$S_{11} \sim 0 \tag{5.2.13}$$

$$S_{21} \sim \mathcal{Z}_t, \tag{5.2.14}$$

where $\mathcal{Z}_t$ stands for the transmission term and

$$\mathcal{Z}_t \sim \exp(-jkd) \tag{5.2.15}$$

and $k = k_0 n$. Eqs. (5.2.13) and (5.2.14) can be satisfied, if the metamaterial has a negative refractive index and limited loss factor(s).

Ziolkowski's method derives ε_r and μ_r by introducing the interface reflection coefficient term $\mathcal{Z}_r$ and transmission term $\mathcal{Z}_t$, both of which are defined in [59]

$$\mathcal{Z}_t = \frac{V_1 - \mathcal{Z}_r}{1 - \mathcal{Z}_r V_1} \tag{5.2.16}$$

$$\mathcal{Z}_r = \frac{\mathcal{Z}_t - V_2}{1 - \mathcal{Z}_t V_2}, \tag{5.2.17}$$

where

$$\begin{aligned} V_1 &= S_{21} + S_{11}, \\ V_2 &= S_{21} - S_{11}. \end{aligned} \tag{5.2.18}$$

Eqs. (5.2.16) and (5.2.17) can be rearranged to yield [59]

$$1 - \mathcal{Z}_t = \frac{(1 - V_1)(1 + \mathcal{Z}_r)}{1 - \mathcal{Z}_r V_1}, \tag{5.2.19}$$

$$z = \frac{1 + \mathcal{Z}_r}{1 - \mathcal{Z}_r} = \frac{1 + \mathcal{Z}_t}{1 - \mathcal{Z}_t} \frac{1 - V_2}{1 + V_2}. \tag{5.2.20}$$

Here, assuming $k'd \leq 1$ where k' is the real part of the complex wave number calculated from $k = \omega\sqrt{\varepsilon_r \mu_r}/c = k_0\sqrt{\varepsilon_r \mu_r}$, the next approximation can be obtained [59]:

$$\mathcal{Z}_t \sim 1 - jkd. \tag{5.2.21}$$

In this case the complex wave number and permeability can be calculated by using eq. (5.2.21) in eqs. (5.2.19) and (5.2.20), i.e.

$$k \sim \frac{1}{jd} \frac{(1 - V_1)(1 + \mathcal{Z}_r)}{1 - \mathcal{Z}_r V_1} \tag{5.2.22}$$

$$\mu_r \sim \frac{2}{jk_0 d} \frac{1 - V_2}{1 + V_2}. \tag{5.2.23}$$

Also, the permittivity can be solved as [59]

$$\varepsilon_r \sim \frac{2}{jk_0 d}\frac{1-V_1}{1+V_1}. \tag{5.2.24}$$

However, in [59] it is reported that if both electric resonance (yielding $\varepsilon_r' < 0$) and magnetic resonance (yielding $\mu_r' < 0$) are very close to each other, this equation may fail to produce physically proper values. Instead, the following equation is applied [59]:

$$S_{11} \sim \frac{2jkd(z^2-1)}{(z+1)^2-(z-1)^2} = 2jkd\frac{z^2-1}{4z}, \tag{5.2.25}$$

which yields [59]

$$\varepsilon_r \sim \mu_r + j\frac{2S_{11}}{k_0 d}. \tag{5.2.26}$$

It is stated in [59] that even if both resonances are in close proximity to each other, when negative index occurs, S_{11} approaches zero and similar responses are found from ε_r' and μ_r' (since $\varepsilon_r \sim \mu_r$).

However, the detailed derivation of eq. (5.2.25) is not clarified in [59]. In addition, since in this chapter the simulated metamaterials are not designed to have electric resonance close to magnetic resonance, eq. (5.2.24) instead of eq. (5.2.25) is used for ε_r. Also, even in Ziolkowski's method the refractive index n was determined from eq. (5.2.4) so that only if both ε_r' and μ_r' were negative, a negative n' was obtained.

5.3 Applications of Retrieval Methods

In this section the retrieval methods introduced in the last section are applied to three simple structures: straight wires, SRRs, and left–handed material (LHM) which combines the first two. The straight wire structure is expected to yield negative permittivity well below the cut off frequency [5, 6], and the SRRs are likely to produce negative values of permeability around the magnetic resonance frequency [7]. The LHM has both straight–wire–like and SRR–like prop-

erties, i.e. this structure is expected to exhibit both negative permittivity and permeability, which results in a negative refractive index [58].

5.3.1 Calculation Conditions

The calculation conditions and models are shown in Figs. 5.1 and 5.2 and Table 5.1. In these simulations three or four metamaterial units were used without gap between the metamaterial units (i.e. the total length along z axis, or the propagation direction of the incident wave, was $3A_z$ or $4A_z$, where A_z is the periodicity along z axis). As may be noticed from the retrieval methods introduced above (e.g. from eqs. (5.2.1) and (5.2.2)), the total metamaterial thickness is involved in the calculation processes. It is possible that the use of only one metamaterial unit leads to misinterpretation of the periodic unit length. In addition, for Smith's method, calculation results with different numbers of metamaterial units need to be compared so that the proper branch integer m is ascertained (see eq. (5.2.8)). According to calculation results of [58], retrieving three units appears to be enough. Therefore, this section compares the results of the three metamaterial units with those of the four for the derivation of the proper branch integer m.

The positions of the metamaterials were changed depending on the structures simulated. For example, the straight wire structure illustrated in the left of Fig. 5.2 was placed next to the left edge of the periodic unit, while for the LHM there was a distance of d_{wire2} between the wire and the left edge. In this way the front position of each structure was placed at the same distance from the excitation source. For the SRRs the wire part was removed from the LHM illustrated in the right of Fig. 5.2.

Boundary conditions:
Matched boundary (*xy*),
Periodic boundary (the others)

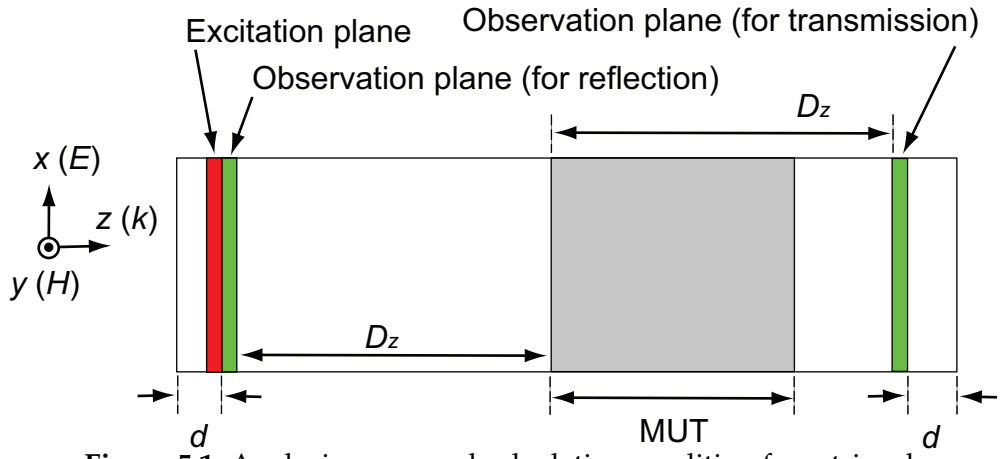

Figure 5.1: Analysis space and calculation condition for retrieval.

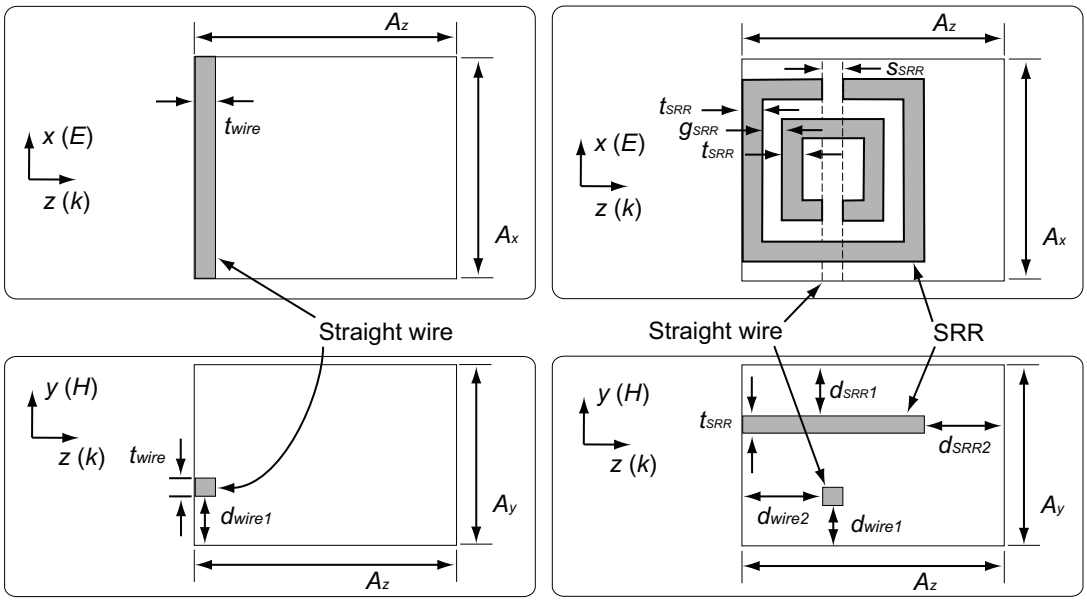

Figure 5.2: Retrieved periodic structures. The left and right figures respectively illustrate a wire structure unit and LHM unit. For a SRR unit the wire part was removed from the LHM unit.

Table 5.1: Details of retrieval simulation space.

Analysis space ($N_x \times N_y \times N_z$)	($11 \times 15 \times 137$) cells
Periodic structure unit ($A_x \times A_y \times A_z$)	($11 \times 15 \times 15$) cells
TLM unit cell size	$0.33 \times 0.33 \times 0.33$ [mm^3]
D_z	8.0 [mm]
d	0.3 [mm]
d_{wire1}	0.3 [mm]
d_{wire2}	0.3 [mm]
t_{wire}	0.1 [mm]
d_{SRR1}	0.4 [mm]
d_{SRR2}	0.6 [mm]
t_{SRR}	0.1 [mm]
g_{SRR}	0.1 [mm]
s_{SRR}	0.1 [mm]

5.3.2 Straight Wires

First of all, n' retrieved by Smith's method is shown in Fig. 5.3 with the different branch integer ms. As expected from eq. (5.2.8), as m increased, the value of n' also increased. It is also found from Fig. 5.3 that $m = 1$ of both three and four units exhibited the closest result from 10 to approximate 13 GHz, while from 13 GHz $m = 1$ of the three units and $m = 2$ of the four units were the closest. Hence, the results of $m = 1$ of the four units from 10 to about 13 GHz and $m = 2$ of the four units from 13 to 16 GHz were used for the following retrieval. As reference data, n' retrieved by Ziolkowski's method is illustrated in Fig. 5.4. This result was found to be closer to zero, compared to the result of Smith's method.

In Fig. 5.5 ε_r' retrieved by both methods is shown in addition to analytically derived values [5]. The analytical values were obtained by approximating the square wire to a round wire (where the original wire thickness t_{wire} was

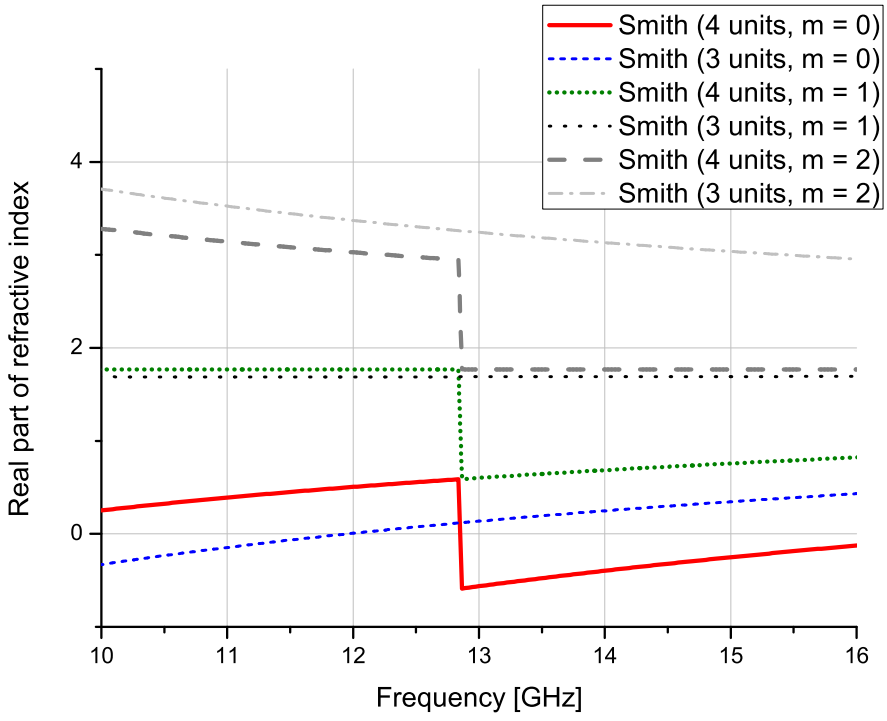

Figure 5.3: n' retrieved by Smith's method using wire units.

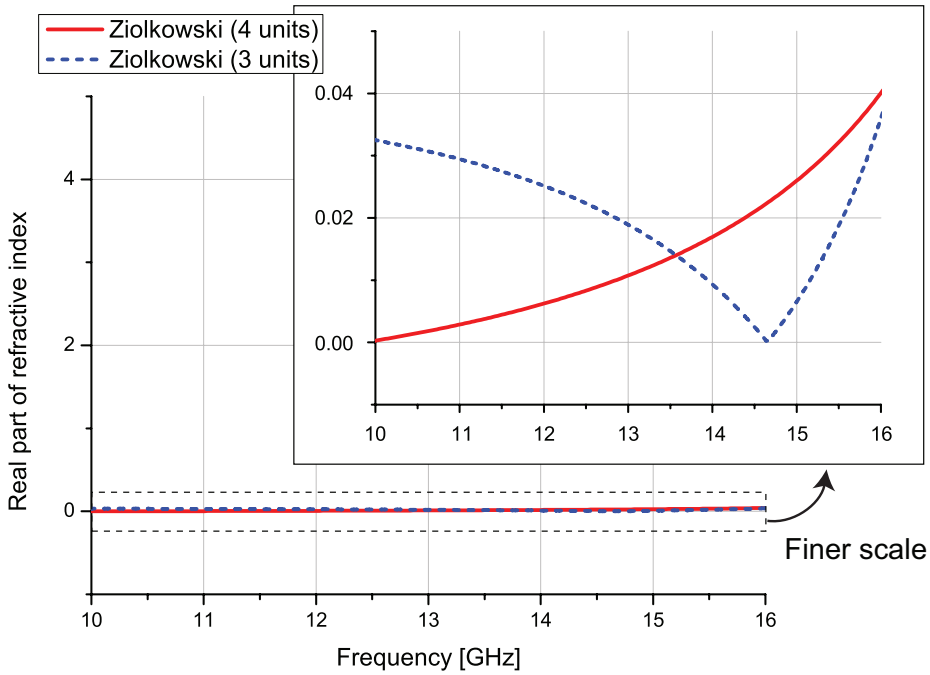

Figure 5.4: n' retrieved by Ziolkowski's method using wire units. The finer scale of the result is described in the inset.

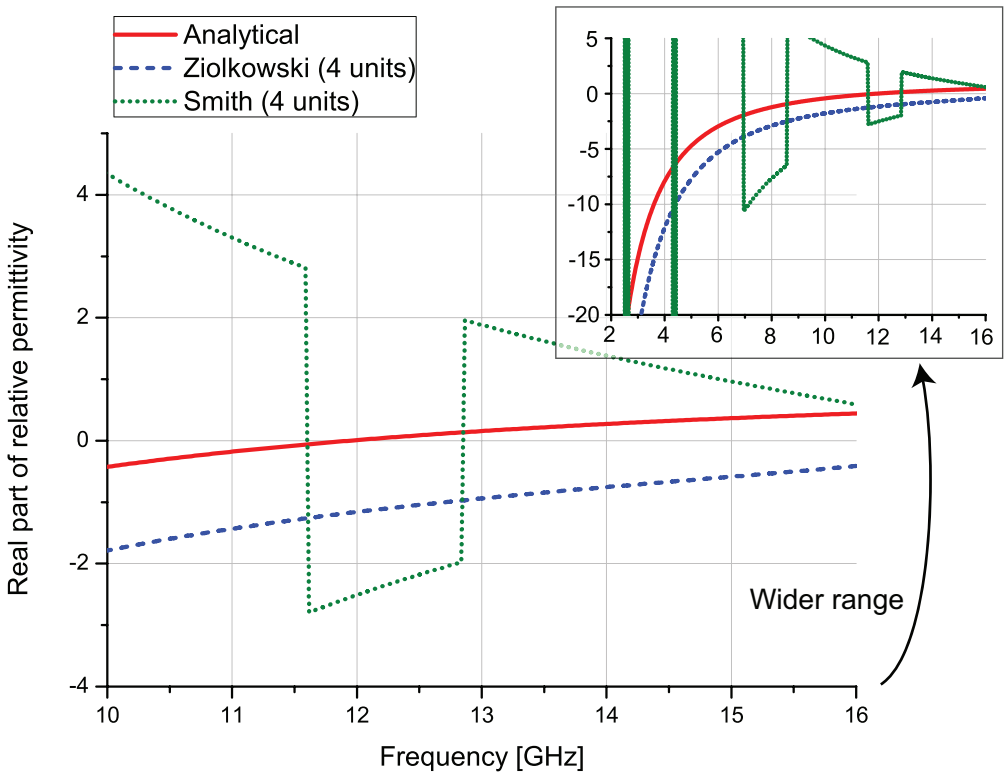

Figure 5.5: ε_r' retrieved by Smith's method and Ziolkowski's method using wire units. The wider range of the result is described in the inset.

associated with the radius of the round wire r through $r = w/4$ [107]) and calculated from [5]

$$\varepsilon_r = 1 - \frac{\omega_p^2}{\omega^2}, \tag{5.3.1}$$

where ω_p is the cutoff frequency obtained from

$$\omega_p^2 = \frac{2\pi c_0^2}{p \ln \frac{p}{r}}, \tag{5.3.2}$$

p is the periodicity (i.e. here $p = A_y = A_z$). It is seen from Fig. 5.5 that the result obtained by Ziolkowski's method is relatively close to the analytical values. For Smith's method, however, the sign of ε_r' was strangely flipped. This is assumed to be due to z, which is used for calculating ε_r through eq. (5.2.12). As confirmed from Fig. 5.6 where z was retrieved by both methods, the sign of the imaginary part calculated by Smith's method changed as well. These sign changes occurred to maintain the requirement of $z' > 0$ (see eq. (5.2.9)).

5.3.3 SRRs

Similarly the SRR structure was retrieved. However, as demonstrated in Fig. 5.7, Smith's method showed complicated results for n', which made it difficult to determine the proper values. It is also found from the results of $m = 0$ that not only z'' but also the signs of n' can be flipped. This is assumed to be due to the requirement of $n'' > 0$ (see eq. (5.2.10)).

Owing to the complicated and ambiguous results obtained by Smith's method, only Ziolkowski's method was used to retrieve the other properties of the SRR units. Fig. 5.8 represents the real part of the relative permeability. It is found that the retrieved permeability becomes negative in parts of the frequency range shown.

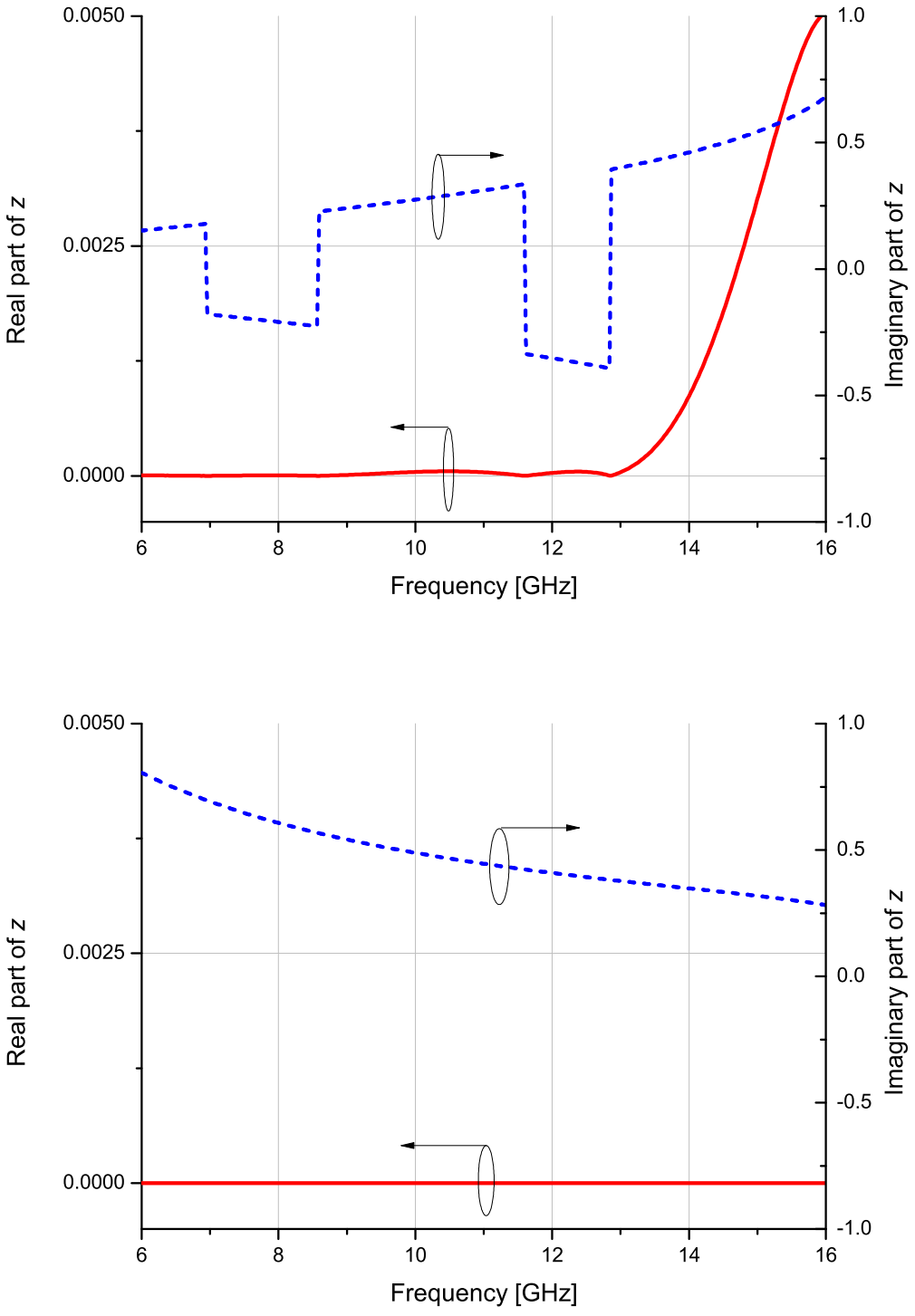

Figure 5.6: z retrieved by Smith's method (top) and Ziolkowski's method (bottom) using four wire units.

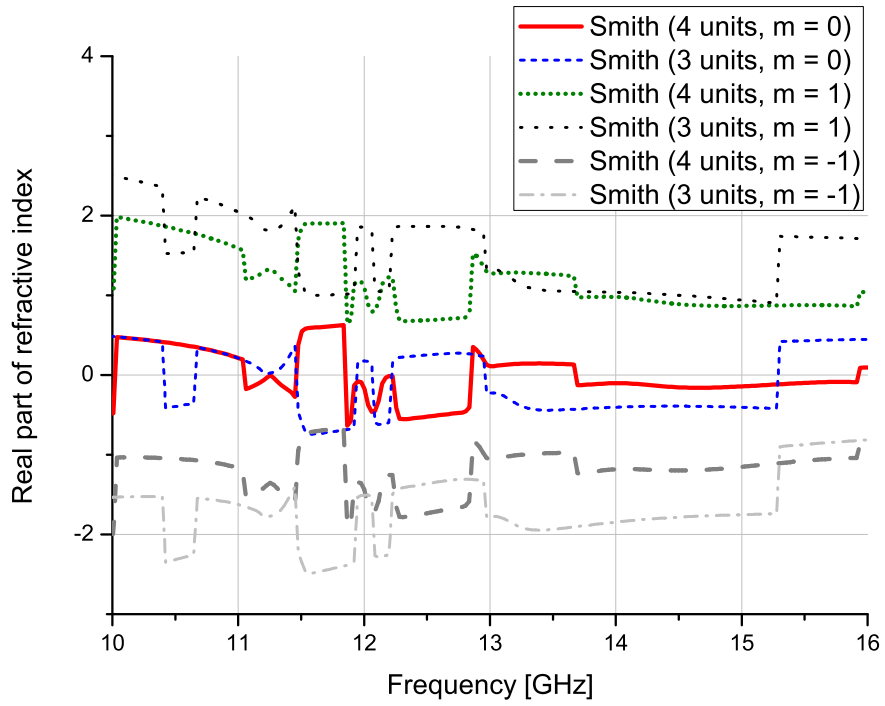

Figure 5.7: n' retrieved by Smith's method using SRR units.

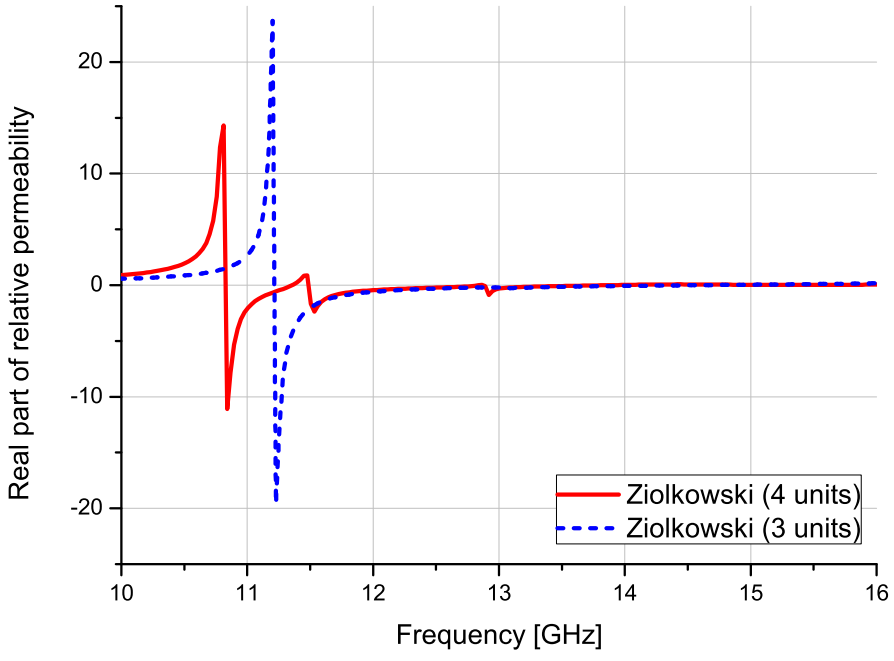

Figure 5.8: Real part of relative permeability retrieved by Ziolkowski's method using SRR units.

5.3.4 LHM

Again, as shown in Fig. 5.9 where the LHM was simulated, the use of Smith's method led to complicated n'. For this reason only Ziolkowski's method was applied for the LHM as well. The calculation result of n' is illustrated in Fig. 5.10. This figure demonstrates that the LHM simulated here can exhibit the negative values of the refractive index.

As found from Figs. 5.11 and 5.12 where the retrieved ε_r' and μ_r' are respectively displayed, both real parts became negative where the negative n' was obtained. Compared to Figs. 5.5 and 5.8 respectively showing ε_r' of the wire units and μ_r' of the SRR units, it was found that the properties of the individual structures were still maintained in the LHM, although interactions between them changed the electromagnetic properties slightly.

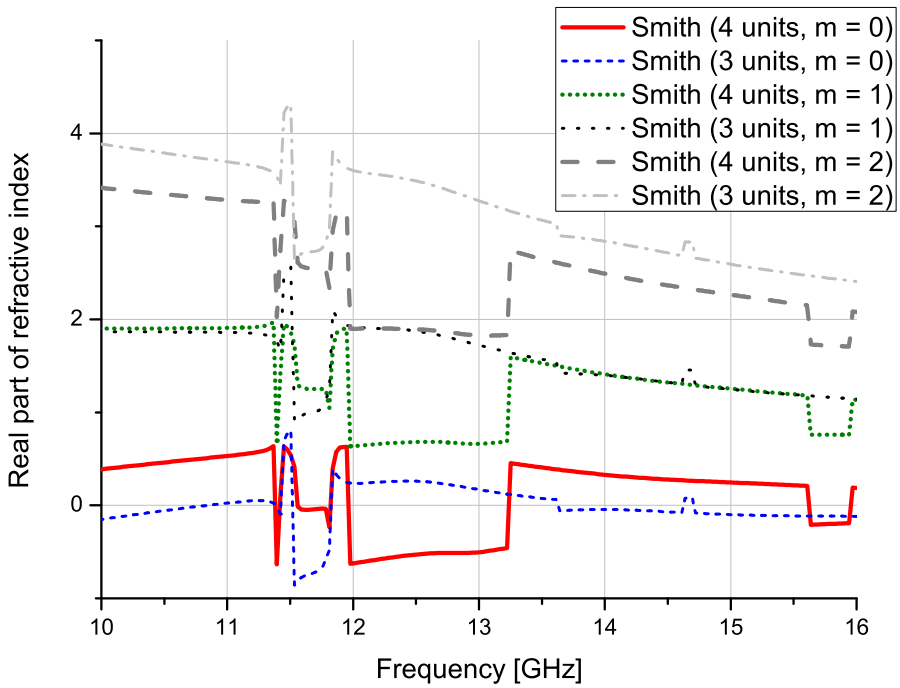

Figure 5.9: n' retrieved by Smith's method using LHM units.

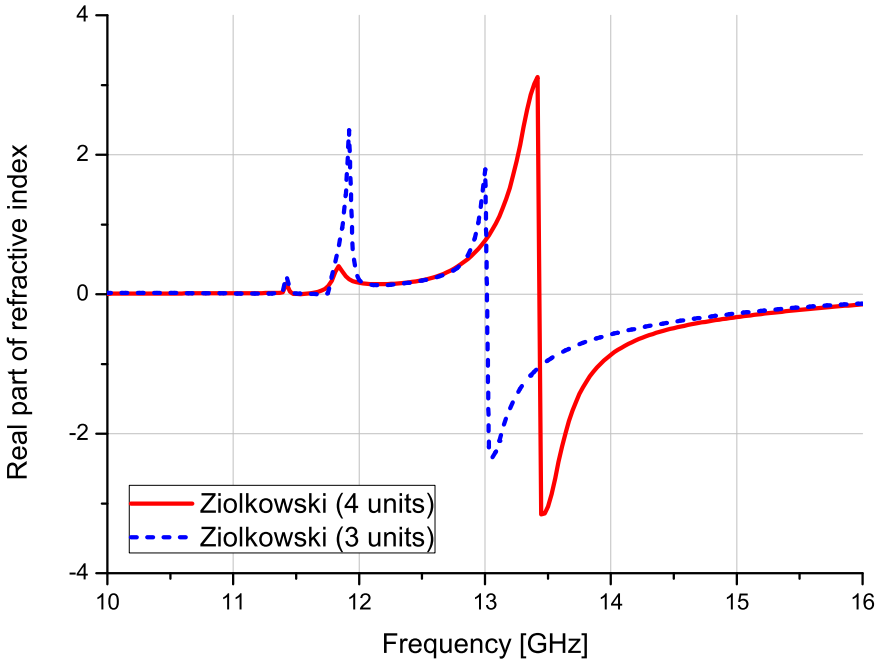

Figure 5.10: n' retrieved by Ziolkowski's method using LHM units.

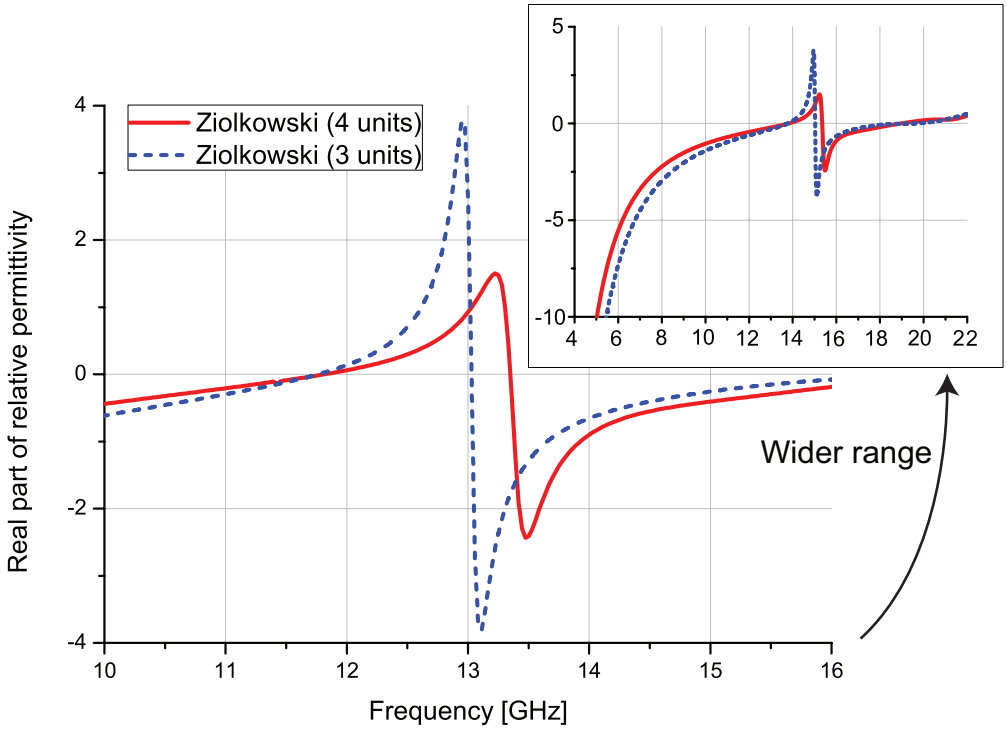

Figure 5.11: ε_r' retrieved by Ziolkowski's method using LHM units. The wider range of the result is illustrated in the inset.

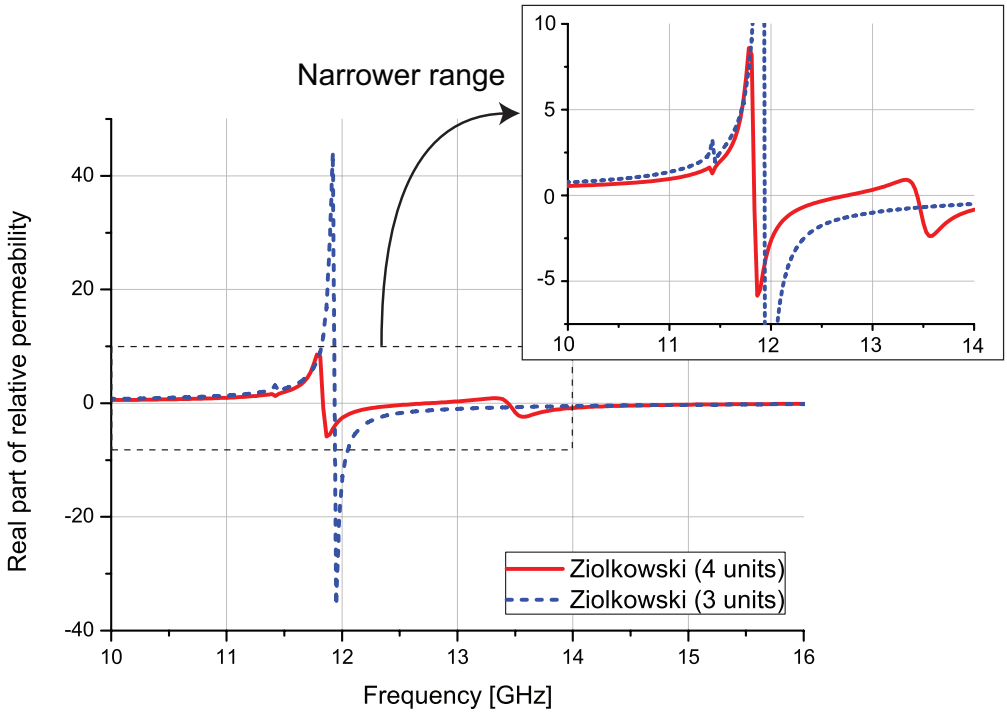

Figure 5.12: μ_r' retrieved by Ziolkowski's method using LHM units. The narrower range of the result is illustrated in the inset.

5.3.5 Discussion

A use of retrieval methods has been demonstrated in this section. However, it was difficult to judge from the calculation results only whether or not the retrieved values are good estimate for the metamaterial properties. It appeared that while Smith's method tended to have difficulties in retrieving the simulated structures, especially the SRRs and LHM, Ziolkowski's method seemed to have succeeded in extracting the metamaterial properties. Despite the successful demonstration of the negative n' in the LHM, one discrepancy arose from the real part of the permittivity, compared to a result of [58] where a similar LHM was retrieved. In Fig. 5.11 the extracted ε_r' increased with frequency and changed largely around the magnetic resonance of the SRRs. However, as illustrated in Fig. 5.13, when the magnetic resonance occurs, the anti–resonance response is generally expected to happen in the permittivity instead. In other words, at the left side of the magnetic resonance frequency the real part of the permittivity decreases, while at the right side ε_r' increases, which is the opposite phenomenon found in the result of Fig. 5.11. This may be partly due to Ziolkowski's method based on some assumptions and approximations, which were not satisfied for the simulated structures (e.g. eqs. (5.2.13) and (5.2.14) are not always satisfactory).

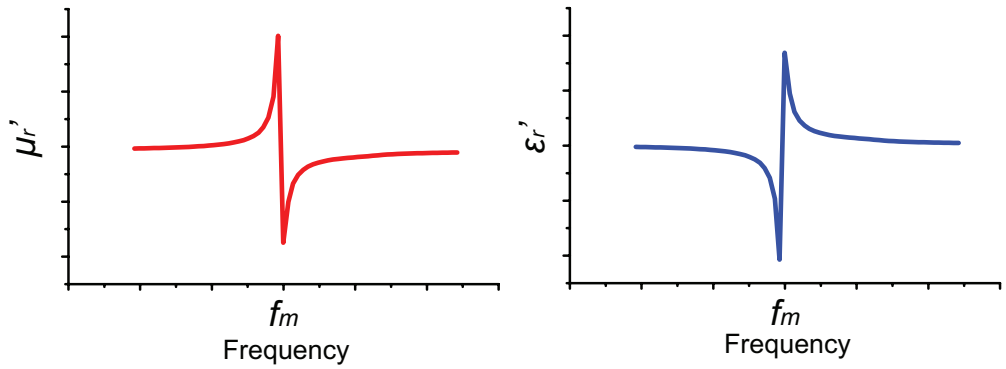

Figure 5.13: Expected anti–resonance behaviour in ε_r' of LHM. f_m stands for the magnetic resonance frequency.

In addition, it is also pointed out that Ziolkowski's method assumes metamaterials having a weak reflection (see eqs. (5.2.13) and (5.2.14)), which does not correspond to the simulated SRRs. Although a reasonable permeability was obtained for the SRRs, the real part of permittivity shown in Fig. 5.14 did not show the anti–resonance behaviour and n' became partially negative as found from the inset of Fig. 5.14. This is assumed to be affected by the scattering parameters contradicting the premise (e.g. eqs. (5.2.13) and (5.2.14)).

Although only simple periodic structures were simulated here, retrieving the electromagnetic properties did not appear to be straightforward processes. The applications to more complicated structures such as ones having bianisotropies, chiralities, non–linearities and gain media are anticipated to encounter more difficulties in obtaining the proper values, since such proper-

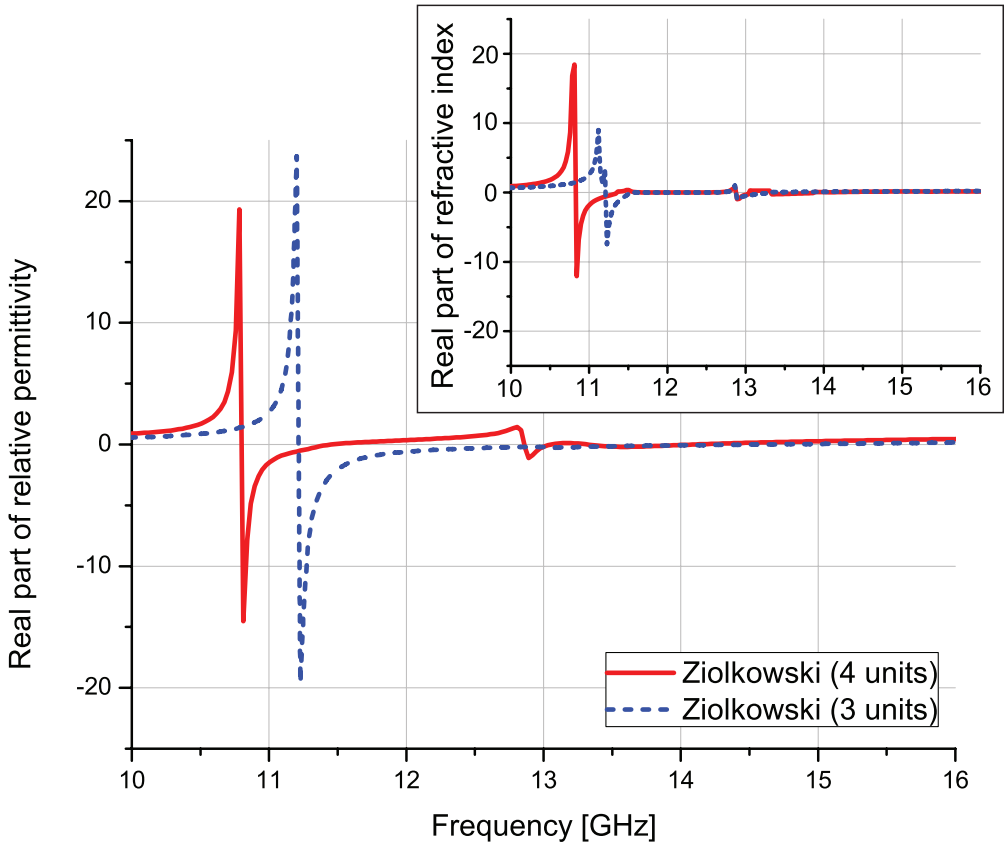

Figure 5.14: Real part of relative permittivity retrieved by Ziolkowski's method using SRR units. The inset describes the retrieved n'.

ties generally require further extra calculation processes. Also, the scattering response is not as straightforward as for the metamaterials simulated here, indicating that it will be more difficult to determine the physically reasonable values.

For the validation of the retrieved properties, one of the most secured ways is to perform numerical simulations using exact models with a fine mesh and compare with the results obtained using retrieved values with a coarse mesh. However, it is not always possible to carry out such large–scale simulations due to limited computational resources.

5.4 Metamaterial Simulations Based on Retrieved Metamaterial Properties

This section describes a simulation method to incorporate retrieved electromagnetic properties of metamaterials. It is possible to represent the negative properties of metamaterials in many simulation methods, e.g. [72, 119–123]. In this section a simulation technique reported in [72] is briefly introduced below to demonstrate the behaviour of negative refractive index metamaterials using the TLM method. The electromagnetic properties of a bulk metamaterial used were set to $\varepsilon_r = \mu_r = -1$ as mentioned later.

5.4.1 Theory

In [72] metamaterial properties are embedded between regular symmetrical condensed nodes (SCNs) as extra stubs called "inter–cell networks," as shown in Fig. 5.15. Compared to regular SCNs (see Fig. 2.1), the positions of the capacitance and inductance elements are opposite, which makes negative properties of metamaterials possible, and the direction of the phase velocity can be opposite to that of the group velocity.

The extra node is connected to that of the neighbouring cell, forming one inter–cell network (see Figs. 5.15 and 5.16). Due to the sharing of the inter–cell networks, the implementation of the negative properties into the TLM method requires six extra calculations per a TLM unit cell. Since the details of the derivation of this technique is introduced in [72], only the scattering matrices used in the following simulations are shown below.

The scattering matrices for the inter–cell networks are different, depending on what type of material is modelled in the next unit cell. For example, a scattering matrix between same metamaterials is given by [72]

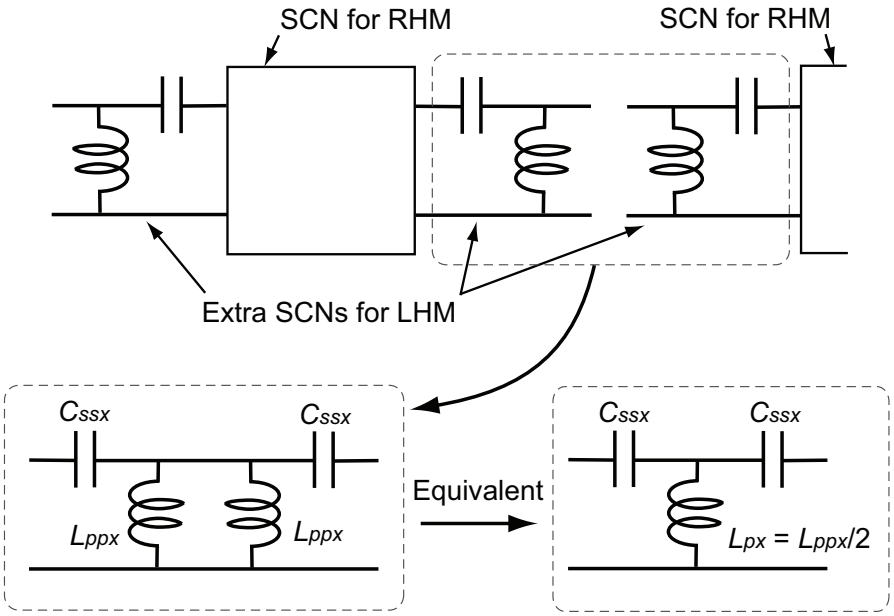

Figure 5.15: Inter–cell network between regular SCNs. RHM and LHM respectively stand for right–handed material and left–handed material here.

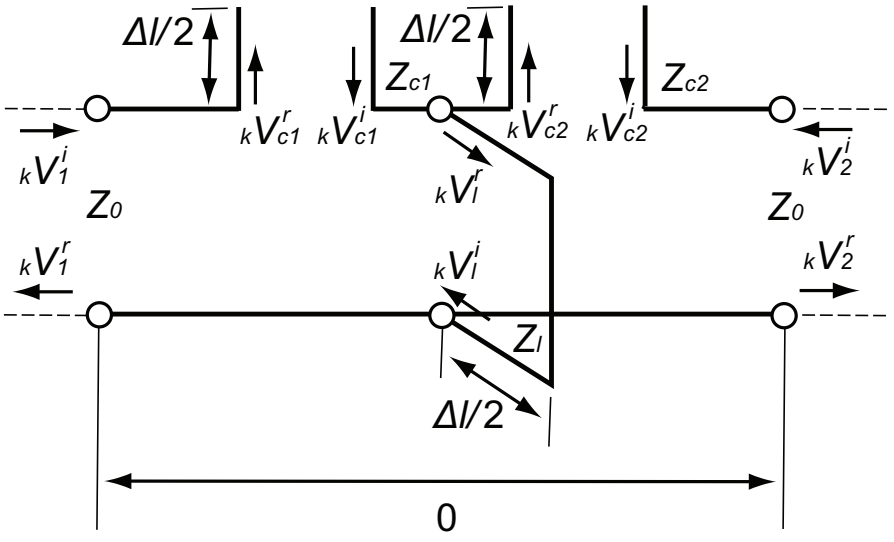

Figure 5.16: Notations of voltage nodes used for inter–cell network between regular SCNs.

$$
{}_k\begin{bmatrix} V_1 \\ V_2 \\ V_{c1} \\ V_{c2} \\ V_{ll} \end{bmatrix}^r = \begin{bmatrix} \alpha & \beta & \chi & -\beta & \delta \\ \beta & \alpha & -\beta & \chi & \delta \\ \kappa & -\tau & \vartheta & \tau & -\zeta \\ -\tau & \kappa & \tau & \vartheta & -\zeta \\ \xi & \xi & -\xi & -\xi & \gamma \end{bmatrix} \times {}_k\begin{bmatrix} V_1 \\ V_2 \\ V_{c1} \\ V_{c2} \\ V_{ll} \end{bmatrix}^i , \tag{5.4.1}
$$

where the notations of each voltage node correspond to those illustrated in Fig. 5.16 (i.e. not to Fig. 2.3) and each coefficient is given in appendix B. The subscript ll of V_{ll} indicates that same properties of metamaterials are used for the TLM unit cells.

A scattering matrix between a metamaterial and regular dielectric material (including vacuum) can be obtained from [72]

$$
{}_k\begin{bmatrix} V_1 \\ V_2 \\ V_{c1} \\ V_{l1} \end{bmatrix}^r = \begin{bmatrix} d_{11} & d_{12} & d_{13} & d_{14} \\ d_{21} & d_{22} & d_{23} & d_{24} \\ d_{31} & d_{32} & d_{33} & d_{34} \\ d_{41} & d_{42} & d_{43} & d_{44} \end{bmatrix} \times {}_k\begin{bmatrix} V_1 \\ V_2 \\ V_{c1} \\ V_{l1} \end{bmatrix}^i . \tag{5.4.2}
$$

Again, each coefficient is introduced in appendix B.

Scattering matrices for different connection patters, such as connections with PEC, PMC, absorbing boundary and different metamaterial, are found in [72].

5.4.2 Calculation Conditions

The details of the metamaterial simulations are summarised in Fig. 5.17 and Table 5.2. The analysis space was composed of $(100 \times 100 \times 120)$ cells for x, y and z axes, respectively, where $\Delta l = 1.0$ mm. For the boundary conditions, matched boundaries were applied for the xy boundaries, while the yz and zx boundaries

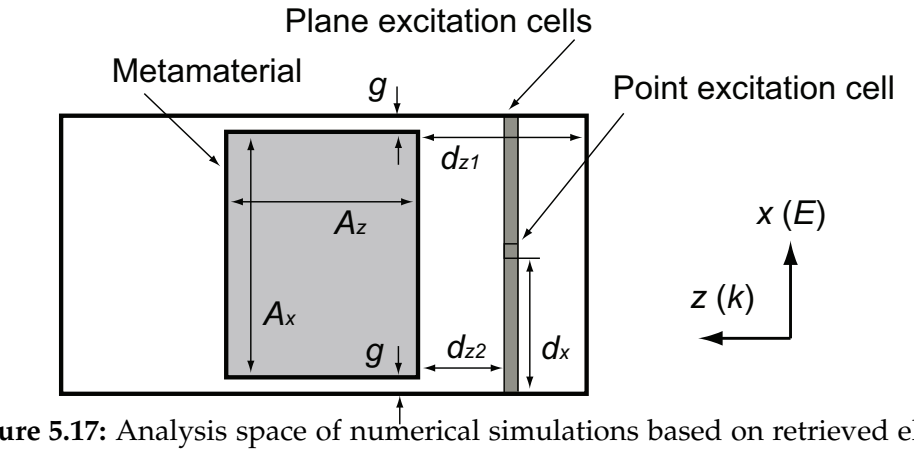

Figure 5.17: Analysis space of numerical simulations based on retrieved electromagnetic properties. Each parameter is given on Table 5.2.

applied periodic boundaries for a plane wave excitation and matched boundaries for a point excitation, respectively. A bulk metamaterial was placed in the centre of z axis with one cell gap from the yz and zx boundaries. The relative permittivity ε_r and relative permeability μ_r of the metamaterial were both set to $-1.0 \cdot (1.0 + j0.0)$. The constant sinusoidal wave of 16.31 GHz was excited at the plane 20.0 mm away from the metamaterial surface to the negative direction of z axis (as a plane source) or at the centre cell of the plane (as a point source). The electric field and magnetic field were oriented along x and y axes, respectively, so that the incident wave propagated along the positive direction of z axis.

5.4.3 Calculation Results

The calculation results for the plane wave excitation are summarised in Fig. 5.18, where the electric field obtained at the centre of y axis is visualised for different numbers of the time step. It was found from Fig. 5.18 that the plane wave excited at the bottom of each figure propagated towards the top, as the

Table 5.2: Parameters used in numerical simulations based on retrieved electromagnetic properties. The analysis space is illustrated in Fig. 5.17.

Analysis space ($N_x \times N_y \times N_z$)	(100 × 100 × 120) cells
Metamaterial size ($A_x \times A_y \times A_z$)	(98 × 98 × 40) cells
TLM unit cell size	$1.0 \times 1.0 \times 1.0$ [mm^3]
Frequency of incident wave	16.31 [GHz]
Relative permittivity of metamaterial	-1.0 · (1.0 +j0.0)
Relative permeability of metamaterial	-1.0 · (1.0 +j0.0)
d_x	50.0 [mm]
d_{z1}	39.0 [mm]
d_{z2}	20.0 [mm]
g	1.0 [mm]

time step increased. However, inside the metamaterial (39 to 79 mm from the bottom) the phase velocity became opposite to the group velocity due to the negative n'. As a result, the wave behaved as it propagated downward in the metamaterial. This can be more clearly confirmed from Fig. 5.19 where the electric field at the centre of xy plane is plotted with finer time step resolutions. In this figure the region of the metamaterial is represented by the DNG indicating **D**ouble **N**e**G**ative, and the others by the DPS indicating **D**ouble **P**o**S**itive.

The results for the point excitation are illustrated in Figs. 5.20 and 5.21 with different numbers of time step. Again the phase velocity was opposite to the group velocity in the metamaterial cells. Another feature confirmed from this simulation is that the incident wave refracted to the negative directions at the first interface of the metamaterial (i.e. at z = 39 mm) was concentrated in the metamaterial (i.e. at around (x, z) = (50, 59) mm). After the second interface (i.e. at z = 79 mm) the incident wave was concentrated in the DPS region again (i.e. at around (x, z) = (50, 99) mm). This is a well–known phenomenon of a

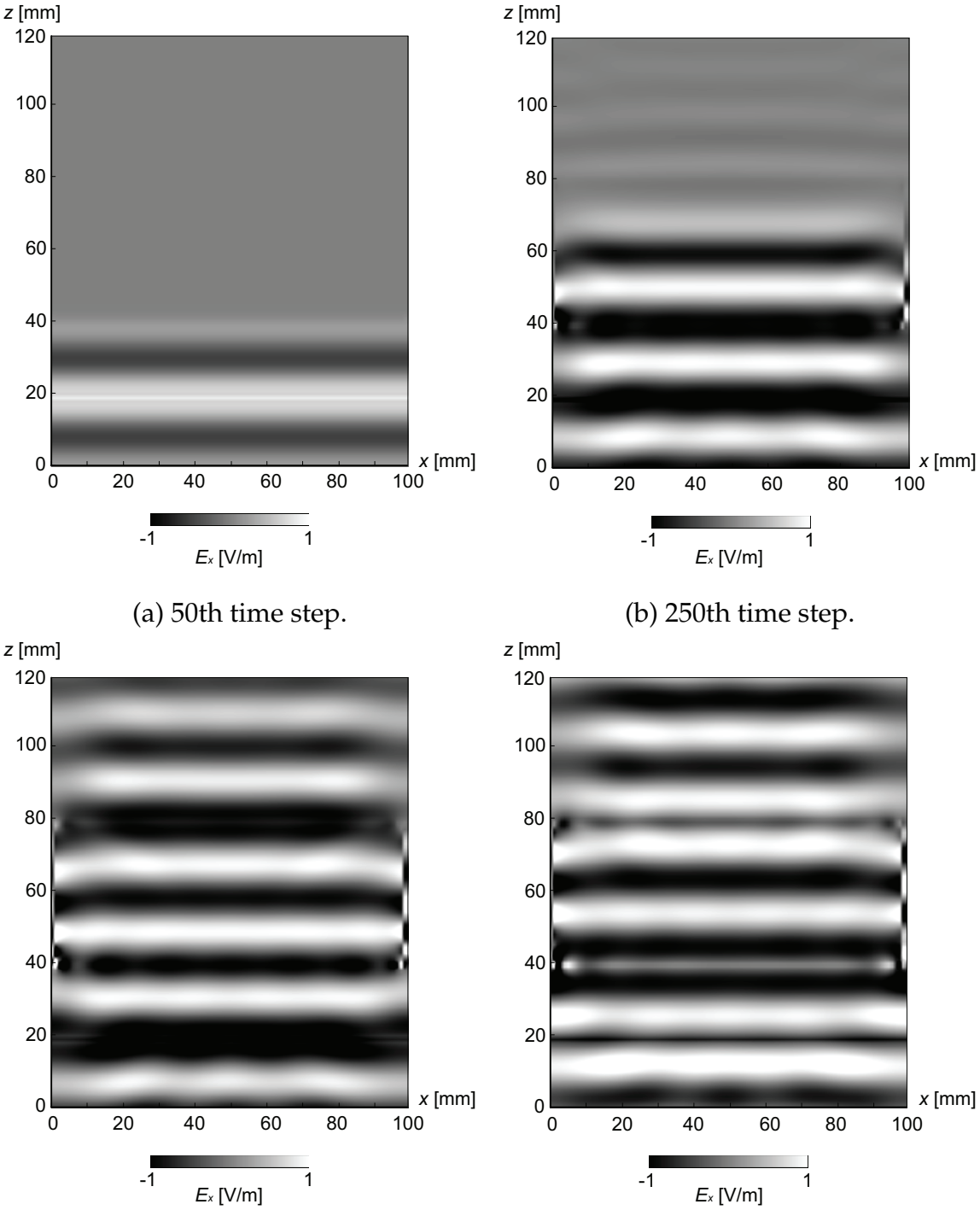

(a) 50th time step.

(b) 250th time step.

(c) 400th time step.

(d) 500th time step.

Figure 5.18: Calculation results of E_x at centre of y axis with various numbers of times step. A plane wave was excited at z = 19 mm.

perfect lens [30].

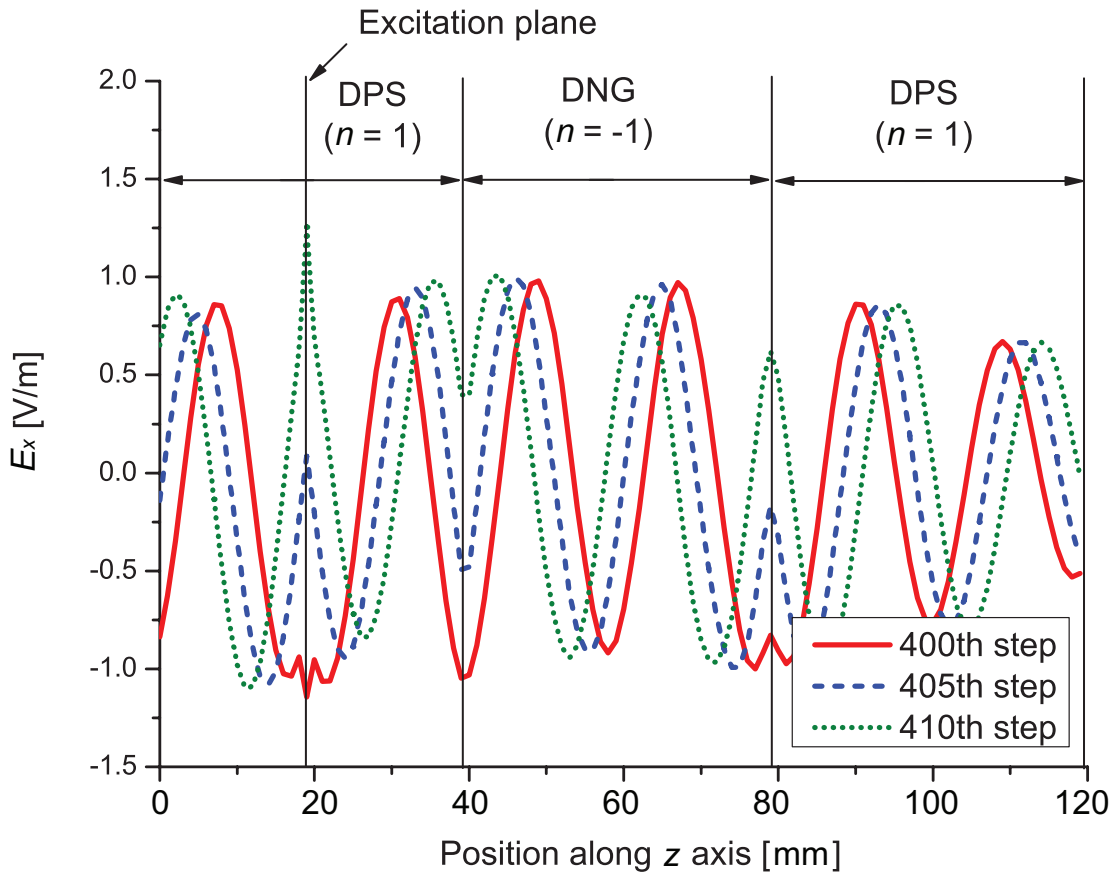

Figure 5.19: Calculation result of E_x at centre of xy plane with various numbers of time step. A plane wave was excited at z = 19 mm.

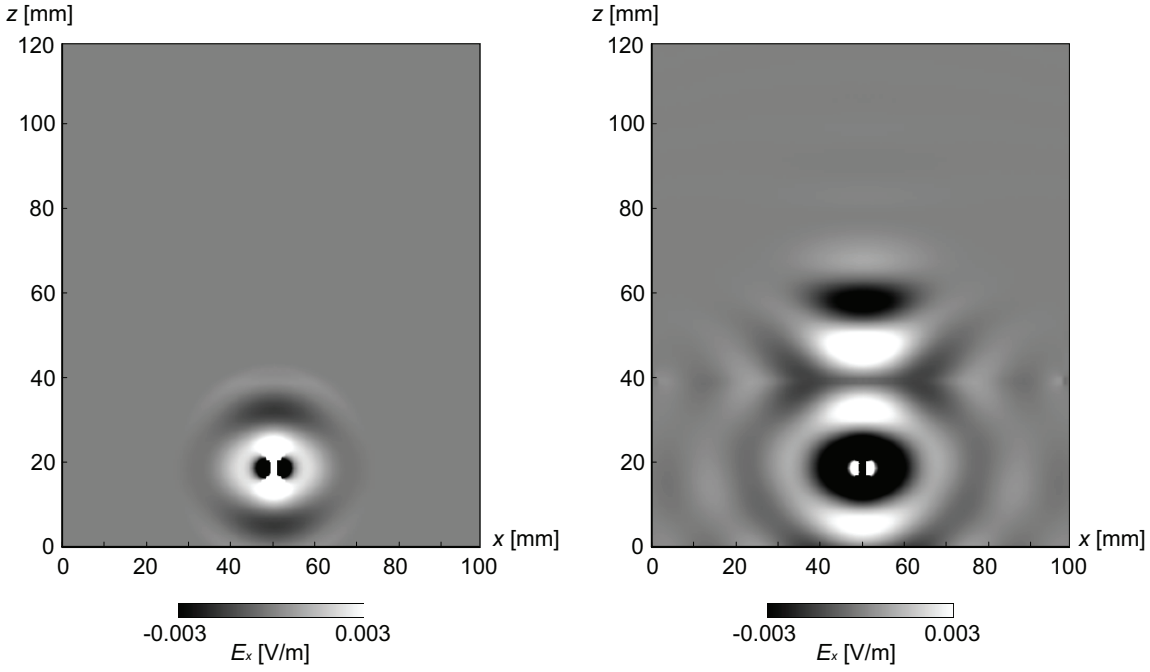

(a) 50th time step.

(b) 250th time step.

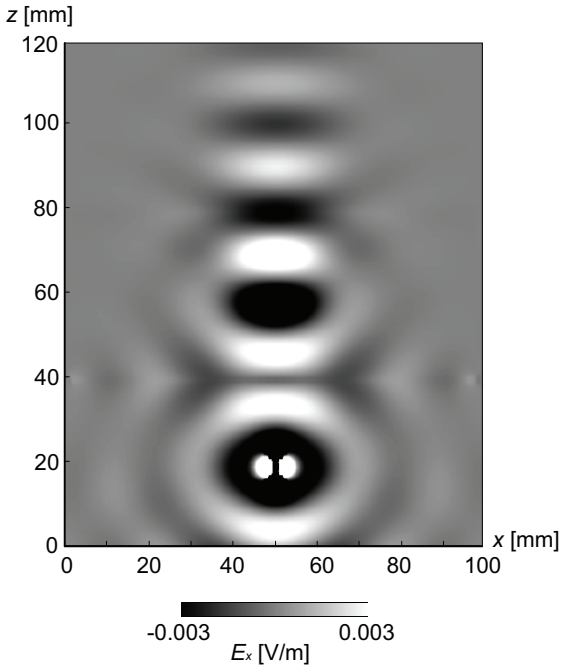

(c) 400th time step.

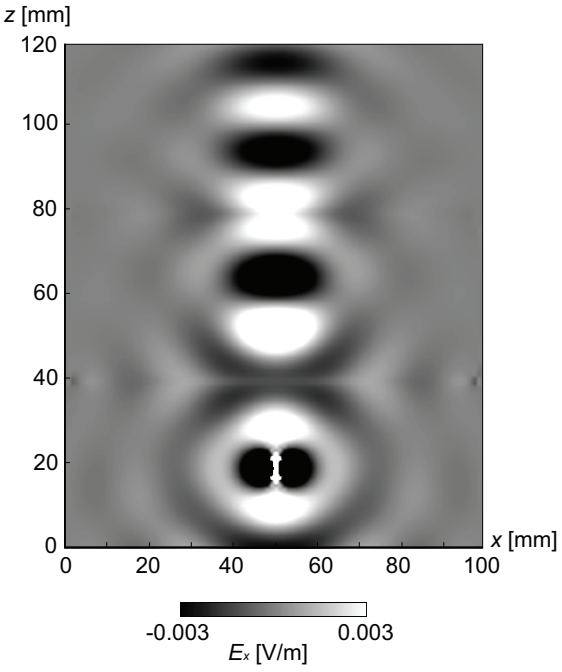

(d) 500th time step.

Figure 5.20: Calculation results of E_x at centre of y axis with various numbers of time step. The excitation point was $(x,\ y,\ z)$ = (49, 49, 19) mm.

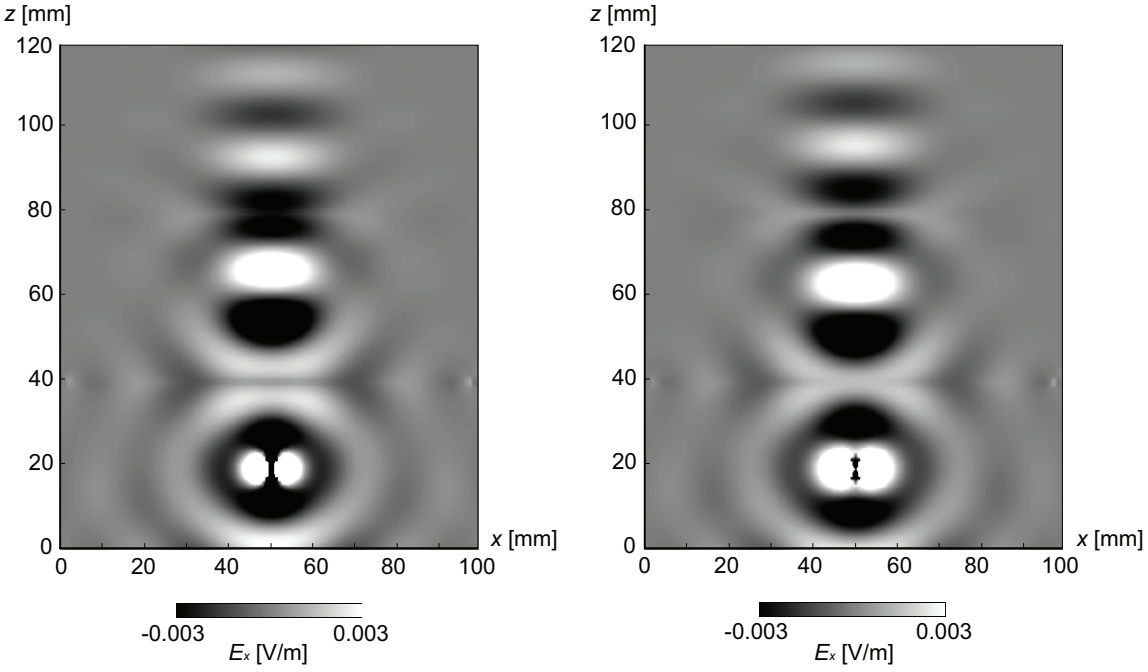

(a) 405th time step.

(b) 410th time step.

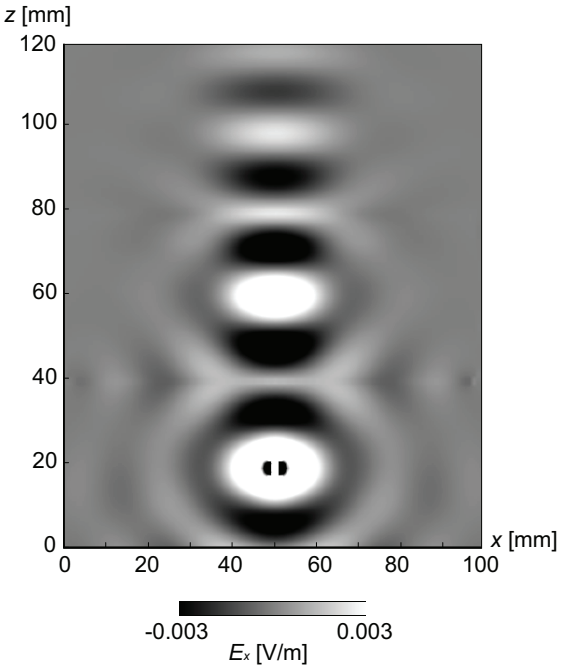

(c) 415th time step.

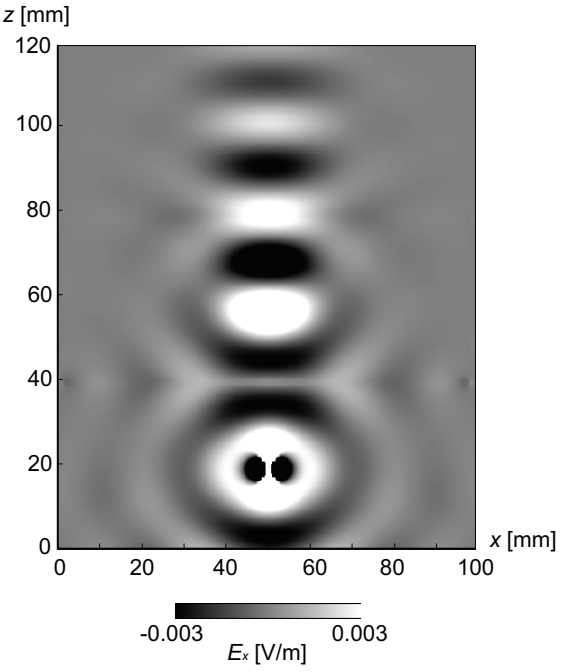

(d) 420th time step.

Figure 5.21: Finer time step resolutions of Fig. 5.20.

5.4.4 Discussion

Numerical simulations based on retrieved properties of metamaterial have been performed. As explained in subsection 5.4.1, this simulation method requires six extra calculations per a TLM unit cell to realise metamaterial properties in the TLM. This implies that the use of this approach may lead to significant increase of the calculation time. For example, in the simulations performed in the last section, the calculation time required for 1000 iterations was 8.4 hours where the CPU speed of the calculation machine was 2.26 GHz (Nehalem E5520 2.26 GHz 8 M). A numerical simulation for the same analysis space without the metamaterial (though the electromagnetic profiles are not shown here) required only 6 minutes to complete, indicating that the calculation time of the metamaterial simulations increased more than 80 fold. This calculation inefficiency may lead to a serious bottleneck in some cases.

5.5 Conclusion

This chapter has introduced retrieval methods and a numerical simulation method to embed the retrieved bulk metamaterial properties into the TLM method. As examples of the retrieval methods Smith's method [58] and Ziolkowski's method [59] were applied to three simple periodic structures: straight wire structure, SRRs and LHM. Although in some cases the use of these methods appeared to have succeeded in extracting the properties, the extraction was not straightforward and appeared to be complicated in some cases. Then, using retrieved metamaterial properties, the behaviour of a negative refractive index metamaterial was confirmed in TLM simulations based on a technique reported in [72]. However, it was also clarified that this simulation technique requires longer simulation time, compared to a simulation without the metamaterial.

CHAPTER 6

Characterisation by DF Techniques

6.1 Introduction

This chapter demonstrates an efficient modelling method for artificial materials using digital filtering (DF) techniques. The DF technique [81–83, 124] is the method used to convert the frequency domain characteristics into the time domain. The modelling efficiency enhanced by the DF techniques results from incorporating the characteristics of the fine features of the artificial materials into the surface of coarse cells (see Fig. 6.1). As described in the beginning of chapter 5, the reason of the modelling inefficiency of artificial materials lies in a huge gap between the minimum cell size resolutions required for precise calculation results in the TLM simulations (i.e. a tenth of wavelength [85]) and those for modelling the fine features of the artificial materials. In general, the artificial materials have finer periodicities than the wavelength of the operating frequency. Moreover, the periodic units are composed of further finer features. Hence, the use of the cell sizes fine enough to resolve the structural details requires using a huge number of the unit cells, resulting in the heavy computational burden and inefficient simulation. To demonstrate the efficiency of the DF technique it is applied to an EBG structure and CLL–based metamaterial.

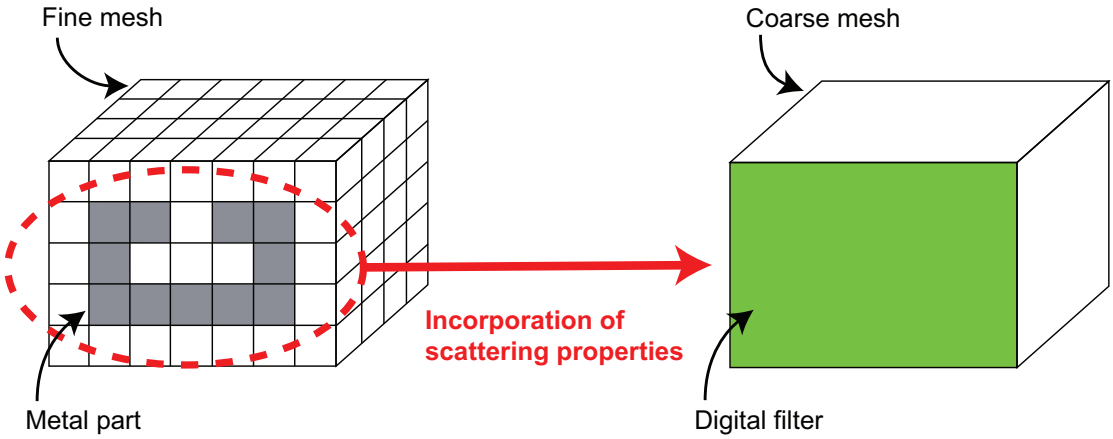

Figure 6.1: Use of DF techniques in the TLM. The scattering properties obtained with the fine mesh can be incorporated in the digital filter deployed on the surface of the coarse TLM unit cell.

For the first step in the DF implementation, this chapter describes fine mesh simulations, in which a very small cell size ($0.1 \times 0.1 \times 0.1$ mm^3) is used to model the details of an element of the structures to calculate the scattering parameters. Secondly, the scattering parameters are approximated with Padé forms and then factorised. Finally the factorised Padé forms are converted from the frequency domain to the time domain. As a result, the initial features in the fine meshes are effectively embedded into a numerical simulation with the DF boundary, in which the use of a coarse mesh is feasible (1,000 times larger in the EBG structure simulation and 680 times larger in the metamaterial simulation in terms of the volumes). The use of the coarse cell size results in much faster yet accurate simulations for artificial materials.

Also, this chapter describes an antenna simulation as a specific application example of the DF techniques in the electromagnetic compatibility (EMC) field. In this simulation, an electric field radiated from a dipole antenna is enhanced by an artificial magnetic conductor surface derived from the CLL–based metamaterial and modelled using the DF techniques as well. As is shown in the antenna simulation, the DF techniques model efficiently and accurately large–scale configurations. The results introduced here can be also

found in [83, 124].

6.2 Theory

To incorporate the DF technique into the TLM method, first of all, it is assumed that the frequency dependent reflection and transmission coefficients may be approximated by a Padé form [81]:

$$F(s) = \frac{\sum_{i=0}^{NP} b_i s^i}{\sum_{i=0}^{NP} a_i s^i} = \frac{b_0 + b_1 s + \cdots + b_{NP} s^{NP}}{a_0 + a_1 s + \cdots + a_{NP} s^{NP}}, \tag{6.2.1}$$

where s is the complex frequency ($s = j\omega$), NP is number of poles, the a and b coefficients are real and a_{NP} is always set at one. The number of the poles is decided depending on the approximated response (e.g. the complexity of the scattering parameters and approximation accuracy required).

The coefficients a_i and b_i, where i is 0 to NP, may be obtained in various ways. For example, in this chapter the frequency–domain Prony method is used [125]. In the Padé form approximation (i.e. eq. (6.2.1)) NS sets of frequency domain data (e.g. $F(\omega_0),\ F(\omega_1),\ \cdots,\ F(\omega_{NS-1})$) are used to solve for the fitting coefficients a_i and b_i. Rearranging eq. (6.2.1) gives

$$F(s) \sum_{i=0}^{NP-1} a_i s^i - \sum_{i=0}^{NP} b_i s^i = -s^{NP} F(s) \tag{6.2.2}$$

By setting $s = j\omega$ and employing the notation $F_k = F(j\omega_k)$, this equation becomes

$$F_k \sum_{i=0}^{NP-1} a_i (j\omega_k)^i - \sum_{i=0}^{NP} b_i (j\omega_k)^i = -(j\omega_k)^{NP} F_k. \tag{6.2.3}$$

Therefore, the matrix equation for the unknown coefficients a_i and b_i is expressed by the next form:

$$\underline{\underline{H}} \cdot \begin{bmatrix} a_0 \\ a_1 \\ \vdots \\ a_{NP-1} \\ b_0 \\ b_1 \\ \vdots \\ b_{NP} \end{bmatrix} = - \begin{bmatrix} (j\omega_0)^{NP} F_0 \\ (j\omega_1)^{NP} F_1 \\ \vdots \\ (j\omega_{NS-1})^{NP} F_{NS-1} \end{bmatrix} \tag{6.2.4}$$

where $\underline{\underline{H}} = [\underline{\underline{H}}_0 | \underline{\underline{H}}_1]$ and

$$\underline{\underline{H}}_0 = \begin{bmatrix} F_0 & (j\omega_0)F_0 & \cdots & (j\omega_0)^{NP-1}F_0 \\ F_1 & (j\omega_1)F_1 & \cdots & (j\omega_1)^{NP-1}F_1 \\ \vdots & \vdots & & \vdots \\ F_{NS-1} & (j\omega_{NS-1})F_{NS-1} & \cdots & (j\omega_{NS-1})^{NP-1}F_{NS-1} \end{bmatrix}, \tag{6.2.5}$$

$$\underline{\underline{H}}_1 = \begin{bmatrix} -1 & -j\omega_0 & \cdots & -(j\omega_0)^{NP-1} \\ -1 & -j\omega_1 & \cdots & -(j\omega_1)^{NP-1} \\ \vdots & \vdots & & \vdots \\ -1 & -j\omega_{NS-1} & \cdots & -(j\omega_{NS-1})^{NP-1} \end{bmatrix}. \tag{6.2.6}$$

By inverting eq. (6.2.4), a_i and b_i can be calculated, i.e.

$$[a_0 \quad a_1 \quad \cdots \quad a_{NP-1} \quad b_0 \quad b_1 \quad \cdots \quad b_{NP-1}]^t = -\underline{\underline{A}}^{-1} \cdot \underline{E}, \tag{6.2.7}$$

where the superscript t indicates taking the transposed matrix,

$$\underline{\underline{A}} = \mathbf{Re}[\underline{\underline{H}}^t \cdot \underline{\underline{H}}], \tag{6.2.8}$$

$$\underline{E} = \mathbf{Re}[\underline{\underline{H}}^t \cdot \underline{R}], \tag{6.2.9}$$

$$\underline{R} = -[(j\omega_0)^{NP} F_0 \quad (j\omega_1)^{NP} F_1 \quad \cdots \quad (j\omega_{NS-1})^{NP} F_{NS-1}]^t \tag{6.2.10}$$

and **Re** stands for the real part of the matrices.

As the second step in the DF technique implementation, eq. (6.2.1) obtained by the above method may be factorised to yield

$$F(s) = \frac{b_{NP}(s - s_{z0})(s - s_{z1}) \cdots (s - s_{z(NP-1)})}{(s - s_{p0})(s - s_{p1}) \cdots (s - s_{p(NP-1)})}, \tag{6.2.11}$$

where s_p and s_z respectively express the poles and zeros. This factorisation was achieved by the Laguerre's method in this study.

To convert this response from the frequency domain to the time domain the bilinear $\mathcal{Z}$–transform is applied to eq. (6.2.11). For instance, assuming that q is p or z, $(s - s_{qi})$ is transformed to

$$(s - s_{qi}) \xrightarrow{\mathcal{Z}} \alpha_{qi} \frac{1 - z^{-1}\beta_{qi}}{1 + z^{-1}} \tag{6.2.12}$$

where

$$\alpha_{qi} = \frac{2 - s_{qi}\Delta t}{\Delta t}, \tag{6.2.13}$$

$$\beta_{qi} = \frac{2 + s_{qi}\Delta t}{2 - s_{qi}\Delta t} \tag{6.2.14}$$

and the arrow with the $\mathcal{Z}$ represents that the bilinear $\mathcal{Z}$–transform is performed. Hence, applying the bilinear $\mathcal{Z}$–transform to eq. (6.2.11) gives

$$F(z) \;=\; B_0 \prod_{i=0}^{NP-1} \frac{1 - z^{-1}\beta_{zi}}{1 - z^{-1}\beta_{pi}}, \tag{6.2.15}$$

where

$$B_0 \;=\; b_{NP} \prod_{i=0}^{NP-1} \frac{\alpha_{zi}}{\alpha_{pi}}. \tag{6.2.16}$$

After some manipulations the next form is obtained:

$$F(z) = \frac{\sum_{i=0}^{NP} B_i z^{-i}}{\sum_{i=0}^{NP} A_i z^{-i}} = B_0 + \frac{\sum_{i=1}^{NP-1} B'_i z^{-i}}{\sum_{i=0}^{NP} A_i z^{-i}}, \tag{6.2.17}$$

where

$$B'_i = B_i - B_0 A_i. \tag{6.2.18}$$

Supposing $F(z)$ represents a reflection function, i.e. $F(z) = {}_{k+1}V^i/{}_kV^r$, then after some algebra, suppressing the k indices, the incident voltage is expressed in the form of

$$V^i = B_0 V^r + \underline{B}' \cdot \underline{X} \tag{6.2.19}$$

where

$$\underline{B}' = [B'_1 \;\; B'_2 \;\; B'_2 \;\; \cdots \;\; B'_{NP}] \tag{6.2.20}$$

$$\underline{X} = z^{-1}\underline{\underline{A}}' \cdot \underline{X} + z^{-1}\underline{1}' V^r, \tag{6.2.21}$$

$$\underline{\underline{A}}' = \begin{bmatrix} -A_1 & -A_2 & -A_3 & \dots & -A_{NP-1} & -A_{NP} \\ 1 & 0 & \dots & \dots & \dots & 0 \\ 0 & 1 & \ddots & & & \vdots \\ \vdots & \ddots & \ddots & \ddots & & \vdots \\ \vdots & & \ddots & 1 & \ddots & \vdots \\ 0 & \dots & \dots & 0 & 1 & 0 \end{bmatrix}, \tag{6.2.22}$$

$$\underline{1}' = [1 \;\; 0 \;\; 0 \;\; \dots \;\; 0]^t. \tag{6.2.23}$$

From eqs. (6.2.18) to (6.2.22), by using $\underline{X}$ and V^r of previous time step, the frequency dependence may be represented in the time domain. The signal–flow diagram to describe eqs. (6.2.19) to (6.2.23) is shown in Fig. 6.2.

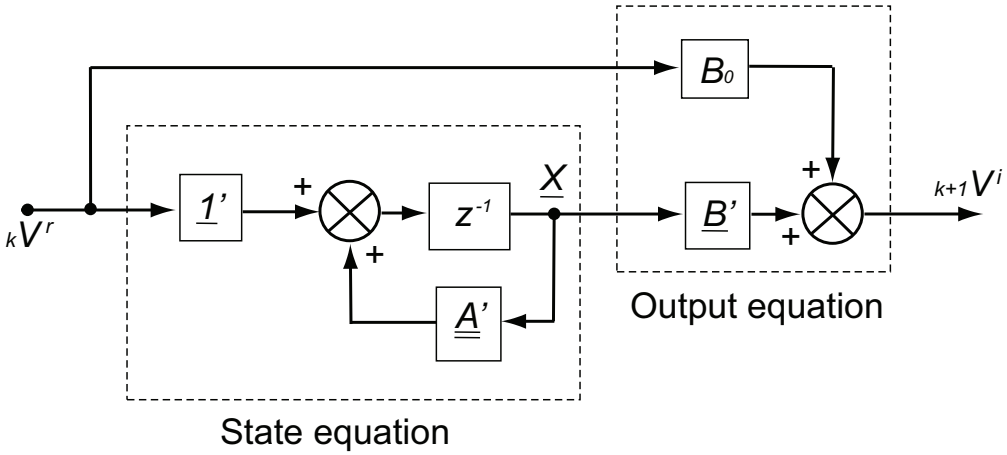

Figure 6.2: Signal–flow diagram to calculate new incident voltages for cells with embedded digital filter.

6.3 Calculation Results

6.3.1 Calculation Models

As examples of the application of the DF techniques, an EBG structure and a CLL–based metamaterial are simulated. The geometries and electromagnetic properties of these structures are the same as those used in chapter 4, except for the metal thickness of the CLL–based metamaterial. These details are summarised in Fig. 6.3 and Table 6.1 for the EBG structure and in Fig. 6.4 and Table 6.2 for the CLL–based metamaterial.

The fine mesh used to model the EBG structure shown in Fig. 6.3 and the

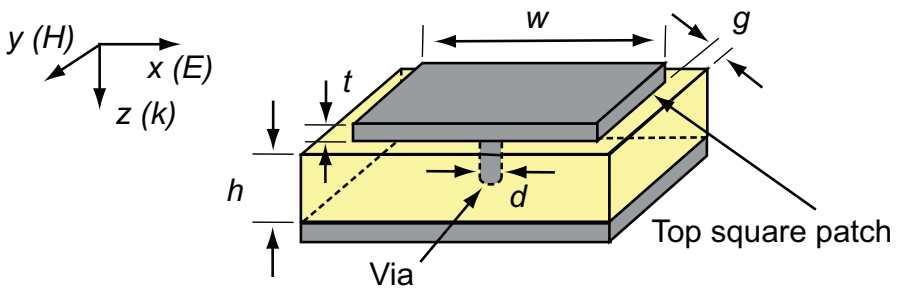

Figure 6.3: EBG structure unit simulated for DF technique implementation.

Table 6.1: Details of EBG structure simulated for DF technique implementation.

w	4.0 [mm]
d	0.8 [mm]
t	0.1 [mm]
h	1.5 [mm]
g	0.2 [mm]
Relative permittivity of substrate	$2.2 \cdot (1.0+j0.0)$
Relative permeability of substrate	$1.0 \cdot (1.0+j0.0)$
TLM unit cell size	$0.1 \times 0.1 \times 0.1$ [mm^3]

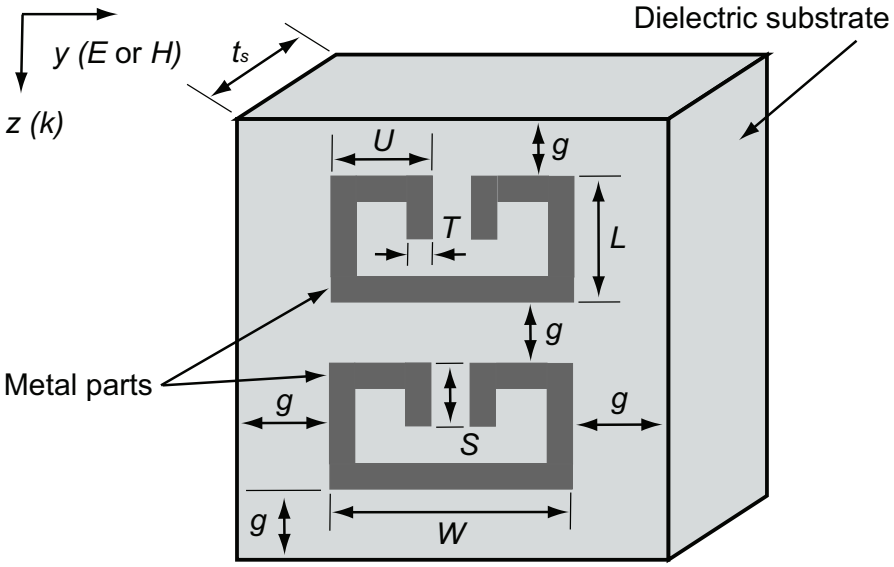

Figure 6.4: CLL–based metamaterial unit simulated for DF technique implementation.

Table 6.2: Details of CLL–based metamaterial simulated for DF technique implementation.

L	2.5 [mm]
S	1.2 [mm]
T	0.5 [mm]
U	1.7 [mm]
W	4.1 [mm]
g	0.5 [mm]
t_s	0.8 [mm]
t_m (thickness of CLL metal)	infinitesimally thin
Relative permittivity of substrate	$2.2 \cdot (1.0\text{-}j0.00090)$
Relative permeability of substrate	$1.0 \cdot (1.0+j0.0)$
TLM unit cell size	$0.1 \times 0.1 \times 0.1$ [mm^3]

CLL–based metamaterial shown in Fig. 6.4 is comprised of cells of size 0.1 $\times$ 0.1 $\times$ 0.1 mm^3. In both simulations an observation plane to sample the reflected wave is placed 40 cells away from the top surface of each structure

Table 6.3: Coefficients of Padé form (eq. (6.2.1)) used for EBG structure.

i	a_i	b_i
0	5.50562×10^{21}	-5.49485×10^{21}
1	2.69504×10^{10}	2.59674×10^{10}
2		-9.92844×10^{-1}

and, at the plane of another one cell above the observation plane, a Gaussian pulse is excited along the positive direction of the z axis. The polarisations of the incident waves in each model are as shown in Figs. 6.3 and 6.4. There is a further 2–cell gap between the excitation plane and the top xy boundary. The boundary conditions on the xy plane are perfectly matched and all other planes have a periodic boundary condition so that each structure is assumed to belong to infinite array on the bottom xy plane.

6.3.2 Calculation Results

To begin with, the reflection coefficients for the single elements of the artificial materials are calculated using a fine mesh, and the result is converted into the Padé forms to obtain each coefficient of eq. (6.2.1). In Fig. 6.5, the complex reflection coefficient of the EBG structure element is compared with that approximated with the Padé form, using two poles. In Table 6.3, the coefficients used for the Padé form approximation are summarised. From Fig. 6.5 and Table 6.3, it is confirmed that in using the two poles, the reflection coefficient obtained from the fine–mesh is accurately described by the Padé form.

Next, the reflection coefficient obtained by the DF technique and that of the fine mesh are compared. First, the result of Fig. 6.5 is factorised and second, $\underline{\underline{A}}'$, B_0 and $\underline{B}'$ of eqs. (6.2.19) and (6.2.22) are calculated to decide the boundary condition of the digital filter. In this calculation, the cell size using the digital filter implementation is set to $1.0 \times 1.0 \times 1.0\,\mathrm{mm}^3$, which is 10 times larger than

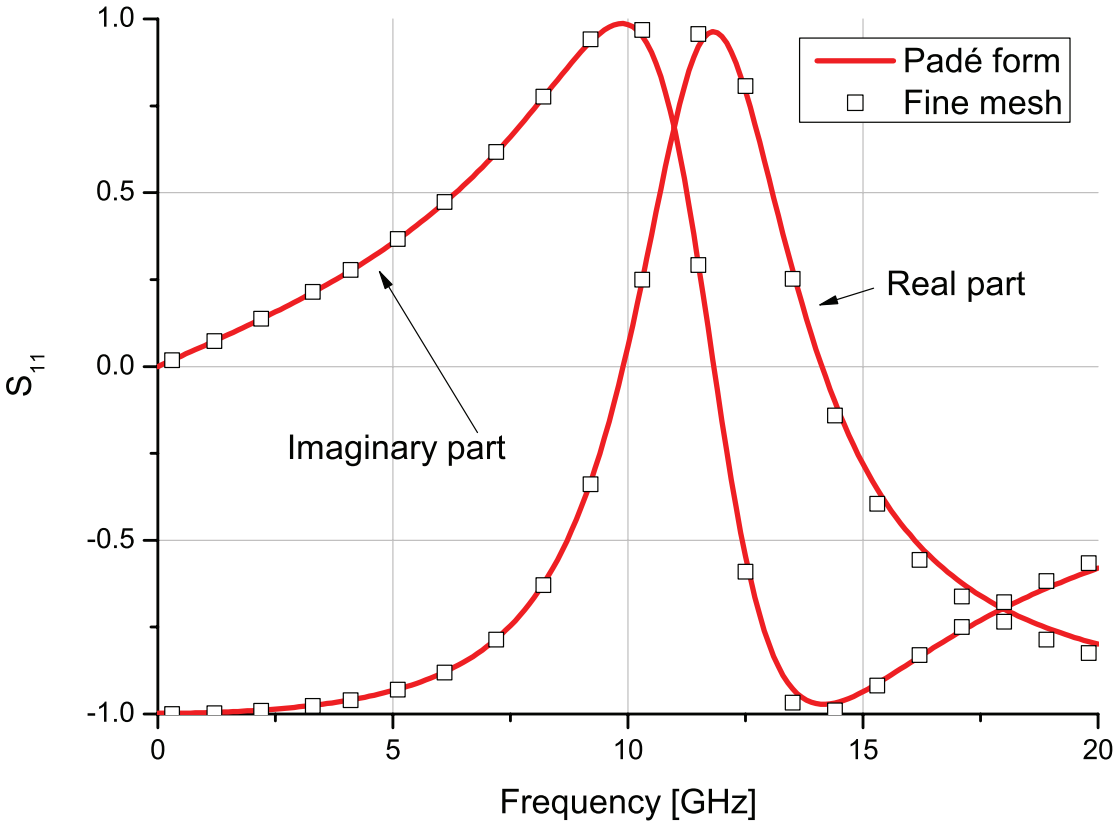

Figure 6.5: Scattering parameter comparison of EBG structure between fine mesh simulation and Padé form.

that of the initial simulation (the fine mesh simulation), yielding a reduction by a factor of a 1,000 in the number of cells compared to the original problem. Nevertheless this cell size is still small enough to simulate the frequency range of interest (around 9 GHz) in which the simulated EBG structure behaves as an artificial magnetic conductor. The comparison result is shown in Fig. 6.6.

As a result of the application of the DF technique, it is found from Fig. 6.6 that, when the coarse mesh is used with the DF simulation, the reflection coefficient shows close agreement with that of the fine mesh. In addition, increasing the cell volume by a factor of a 1,000 means that the simulation to model the EBG structure can be implemented at a fraction of the computational cost of the fine–mesh simulation.

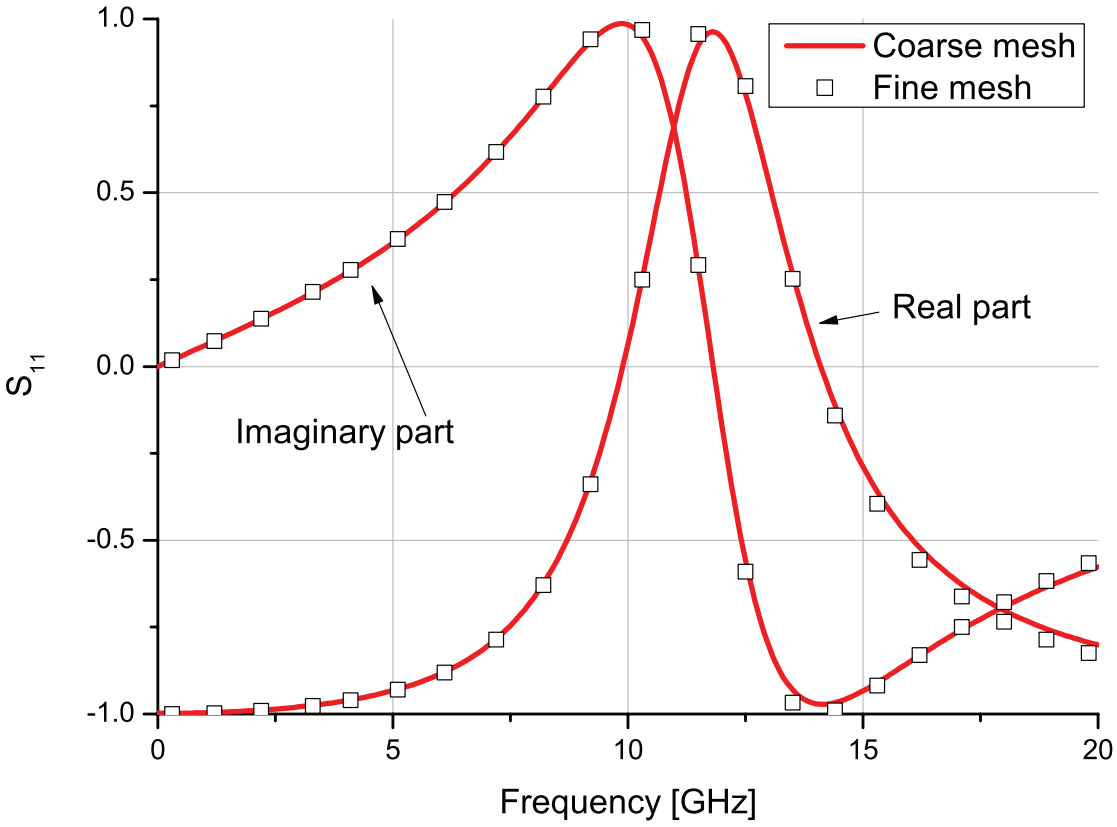

Figure 6.6: Scattering parameter comparison of EBG structure between fine mesh and coarse mesh simulations.

The improvement of the calculation efficiency by the DF techniques can be confirmed from Table 6.4 where the details of both simulations are summarised. For these simulations a calculation machine composed of AMD Athlon (tm) 64 Processor 2.00 GHz and 2.00 GByte RAM was used. As found from Table 6.4, the simulated area of the xy plane in the coarse mesh was slightly bigger than that in the fine mesh, although the length along the z axis was far longer to put the same number of the unit cells as that used for the fine mesh simulation (i.e. 40 cells) between the observation plane and surface of the MUT. However, the calculation time was improved from 3 hours to less than 1 minute. This is primarily because the total number of the simulated cells was reduced by the use of the coarser mesh. In addition, the reduction in the calculation time can also be accounted in part for the removal of the EM field calculation for the dielectric substrate, which makes the calculation

Table 6.4: Comparison between fine and coarse mesh simulations. Details of calculation machine used for both calculations are as are followed: CPU is AMD Athlon (tm) 64 Processor 2.00 GHz; memory is 2.00 GB RAM.

	Coarse mesh	Fine mesh
Cell size [mm^3]	$1.0 \times 1.0 \times 1.0$	$0.1 \times 0.1 \times 0.1$
Analysis space size ($N_x \times N_y \times N_z$)	$(5 \times 5 \times 44)$	$(44 \times 44 \times 60)$
Calculation time	$<$ 1 minute	3 hours

slower than that for the free space. Furthermore, from the viewpoint of not only the calculation time, but also of the computer memory requirements, this method is very efficient as the total numbers of the simulated cells are reduced from 116,160 to 1,100. These facts confirm the efficiency of the DF technique in modelling artificial materials.

In a similar manner with the approach used for the EBG structure, the DF technique was applied for the CLL–based metamaterial but in this case both polarisations needed to be considered, since it had an asymmetrical design in respect of the x polarisation and y polarisation. Using the coefficients represented in Tables 6.5 and 6.6 for the x and y polarisations, respectively, close agreement between the fine mesh results and Padé forms was obtained (not shown here). Furthermore, the agreement was still maintained in both coarse mesh simulations, as is seen in Fig. 6.7. In the coarse mesh solutions, the cell size was set to $0.88 \times 0.88 \times 0.88$ mm^3, which is 8.8 times larger than that of the fine mesh, resulting in the use of the unit cell volume approximately 680 times larger in volume than that of the fine mesh. Again, the CLL–based metamaterial has effectively been modelled with the coarse mesh as well as the EBG structure.

Table 6.5: Coefficients of Padé form (eq. (6.2.1)) used for x polarisation of CLL–based metamaterial.

i	a_i	b_i
0	2.68826×10^{21}	-6.95509×10^{19}
1	4.57198×10^{10}	-1.70162×10^{10}
2		-1.31087×10^{-2}

Table 6.6: Coefficients of Padé form (eq. (6.2.1)) used for y polarisation of CLL–based metamaterial.

i	a_i	b_i
0	1.51919×10^{33}	-1.45125×10^{33}
1	9.87916×10^{21}	9.44325×10^{21}
2	4.09534×10^{11}	-3.91523×10^{11}
3		8.95901×10^{-1}

In the above simulations the unit cell sizes of the coarse mesh simulations for the EBG structure and the CLL–based metamaterial were respectively set to $1.0 \times 1.0 \times 1.0$ and $0.88 \times 0.88 \times 0.88$ mm^3. As long as the coarse mesh is finer than $\lambda/10$ then basic accuracy in the TLM is maintained. The important factors affecting overall accuracies here are the approximations by the Padé form and the factorised Padé form, i.e. as long as these forms are in good agreement with the fine mesh results, the original properties obtained in the fine mesh simulations are maintained.

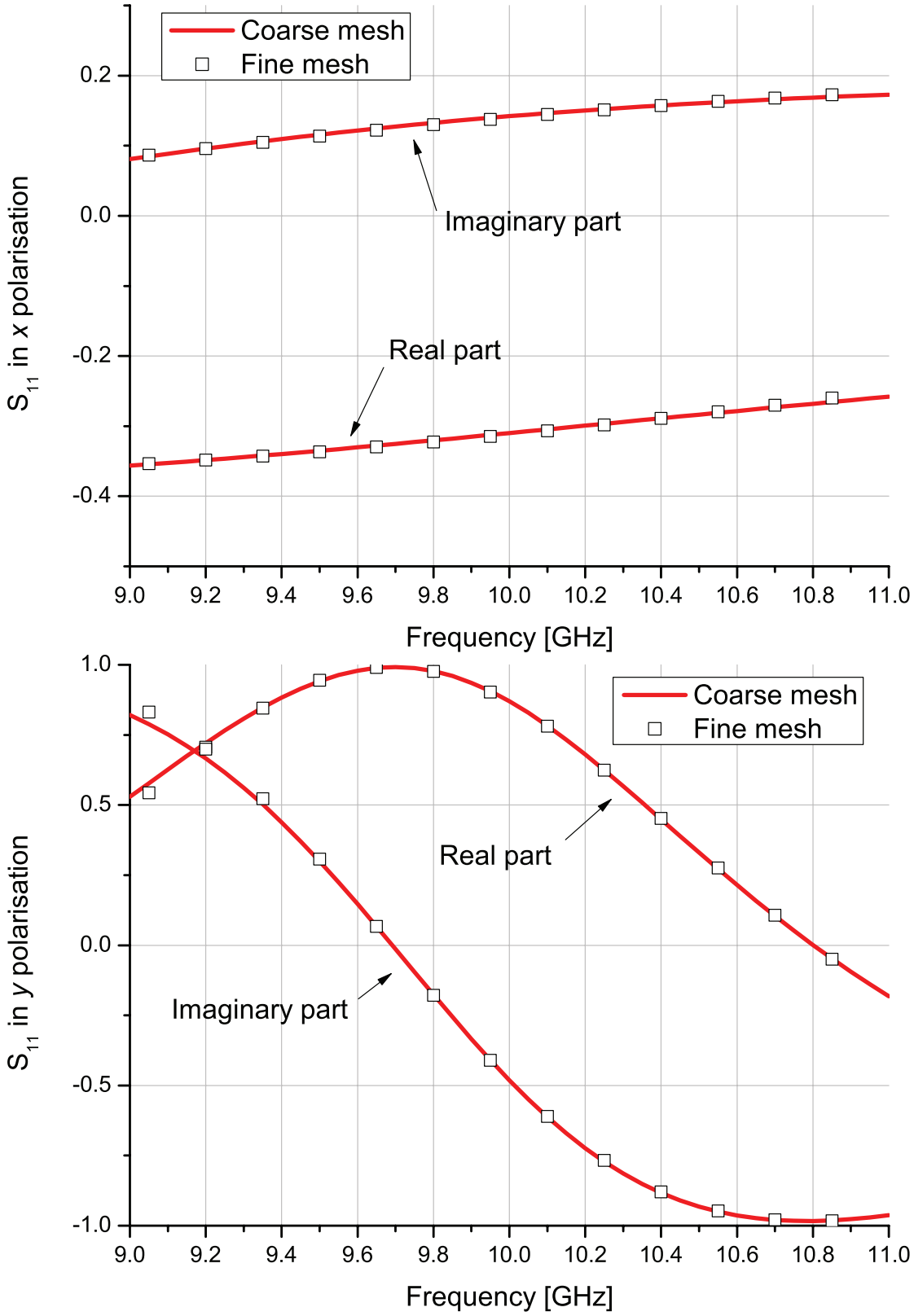

Figure 6.7: Scattering parameter comparisons in x polarisation (top) and y polarisation (bottom) of CLL–based metamaterial between fine mesh and coarse mesh simulations.

6.4 Large–Scale Metamaterial Simulation Based on DF Techniques

This section demonstrates an antenna simulation to show that the DF technique is applicable in realistic EMC problems as an example of large–scale simulations. In this simulation a dipole antenna is placed close to a DF boundary representing the CLL–based metamaterial simulated above. Since the CLL–based metamaterial has the complex reflection coefficient of nearly $(1.0 + j0.0)$ behaving like a perfect magnetic conductor (PMC), the DF boundary behaves as an artificial magnetic conductor (AMC) so that the electric field radiated from the antenna should be enhanced at the front side [42].

The analysis conditions including the simulated model are summarised in Fig. 6.8 and Table 6.7. The dipole antenna was located at the centre of the TLM unit cells of $0.88 \times 0.88 \times 0.88$ mm^3 along the y axis. The radius of the cylindrical dipole antenna was set to 0.1 mm and the total length was set to 11–cell long (9.68 mm). All parts of the antenna were composed of the

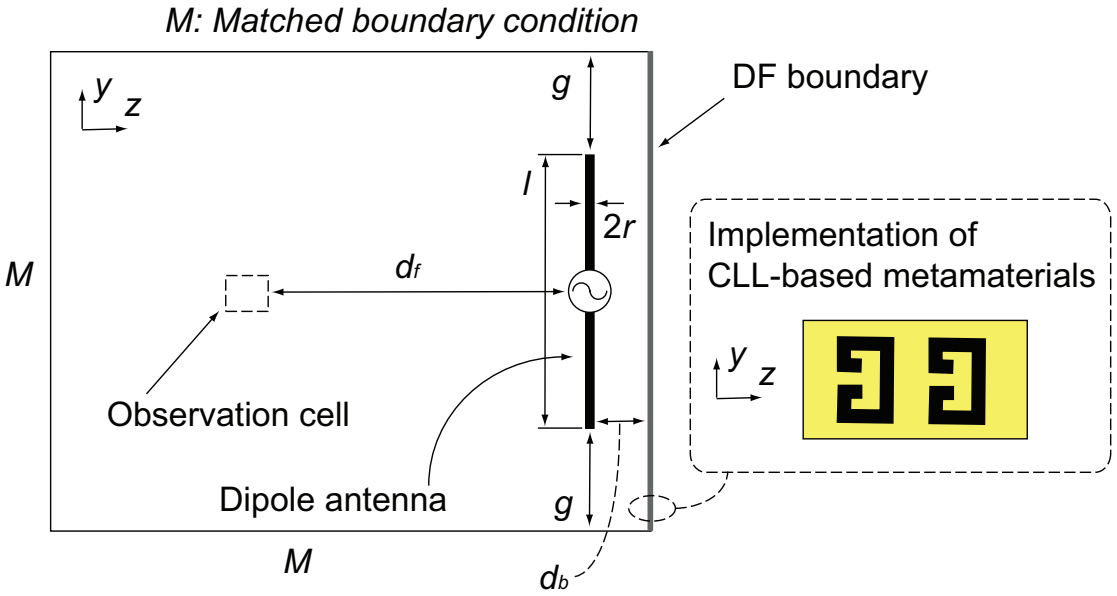

Figure 6.8: Calculation conditions of antenna simulation to show practical application example of DF techniques in EMC field.

Table 6.7: Details of calculation conditions of antenna simulation illustrated in Fig. 6.8.

Analysis space ($N_x \times N_y \times N_z$)	($21 \times 27 \times 60$) cells
TLM unit cell size	$0.88 \times 0.88 \times 0.88$ [mm^3]
d_f	3.86 [mm]
d_b	0.34, 1.22 or 2.10 [mm]
g	7.04 [mm]
r	0.10 [mm]
l	9.68 [mm]
Resistance of centre cell of antenna	50.0 [Ω]

metal without conductive loss except for the centre cell which contained a 50 Ω resistor. The modelling method for the cylindrical dipole antenna was as described in section 2.2. The DF boundary was placed behind the antenna at various distances d_b (0.34, 1.22 or 2.10 mm corresponding to the lengths of half, 1.5 or 2.5 cells subtracted by the radius, respectively). The distance between the observation cell to sample the electric field and the centre cell of the antenna, d_f, was 3.86 mm.

The simulation results are illustrated in Fig. 6.9, in which the magnitudes of the electric fields were divided by those obtained using the matched condition (the top figure) or the PEC (the bottom figure) instead of the DF boundary. It is found from the top of Fig. 6.9 that the ratio of the electric field before and after replacing the DF boundary with the matched condition is improved in the lower part of the calculated frequency range due to the AMC–like response confirmed in the bottom of Fig. 6.7. In addition, a similar improvement is shown in the bottom of Fig. 6.9 as well.

In these antenna simulations, similar to the individual CLL–based meta-material simulation performed in the last section, the calculation method

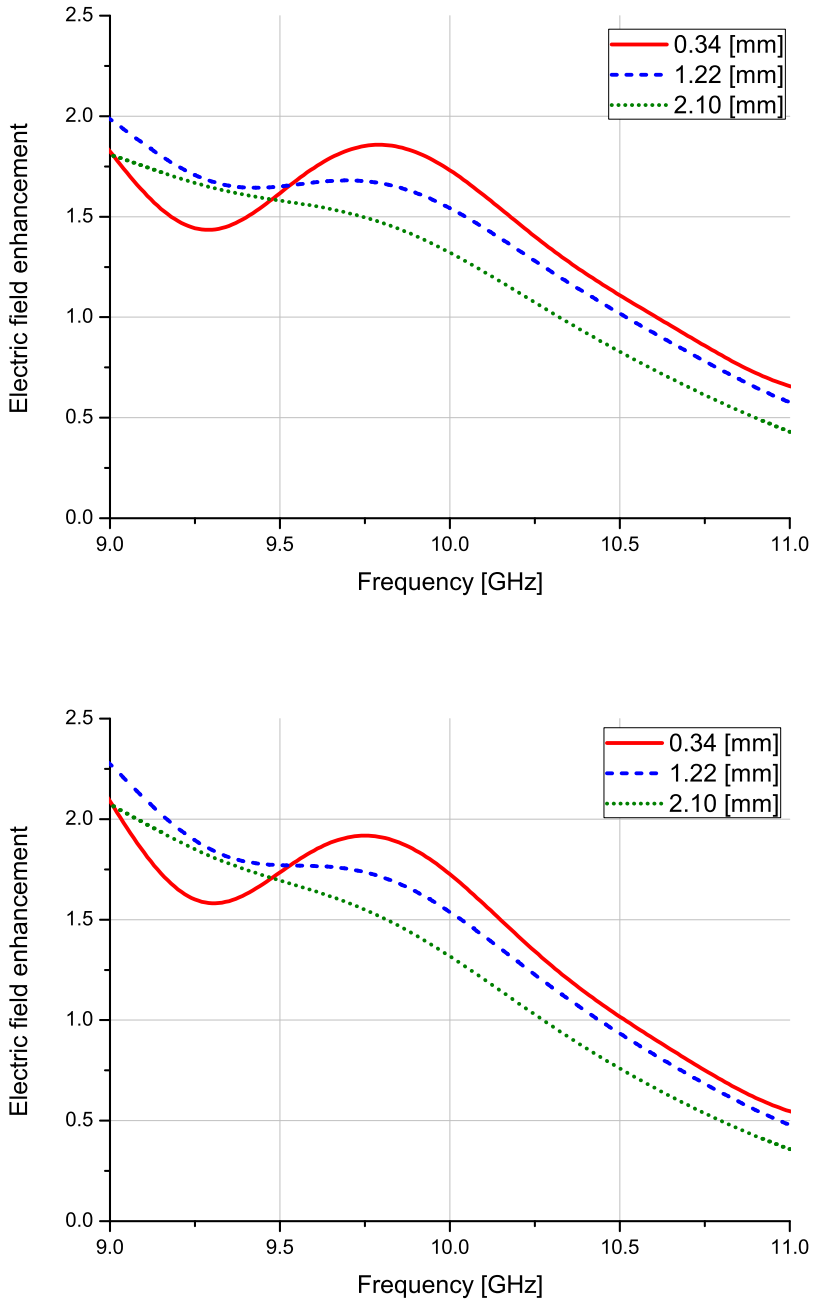

Figure 6.9: Comparisons of electric fields obtained with DF and matched boundaries (top) or PEC boundaries (bottom) having various gaps between dipole antenna and the DF boundary. The electric field when the DF boundary was deployed behind the antenna was divided by that obtained in the matched boundary case or PEC case.

shows even greater efficiency than the conventional fine mesh simulation due to the use of the approximately 680 times larger cell volume. These confirm that the DF techniques can be used as an efficient technique in modelling large scale problems in EMC which otherwise would be intractable by simply fine–mesh modelling.

6.5 Discussion

As clarified on Table 6.4, the modelling efficiency of the artificial materials (including the EBG structure and the metamaterial) was markedly improved through the implementation of the DF techniques into the TLM method. The DF techniques are similar to using retrieval methods from the viewpoint that both of them do not require us to model the fine features of the structures. Thus, the use of a coarse mesh becomes possible and computational effort is reduced in both cases. However, there are some differences as explained below.

Firstly, one of the major differences between the two methods in terms of the computational efficiency is where and how the metamaterial properties are implemented. In the simulations based on the retrieved properties, the metamaterial is modelled as a bulk structure, which indicates that extra calculations are necessary for all the TLM voltage ports to incorporate the metamaterial properties [72]. However, in the case of the DF techniques the metamaterial properties are implemented as a digital filter at boundary between TLM unit cells, which implies the extra calculations are needed at two ports. This difference points to the DF techniques being more efficient.

Another advantage of the DF techniques is that they avoid problem encountered in thin metamaterial property retrieval. As reported in [70], for example, retrieved electromagnetic properties of CW metamaterials and fish–net structures can depend on the number of the metamaterial units used.

The reason for this issue lies in the strong interactions between metamaterial slab units. These nonnegligible interactions affect the retrieved results so that the electromagnetic properties can depend on the number of the metamaterial units. However, this dependence is physically unreasonable, and the properties of the same structures must not relate to the structure sizes, because this means that the bulk metamaterial changes its electromagnetic properties depending on the structure size. For this reason, applying the retrieval methods to thin metamaterials is still a controversial issue [70, 71]. However, in the DF techniques this problem can be avoided, since these techniques do not rely on deriving the electromagnetic properties but just scattering parameters. It is possible that the scattering parameters vary depending on the number of the metamaterial units, or the metamaterial bulk size. In view of the difficulties in interpreting results obtained using retrieval methods, the use of the proposed DF techniques appears to have distinct advantages both conceptual and in practical implementation.

Thirdly, retrieval needs to be performed based on proper retrieval methods. Some metamaterials have bianisotropies [67], chiralities [68] or gain media [54–57], which cannot be properly taken into account in the retrieval methods used in the last chapter [58–60]. To incorporate these characteristics some modifications are necessary (e.g. [56, 67, 126, 127]). At the same time, however, such modifications can lead to complicated solutions so that implementation in numerical simulations becomes difficult [128]. In contrast, in the DF techniques the necessary step is just associating the incident voltage ports with the relevant voltage ports for the reflection or transmission, and no complex process is involved. Also, the bianisotropic properties can be incorporated by using different DF boundaries for the two sides of the metamaterial surfaces.

Moreover, the application range of the DF techniques is not limited to metamaterials but can include EBG structures, as demonstrated in this chapter. In the retrieval methods the structures retrieved need to be small enough to

be regarded as homogenised structures. This is the same as when using the properties of natural materials. In principle the naturally available materials can be represented by macroscopic properties (i.e. electromagnetic properties), since the components determining their properties (i.e. molecules) are small enough compared to the wavelength of the incident wave. In other words, from the macroscopic viewpoint these nature materials can be modelled as homogenised (or bulk) materials. This premise must also hold when using retrieval methods for artificial materials. However, the periodicities of the EBG structures are multiples of the half–wavelength [9] and comparable to the wavelength of the incident wave, resulting in the failure of the homogenization. In contrast, the DF techniques do not have such a limitation. As long as enough distance is taken from the simulated structure surface, the evanescent region can be avoided and the scattering characteristics can be properly extracted.

Despite these advantages some improvements could make the DF techniques a more powerful simulation tool. Firstly, incorporating the angular characteristics of scattering parameters is necessary to simulate more complex and more realistic situations. Secondly, in this chapter the Padé form was approximated by the frequency domain Prony method. This approximation was performed based on sampled frequency data (as used in eq. (6.2.1)), and the results needed to be close enough to the original scattering parameters depending on the simulation accuracy required. In some cases, however, it was found that the coefficients used for eq. (6.2.1) could not be obtained or very long time was needed to obtain the answers. Hence, solving these issues can make the DF techniques easier to implement.

6.6 Conclusion

In this chapter an efficient modelling method for artificial materials has been presented through the application of DF techniques in TLM simulations. It was

shown that a reflection coefficient in a simulated EBG structure can be accurately represented. This result was then used to obtain the constants required to embed the DF boundary into a coarse mesh TLM. The comparison of the fine–mesh simulation of the EBG element with the coarse–mesh simulation supplemented by the DF boundary showed very close agreement but in the latter case at a fraction of the computational cost. Next the DF technique was applied for a CLL–based metamaterial. Again, close agreement between the fine mesh and coarse mesh solutions was confirmed for both polarisations. Finally the DF boundary incorporating the properties of the CLL–based metamaterial was used in an antenna simulation to offer a practical large–scale application example in EMC field. Due to the AMC–like behaviour of the CLL–based metamaterial, the radiated electric field from the antenna improved in parts of the simulated frequency range. It has been demonstrated in this chapter that these efficient models can be used in large–scale EMC simulations which are capable of describing the complex behaviour of the artificial materials in a coarse mesh. In addition to these simulation results, differences between the DF techniques and retrieval methods were discussed and improvements to the DF techniques were suggested.

CHAPTER 7

Metamaterial Absorbers

7.1 Introduction

7.1.1 Past Achievements and Outstanding Issues

So far metamaterial absorbers have exhibited attractive features which are not available from conventional wave absorbers [73–80]. One example is in the manipulation of the electromagnetic properties. In conventional absorber design options are limited by the properties of the substrate and its mixture ratios to realise the desired permittivity and permeability values. In some cases, however, this is not easy to accomplish. In metamaterial absorbers changes of metallisation length and geometry enable us to modify the electromagnetic properties with relative ease [77, 129].

More importantly the use of metamaterials makes the absorber substrate thicknesses significantly smaller. In the conventional absorbers the total thickness of the structures needs to be comparable to a quarter wavelength λ_0 of the operating frequency. However, the $\lambda_0/4$ thickness can limit the range of application, for example, where available working space is restricted. This issue has successfully been solved by use of thin metamaterials, which allowed us to relax the limitation of the physical size remarkably (e.g. in [130] 1 mm

thickness at operating frequency 6 GHz, i.e. approximately one fiftieth of the wavelength), and more flexible design options became possible.

Despite past achievements there still remain some problems unsolved. One of the outstanding issues is the limitation of the absorption band width. In most cases absorption is concentrated in a narrow frequency band. Although narrow band absorbers may be useful in some applications, the real need is for broadband absorbers with customised characteristics to meet specific user demands.

7.1.2 Focus

To address this issue, this chapter shows that highly customisable broadband absorption is possible using metamaterials as wave absorbers. This property is obtained, when different lengths of conductive and lossy CWs are deployed as a periodic metamaterial absorber unit and independent conductive loss optimisation is performed in each CW. In addition, this property can be obtained for arbitrary polarisations without any serious absorptance reduction, when other pairs of CWs are introduced. Furthermore, it is also demonstrated that not only enhancing absorptance but also reducing it are possible by suitable use of lossless CWs. These results indicate that the CWs make it possible to design very flexible absorptance characteristics. Before the customisable absorber configurations are explained in detail, the basic properties of single CW metamaterial absorbers and paired CW metamaterial absorbers are presented. The related work can be found from [78, 79], although these results did not fully consider reflections of both polarisations. Also, most metamaterial designs introduced here include conductive loss. This indicates that the structures take account of the conductive loss issue pointed out in subsection 1.4.1 and are thus expected to be a more realistic metamaterial representation.

7.2 Calculation Models and Conditions

This thesis uses CWs as the basic geometry of metamaterial absorbers for the following reasons (some other advantages were discussed in subsection 4.1.2). First, compared to fishnet structures which have some similar properties to CW metamaterials, the CW metamaterials can exhibit greater losses, which although undesirable in most other metamaterial applications they are needed in absorber applications [11]. Moreover, from the fabrication viewpoint the CW form is straightforward to manufacture due to its simple geometry. This is expected to be useful in reducing the periodicity and increasing the operating frequency, indicating that the CW metamaterials are easily scalable. Finally, CWs with conductive loss can produce multi–absorptance peaks as will be demonstrated in this chapter.

In absorber applications described in this thesis conductive loss is exploited instead of dielectric loss which is assumed to be the primary loss mechanism in most conventional metamaterial absorbers (e.g. [76]). One of the reasons is that materials with suitable conductive losses are readily available through recently developed technologies, e.g. conductive inks [131–133]. Also, independent optimisation of the metal resistances gives us more flexible options for the design of absorption profiles (shown in section 7.6).

The default structures of the simulated CW metamaterials are summarised in Fig. 7.1 and Table 7.1. They are the same as those used in Fig. 4.1. To simplify the situation and consider the absorption effect due only to the conductive loss of the CW metals, the relative permittivity ε_r of the substrate was set $\varepsilon_r = 1$ and all other loss mechanisms were removed. The CW structure had a width of 0.3 mm along the y axis (H–field) and length of 5.1 mm along the x axis (E–field). The dimension of the unit cell was $A_x = A_y = 6.3$ mm. This structure was modelled using cubical TLM unit cells having edge lengths of 0.075 mm. The conductive loss was quantified by the unit of $\Omega\square^{-1}$ (see subsection 2.4.3).

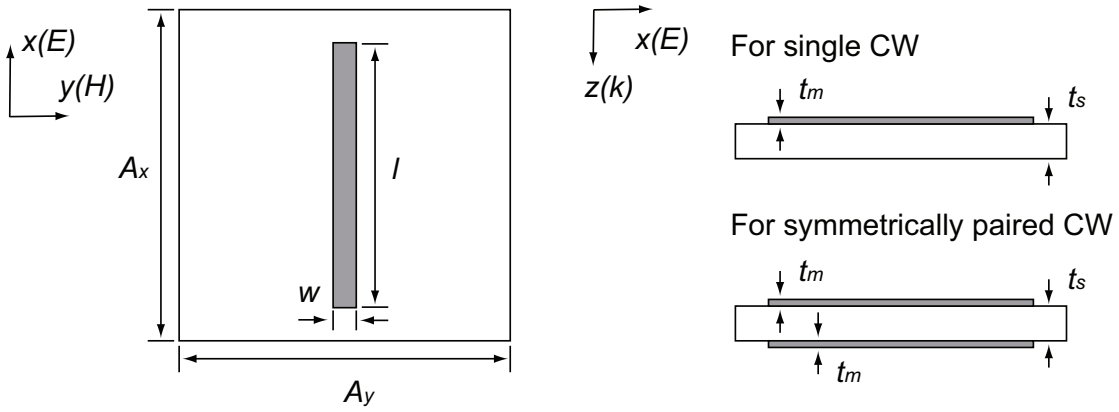

Figure 7.1: Simulated CW metamaterials. The default parameters are summarised on Table 7.1.

Table 7.1: Default parameters of single CW metamaterial absorber illustrated in Fig. 7.1.

A_x	6.3 [mm]
A_y	6.3 [mm]
l	5.1 [mm]
w	0.3 [mm]
t_m	0.0 [mm]
t_s	1.2 [mm]
Relative permittivity of substrate	$1.0 \cdot (1.0 + j\,0.0)$
Relative permeability of substrate	$1.0 \cdot (1.0 + j\,0.0)$
TLM unit cell size	$0.075 \times 0.075 \times 0.075$ [mm^3]

The scattering parameters were calculated using observation planes 15 mm away from the absorber surface and a Gaussian pulse was excited on a plane one cell above the observation plane for the reflection coefficient. Since periodic boundaries were applied for the xz and yz plane boundaries, the CW metamaterial absorber unit modelled was assumed to belong to infinite array at xy plane.

7.3 Single CW Metamaterial Absorbers

This section investigates the fundamental absorptance characteristics of the single CW metamaterial absorbers. First of all, conductive loss is distributed in one of three ways: allocations to all the metal part, both of the edges (0.9 mm from each edge and 1.8 mm in total) and one of the edges (1.8 mm or 1.2 mm). Secondly, the conductive loss is inhomogeneously distributed. Thirdly, the absorptances of different CW lengths are investigated and they are combined as one metamaterial unit to achieve broadband absorption. In the first and third simulations all the lossy parts have the same value of sheet resistance R and the resistance value does not depend on position of the CW, while in the second simulations R is dependent on the position.

In Fig. 7.2 the absorptance A of the single CW composed of only lossy metal is shown for various sheet resistance values. The absorptance was calculated from

$$A = 1 - |S_{11}|^2 - |S_{21}|^2. \tag{7.3.1}$$

It is found from Fig. 7.2 that the positions of the maximum absorptance are fixed at around 26.59 GHz, which is close to the resonant frequency found in the top of Fig. 4.1, where the same dimension but lossless single CW (i.e. the 5.1×0.3 mm^2 CW with 6.3×6.3 mm^2 periodicity) was simulated.

In addition, it turns out that the absorptance peak curve reaches the maximum values with a sheet resistance $R = 6.0\ \Omega\square^{-1}$, as described in the inset of Fig. 7.2. This absorptance peak dependence can be easily explained with the equivalent circuit drawn in the inset of Fig. 7.3. This equivalent circuit is composed of the sheet resistance R, the total inductance L and the total capacitance C. At the resonant frequency the circuit impedance becomes $Z = R$ (refer eq. (4.1.3)). In terms of the conduction current I, numerical simulations revealed its dependence on R as the curve with closed circles shown in Fig.

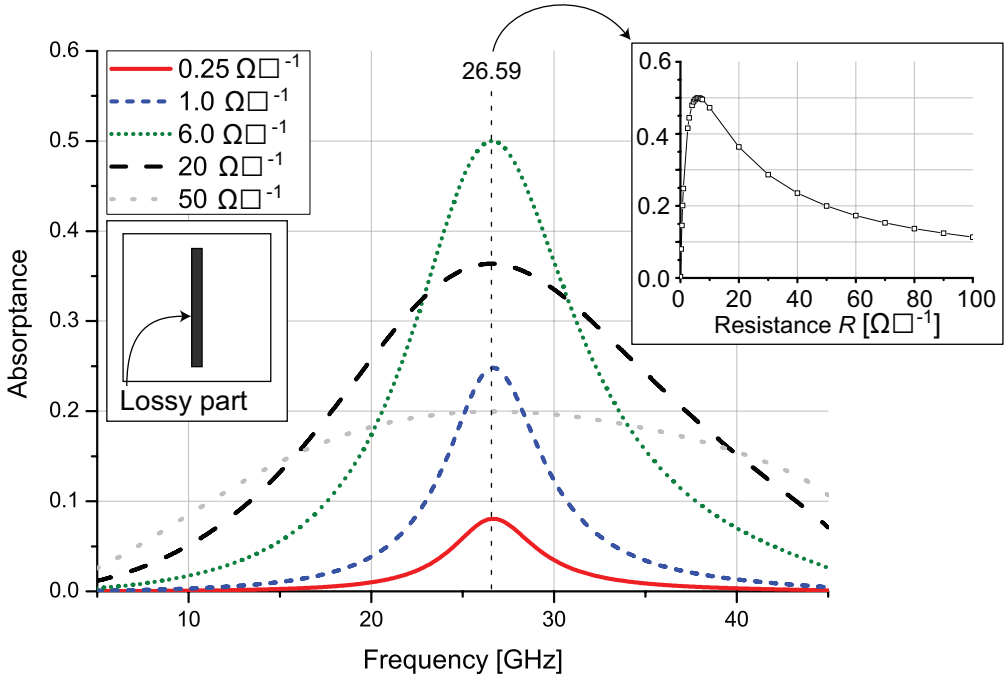

Figure 7.2: Absorptance of the single CW composed of only lossy metal. In the inset the absorptance dependence on R at 26.59 GHz is illustrated.

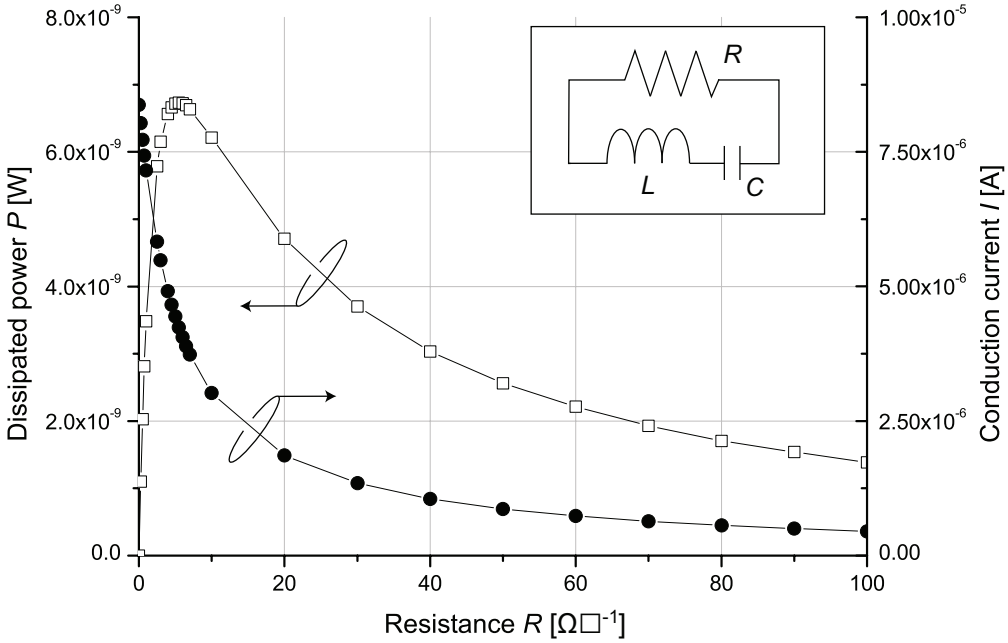

Figure 7.3: Conduction current I and dissipated power P ($= IR^2$) in CW with various values of R. The inset describes an equivalent circuit for the single CW, where R, L and C represent the sheet resistance, the total inductance and the total capacitance, respectively.

7.3. Therefore, the power dissipated in the circuit, P ($= I^2R$), as illustrated by

the curve with open squares in Fig. 7.3, corresponds well to the result in the inset of Fig. 7.2. Note that this equivalent circuit is applicable to only a single CW, and it is expected that in other structures (e.g. paired CW simulated later) some modifications are necessary, since the structures and resonant behaviour becomes more complicated.

Similar maximum absorptance peaks were obtained when the conductive loss area was restricted to one or both of the edges of the CW metal (see Figs. 7.4 to 7.6). However, further increase of the loss amount exhibited different absorptance peaks at higher frequencies. These absorption positions were expected to correspond to resonances of CWs effectively shortened by the lossy metal part(s), since the conductive losses were so high at to cause a highly distorted current distribution. Numerical simulations confirmed that the 3.3 mm–length CW, whose length corresponds to the lossless parts of Figs. 7.4 and 7.5, has resonant frequency at 38.06 GHz, which is in the vicinity of the

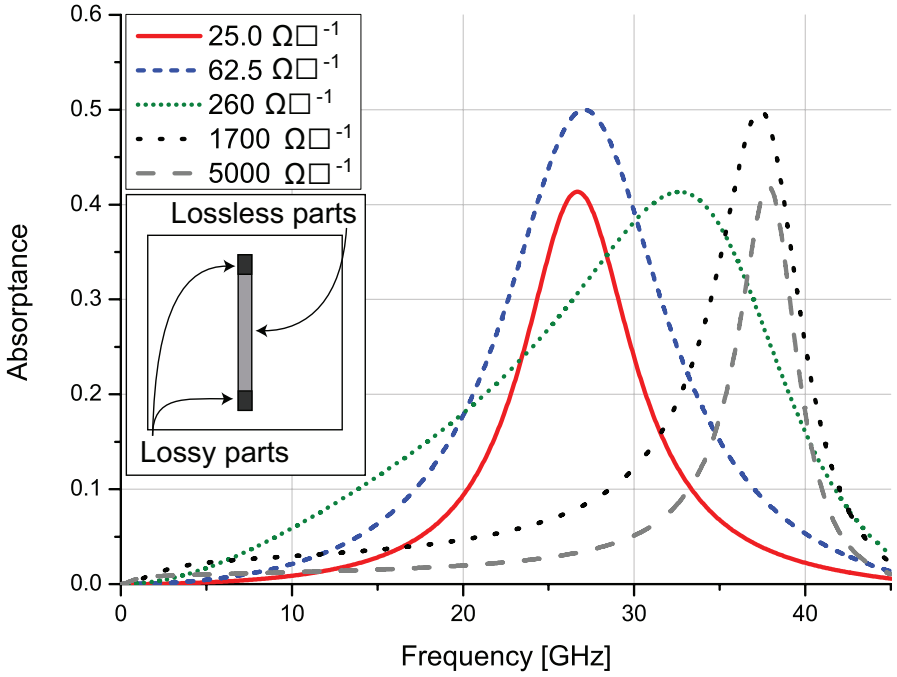

Figure 7.4: Absorptances of single CW composed of both lossless metal part and lossy metal part. The lossy metal parts were restricted to both edges (0.9 mm per each edge and 1.8 mm in total).

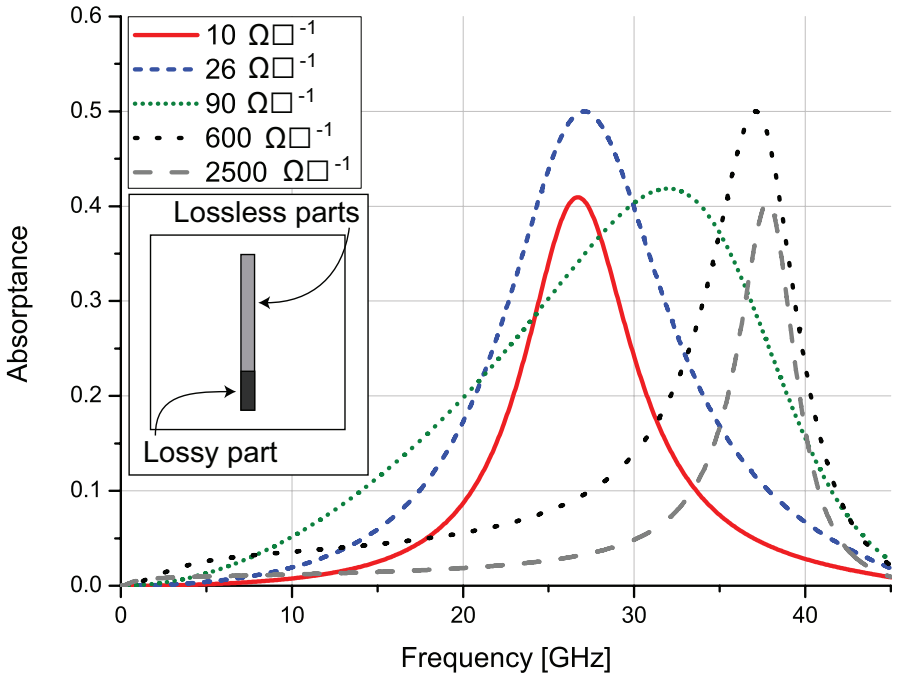

Figure 7.5: Absorptances of single CW composed of both lossless metal part and lossy metal part. The lossy metal parts were restricted to one edge (1.8 mm).

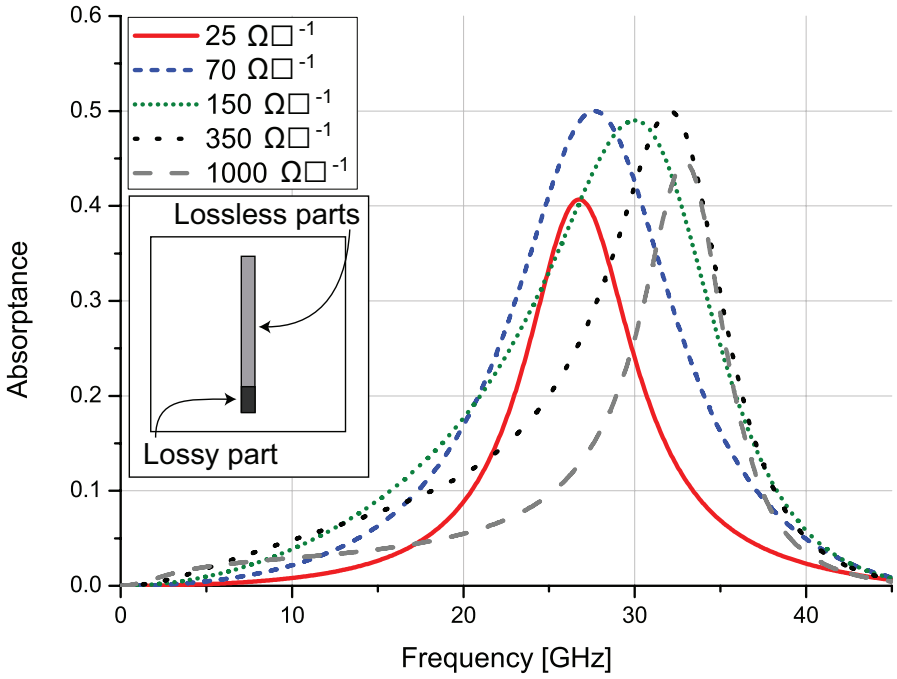

Figure 7.6: Absorptances of single CW composed of both lossless metal part and lossy metal part. The lossy metal parts were restricted to one edge (1.2 mm).

absorptance peaks at the higher frequencies in Figs. 7.4 and 7.5. Similarly the 3.9 mm–length CW, whose metal length is same with the lossless part of Fig. 7.6, was found to have resonant frequency at 33.55 GHz, which is also close to another absorptance peak of Fig. 7.6. Although the absorptance effect obtained from these structures is weak, one point noticed from Figs. 7.5 and 7.6 is that the decrease of the absorptance at the frequency range between the two peaks can be reduced by restricting the lossy metal part to a narrow area.

Secondly, the conductive loss values were inhomogeneously distributed along the CW. The distribution patterns used here are illustrated in the top of Fig. 7.7 and the maximised absorptances for each case are summarised in the bottom of Fig. 7.7, where the resistance values in the legend were used as maximum resistance (i.e. R in the top of Fig. 7.7) of each distribution. It turns out from these results that the loss distributions do not significantly improve the maximum absorptance.

Thirdly, the absorptances of different CW lengths were calculated. The calculation results are summarised in the top of Fig. 7.8 where the simulated CWs had lengths of 3.3 to 5.1 mm in 0.6 mm steps. It is found from the top of Fig. 7.8 that as expected the absorptance peak depends on the CW length.

Next several of the single CWs studied at the top of Fig. 7.8 were combined as one metamaterial unit and the resultant absorptance curves are illustrated in the bottom of Fig. 7.8. The inset in the bottom of Fig. 7.8 describes a structure consisting of the four CWs. In this structure the distance between the CWs was 0.3 mm and one end of the CWs were positioned at a same x axis position (0.3 mm from one of the xz plane boundaries). In the other structures only the corresponding parts were included at the same positions with those of the four CW case (e.g. for the result of 5.1 and 4.5 mm CWs the right two CWs were removed). Compared to the results in the top of Fig. 7.8, the results in the bottom figure exhibited broadband behaviour. However, the maximum

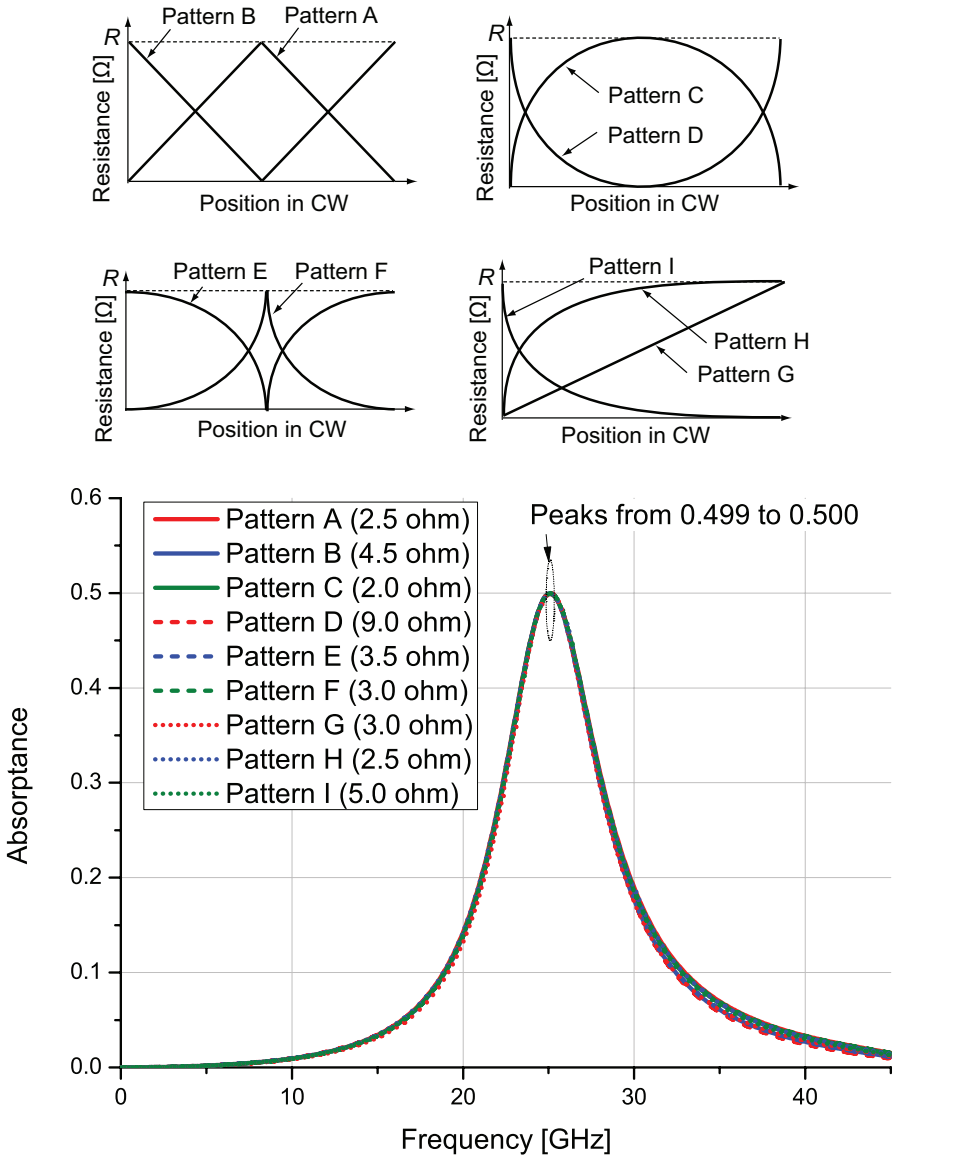

Figure 7.7: Absorptance of single CW with various loss distributions. The distributions used here are illustrated in the top figure. The calculation results are summarised in the bottom figure. The resistance values in the legend of the bottom figure are used as maximum resistance R in the top figure.

absorptance values of all the single CW metamaterial absorbers simulated here were only 0.5.

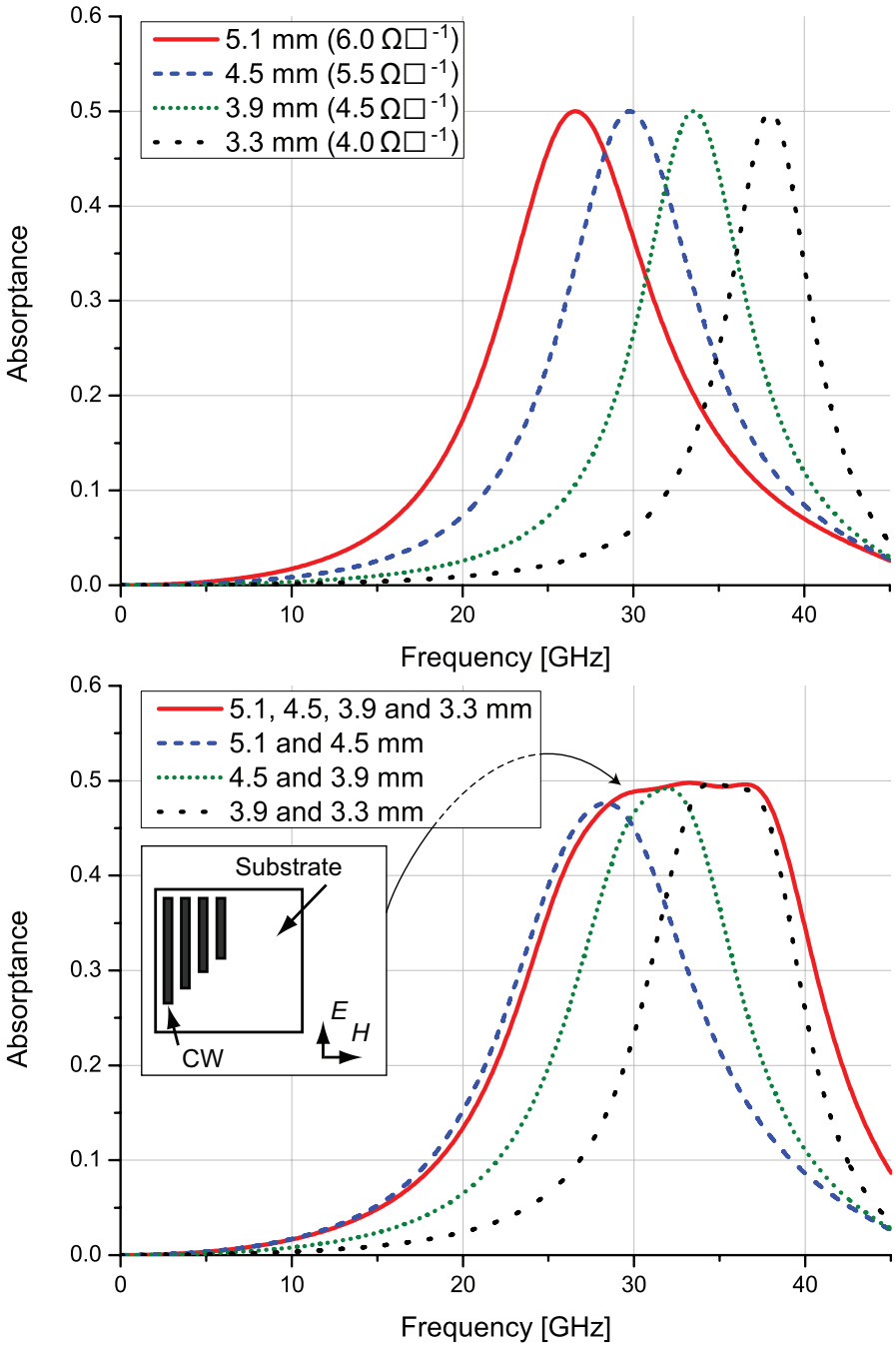

Figure 7.8: Absorptance of different lengths of single CWs (top) and absorptance of structure composed of part or all of the CWs (bottom). The lengths and the resistances in the legends represent the CW length and R, respectively.

7.4 Paired CW Metamaterial Absorbers

This section examines absorptance characteristics of paired CW metamaterials. As was demonstrated in subsection 4.1.2, the paired CW metamaterials have two types of resonance: electric resonance and magnetic resonance. These resonant frequency positions can be manipulated and in [104], for example, one of the CW pairs is shifted a distance d_x (see Fig. 7.9). In this case the magnetic resonance frequency is increased, while the electric resonance frequency is reduced. This effect can be also confirmed from Fig. 7.10 where the dependence of the scattering parameter curves on the offset lengths d_x is shown. It is known that, when the magnetic resonance frequency is greater than the electric resonance frequency, a NRI is obtained in the paired CW metamaterial due to overlap of the negative permeability with the negative permittivity [22]. In [104], for instance, a similar model is simulated to exhibit a negative refractive index. Since the scattering parameters of Fig. 7.10 are analogous to those in [104], the paired CW simulated here is also expected to show a negative value of refractive index. In this section the geometrical asymmetry is utilised to change the resonance positions and investigate the possibility of enhancing absorption characteristics due to this change.

Before the asymmetrically paired CW is simulated, the absorption characteristics of the symmetrically paired CWs are investigated. The calculation

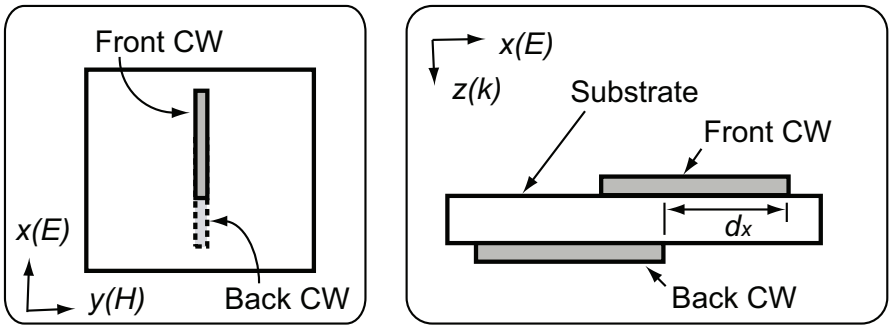

Figure 7.9: Configurations of simulated asymmetrically paired CW metamaterial.

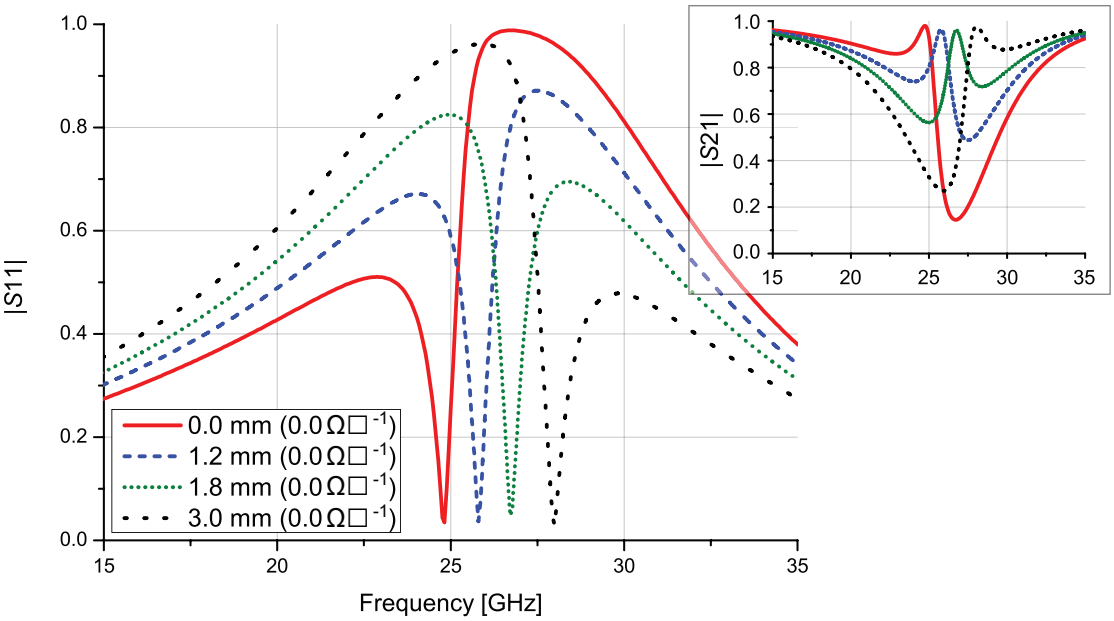

Figure 7.10: $|S_{11}|$ of lossless paired CW having various geometrical offset length d_x. The inset shows $|S_{21}|$ of each structure. d_x is expressed in each legend. In this figure same values of R described in the brackets of the legends were used for the front CW and the back CW.

results are summarised in Fig. 7.11 in which various sheet resistance values, R, are applied equally to the front and back CWs. In Fig. 7.11 the electric and magnetic resonant frequencies (f_e and f_m) obtained in Fig. 7.10 are marked and it is seen that the absorptance peak shifts from f_m to f_e as R increases. It is also found that with the sheet resistance of 6.5 $\Omega\square^{-1}$, the symmetrically paired CW shows the stronger absorption ($A \simeq 0.696$) than that of the single CWs ($A \simeq 0.500$).

Next, the absorptance of the paired CW metamaterial absorber with various values of d_x was optimised. The calculation results are summarised in Table 7.2 and Fig. 7.12. Again, the same resistance values were applied for both front CW and back CW. It turns out in this case that the maximum absorptance of the symmetrically paired CW is increased by nearly 10 % for $d_x = 1.8$ mm.

Moreover the absorptance of the paired CW was further enhanced by us-

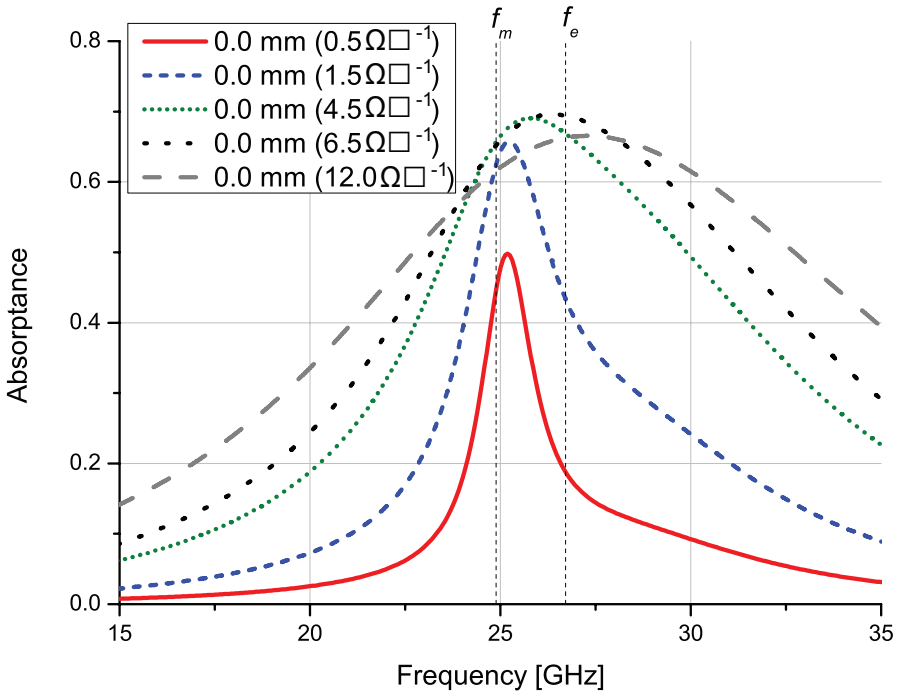

Figure 7.11: Absorptance of the symmetrically paired CW with various R. In this figure same values of R described in the brackets of the legends were used for the front CW and the back CW.

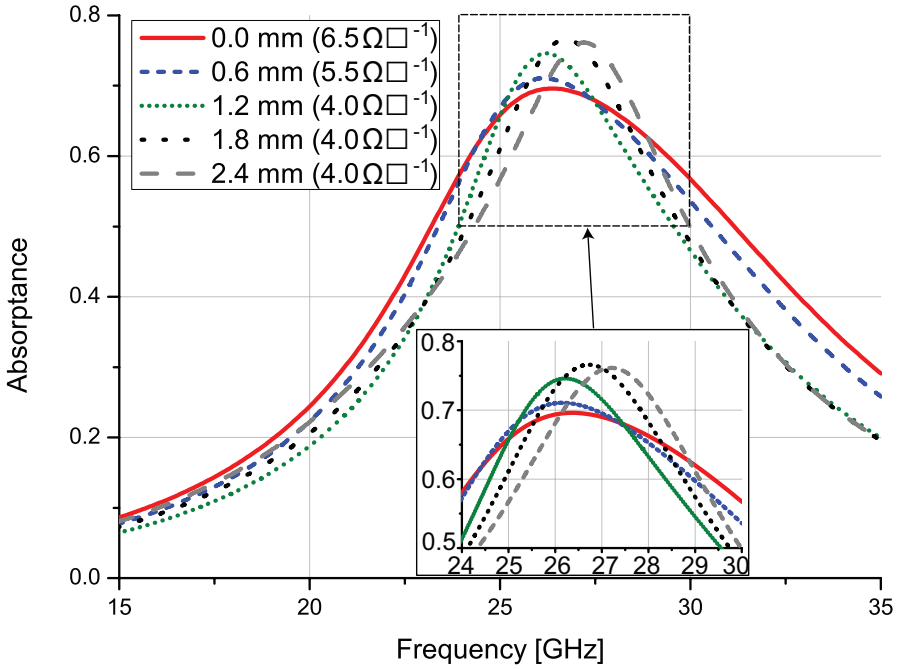

Figure 7.12: Absorptances of the paired CW with various d_x. d_x is expressed in each legend. In this figure same values of R described in the brackets of the legends were used for the front CW and the back CW.

Table 7.2: Absorptance peaks of paired CW with various x axis offset d_x.

d_x [mm]	Absorptance	Frequency [GHz]	R [$\Omega\square^{-1}$]
0.0	0.696	26.35	6.5
0.6	0.711	26.17	5.5
1.2	0.746	26.23	4.0
1.8	0.766	26.71	4.0
2.4	0.761	27.20	4.0
3.0	0.754	27.45	4.0
3.6	0.757	27.39	4.0

ing different sheet resistance values for the front CW and the back CW. In Fig. 7.13 the absorptances for $d_x = 0.0$ mm, 1.2 mm and 2.4 mm are illustrated. Each distribution was calculated at the frequency corresponding to each absorptance peak in Fig. 7.12: 26.35, 26.23 and 27.20 GHz, respectively. In this figure the sheet resistance values were varied from 0 to 12 $\Omega\square^{-1}$ in 2 $\Omega\square^{-1}$ steps. The intermediate values between the calculated results were estimated using spline interpolation. Despite the coarse resolution, the simulations confirm that the absorptance is further increased in each case by the use of the different sheet resistance values. In addition, the distribution of the absorptance depends on the offset length d_x. Although the absorptance of the symmetrically paired CW metamaterial was enhanced by the manipulation of the resonant frequency positions and by the use of the different resistance values, the maximum value was still far from perfect absorption (i.e. $A \sim 1.0$). In the next section the absorptance of the CW metamaterial absorber is significantly improved and approaches perfect absorption by placing a single CW metamaterial on a PEC wall.

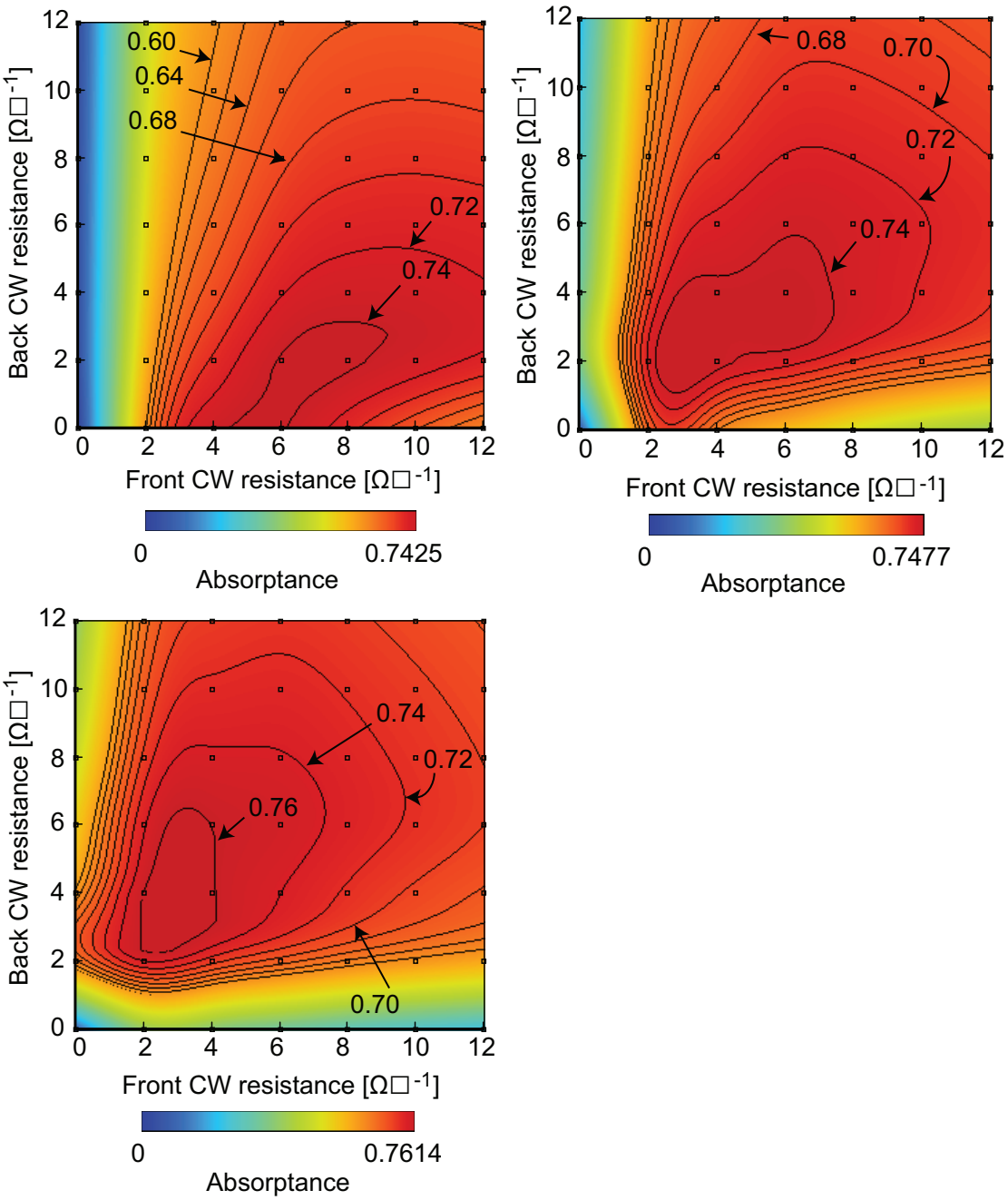

Figure 7.13: Various combinations of R applied for paired CW. The top left, top right and bottom left figures show the absorptances of no offset at 26.35 GHz, 1.2 mm offset at 26.23 GHz and 2.4 mm offset at 27.20 GHz, respectively. The dots in the figures represent the calculated sheet resistance patterns and the intermediate values were estimated by using spline interpolation.

7.5 Single CW Metamaterial Absorbers on PEC Wall

This section studies single CW metamaterial structures placed on a PEC wall (see the inset of Fig. 7.14 for this configuration). The use of the PEC wall as a back metal is described in some past metamaterial absorbers and leads to strong absorptance value (e.g. [77, 130]). In the simulations performed here the CW length was changed from 3.3 to 5.1 mm in 0.6 mm steps again. The CW positions were the same as those used in the inset of the bottom figure of Fig. 7.8, while the sheet resistance values were optimised to extract the maximum absorptances. The calculation results are shown in Fig. 7.14. As demonstrated in this figure, these structures exhibited very strong absorptances of $A \sim 1.0$.

Considering the results obtained, the case of the CW with the metal backing gives the highest absorptance ($A \sim 1.0$) followed by two CWs without the metal backing ($A \sim 0.75$). Finally a single CW gives the lowest absorption ($A \sim 0.5$). It is also pointed out that the conduction current in the single CW with the PEC wall is different from that in the symmetrically paired CW as already demonstrated in the bottom of Fig. 4.3.

Next the same pattern of CWs was deployed along the y axis to reduce polarisation dependence. The calculation results are shown in Fig. 7.15, where the sheet resistance of each CW was optimised again. The inset of Fig. 7.15 describes the simulated structure. Comparing with Fig. 7.14, we observe that the absorptance is still maintained at strong level despite the use of another orthogonal CW. According to [6], straight conductors orthogonal to the electric field do not react with the external field significantly so that the electromagnetic properties of the whole structure are not significantly affected. Although the absorptance values of the short CW pairs tended relatively small, an extended work of the author in [134] introduces improvement methods of the absorbing performance by simple geometrical modifications. In the following sections of this thesis, however, we can still confirm important characteristics of the

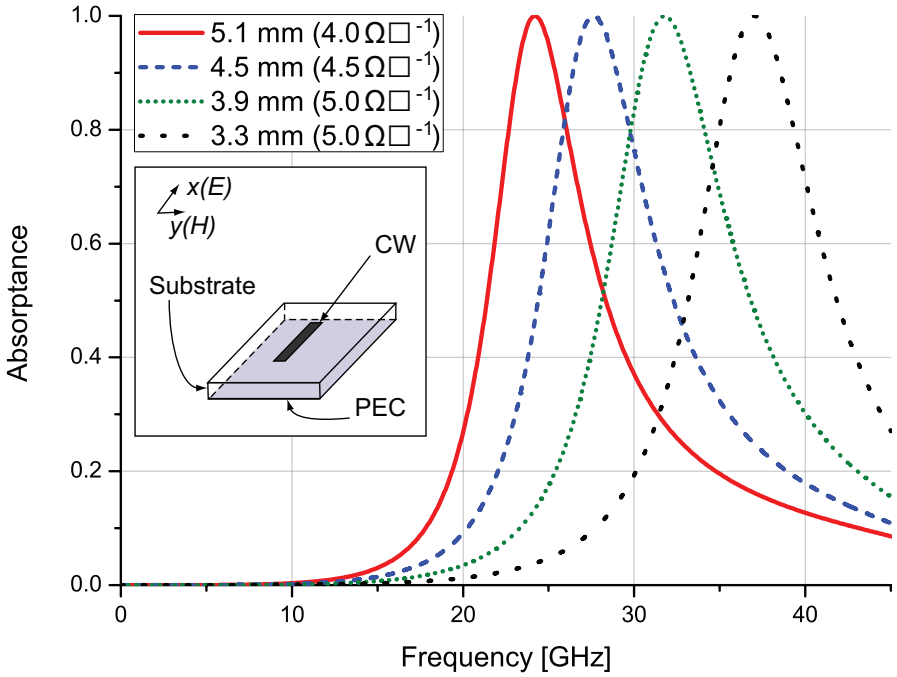

Figure 7.14: Absorptances of different lengths of CWs placed near to PEC wall. The inset describes the simulated situation.

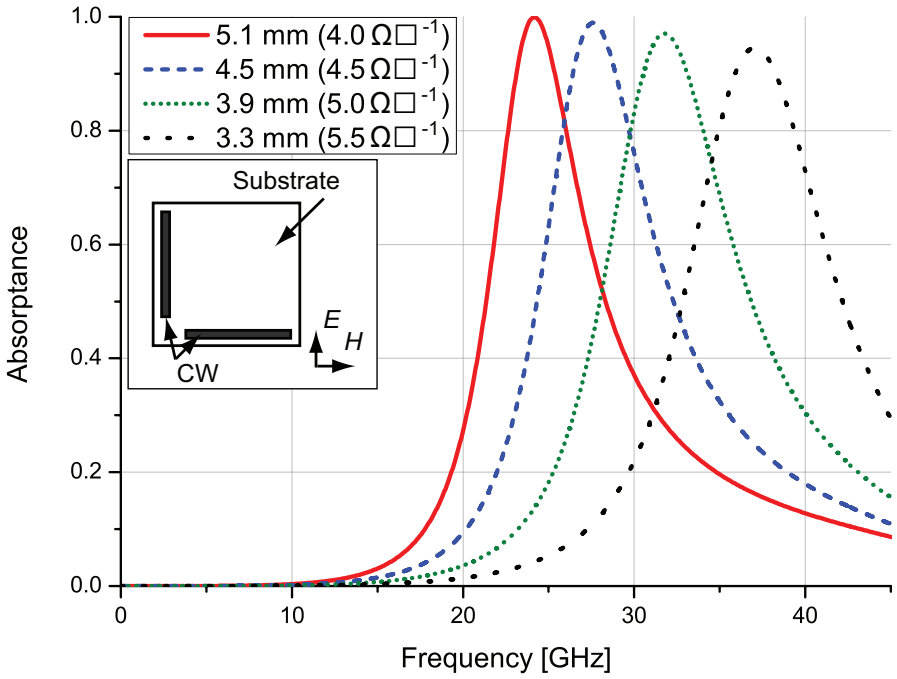

Figure 7.15: Influence of another pair of CW used in Fig. 7.14. The pair of each CW was placed orthogonally, as is illustrated in the inset.

CW metamaterial absorbers, such as broadband behaviour and customisable absorbing performance.

7.6 Customisation of Absorptances

In this section the customisation performance of the absorptance of CW–based metamaterial absorbers is investigated. First, to obtain broadband behaviour some or all of the pairs of the CWs used in Fig. 7.15 were combined as one metamaterial unit. The inset of Fig. 7.16 illustrates the structure having all the CW pairs. In these simulations the sheet resistance values were the same as those used in Fig. 7.15. The calculation results are shown in Fig. 7.16. This figure indicates that the absorptance properties in the high frequency region are improved by the use of the additional lossy pairs.

Also, the addition of extra CWs can introduce additional absorption peaks, as shown in Fig. 7.17 where the two CW pairs of 5.1 and 3.3 mm show two absorptance peaks corresponding to those of the individual CWs. The sheet

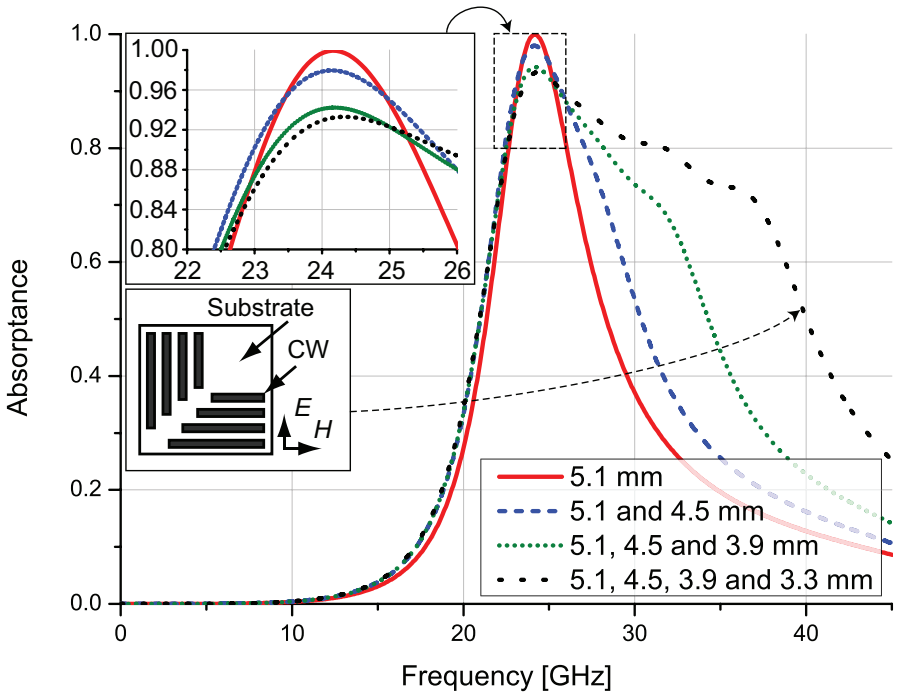

Figure 7.16: Absorptance of combinations of CW pairs used in Fig. 7.15. In this figure part or all of the CW pairs used in Fig. 7.15 were combined as one metamaterial unit. The inset shows the structure having all the CW pairs.

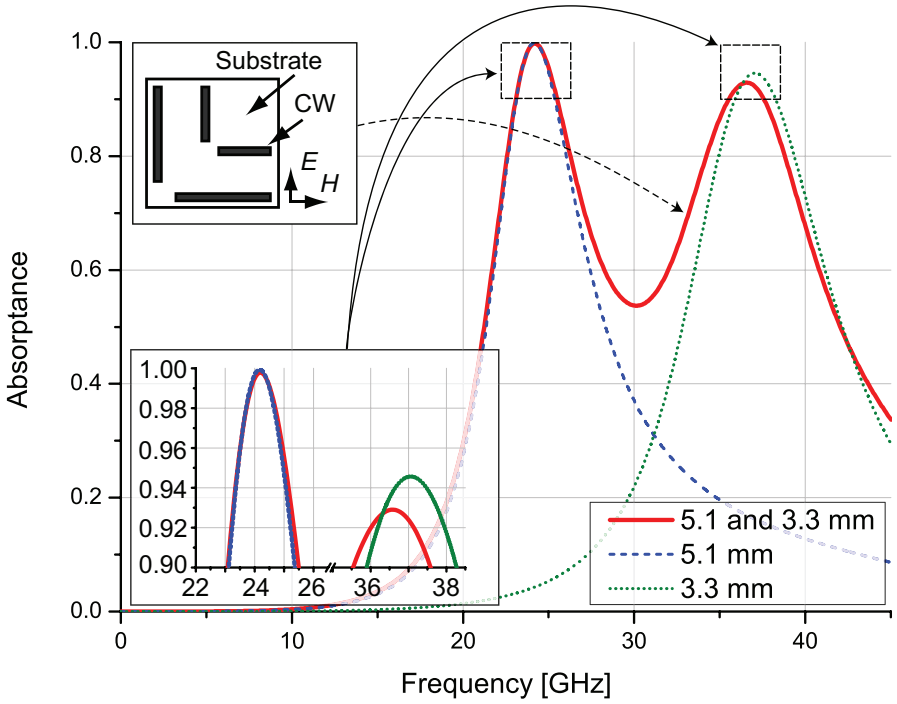

Figure 7.17: Demonstration of double absorptance peak. 5.1 and 3.3 mm CW pairs were combined as one metamaterial unit here.

resistance values were unchanged from Fig. 7.15. Although the case of two absorptance peaks has been recently reported [77, 135], the advantage of using the lossy CWs introduced here is to easily customise the absorptance characteristics for *both* polarisations. Furthermore, as is explained below, it is also easy to realise several absorptance peaks (i.e. not just two peaks) by adding extra pairs of CWs.

The absorption characteristics may be further enhanced by optimising the sheet resistance values. This is shown in Fig. 7.18 in which the three CW pairs of 5.1, 3.9 and 3.3 mm are deployed. In this figure the sheet resistance value of only the 3.3 mm CWs is varied, while the values of the other CWs are the same as those of Fig. 7.15. It is found from Fig. 7.18 that the absorption characteristics are improved by the use of the adjusted resistance values, leading to a triple absorptance peak (0.985 at 24.28 GHz, 0.918 at 32.08 GHz and 0.928 at 35.68 GHz). Despite the use of the *lossless* CWs, Fig. 7.18 still showed the third absorptance peak, which corresponds to the individual resonance

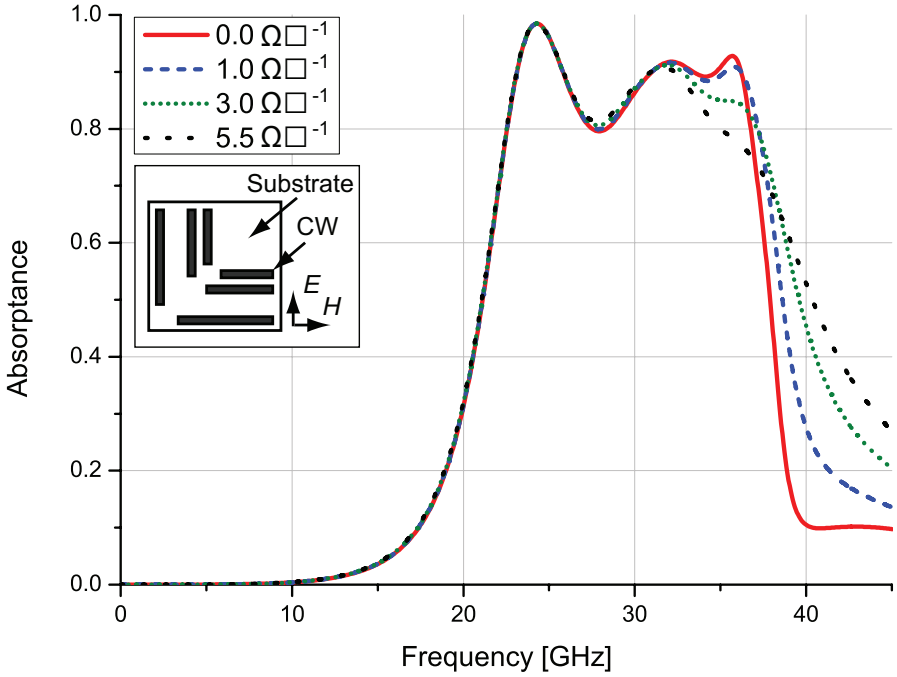

Figure 7.18: Demonstration of triple absorptance peak. 5.1, 3.9 and 3.3 mm CW pairs were combined as one metamaterial unit here. Modification of the resistance value used for the 3.3 mm CW leads to the triple absorptance peak. The resistance values used for the 3.3 mm CW are shown in the legend. The other resistance values are the same as those of Fig. 7.15.

of the 3.3 mm CWs. This is assumed to be because the absorption occurred in the other CW pairs which were coupled to and resonated by the 3.3 mm CW. Again, this structure will interact with both polarisations, compared to those of [77, 135] and is an important advantage of the lossy CW metamaterial absorber. Although only the triple absorptance peak was demonstrated here, further absorptance peaks are possible by using extra CW pairs.

Use of additional pairs of CWs enables us not only to increase absorption, but also to decrease it. In Fig. 7.19 a lossless 4.5 mm CW pair was introduced in the 5.1 and 3.3 mm CW structure used in Fig. 7.17, where R of the 3.3 mm CWs was changed to 3.5 $\Omega\square^{-1}$. The inset of Fig. 7.19 illustrates the configuration of this structure. Compared to Fig. 7.17, the absorptance magnitude between the two absorption peaks is markedly reduced due to the

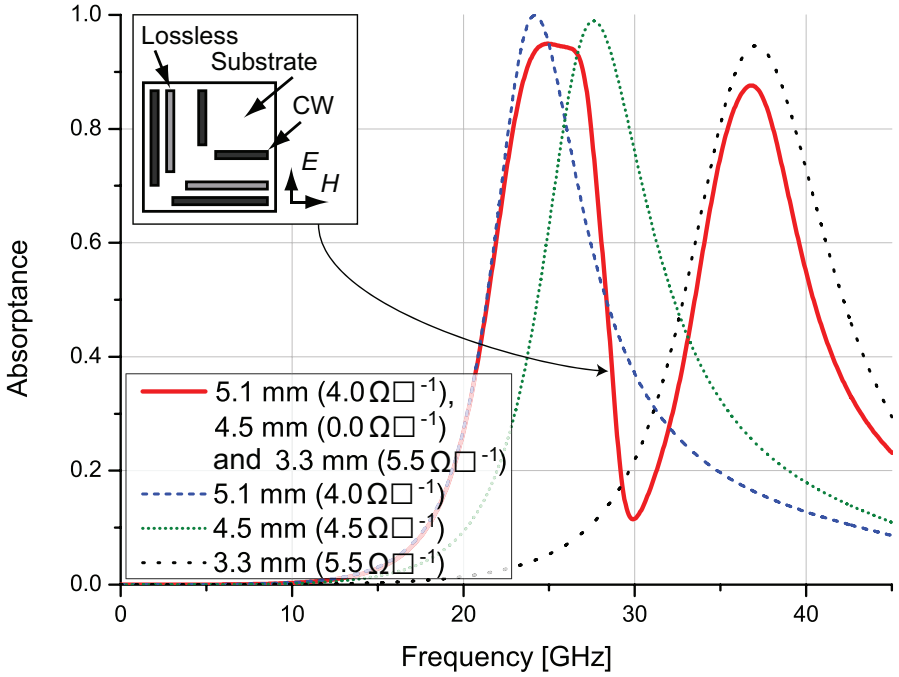

Figure 7.19: Absorptance of two CW pairs of 5.1 and 3.3 mm is improved by use of adjusted resistance values. In addition, the use of a lossless 4.5 mm CW pair exhibits a strong reduction of the absorptance at about 30 GHz.

resonance of the 4.5 mm CW pair. As expected, the centre of the absorptance reduction is close to the resonant frequency of the 4.5 mm CW. This allows a fully customised absorptance characteristic.

7.7 Experimental Validation

This section provides an experimental validation of results obtained for conductively lossy metamaterial absorbers. At the final step the metamaterial absorber is deployed in a metal box to reduce its resonance frequency and enhance its shielding effectiveness. The metal geometry of the metamaterial used is transformed from CW shape to I–shape [59, 136], as a straight CW was too large to fit inside the metal box. Essentially the nature of the resonance in an I–shaped or straight strip is the same as shown in Fig. 7.20, but the height of the I–shape became almost half of the CW–shape.

7.7.1 Models

The actual metal box and measurement system used are shown in Fig. 7.21. The metal box was composed of the top part and bottom plate and had the external dimension of $(118 \times 295 \times 295)$ mm^3, respectively for x, y and z axes, where the directions of each axis correspond to those shown in the centre of Fig. 7.21. The top part of the metal box had (5×50) mm^2 of a slot along y axis at the negative direction of z axis. The position of the slot was located at the centre of xy plane of the metal box. The incident wave was excited from a log–periodic antenna (The Electro–Mechanics Company; Model 3146) connected to an amplifier (ENI; 604L Broadband Power Amplifier) and placed

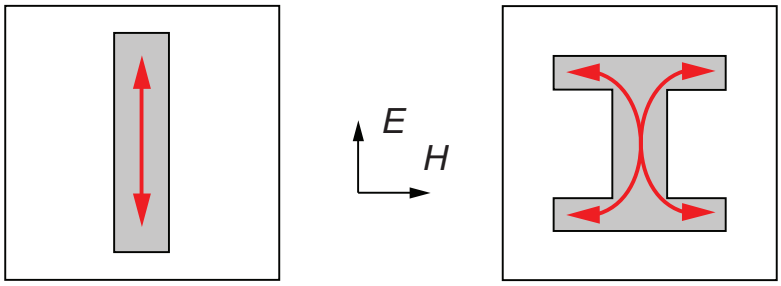

Figure 7.20: Resonances of CW metamaterial (left) and I–shaped metamaterial (right). The red arrows represent the movements of the induced electric charges.

at 1.5 m away from the box. The electric field was measured by using the value of conduction current flowing in 2.5 mm of a straight wire (the bottom left of Fig. 7.21) connected to a network analyzer (Agilent Technologies; E5062A ENA series 300 kHz – 3 GHz Network Analyzer) through the bottom plate of the metal box. The position of the straight wire was the centre of the bottom plate. All the measurements were performed in a screened room (Belling & Lee LTD.; Shielded enclosure), as shown in the centre of Fig. 7.21.

The numerical model of the metal box used for the simulation is illustrated in Fig. 7.22. This box was placed in the centre of a $(44 \times 81 \times 81)$–cell–space surrounded by Huygen's surface (see section 2.3 for the implementation to the TLM method), where $\Delta l \sim 4.9$ mm. Another five cells were placed between the Huygen's surface and matched boundary. The metal of the box was modelled by infinitesimally thin lossless metal (i.e. 0.0 $\Omega\square^{-1}$). Similarly to the metal box used for the measurements, the simulation model of the metal box was composed of the top part and bottom plate. The bottom plate had a sampling port and this consisted of metal blocks and wire (see the right of Fig. 7.22 for the configuration and section 2.2 for the wire modelling). The wire had a 5Δ length and only the bottom one cell had resistance of 50 Ω (i.e. the other parts were lossless). The metal box size in the simulation was slightly smaller than the external dimension of the box used in the measurements. This was to remove the thickness of the metal box and approximate the *internal* dimension of the measurement model.

The left of Fig. 7.23 shows the experimental model of the I–shaped meta-material. By using a commercial nickle spray (RS; RS247–4267 Nickel screening compound), 5 mm width of the metal geometry was drawn on the centre of an epoxy substrate (Injectorall electronics corp.; Epoxy glass board PC7 Unclad), where the relative permittivity and thickness were approximately 4.5 and 1.6 mm, respectively. The height and width of the I–shaped strip were both 70 mm, while those of the substrate were respectively 114 and 230 mm. The top

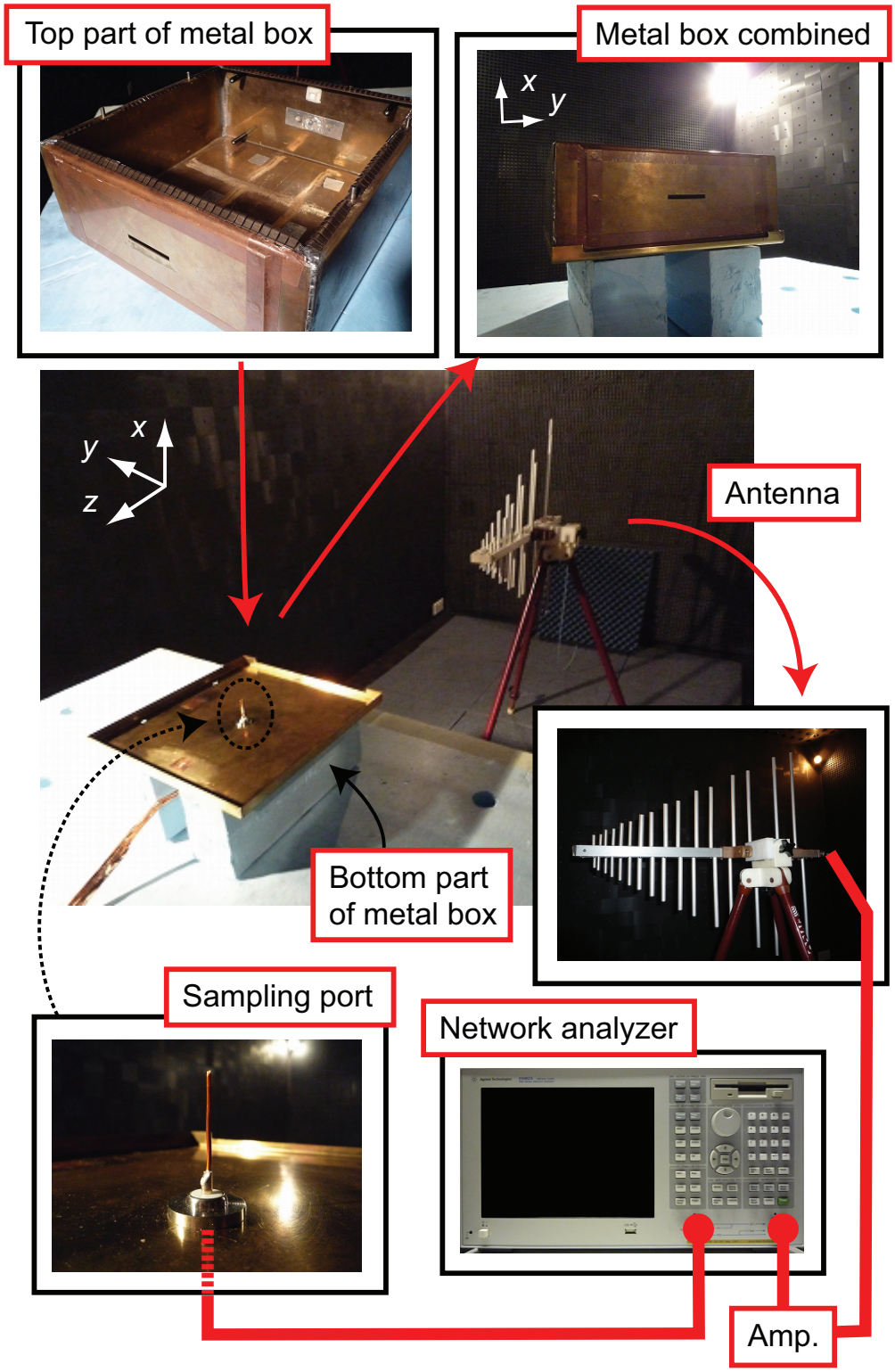

Figure 7.21: Experimental setup and metal box.

part of the substrate was connected to the top of the metal box with almost no gap, and for the y axis position the substrate was placed at the centre of

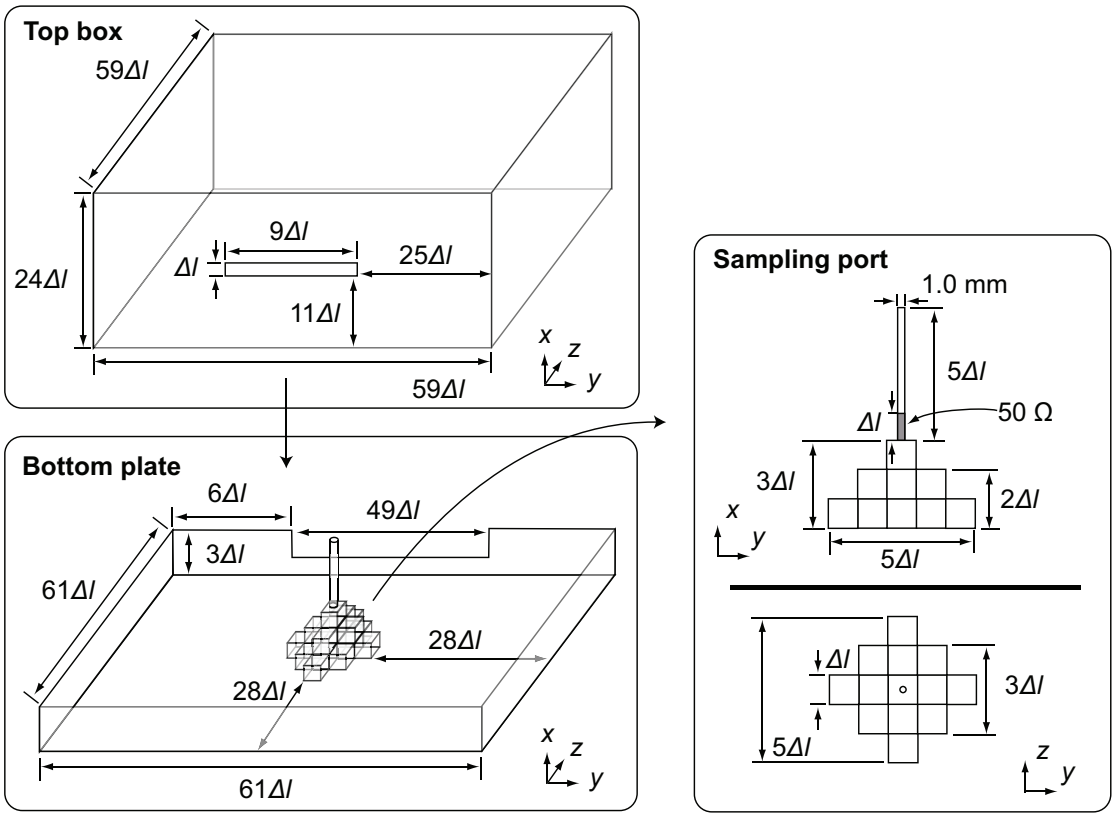

Figure 7.22: Simulation model of metal box.

the metal box. The distance between the back surface of the epoxy substrate and the back wall of the metal box was 3.0 cm, and the four corners of the substrate were fixed with screws (see the bottom left of Fig. 7.23). The sheet resistance of the nickle spray was measured by a tester (Tenma; 72–7730 20,000 Count 4–1/2 digit true RMS USB multimeter DMM) and found to be 1.5 $\Omega\square^{-1}$.

The simulation model of the I–shaped strip is described in the right of Fig. 7.23. The structure was modelled by 1.5 $\Omega\square^{-1}$ of infinitesimally thin metal. The strip width was expressed by one unit cell. The height and width of the I–shaped metal were respectively 14 and 13 cells. Since the thickness of the epoxy substrate used for the measurement (i.e. $\sim$ 1.6 mm) was much thinner than Δl (i.e. $\sim$ 4.9 mm), the substrate was excluded from the simulation space.

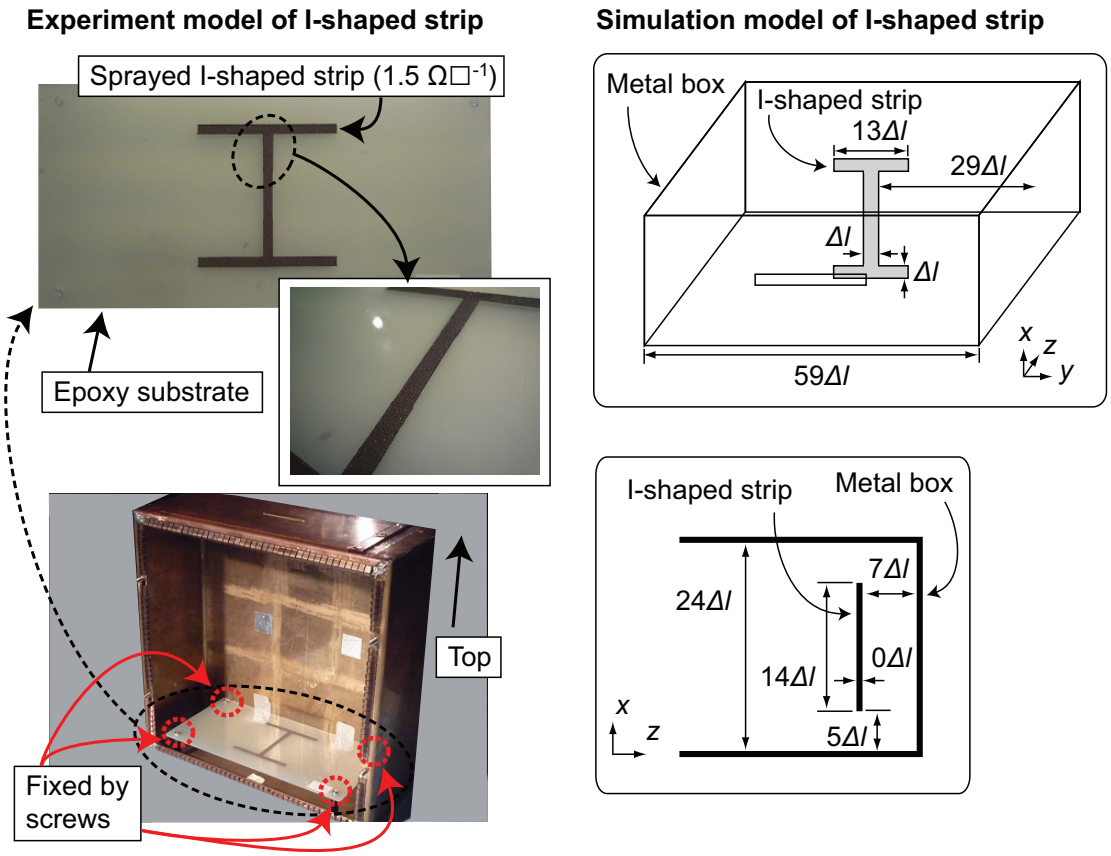

Figure 7.23: Experiment model (left) and calculation model (right) of I–shaped strip.

7.7.2 Results

The measurement and simulation results of the shielding effectiveness of the empty metal box (i.e. without the I–shaped strip) are drawn by the solid curves in Fig. 7.24. In both cases, first the magnitudes of the incident wave were obtained without the top box, and then the differences with those using the top box were calculated for the shielding effectivenesses. As seen from Fig. 7.24, the shielding effectivenesses in both simulation and measurement became less than 0 at around 0.72 GHz due to the resonance of the metal box. These results can be corroborated by the analytical value for the resonance. According to [137, 138], the resonance frequencies f_{box} of metal boxes can be calculated from

$$f_{box} = \frac{c_0}{2}\sqrt{\left(\frac{m}{a}\right)^2 + \left(\frac{n}{b}\right)^2 + \left(\frac{p}{d}\right)^2} \quad [\mathrm{Hz}], \tag{7.7.1}$$

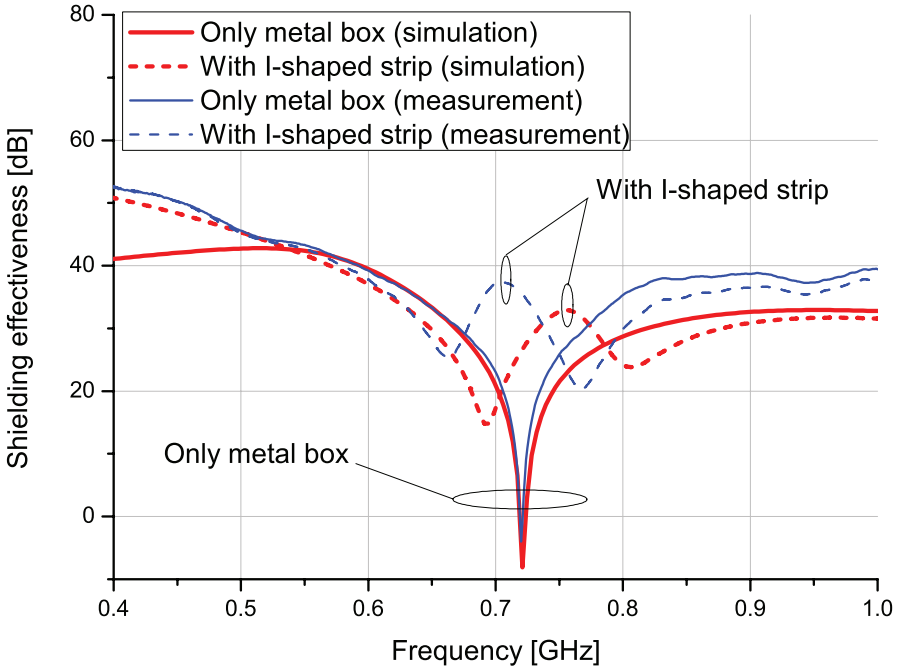

Figure 7.24: Measurement and simulation results of shielding effectiveness of metal box and its improvement by I–shaped strip. The resistance part of the I–shaped strip was composed of 1.5 $\Omega\square^{-1}$ of sprayed resistor.

where a, b and d are each internal dimension of the box in meters. m, n and p are integers where no more than two can be zero. Using the dimension of the metal box, the analytical value became 0.71 GHz and corresponded well to the simulation and measurement results.

The improvement of the shielding effectiveness by the I–shaped strip can be confirmed from the dashed curves of Fig. 7.24. In this case the shielding effectiveness dips found at around 0.72 GHz were split into two weaker dips. In the measurement the shielding effectiveness at the resonant frequency was improved from -4.0 to 35.7 dB, while at 0.767 GHz the value decreased from 29.2 to 20.2 dB. However, the shielding effectiveness decrease was still far above 0 dB, indicating that in total the shielding effectiveness of the metal box was significantly enhanced by deploying the I–shaped strip only.

The similar trend was found in the simulation result in Fig. 7.24. The

shift to the high frequency can be partly attributed to neglecting the substrate in the simulation, which can shift the resonant frequency of the I–shaped strip to a lower value. However, even in the simulation result, the shielding effectiveness was much higher than 0 dB across the frequency range shown here, which agrees with the measurement result.

A similar improvement can be obtained, when a lumped resistor is used instead of the nickel spray for the resistance of the I–shaped strip. The measurement model is shown in the top of Fig. 7.25. In this case, the metal strip was fabricated by copper tape, and a 50 Ω lumped resistor was deployed in the centre of the strip. In the simulation, all the metal parts were modelled by lossless metal except for the centre two cells which had 25 $\Omega\square^{-1}$ per each so that the total resistance became 50 Ω (the detail of this conversion is found from appendix A). As seen from Fig. 7.25, the shielding effectiveness of the empty metal box was also improved by using the lumped resistor. In addition, the improvement was confirmed in both measurement and simulation.

In this section an experimental validation of conductively lossy metamaterial absorbers was provided using the metal box and I–shaped strip. It was demonstrated that the conductively lossy I–shaped strip numerically and experimentally enhances the shielding effectiveness of the metal box. More results can be found in [139].

7.8 Discussion

Before general conclusions are reached, five points about the proposed absorbers are highlighted . Firstly, when other CWs were deployed orthogonally in Fig. 7.15, the magnitude of the absorptance was slightly decreased from those of Fig. 7.14, especially for the shorter CW pairs. This may be attributed to the weak mutual coupling with the orthogonal CWs. These decreased

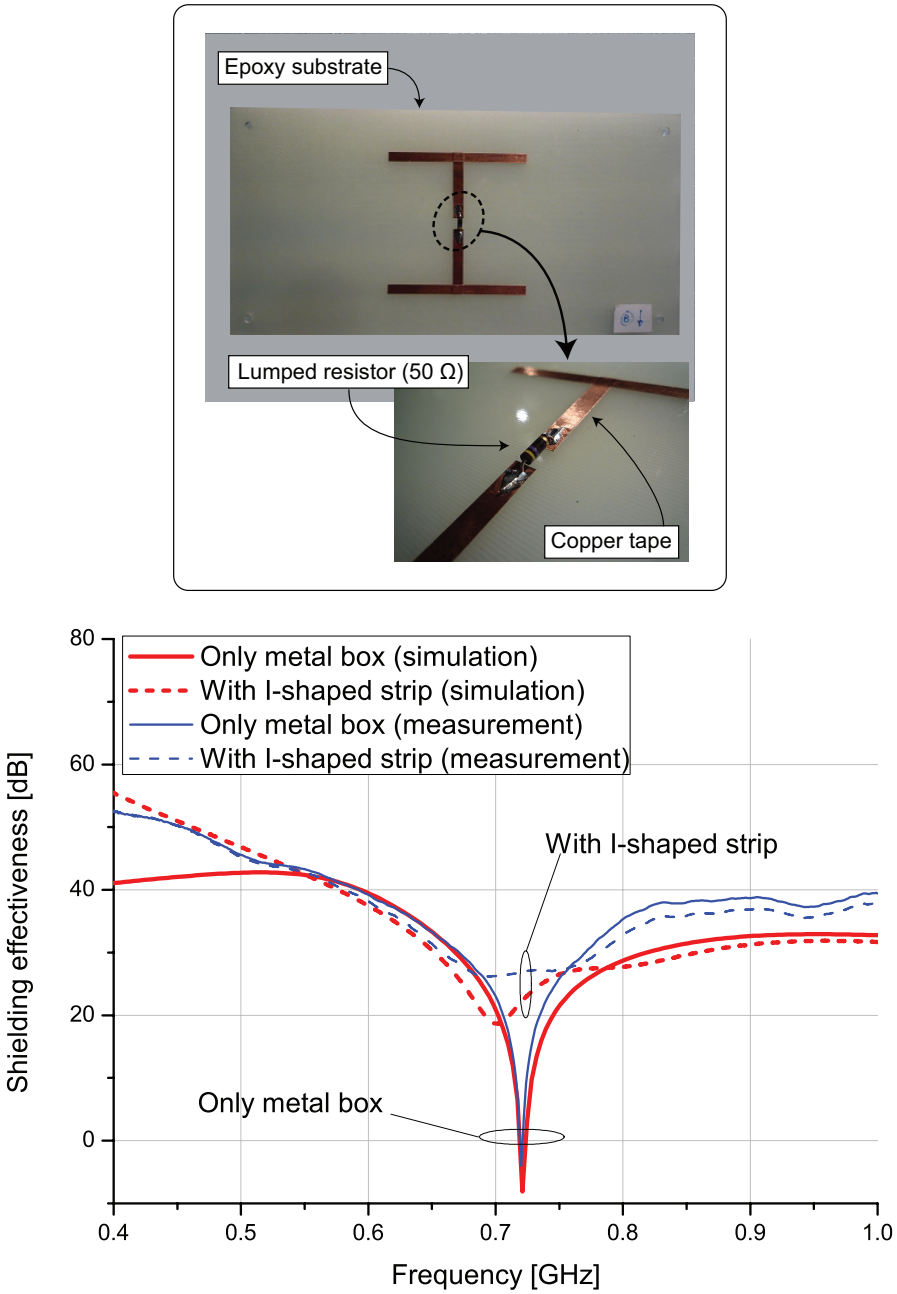

Figure 7.25: Measurement and simulation results of shielding effectiveness of metal box and its improvement by I–shaped strip. The top figure shows the I-shaped strip used. 50 Ω of a lumped resistor was used for this structure. The other part of the structure was composed of copper tape. The measurement and simulation results using the lumped resistor type of the I–shaped strip in the metal box are shown in the bottom figure.

magnitudes could be enhanced by modifying the configurations (e.g. by increasing the CW widths to enhance the mutual coupling with the images of the CWs beyond the PEC wall). However, the calculation results shown in this chapter are sufficient to demonstrate the customisation possibilities for the absorptance of the CW metamaterial absorbers.

Secondly, in the simulations introduced in this chapter, the relative permittivity ε_r of the substrate was set to 1 to simplify the situation and strong absorptances were demonstrated under this condition. However, even if $\varepsilon_r > 1$, the principles of the interactions remain unaffected, although the absorptance peaks will be shifted to lower frequency and the sheet resistances need to be modified accordingly to optimise each configuration again.

Thirdly, the resistance of the PEC wall was fixed at zero in this study, although this is strictly an idealisation. This idealisation is not plausible at high frequencies such as in the THz region, the infrared region and the optical region. However, the conductive loss becomes very low at lower frequencies, such as in the microwave region, or for the frequency range of the simulations performed here. Therefore, approximating the conductive loss of the back wall as zero is satisfactory.

The structures of the metamaterial absorbers studied here were limited to one layer (single CWs) or two (paired CWs and single CW close to PEC), primarily because this research aims at thin wave absorbers (less than $\lambda/4$), which is the major advantage of metamaterial wave absorbers over conventional wave absorbers, such as Salisbury screens. However, in general, it is also interesting to study such structures composed of more than two layers, since this may lead to enhancement of the absorptance (e.g. by analogy to the paired CW case).

Finally, in order to check the performance of metamaterial absorbers at various angles of incidence, the capability was developed of launching waves

at an angle and improving the absorbing boundary condition at incidence angles other than normal. This work is described in appendix D. Some tests were done, confirming that the metamaterials work well at other angles but further tests are needed to fully validate this model.

7.9 Conclusion

This chapter demonstrated by numerical simulations that highly customisable broadband absorption for arbitrary polarisation is possible by the use of conductively lossy CWs as metamaterial absorbers. To begin with, the fundamental properties of the conductively lossy CW metamaterial absorbers were investigated. A dependence of absorptance peak on the conductive loss was explained with a simple equivalent circuit. In paired CW metamaterials, absorptance peaks were improved by manipulating the two resonance frequency positions and by using independent sheet resistance values for the front and back CWs. The absorptance of the conductively lossy CW metamaterial was further improved, when single CW metamaterials were placed on a PEC wall. The deployment of orthogonal pairs of CWs showed that the structure simulated here works for both polarisations. Moreover, when different lengths of CWs were combined as one metamaterial unit, broadband absorption was exhibited. Finally, an experimental validation was obtained for the performance of the conductively lossy metamaterial inside a metal box. Due to the flexible absorptance characteristics, the idea of using conductively lossy CW pairs offers additional advantages to metamaterial absorbers and opens up a new area for metamaterial applications. The interesting properties of CW metamaterials may be further improved, when the structures are designed and optimised to absorb off–normal incident waves. This may be possible by using multiple CWs whose lengths and sheet resistance values are suitably selected.

CHAPTER 8

Conclusions

This thesis has introduced results of computational studies on electromagnetic properties of metamaterials and applications. In chapter 2 the time–domain TLM method [84–86] and some other simulation techniques used in this thesis were explained. In chapter 3, based on these simulation methods, the fundamental scattering properties of metamaterials were shown. The scattering parameters at two types of resonances, electric resonance and magnetic resonance, were studied with a **y**–shaped metamaterial and CLL–based metamaterial. In addition, the scattering parameters were investigated in more detail by decomposing these structures into smaller components or by changing each component size. In this way important factors contributing to resonances were clarified. Furthermore, the scattering parameters of another type of artificial structure, the so–called EBG structures, were studied in this chapter as well.

Chapter 4 addressed the first major objective of the thesis and predicted resonant frequencies of some forms of CW metamaterials by using approximate equivalent circuits. The resonant frequencies were calculated from the equivalent circuits composed of self and mutual capacitive and inductive parameters. Comparison results with detailed numerical simulations showed good agreement. Improvements to the equivalent circuits were proposed and differences with one of the most cited equivalent circuits applicable to CW

metamaterials were discussed.

Chapter 5 described details of two retrieval methods and showed calculation results of electromagnetic properties obtained by these methods. Then, a numerical simulation method able to incorporate retrieved properties was introduced and some numerical simulation results were shown. This chapter pointed out some difficulties with these methods, e.g. unclear results obtained from retrieval methods and a significant increase of calculation time in the numerical simulation method.

Chapter 6 addressed the second major objective of the thesis, which was the application of DF techniques for improving metamaterial simulation efficiency. First of all, the principle of DF techniques was explained in detail and this technique was illustrated by some examples. Furthermore, a large scale simulation was performed to demonstrate the applicability of the DF techniques to realistic situations. In this simulation, metamaterial properties characterised by the DF techniques were used to improve a directivity of an antenna. Some discussions were also made to clarify differences between the simulation method based on retrieval methods and that on the DF techniques.

Chapter 7 presented a study of metamaterial absorbers, which was the third objective of the thesis. The chapter explored a possibility of using metamaterials in realistic application such as absorbers. In this study the metal geometries were based on a simple CW or combinations. The important finding of this chapter was that the CW metamaterial absorbers made it possible to realise customisable absorptance characteristics for arbitrary polarisation in a relatively simple way. These structures showed not only customised enhancement of absorptance but also, if required, reduction of absorptance. The chapter concluded with an experimental validation of the numerical results.

CHAPTER 9

Discussion and Further Work

Since individual discussion has been made at the end of each chapter, the focus of this final discussion chapter is to summarise findings and look into future possibilities for metamaterial studies based on results obtained in this thesis and other research works.

Firstly, in this thesis very simple metamaterial structures have been studied and it is obvious that their performance can be further enhanced. The metamaterial used here were composed of simple metal geometries, such as split–ring shapes shown in chapter 5 and cut–wire shapes in chapters 4 and 7. In the recent metamaterial research extra elements are usefully applied to metamaterials to control their performance. For example, use of semiconductors for metamaterial substrates makes real–time control of scattering characteristics possible, depending on the applied voltage [140–142]. In [143] scattering parameters are thermally controlled by forming the CW geometry with vanadium dioxide, which has a structural transition from an insulating monoclinic phase to a metallic rutile phase. In [144] the scattering characteristics are changed by tilting each periodic unit. This is achieved by fabricating the metal geometries on bimaterial cantilevers which can be tilted in response to a thermal stimulus. The use of these materials may improve the performance of the metamaterials introduced here. These metamaterials exhibit unusual behaviour which is not easily available (or unavailable) from naturally existing mate-

rials (e.g. negative properties and customisation of absorptance characteristics).

Another point found from these recent works is that metamaterials are changing from static materials to dynamic materials (time–varying materials). In a recent metamaterial conference held in 2010 [145], Zheludev described that the current metamaterial research is in a transient phase where the use of metamaterials is changed focusing on applications, such as wave absorbers studied in this thesis too. Then, he speculated that at the next stage, metamaterials would be treated as systems in which systematically and in large scale the input signal (i.e. incident wave) is controlled by changing the properties of each periodic unit separately and dynamically (see Fig. 9.1). In this case the switchable performances introduced above become essential to realise real–time–controllable systems. Also, for the realisation of such systems, not just interactions between the same periodic structures but also those between different periodic metamaterial units may need to be studied.

Secondly, another recent metamaterial research trend is that metamaterials are becoming multi–band materials. This has been exemplified in chapter 7, where metamaterial absorbers composed of multi pairs of CWs demonstrated more than two absorptance peaks. This multi–band function is not limited to metamaterial absorbers. For example, in [146] Ziolkowski et al. reported

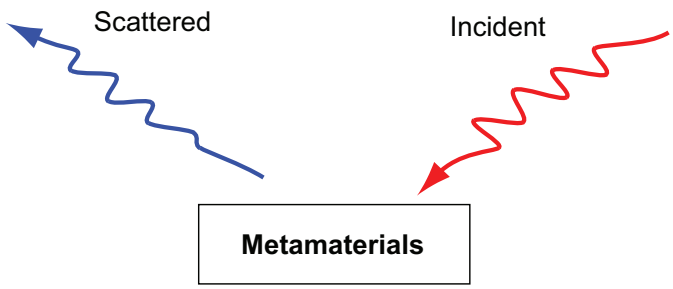

Figure 9.1: Image of metamaterial system. The scattered field is dynamically adjusted depending on the state of the incident field according to user defined criteria. This control is performed either locally or on a large scale.

electrically small and *dual* band metamaterial antennas. The key issue on the realisation of the multi–band properties is how to effectively increase the multiple functions and with what kind of metamaterial geometries. As is well known, metamaterials have periodicities shorter than the wavelength of the incident wave, which implies that the metamaterial elements engineering the electromagnetic properties, such as metal composites or high dielectric materials, are closely placed to each other. Therefore, with the close proximity, the additional resonance elements need to coexist in the periodic unit without weakening the original resonance profile, while exhibiting extra characteristics. In some cases the additional elements share the geometry with the original structure, as illustrated in Fig. 9.2, where a metal geometry able to produce a double absorptance peak is drawn [77]. However, the overlapping of the metal geometry can result in the disruption of the original feature. For this reason, as demonstrated in chapter 7, the use of multi–CW pairs can be a relatively easy and effective ways to add extra functions. Another way leading to multi–functions may be stratifications. In some EBG structure designs [147], this idea has been applied for the realisation of multi–stop band. However,

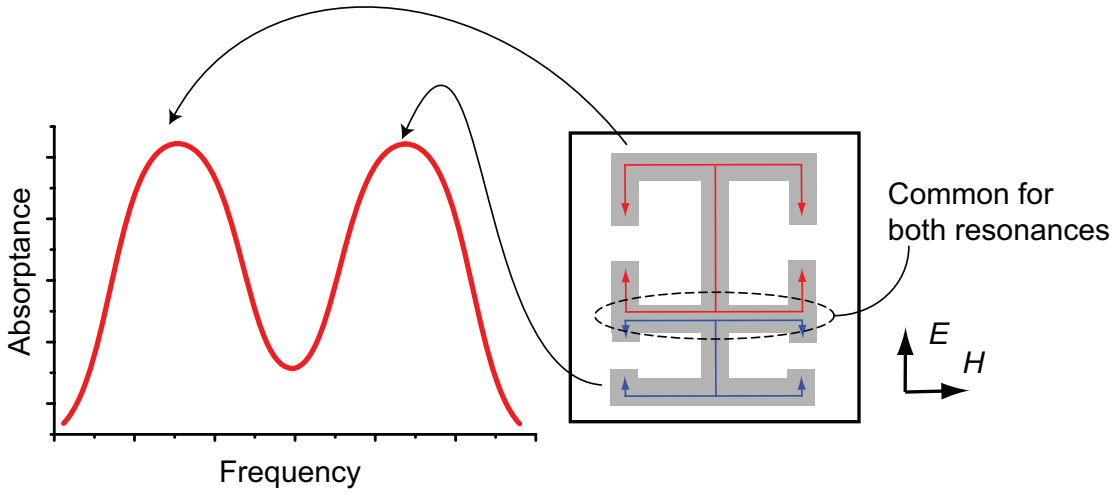

Figure 9.2: Example of metamaterial absorbers sharing metal geometry for double absorptance peak [77]. The metal geometry is placed close to a PEC wall. The middle part of the metal geometry is used for both first and second absorptance peaks (resonances).

note that this leads to increase of the periodic structure thickness and difficult fabrication processes, if further stratifications are needed.

Thirdly, the use of multi–CWs may be useful in designing powerful filtering devices. As explained above, the conductively lossy CW pairs can produce multiple absorptance peaks. If necessary, one of the pairs can be removed to achieve polarisation dependence. Also, when the lossless CW pairs are connected to each other so that *L*–shaped geometry is made as described in Fig. 9.3, the reflection coefficient approaches 1.0 with 90 degrees of the polarisation change. Also, it is reported in [148] two layers of the complementary *L*–shaped metamaterials can realise almost perfect transmission with 90 degree polarisation change. Combining the idea of the *L*–shaped metamaterials with the CW–based metamaterials can provide wider options of scattering characteristic design due to the multi–band function, such as rejection (i.e. 100 % reflection) of the incident wave, collection (i.e. 100 % absorption), transparency (i.e. 100 % transmission), half condition (such as 50 % reflection and 50 % transmission) in addition to the polarisation control. Performance can be further improved by using the time–varying elements mentioned above (e.g. use of semiconductor for the connection of CW pair). A related work of the author for this study is found in [149].

Finally, the realisation of the multi–band functions may introduce further questions in metamaterial research, which is how to simulate these situations in computational studies. Chapter 5 introduced a numerical simulation method to describe negative behaviour in the TLM method. Likewise, many numerical simulation methods cannot represent the frequency dependences of the metamaterial properties (e.g. the relative permittivity and permeability). One solution to this problem is the use of the DF techniques, which converts the frequency–domain characteristics into time–domain characteristics. As explained in the discussion part of chapter 6, incorporating the dependence on the incident angle is an important aspect of this work.

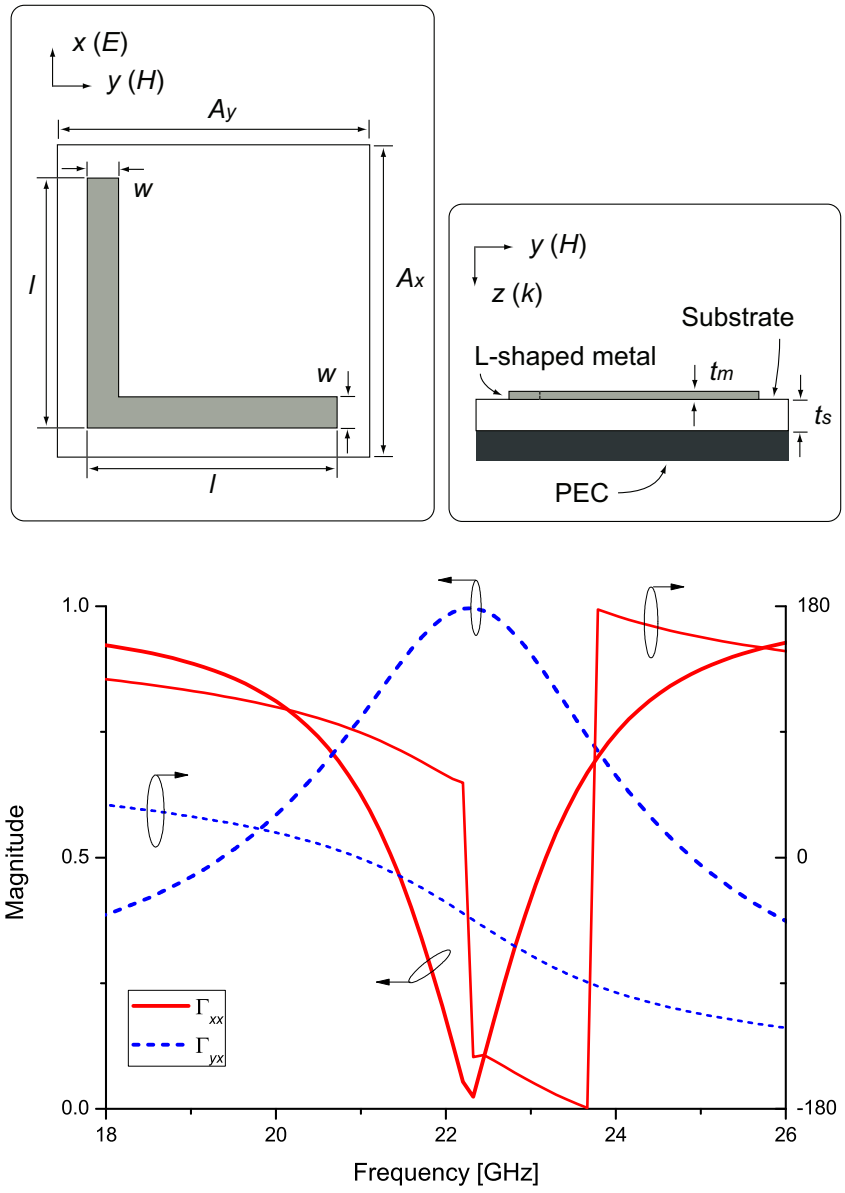

Figure 9.3: *L*–shaped metamaterial (top) and its reflection coefficients (bottom). A_x, A_y, l, w, t_m and t_s were modelled to be 6.3, 6.3, 5.7, 0.3, 0.0 and 1.2 mm by cubical unit cells of $\Delta l = 0.075$ mm. The electromagnetic properties of the substrate were $\varepsilon_r = 1.0$ and $\mu_r = 1.0$. No loss factor was implemented. The reflection coefficients were calculated along x axis which was the same as the incident electric field direction (Γ_{xx}) and y axis (Γ_{yx}). The polarisation of the electric field was changed by 90 degrees at around 22 GHz.

References

[1] D. R. Smith, W. J. Padilla, D. C. Vier, S. C. Nemat–Nasser, and S. Schultz, "Composite medium with simultaneously negative permeability and permittivity," *Phys. Rev. Lett.*, vol. 84, no. 18, pp. 4184–4187, 2000.

[2] R. A. Shelby, D. R. Smith, S. C. Nemat–Nasser, and S. Schultz, "Microwave transmission through a two–dimensional, isotropic, left–handed metamaterial," *Appl. Phys. Lett.*, vol. 78, no. 4, pp. 489–491, 2001.

[3] R. A. Shelby, D. R. Smith, and S. Schultz, "Experimental verification of a negative index of refraction," *Science*, vol. 292, pp. 77–79, 2001.

[4] V. G. Veselago, "The electrodynamics of substances with simultaneously negative values of ε and μ," *Soviet Physics Uspekhi*, vol. 10, no. 4, pp. 509–514, Jan.–Feb. 1968.

[5] J. B. Pendry, A. J. Holden, W. J. Stewart, and I. Youngs, "Extremely low frequency plasmons in metallic mesostructures," *Phys. Rev. Lett.*, vol. 76, no. 25, pp. 4773–4776, 1996.

[6] J. B. Pendry, A. J. Holden, D. J. Robbins, and W. J. Stewart, "Low frequency plasmons in thin–wire structures," *J. Phys. Condens. Matter*, vol. 10, pp.4785–4809, 1998.

[7] J. B. Pendry, A. J. Holden, D. J. Robbins, and W. J. Stewart, "Magnetism from conductors and enhanced nonlinear phenomena," *IEEE Trans. Microw. Theory Tech.*, vol. 47, no. 11, pp. 2075–2084, 1999.

[8] N. Engheta and R. Ziolkowski, *Metamaterials Physics and engineering explorations*," IEEE press, John Wiley & Sons, Piscataway, NJ, 2006.

[9] C. Caloz and T. Itoh, *Electromagnetic metamaterials: transmission line theory and microwave applications*, Wiley–IEEE Press, Hoboken, NJ, 2006.

[10] K. Busch, G. von Freymann, S. Linden, S. F. Mingaleev, L. Tkeshelashvili, and M. Wegener, "Periodic nanostructures for photonics," *Phys. Rep.*, vol. 444, pp. 101–202, 2007.

[11] C. M. Soukoulis, J. Zhou, T. Koschny, M. Kafesaki, and E. N. Economou, "The science of negative index materials," *J. Phys. Condens. Matter*, vol. 20, no. 30, **304217**, 2008.

[12] C. M. Bingham, H. Tao, X. Liu, R. D. Averitt, X. Zhang, and W. J. Padilla, "Planar Wallpaper Group Metamaterials for Novel Terahertz Applications," *Opt. Express*, vol.16, no.23, pp. 18565–18575, 2008.

[13] X. Liu, S. MacNaughton, D. B. Shrekenhamer, H. Tao, S. Selvarasah, A. Totachawattana, R. D. Averitt, M. R. Dokmeci, S. Sonkusale, and W. J. Padilla, "Metamaterials on parylene thin film substrates: design, fabrication, and characterization at terahertz frequency," *Appl. Phys. Lett.*, vol. 96, **011906**, 2010.

[14] M. Walther, A. Ortner, H. Meier, U. Löffelmann, P. J. Smith, and J. G. Korvink, "Terahertz metamaterials fabricated by inkjet printing," *Appl. Phys. Lett.*, vol. 95, **251107**, 2009.

[15] G. Dolling, C. Enkrich, M. Wegener, J. F. Zhou, C. M. Soukoulis, and S. Linden, "Cut–wire pairs and plate pairs as magnetic atoms for optical metamaterials," *Opt. Lett.*, vol. 30, no. 23, pp. 3198–3200, 2005.

[16] V. M. Shalaev, W. Cai, U. K. Chettiar, H. Yuan, A. K. Sarychev, V. P. Drachev, and A. V. Kildishev, "Negative index of refraction in optical metamaterials," *Opt. Lett.*, vol. 30, no. 24, pp. 3356–3358, 2005.

[17] D. A. Powell, I. V. Shadrivov, and Y. S. Kivshar, "Cut–wire–pair structures as two–dimensional magnetic metamaterials," *Opt. Express*, vol. 16, no. 19, pp. 15185–15190, 2008.

[18] S. Zhang, W. Fan, K. J. Malloy, S. R. J. Brueck, N. C. Panoiu, and R. M. Osgood, "Near–infrared double negative metamaterials," *Opt. Express*, vol. 13, no. 13, pp. 4922–4930, 2005.

[19] S. Zhang, W. Fan, N. C. Panoiu, K. J. Malloy, R. M. Osgood, and S. R. J. Brueck, "Experimental demonstration of near–infrared negative index metamaterials," *Phys. Rev. Lett.*, vol. 95, no. 13, **137404**, 2005.

[20] G. Dolling, C. Enkrich, M. Wegner, C. M. Soukoulis, and S. Linden, "Low–loss negative–index metamaterial at telecommunication wavelengths," *Opt. Lett.*, vol. 31, no. 12, pp. 1800–1802, 2006.

[21] G. Dolling, C. Enkrich, M. Wegener, C. M. Soukoulis, and S. Linden, "Simultaneous negative phase and group velocity of light in a metamaterial," *Science*, vol. 312, pp. 892–894, 2006.

[22] J. Zhou, E. N. Economon, T. Koschny, and C. M. Soukoulis, "Unifying approach to left–handed material design," *Opt. Lett.*, vol. 31, no. 24, pp. 3620–3622, 2006.

[23] H. Guo, N. Liu, L. Fu, H. Schweizer, S. Kaiser, and H. Giessen, "Thickness dependence of the optical properties of split–ring resonator metamaterials," *Phys. Status Solidi B*, vol. 244, no. 4, pp. 1256–1261, 2007.

[24] J. B. Pendry, D. Schurig, and D. R. Smith, "Controlling electromagnetic fields," *Science*, vol. 312, pp. 1870–1872, 2006.

[25] A. Alù and N. Engheta, "Achieving transparency with plasmonic and metamaterial coatings," *Phys. Rev. E*, vol. 72, no. 1, **016623**, 2005.

[26] A. Alù and N. Engheta, "Cloaking a sensor," *Phys. Rev. Lett.*, vol. 102, no. 23, **233901**, 2009.

[27] A. Alù, "Mantle cloak: invisibility induced by a surface," *Phys. Rev. B*, vol. 80, no. 24, **245115**, 2009.

[28] Y. Lai, H. Chen, Z. Q. Zhang, and C. T. Chan, "Complementary media invisibility cloak that cloaks objects at a distance outside the cloaking shell," *Phys. Rev. Lett.*, vol. 102, **093901**, 2009.

[29] Y. Lai, J. Ng, H. Y. Chen, D. Han, Z. Q. Zhang, and C. T. Chan, "Illusion optics: the optical transformation of an object into another object," *Phys. Rev. Lett.*, vol. 102, **253902**, 2009.

[30] J. B. Pendry, "Negative refraction makes a perfect lens," *Phys. Rev. Lett.*, vol. 85, no. 18, pp. 3966–3969, 2000.

[31] D. O. S. Melville and R. J. Blaikie, "Super–resolution imaging through a planar silver layer," *Opt. Express*, vol. 13, no. 6, pp. 2127–2134, 2005.

[32] N. Fang, H. Lee, C. Sun, and X. Zhang, "Sub–diffraction–limited optical imaging with a silver superlens," *Science*, vol. 308, pp. 534–537, 2005.

[33] Z. Liu, H. Lee, Y. Xiong, C. Sun, and X. Zhang, "Far–field optical hyperlens magnifying sub–diffraction–limited objects," *Science*, vol. 315, pp. 1686, 2007.

[34] S. Schwaiger, M. Bröll, A. Krohn, A. Stemmann, C. Heyn, Y. Stark, D. Stickler, D. Heitmann, and S. Mendach, "Rolled–up three dimensional metamaterials with a tunable plasma frequency in the visible regime," *Phys. Rev. Lett.*, vol. 102, no. 16, **163903**, 2009.

[35] G. Brumfiel, "Metamaterials: ideal focus," *Nature*, vol. 459, no. 7246, pp. 504–505, 2009.

[36] B. Wood, J. B. Pendry, and D. P. Tsai, "Directed subwavelength imaging using a layered metal–dielectric system," *Phys. Rev. B*, vol. 74, no. 11, **115116**, 2006.

[37] A. P. Feresidis and J. C. Vardaxoglou, "High gain planar antenna using optimised partially reflective surfaces," *IEE Proc. Microw. Antennas Propag.*, vol. 148, no. 6, pp. 345–350, 2001.

[38] S. Enoch, G. Tayeb, P. Sabouroux, N. Guérin, and P. Vincent, "A metamaterial for directive emission," *Phys. Rev. Lett.*, vol. 89, no. 21, **213902**, 2002.

[39] E. Lier, D. H. Werner, C. P. Scarborough, Q. Wu, and J. A. Bossard, "An octave–bandwidth negligible–loss radiofrequency metamaterial," *Nature Mater.*, vol. 10, pp. 216–222, 2011.

[40] R. W. Ziolkowski and A. Erentok, "Metamaterial–based efficient electrically small antennas," *IEEE Trans. Antennas Propag.*, vol. 54, no. 7, pp. 2113–2130, 2006.

[41] C. C. Lin, R. W. Ziolkowski, J. A. Nielsen, M. H. Tanielian, and C. L. Holloway, "An efficient, low profile, electrically small, three–dimensional, very high frequency magnetic EZ antenna," *Appl. Phys. Lett.*, vol. 96, no. 10, **104102**, 2010.

[42] A. Erentok and R. W. Ziolkowski, "Characterization of a volumetric metamaterial realization of an artificial magnetic conductor for antenna applications," *IEEE Trans. Antennas Propag.*, vol. 53, no. 1, pp. 160–172, 2005.

[43] R. F. Service, "Next wave of metamaterials hopes to fuel the revolution," *Science*, vol. 327, pp. 138–139, 2010.

[44] C. L. Holloway, E. F. Kuester, J. Baker–Jarvis, and P. Kabos, "A double negative (DNG) composite medium composed of magnetodielectric spherical particles embedded in a matrix," *IEEE Trans. Antennas Propag.*, vol. 51, no. 10, pp. 2596–2603, 2003.

[45] M. S. Wheeler, J. S. Aitchison, and M. Mojahedi, "Three–dimensional array of dielectric spheres with an isotropic negative permeability at infrared frequencies," *Phys. Rev. B*, vol. 72, no. 19, **193103**, 2005.

[46] L. Peng, L. Ran, H. Chen, H. Zhang, J. A. Kong, and T. M. Grzegorczyk, "Experimental observation of left–handed behavior in an array of standard dielectric resonators," *Phys. Rev. Lett.*, vol. 98, no. 15, **157403**, 2007.

[47] Q. Zhao, L. Kang, B. Du, H. Zhao, Q. Xie, X. Huang, B. Li, J. Zhou, and L. Li, "Experimental demonstration of isotropic negative permeability in a three–dimensional dielectric composite," *Phys. Rev. Lett.*, vol. 101, no. 2, **027402**, 2008.

[48] A. Ahmadi and H. Mosallaei, "Physical configuration and performance modeling of all–dielectric metamaterials," *Phys. Rev. B*, vol. 77, no. 4, **045104**, 2008.

[49] S. Ghadarghadr and H. Mosallaei, "Dispersion diagram characteristics of periodic array of dielectric and magnetic materials based spheres," *IEEE Trans. Antennas Propag.*, vol. 57, no. 1, pp. 149–160, 2009.

[50] R. A. Shore and A. D. Yaghjian, "Traveling waves on three–dimensional periodic arrays of two different alternating magnetodielectric spheres," *IEEE Trans. Antennas Propag.*, vol. 57, no. 10, pp. 3077–3091, 2009.

[51] A. A. Govyadinov, V. A. Podolskiy, and A. Noginov, "Active metamaterials: sign of refractive index and gain–assisted dispersion management," *Appl. Phys. Lett.*, vol. 91, **191103**, 2007.

[52] E. Plum, V. A. Fedotov, P. Kuo, D. P. Tsai, and N. I. Zheludev, "Towards the lasing spacer: controlling metamaterial optical response with semiconductor quantum dots," *Opt. Express*, vol. 17, no. 10, pp. 8548–8551, 2009.

[53] Z. Dong, H. Liu, T. Li, Z. Zhu, S. Wang, J. Cao, S. Zhu, and X. Zhang, "Optical loss compensation in a bulk left–handed metamaterial by the gain in quantum dots," *Appl. Phys. Lett.*, vol. 96, **044104**, 2010.

[54] J. Seidel, S. Grafström, and L. Eng, "Stimulated emission of surface plasmons at the interface between a silver film and an optically pumped dye solution," *Phys. Rev. Lett.*, vol. 94, **177401**, 2005.

[55] M. A. Noginov, G. Zhu, M. Bahoura, J. Adegoke, C. E. Small, B. A. Ritzo, V. P. Drachev, and V. M . Shalaev, "Enhancement of surface plasmons in an Ag aggregate by optical gain in a dielectric medium," *Opt. Lett.*, vol. 31, no. 20, pp. 3022–3024, 2006.

[56] S. Wuestner, A. Pusch, K. L. Tsakmakidis, J. M. Hamm, and O. Hess, "Overcoming losses with gain in a negative refractive index metamaterial," *Phys. Rev. Lett.*, vol. 105, **127401**, 2010.

[57] S. Xiao, V. P. Drachev, A. V. Kildishev, X. Ni, U. K. Chettiar, H. Yuan, and V. M. Shalaev, "Loss–free and active optical negative–index metamaterials," *Nature*, vol. 466, pp. 735–738, 2010.

[58] D. R. Smith, S. Schultz, and P. Markos, and C. M. Soukoulis, "Determination of effective permittivity and permeability of metamaterials from reflection and transmission coefficients," *Phys. Rev. B*, vol. 65, no. 19, **195104**, 2002.

[59] R. W. Ziolkowski, "Design, fabrication, and testing of double negative metamaterials," *IEEE Trans. Antennas Propagat.*, vol. 51, no. 7, pp. 1516–1529, 2003.

[60] R. W. Ziolkowski, "Author reply to comments on "Design, fabrication, and testing of double negative metamaterials,"" *IEEE Trans. Antennas Propagat.*, vol. 53, no. 2, pp. 891–892, 2005.

[61] X. Chen, T. M. Grzegorczyk, B. I. Wu, J. Pacheco Jr, and J. A. Kong, "Robust method to retrieve the constitutive effective parameters of metamaterials," *Phys. Rev. B*, vol. 70, no. 1, **016608**, 2004.

[62] A. M. Nicolson and G. F. Ross, "Measurement of the intrinsic properties

of materials by time–domain techniques," *IEEE Trans. Instrum. Meas.*, vol. IM–19, no. 4, pp. 377–382, 1970.

[63] W. B. Weir, "Automatic measurement of complex dielectric constant and permeability at microwave frequencies," *Proc. IEEE*, vol. 62, pp. 33–36, 1974.

[64] P. K. Kadaba, "Simultaneous measurement of complex permittivity and permeability in the millimeter region by a frequency–domain technique," *IEEE Trans. Instrum. Meas.*, vol. IM–33, no. 4, pp. 336–340, 1984.

[65] D. K. Ghodgaonkar, V. V. Varadan, and V. K. Varadan, "Free–space measurement of complex permittivity and permeability of magnetic materials at microwave frequencies," *IEEE Trans. Instrum. Meas.*, vol. 39, pp. 387–394, 1990.

[66] J. Barker–Jarvis, E. J. Vanzura, and W. A. Kissick, "Improved techniques for determining complex permittivity with the transmission/reflection method," *IEEE Trans. Microw. Theory Tech.*, vol. 38, no. 2, pp. 1096–1103, 2002.

[67] X. Chen, B. I. Wu, J. A. Kong, and T. M. Grzegorczyk, "Retrieval of the effective constitutive parameters of bianisotropic metamaterials," *Phys. Rev. E*, vol. 71, no. 4, **046610**, 2005.

[68] J. B. Pendry, "A chiral route to negative refraction," *Science*, vol. 306, pp. 1353–1355, 2004.

[69] R. Zhao, T. Koschny, and C. M. Soukoulis, "Chiral metamaterials: retrieval of the effective parameters with and without substrate," *Opt. Express*, vol. 18, no. 14, pp. 14553–14567, 2010.

[70] J. Zhou, T. Koschny, M. Kafesaki, and C.M. Soukoulis, "Size dependence and convergence of the retrieval parameters of metamaterials," *Photon. and Nanostruct.: Fundam. and Appl.*, vol. 6, no. 1, pp. 96–101, 2008.

[71] C. L. Holloway, A. Dienstfrey, E. F. Kuester, J. F. O'Hara, A. K. Azad, and A.J. Taylor, "A discussion on the interpretation and characterization of metafilms/metasurfaces: the two–dimensional equivalent of metamaterials," *Metamaterials*, vol. 3, no. 2, pp. 100–112, 2009.

[72] P. P. M. So, H. Du, and W. J. R. Hoefer, "Modeling of metamaterials with negative refractive index using 2–D shunt and 3–D SCN TLM networks," *IEEE Trans. Microw. Theory Tech.*, vol. 53, no. 4, pp. 1496–1505, 2005.

[73] N. Engheta, "Thin absorbing screens using metamaterial surfaces," *Proc. IEEE Int. Symp. on Antennas Propag.*, vol. 2, pp. 392–395, San Antonio, Texas, June 2002.

[74] N. I. Landy, S. Sajiuyigbe, J. J. Mock, D. R. Smith, and W. J. Padilla, "Perfect metamaterial absorber," *Phys. Rev. Lett.*, vol. 100, no. 20, **207402**, 2008.

[75] H. Tao, N. I. Landy, C. M. Bingham, X. Zhang, R. D. Averitt, and W. J. Padilla, "A metamaterial absorber for the terahertz regime: design, fabrication and characterization," *Opt. Express*, vol. 16, no. 10, pp. 7181–7188, 2008.

[76] H. Tao, C. M. Bingham, A. C. Strikwerda, D. Pilon, D. Shrekenhamer, N. I. Landy, K. Fan, X. Zhang, W. J. Padilla, and R. D. Averitt, "Highly flexible wide angle of incidence terahertz metamaterial absorber: design, fabrication, and characterization," *Phys. Rev. B*, vol. 78, no. 24, **241103 (R)**, 2008.

[77] H. Tao, C. M. Bingham, D. Pilon, K. Fan, A. C. Strikwerda, D. Shrekenhamer, W. J. Padilla, X. Zhang, and R. D. Averitt, "A dual band terahertz metamaterial absorber," *J. Phys. D: Appl. Phys.*, vol. 43, no. 22, **225102**, 2010.

[78] H. Wakatsuchi, S. Greedy, C. Christopoulos, and J. Paul, "Customised broadband metamaterial absorbers for arbitrary polarisation," *Opt. Express*, vol. 18, no. 21, pp. 22187–22198, 2010.

[79] H. Wakatsuchi, J. Paul, S. Greedy, and C. Christopoulos, "Contribution of conductive loss to cut–wire metamaterial absorbers," *2010 Asia–Pacific Radio Science Conference (AP–RASC'10)*, pp. DC1–7, Toyama, Japan, Sep. 2010.

[80] H. Tao, W. J. Padilla, X. Zhang, and R. D. Averitt, "Recent progress in electromagnetic metamaterial devices for terahertz applications," *IEEE J. Sel. Top. Quantum Electron.*, vol. 17, no. 1, pp. 92–101, 2011.

[81] J. Paul, V. Podlozny, and C. Christopoulos, "The use of digital filtering techniques for the simulation of fine features in EMC problems solved in the time domain," *IEEE Trans. Electromagn. Compat.*, vol. 45, no. 2, pp. 238–244, 2003.

[82] J. Paul, V. Podlozny, D. W. P. Thomas, and C. Christopoulos, "Time–domain simulation of thin material boundaries and thin panels using digital filters in TLM," *Turk. J. Elec. Engin.*, vol. 10, no. 2, pp. 185–198, 2002.

[83] H. Wakatsuchi, S. Greedy, J. Paul, and C. Christopoulos, "Efficient modelling method for artificial materials using digital filtering techniques and EMC design," *IEICE Trans. Commun.*, vol. E93–B, no. 7, pp. 1760–1767, 2010.

[84] P. B. Johns, "A symmetrical condensed node for the TLM method," *IEEE Trans. Microw. Theory Tech.*, vol. 35, no. 4, pp. 370–377, 1987.

[85] C. Christopoulos, *The transmission–line modeling method: TLM*, IEEE press, Oxford University Press, Piscataway, NJ, 1995.

[86] C. Christopoulos, *The transmission–line modeling (TLM) method in electromagnetics*, USA: Morgan & Claypool Publisher series, US, 2006.

[87] J. Paul, C. Christopoulos, D. W. P. Thomas, and X. Liu, "Time–domain modeling of electromagnetic wave interaction with thin–wires using TLM," *IEEE Trans. Electromagn. Compat.*, vol. 47, no. 3, pp. 447–455, 2005.

[88] J. Paul, C. Christopoulos, and D. W. P. Thomas, "Correction to "Time–domain modeling of electromagnetic wave interaction with thin–wires using TLM,"" *IEEE Trans. Electromagn. Compat.*, vol. 50, no. 2, pp. 450–451, 2008.

[89] J. Paul, C. Christopoulos, and D. W. P. Thomas, "Generalized material models in TLM—part 1: materials with frequency–dependent properties," *IEEE Trans. Antennas Propagat.*, vol. 47, no. 10, pp. 1528–1534, 1999.

[90] R. Holland and L. Simpson, "Implementation and optimization of the thin–strut formalism in THREDE," *IEEE Trans. Nucl. Sci.*, vol. NS–27, no. 6, pp. 1625–1630, 1980.

[91] D. E. Merewether, R. Fischer, and F. W. Smith, "On implementing a numeric Huygen's source scheme in a finite difference program to illuminate scattering bodies," *IEEE Trans. Nucl. Sci.*, vol. NS–27, no. 6, pp. 1829–1833, 1980.

[92] Z. Chen, M. M. Ney, and W. J. R. Hoefer, "Absorbing and connecting boundary conditions for the TLM method," *IEEE Trans. Microw. Theory Tech.*, vol. 41, no. 11, pp. 2016–2024, 1993.

[93] R. F. Harrington, *Time–harmonic electromagnetic fields*, McGraw–Hill, New York, NY, 1961.

[94] D. Sievenpiper, L. Zhang, R. F. J. Broas, N. G. Alexópolous, and E. Yablonovitch, "High–impedance electromagnetic surfaces with a forbidden frequency band," *IEEE Trans. Microw. Theory Tech.*, vol. 47, no. 11, pp. 2059–2074, 1999.

[95] D. Sievenpiper, *High–impedance electromagnetic surfaces*, PhD. dissertation, Dept. Elect. Eng., Univ. California at Los Angeles, Los Angeles, CA, 1999.

[96] H. Chen, L. Ran, J. Huangfu, X. Zhang, K. Chen, T. M. Grzegorczyk, and J. A. Kong, "Left–handed materials composed of only S–shaped resonators," *Phys. Rev. E*, vol. 70, **057605**, 2004.

[97] N. Wongkasem, A. Akyurtlu, K. A. Marx, Q. Dong, J. Li, and W. D. Goodhue, "Development of chiral negative refractive index metamaterials for the terahertz frequency regime," *IEEE Trans. Antennas Propag.*, vol. 55, no. 11, pp. 3052–3062, 2007.

[98] N. Liu, S. Kaiser, and H. Giessen, "Magnetoinductive and electroinductive coupling in plasmonic metamaterial molecules," *Adv. Mater.*, vol. 20, pp. 1–5, 2008.

[99] B. Mohajer–Iravani, S. Shahparnia, and O. M. Ramahi, "Coupling reduction in enclosures and cavities using electromagnetic band gap structures," *IEEE Trans. Electromagn. Compat.*, vol. 48, no. 2, pp. 292–303, 2006.

[100] D. Sievenpiper, J. H. Schaffner, H. J. Song, R. Y. Loo, and G. Tangonan, "Two–dimensional beam steering using an electrically tunable impedance surface," *IEEE Trans. Antennas Propag.*, vol. 51, no. 10, pp. 2713–2722, 2003.

[101] D. Sievenpiper, J. Colburn, B. Fong, J. Ottusch, and J. Visher, "Holographic artificial impedance surfaces for conformal antennas," *IEEE Int. Symp. Antennas Propag.*, pp. 1B 256–259, Washington D.C., July 2005.

[102] B. H. Fong, J. S. Colburn, J. J. Ottusch, J. L. Visher, and D. F. Sievenpiper, "Scalar and tensor holographic artificial impedance surface," *IEEE Trans. Antennas Propag.*, vol. 58, no. 10, pp. 3212–3221, 2010.

[103] L. Yousefi, B. M. Iravani, and O. M. Ramahi, "Enhanced bandwidth artificial magnetic ground plane for low–profile antennas," *IEEE Antennas Wireless Propag. Lett.*, vol. 6, pp. 289–292, 2007.

[104] S. N. Burokur, A. Sllier, B. Kanté, and A. D. Lustrac, "Symmetry breaking in metallic cut wire pairs metamaterials for negative refractive index," *Appl. Phys. Lett.*, vol. 94, **201111**, 2009.

[105] H. Wakatsuchi and J. Paul, "Predictions of resonant frequency shifts in asymmetrical cut–wire metamaterials," *Fourth International Congress on*

Advanced Electromagnetic Materials in Microwave and Optics (Metamaterials'2010 Karlsruhe), pp. 881–883, Karlsruhe, Germany, Sep. 2010.

[106] H. Wakatsuchi, J. Paul, S. Greedy, and C. Christopoulos, "Use of effective equivalent circuits for the prediction of resonant and absorbing behaviour of cut–wire–based metamaterials," *IEEE Trans. Microw. Theory Tech.* (submitted).

[107] W. L. Stutzman and G. A. Thiele, *Antenna theory and design*, New York, NY, John Willey & Sons, Inc., 1998.

[108] C. R. Paul, *Introduction to electromagnetic compatibility*, New York, NY, John Willey & Sons, Inc., 1992.

[109] S. Y. Poh, W. C. Chew, and J. A. Kong, "Approximate formulas for line capacitance and characteristic impedance of microstrip line," *IEEE Trans. Microwave Theory Tech.*, vol. MTT–29, no. 2, pp. 135–142, 1981.

[110] H. M. Greenhouse, Design of planar rectangular microelectronic inductors, *IEEE Trans. Parts Hybrids Packaging*, vol. PHP–10, no. 2, pp. 101–109, 1974.

[111] R. S. Penciu, K. Aydin, M. Kafesaki, Th. Koschny, E. Ozbay, E. N. Economou, and C. M. Soukoulis, "Multi–gap individual and coupled split–ring resonator structures," *Opt. Express*, vol. 16, no. 22, pp. 18131–18144, 2008.

[112] A. Andryieuski, R. Malureanu, and A. V. Lavrinenko, "Wave propagation retrieval method for metamaterials: unambiguous restoration of effective parameters," *Phys. Rev. B*, vol. 80, no. 19, **193101**, 2009.

[113] D. R. Smith and J. B. Pendry, "Homogenization of metamaterials by field averaging," *J. Opt. Soc. Am. B*, vol. 23, no. 3, pp. 391–403, 2006.

[114] J. –M. Lerat, N. Malléjac, and O. Acher, "Determination of the effective

parameters of a metamaterial by field summation method," *J. Appl. Phys.*, vol. 100, no. 8, **084908**, 2006.

[115] S. Sun, S. T. Chui, and L. Zhou, "Effective–medium properties of metamaterials: a quasimode theory," *Phys. Rev. E*, vol. 79, no. 6, **066604**, 2009.

[116] B. I. Popa and S. A. Cummer, "Determining the effective electromagnetic properties of negative–refractive–index metamaterials from internal fields," *Phys. Rev. B*, vol. 72, no. 16, **165102**, 2005.

[117] J. Valentine, S. Zhang, T. Zentgraf, E. Ulin–Avila, D. A. Genov, G. Bartal, and X. Zhang, "Three–dimensional optical metamaterial with a negative refractive index," *Nature*, vol. 455, pp. 376–379, 2008.

[118] J. Wang, S. Qu, Z. Xu, H. Ma, S. Xia, Y. Yang, X. Wu, Q. Wang, and C. Chen, "Normal–incidence left–handed metamaterials based on symmetrically connected split–ring resonators," *Phys. Rev. E*, vol. 81, no. 3, **036601**, 2010.

[119] R. W. Ziolkowski and E. Heyman, "Wave propagation in media having negative permittivity and permeability," *Phys. Rev. E*, vol. 64, **056625**, 2001.

[120] R. W. Ziolkowski, "Pulsed and CW gaussian beam interactions with double negative metamaterial slabs," *Opt. Express*, vol. 11, no. 7, pp. 662–681, 2003.

[121] C. Caloz, C. C. Chang, and T. Itoh, "Full–wave verification of the fundamental properties of left–handed materials (LHMs) in waveguide configurations," *J. App. Phys.*, vol. 90, no. 11, pp. 5482–5486, 2001.

[122] P. Markoŏs and C. M. Soukoulis, "Transmission studies of left–handed materials," *Phys. Rev. B*, vol. 65, **033401**, 2001.

[123] P. Markoŏs and C. M. Soukoulis, "Numerical studies of left–handed materials and arrays of split ring resonators," *Phys. Rev. E*, vol. 65, **036622**, 2002.

[124] H. Wakatsuchi, S. Greedy, J. Paul, and C. Christopoulos, "Efficient modelling of band–gap and metamaterial structures in EMC," *2009 Int. Symp. Electromagn. Compat. Kyoto*, pp. 745–748, Kyoto, Japan, July 2009.

[125] J. N. Brittingham, E. K. Miller, and J. L. Willows, "Pole extraction from real–frequency information," *Proc. IEEE*, vol. 68, pp. 263–273, 1980.

[126] R. Zhao, T. Koschny, and C. M. Soukoulis, "Chiral metamaterials: retrieval of the effective parameters with and without substrate," *Opt. Express*, vol. 18, no. 14, pp. 14553–14567, 2010.

[127] J. Zhou, J. Dong, B. Wang, T. Koschny, M. Kafesaki, and C. M. Soukoulis, "Negative refractive index due to chirality," *Phys. Rev. B*, vol. 79, no. 12, **121104**, 2009.

[128] Z. Li, K. Aydin, and E. Ozbay, "Determination of the effective constitutive parameters of bianisotropic metamaterials from reflection and transmission coefficients," *Phys. Rev. E*, vol. 79, no. 2, **026610**, 2009.

[129] N. I. Landy, C. M. Bingham, T. Tyler, N. Jokerst, D. R. Smith, and W. J. Padilla, "Design, theory, and measurement of a polarization–insensitive absorber for terahertz imaging," *Phys. Rev. B*, vol. 79, no. 12, **125104**, 2009.

[130] D. J. Kern and D. H. Werner, "A genetic algorithm approach to the design of ultra–thin electromagnetic bandgap absorbers," *Microwave Opt. Technol. Lett.*, vol. 38, no. 1, pp. 61–64, 2003.

[131] K. Kordás, T. Mustonen, G. Tóth, H. Jantunen, M. Lajunen, C. Soldano, S. Talapatra, S. Kar, R. Vajtai, and P. Ajayan, "Inkjet printing of electrically conductive patterns of carbon nanotubes," *Small*, vol. 2, pp. 1021–1025, 2006.

[132] W. R. Small, F. Masdarolomoor, G. G. Wallace, and M. In Het Panhuis, "Inkjet deposition and characterization of transparent conducting electroactive polyaniline composite films with a high carbon nanotube loading fraction," *J. Mater. Chem.*, vol. 17, no. 41, pp. 4359–4361, 2007.

[133] D. Redinger, S. Molesa, S. Yin, R. Farschi, and V. Subramanian, "An ink–jet–deposited passive component process for RFID," *IEEE Trans. Electron Devices*, vol. 51, no. 12, pp. 1978–1983, 2004.

[134] H. Wakatsuchi, J. Paul, S. Greedy, and C. Christopoulos, "Performance enhancement of cut–wire–based metamaterial absorbers," *Fifth International Congress on Advanced Electromagnetic Materials in Microwave and Optics (Metamaterials'2011 Barcelona)*, Barcelona, Spain (accepted).

[135] Q. Y. Wen, H. W. Zhang, Y. S. Xie, Q. H. Yang, and Y. L. Liu, "Dual band terahertz metamaterial absorber: design, fabrication, and characterization," *Appl. Phys. Lett.*, vol. 95, **241111**, 2009.

[136] M. Choi, S. H. Lee, Y. Kim, S. B. Kang, J. Shin, M. H. Kwak, K. Kang, Y. Lee, N. Park, and B. Min, "A terahertz metamaterial with unnaturally high refractive index," *Nature*, vol. 470, pp. 369–373, 2011.

[137] C. Christopoulos, *Principles and techniques of electromagnetics compatibility, second edition*, CRC Press Taylor & Francis Group, London, U.K., 2007.

[138] S. Ramo, J. R. Whinnery, and T. V. Duzer, *Fields and waves in communication electronics, third edition*, John Wiley and Sons Inc., Hoboken, NJ, 1994.

[139] J. Paul, S. Greedy, H. Wakatsuchi, and C. Christopoulos, "Measurements and simulations of enclosure damping using loaded antenna elements," (submitted to *EMC Europe 2011*, York, U.K.).

[140] W. J. Padilla, A. J. Taylor, C. Highstrete, M. Lee, and R. D. Averitt, "Dynamic electric and magnetic metamaterial response at Terahertz frequencies," *Phys. Rev. Lett.*, vol. 96, **107401**, 2006.

[141] H. Chen, W. J. Padilla, J. M. O. Zide, A. C. Gossard, A. J. Taylor, and R. D. Averitt, "Active terahertz metamaterial devices," *Nature*, vol. 444, pp. 597–600, 2006.

[142] X. Miao, B. Passmore, A. Gin, W. Langston, S. Vangala, W. Goodhue, E. Shaner, and I. Brener, "Doping tunable resonance: toward electrically tunable mid–infrared metamaterials," *Appl. Phys. Lett.*, vol. 96, no. 10, **101111**, 2009.

[143] Q. Wen, H. Zhang, Q. Yang, Y. Xie, K. Chen, and Y. Liu, "Terahertz metamaterials with VO_2 cut–wires for thermal tunability," *Appl. Phys. Lett.*, vol. 97, no. 2, **021111**, 2010.

[144] H. Tao, A. C. Strikwerda, K. Fan, W. J. Padilla, X. Zhang, and R. D. Averitt, "Reconfigurable terahertz metamaterials," *Phys. Rev. Lett.*, vol. 103, no. 14, **147401**, 2009.

[145] N. Zheludev, "Nonlinear and switchable photonic metamaterials," *Fourth International Congress on Advanced Electromagnetic Materials in Microwave and Optics (Metamaterials'2010 Karlsruhe)*, pp. 3, Karlsruhe, Germany, Sep. 2010.

[146] R. Ziolkowski, P. Jin, and C. Lin, "Metamaterial–inspired, multi–functional, electrically small, near–field resonant parasitic antennas," *Fourth International Congress on Advanced Electromagnetic Materials in Microwave and Optics (Metamaterials'2010 Karlsruhe)*, pp. 958–960, Karlsruhe, Germany, Sep. 2010.

[147] T. Kamgaing and O. M. Ramahi, "Multiband electromagnetic–bandgap structures for applications in small form–factor multichip module packages," *IEEE Trans. Microw. Theory Tech.*, vol. 56, no. 10, pp. 2293–2300, 2008.

[148] T. Li, S. M. Wang, J. X. Cao, H. Liu, and S. N. Zhu, "Cavity–involved plasmonic metamaterial for optical polarization conversion," *Appl. Phys. Lett.*, vol. 97, no. 26, **261113**, 2010.

[149] H. Wakatsuchi and C. Christopoulos, "Generalized scattering control using cut–wire–based metamaterials," *Appl. Phys. Lett.*, vol. 98, no. 22, **221105**, 2011.

[150] R. T. Lee, *A novel method for incorporating periodic boundaries into the FDTD method and the application to the study of structural color of insects*, PhD. dissertation, School Elect. Comp. Eng., Georgia Institute of Technology, Atlanta, GA, 2009.

[151] J. A. Roden and S. D. Gedney, "Convolution PML (CPML): an efficient FDTD implementation of the CSF–PML for arbitrary media," *Microwave Opt. Technol. Lett.*, vol. 27, pp. 334–339, 2000.

[152] N. R. S. Simons and E. Bridges, "Method for modelling free space boundaries in TLM situations," *Electron. Lett.*, vol. 26, no. 7, pp. 453–455, 1990.

APPENDIX A

Use of Sheet Resistance Unit in the TLM Method

Resistance R_0 [Ω] of the metal illustrated in the top of Fig. A.1 can be expressed with the resistivity ρ [Ωm]:

$$R_0 = \frac{\rho L}{TW} = \frac{\rho}{T}\frac{L}{W}, \tag{A.0.1}$$

where L, W and T are respectively the length, thickness and width of the metal (all in meter). Assuming that the sheet resistance is R [$\Omega\square^{-1}$], from the above expression

$$R_0 = R\frac{L}{W}. \tag{A.0.2}$$

When TLM unit cells are cubical forms as the bottom of Fig. A.1, i.e. $\Delta l = \Delta x = \Delta y = \Delta z$, where Δx, Δy and Δz are respectively the edge lengths of the unit cells along x, y and z axes, eq. (A.0.2) becomes

$$\begin{aligned} R_0 &= R\frac{\Delta l}{\Delta l} \\ &= R. \end{aligned} \tag{A.0.3}$$

Therefore, for example, 50 Ω can be modelled by 25 $\Omega\square^{-1}$ of two square unit cells to represent the same resistance.

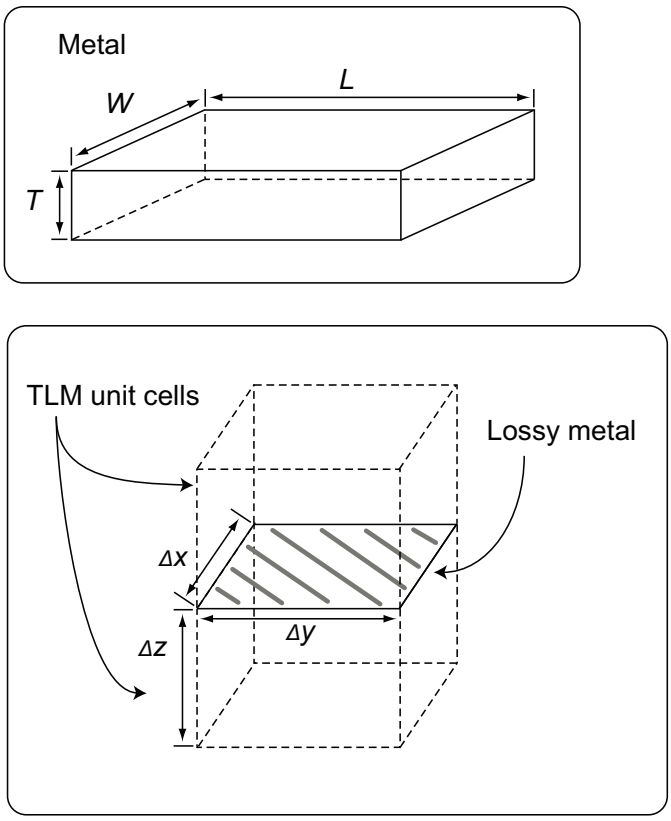

Figure A.1: Dimension of metal (top) and infinitesimally thin metal modelled in the TLM (bottom).

APPENDIX B

Scattering Matrices Used for Representation of Metamaterial Properties

In subsection 5.4.1 scattering matrices applicable to an inter–cell network between same metamaterials and that between a metamaterial (i.e. eq. (5.4.1)) and regular dielectric material (including vacuum) (i.e. eq. (5.4.2)) were introduced. The coefficients used for these matrix equations are given below. For the inter–cell network between same metamaterials, the following equations can be used [72]:

$$\begin{aligned}
\alpha &= \frac{Z_c + Z_a - Z_0}{Z_c + Z_a + Z_0} \\
\beta &= \frac{2 \cdot Z_a \cdot Z_0}{(Z_c + Z_a + Z_0) \cdot (Z_c + Z_0)} \\
\chi &= \frac{2 \cdot Z_0}{Z_c + Z_a + Z_0} \\
\delta &= \frac{2 \cdot Z_b \cdot Z_0}{(Z_l + Z_b) \cdot (Z_c + Z_0)} \\
\kappa &= \frac{2 \cdot Z_c}{Z_c + Z_a + Z_0} \\
\tau &= \frac{2 \cdot Z_a \cdot Z_c}{(Z_c + Z_a + Z_0) \cdot (Z_c + Z_0)}
\end{aligned}$$

$$
\begin{aligned}
\vartheta &= \frac{Z_0 + Z_a - Z_c}{Z_c + Z_a + Z_0} \\
\zeta &= \frac{2 \cdot Z_b \cdot Z_c}{(Z_{ll} + Z_b) \cdot (Z_{ll} + Z_0)} \\
\xi &= \frac{2 \cdot Z_a}{Z_c + Z_a + Z_0} \\
\gamma &= \frac{Z_b - Z_{ll}}{Z_b - Z_{ll}} \\
Z_a &= \frac{(Z_c + Z_0) \cdot Z_{ll}}{Z_c + Z_{ll} + Z_0} \\
Z_b &= \frac{Z_c + Z_0}{2} \\
Z_c &= \frac{\Delta l}{2 C_{sx} v_{ph}} \\
Z_l &= Z_{ll} = \frac{2 L_{px} v_{ph}}{\Delta l} \\
C_{sx} &= C_{ssx} \\
L_{px} &= \frac{L_{ppx}}{2} \\
C_{ssx} &= -\frac{4}{\omega^2 (\mu_m - \mu_0) \Delta l} \\
L_{ppx} &= -\frac{4}{\omega^2 (\varepsilon_m - \varepsilon_0) \Delta l} \\
v_{ph} &= \frac{2}{\sqrt{\varepsilon_m \mu_m}} \\
\varepsilon_m &= \varepsilon_0 \cdot \varepsilon_r' \\
\mu_m &= \mu_0 \cdot \mu_r',
\end{aligned}
\tag{B.0.1}
$$

where the subscript ll of Z_{ll} indicates that the same value of two L_{ppx}s is used between the TLM unit cells (refer Fig. 5.15).

For the inter–cell network between a metamaterial and regular dielectric material, the following equations can be applied [72]:

$$
d_{11} = \frac{Z_l Z_c + Z_0 Z_c - Z_0^2}{(Z_0 + Z_l)(Z_0 + Z_c) + Z_0 Z_l}
$$

$$
\begin{aligned}
d_{21} &= d_{41} = d_{12} = -d_{23} = -d_{43} \\
&= \frac{2Z_l Z_0}{(Z_0+Z_l)(Z_0+Z_c)+Z_0 Z_l} \\
d_{31} &= \frac{2Z_c(Z_l+Z_0)}{(Z_0+Z_l)(Z_0+Z_c)+Z_0 Z_l} \\
d_{22} &= \frac{Z_l Z_c - Z_0 Z_c - Z_0^2}{(Z_0+Z_l)(Z_0+Z_c)+Z_0 Z_l} \\
d_{32} &= \frac{-2Z_l Z_c}{(Z_0+Z_l)(Z_0+Z_c)+Z_0 Z_l} \\
d_{42} &= \frac{2Z_l(Z_c+Z_0)}{(Z_0+Z_l)(Z_0+Z_c)+Z_0 Z_l} \\
d_{13} &= \frac{2Z_0(Z_l+Z_0)}{(Z_0+Z_l)(Z_0+Z_c)+Z_0 Z_l} \\
d_{33} &= \frac{Z_0^2 - Z_l Z_c - Z_0 Z_c + 2Z_0 Z_l}{(Z_0+Z_l)(Z_0+Z_c)+Z_0 Z_l} \\
d_{14} &= \frac{2Z_0^2}{(Z_0+Z_l)(Z_0+Z_c)+Z_0 Z_l} \\
d_{24} &= \frac{2Z_0(Z_c+Z_0)}{(Z_0+Z_l)(Z_0+Z_c)+Z_0 Z_l} \\
d_{34} &= \frac{-2Z_0 Z_c}{(Z_0+Z_l)(Z_0+Z_c)+Z_0 Z_l} \\
d_{44} &= \frac{Z_0^2 - 2Z_l Z_0 + Z_0 Z_c - Z_c Z_l}{(Z_0+Z_l)(Z_0+Z_c)+Z_0 Z_l}.
\end{aligned}
\tag{B.0.2}
$$

APPENDIX C

Solution for n' in Retrieval Method

C.1 Method

For the ambiguous branch integer m in retrieval methods (see eq. (5.2.8)), the Taylor series can be applied to approximating n' and comparing this to the result obtained with m. This method is introduced in [61]. If n' at frequency f_0, i.e. $n'(f_0)$, is known and n' at the next frequency f_1, i.e. $n'(f_1)$, is continuous from $n'(f_0)$, then $n'(f_1)$ can be predicted from

$$\exp\left(jn(f_1)k_0(f_1)d\right) \sim \left(\exp\left(jn(f_0)k_0(f_0)d\right)\right)(1+\Delta+\frac{1}{2}\Delta^2), \tag{C.1.1}$$

where up to the third term of the Taylor series was used for the approximation, the wave number in vacuum k_0 is also expressed as a function of frequency (i.e. as $k_0(f_0)$ and $k_0(f_1)$), and d is the thickness of the whole metamaterial structure considered. n' calculated from eq. (5.2.8) with m is expected to be close to the result from eq. (C.1.1). Also, Δ is obtained from

$$\Delta = jn(f_1)k_0(f_1)d - jn(f_0)k_0(f_0)d \tag{C.1.2}$$

$$= A'' + j(N' + A'), \tag{C.1.3}$$

where

$$N' = a_1 n'(f_1), \tag{C.1.4}$$

$$A' = -a_0 n'(f_0), \tag{C.1.5}$$

$$A'' = a_0 n''(f_0) - a_1 n''(f_1), \tag{C.1.6}$$

$$a_i = k_0(f_i) d \tag{C.1.7}$$

and $i = 0$ or 1. Hence,

$$\begin{aligned} 1 + \Delta + \frac{1}{2}\Delta^2 = & \left\{ 1 + A'' + \frac{1}{2}\left[A''^2 - \left(N'^2 + 2A'N' + A'^2 \right) \right] \right\} \\ & + j[N' + A' + A''(N' + A')]. \end{aligned} \tag{C.1.8}$$

The only unknown in eq. (C.1.8) is N', since $n'(f_1)$ is included only in N'. If $|z'| < \delta_z$ where δ_z is a small positive number, the values of $\exp(jn(f_i)k_0(f_i)d)$ are determined from [61]

$$\exp(jn(f_i)k_0(f_i)d) = \frac{S_{21}}{1 - S_{11}\frac{z-1}{z+1}}. \tag{C.1.9}$$

Therefore, eq. (C.1.2) can be expressed by

$$A_1 + jB_1 = (A_0 + jB_0)(1 + \Delta + \Delta^2) \tag{C.1.10}$$

where A_i and B_i are real numbers standing for the real and imaginary parts of $\exp(jn(f_i)k_0(f_i)d)$, respectively, and both known. Substituting eq. (C.1.8) into eq. (C.1.10) leads to

$$\begin{aligned} A_1 + jB_1 = & \left\{ -\frac{1}{2}A_0 N'^2 + [A_0 A' - B_0(1 + A'')]N' \right. \\ & \left. + A_0\left[1 + A'' + \frac{1}{2}\left(A''^2 - A'^2 \right) \right] - B_0 A'(1 + A'') \right\} \\ & + j\left\{ -\frac{1}{2}B_0 N'^2 + [B_0 A' + A_0(1 + A'')]N' \right. \\ & \left. + B_0\left[1 + A'' + \frac{1}{2}\left(A''^2 - A'^2 \right) \right] + A_0 A'(1 + A'') \right\}. \end{aligned} \tag{C.1.11}$$

Using $N' = a_1 n'(f_1)$, the real part of eq. (C.1.11) can be solved for $n'(f_1)$, i.e.

$$\alpha(n'(f_1))^2 + \beta n'(f_1) + \gamma = 0, \tag{C.1.12}$$

where

$$\alpha = a_1^2 A_0/2 \tag{C.1.13}$$

$$\beta = -a_1[A_0 A' - B_0(1 + A'')] \tag{C.1.14}$$

$$\gamma = A_1 - A_0[1 + A'' + \frac{1}{2}(A''^2 - A'^2)] + B_0 A'(1 + A''). \tag{C.1.15}$$

Eq. (C.1.12) gives two answers for $n'(f_1)$. However, substituting these two into the imaginary part of eq. (C.1.11), i.e. solving

$$\begin{aligned} B_1 = & -\frac{1}{2}B_0(a_1 n'(f_1))^2 + [B_0 A' + A_0(1 + A'')](a_1 n'(f_1)) \\ & + B_0\left[1 + A'' + \frac{1}{2}\left(A''^2 - A'^2\right)\right] + A_0 A'(1 + A''), \end{aligned} \tag{C.1.16}$$

and comparing to B_1 calculated from eq. (C.1.9) provide the answer. The use of the right answer of $n'(f_1)$ in eq. (C.1.16) is expected to be a closer result to B_1.

n' calculated from eq. (5.2.8) gives many answers due to m. However, the right answer is estimated to be close to n' calculated from the above processes. In this way the proper branch integer m can be found. This procedure is repeated for as many frequency points as required.

As mentioned in the beginning of this appendix, this method is based on the assumption that n' at a finite frequency is already known so that eq. (C.1.1) can be repeatedly applied. The first retrieval may be performed at a frequency satisfying the following condition:

$$|n'z''| \leq n''z' \tag{C.1.17}$$

where this condition is obtained from

$$\varepsilon_r'' \geq 0, \tag{C.1.18}$$

$$\mu_r'' \geq 0, \tag{C.1.19}$$

$$\varepsilon_r'' = \frac{1}{|z|^2}(-n'z'' + n''z'), \tag{C.1.20}$$

$$\mu_r'' = n'z'' + n''z'. \tag{C.1.21}$$

m can be easily detected, when the right hand side of eq. (C.1.17) approaches zero but z'' is not zero. If only one integer m satisfies this condition, then that can be the answer and becomes the starting point. If more than two answers are obtained, then retrieving is performed for each answer in a wider range and the proper branch integer is determined later with other results.

C.2 Limitation

The retrieval method using the Taylor series can give a solution for the ambiguous branch integer m in many cases. However, a limitation may be found, when the method is applied for thin metamaterial structure. In this case, the starting point determined by eq. (C.1.17) may not be found. This is explained with Fig. C.1, where the scattering properties of the paired CW metamaterial simulated in subsection 4.3.2 (9.6 mm length of the paired CW) were used.

Fig. C.1 shows the right hand side of eq. (C.1.17) and one step of the left hand side of eq. (C.1.17), which is determined from z'' and the second term of the right side of eq. (5.2.8) without m. As seen in this figure, the steps of $|n'z''|$ in eq. (C.1.17) is far larger than the values of the right hand side so that eq. (C.1.17) was not satisfied at any frequency point. This is possible, if the method is applied for thin metamaterial, because the whole structure thickness d used in the left of eq. (C.1.17) becomes so small, resulting in an extremely large step of $|n'z''|$. For this reason, the application of this method to thin metamaterial structures, e.g. thin metamaterial absorbers may not be possible. It is also

pointed out that even in this situation, the DF techniques described in this thesis are applicable.

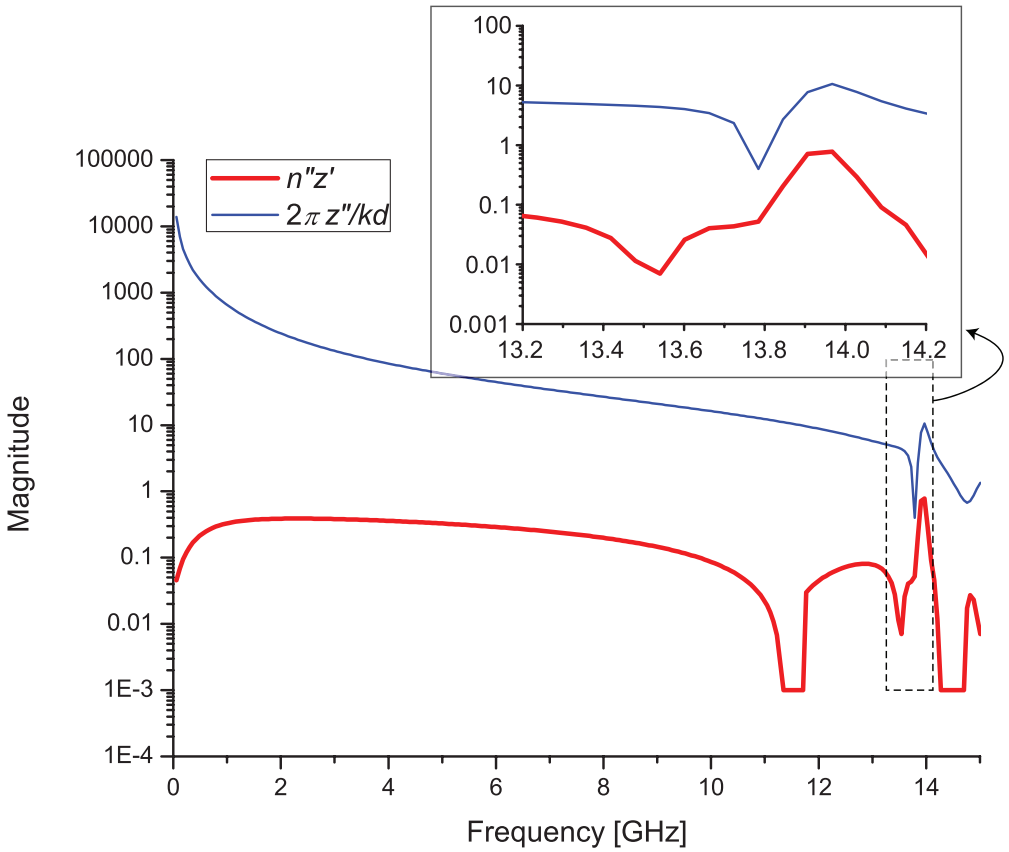

Figure C.1: Comparison between magnitudes of $n''z'$ and $2\pi z''/k_0 d$ of one paired CW metamaterial unit.

APPENDIX D

Oblique Wave Excitation with Periodicity

D.1 Calculation Methods

D.1.1 Overview

A simulation method for oblique wave illumination to periodic structures is introduced. The original idea of this method was developed for the FDTD (Finite Difference Time Domain) method [150]. In this appendix the method is modified for the TLM.

The overview of this method is described in Fig. D.1. The whole space consists of the main periodic unit (where the scattering parameters and electromagnetic profile are calculated), sub periodic unit and auxiliary space. The oblique wave enters the analysis space from the left of the Huygen's surface (refer section 2.3 for its implementation into the TLM) deployed at five cells away from the top boundary (i.e. the top xy boundary). Then, the wave propagates to the bottom right as indicated by the green arrow in this figure. Matched condition is applied for the left and right boundaries, and impedance boundary (explained in section D.2) is deployed for the top and bottom

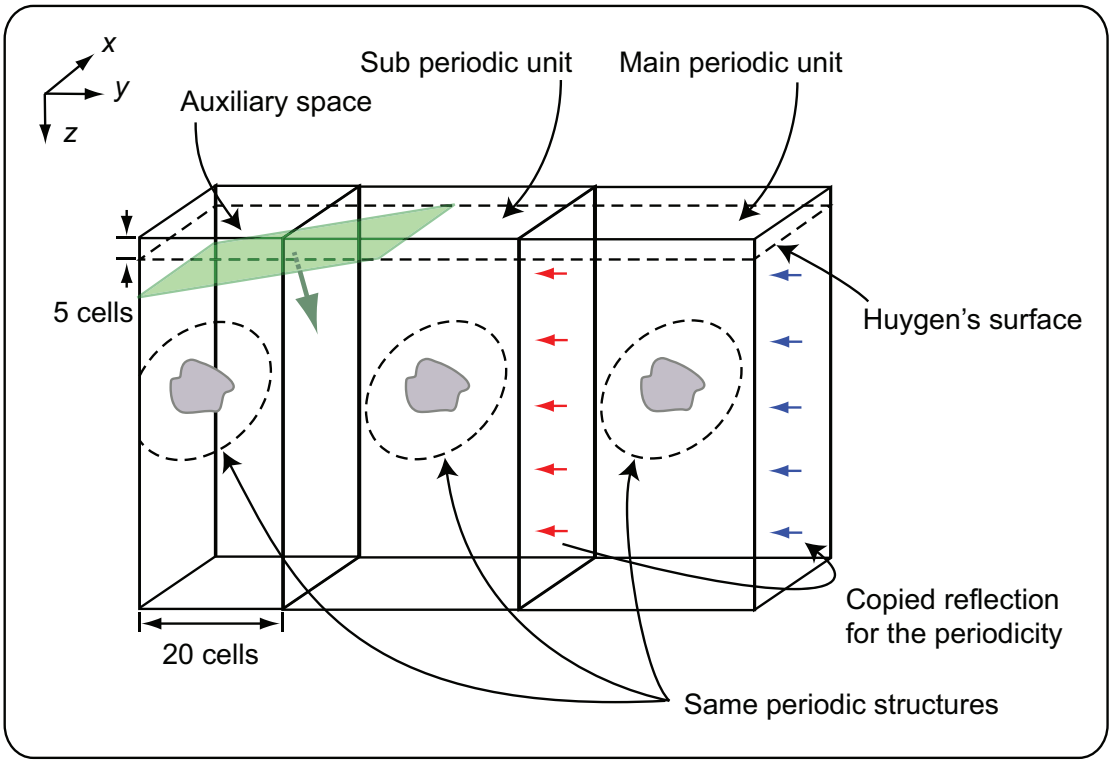

Figure D.1: Calculation space for oblique incidence with periodicity.

boundaries. The other boundaries (on yz planes) use periodic boundary.

It is found from the configuration given that the rest of the conditions required for the periodicity is to realise the periodicity of the left and right boundaries in the main unit. This can be satisfied by the next two conditions: i) the use of the reflection in the sub unit for the right boundary in the main unit and ii) the removal of the error coming from the left side of the whole analysis space.

For the right boundary the reflection sampled at the boundary between the main and sub periodic units (i.e. the red arrows in Fig. D.1) can be used at several time steps later (i.e. as the blue arrows in Fig. D.1).

Since the sub periodic unit has the same structure as that used in the

main unit, the periodicity can be maintained, as long as any error does not enter the main unit. This error happens as the matched condition is applied for the left boundary of the whole simulation space. This indicates that as the time increases, the periodicity is gradually broken from the left to the right. In [150] this error is removed both by copying the correct electromagnetic fields in the right space to those in the left and by returning the time step.

This copy process is summarised in Fig. D.2, where the auxiliary space is removed for simplicity and the time of the main periodic unit (each right) is not increased at some phases for the calculation efficiency (see "ON" and "OFF" in Fig. D.2). First, while the time of the sub unit begins from 0 and increases, the time t of the main unit is stopped at

$$t = \tau_{dy}. \tag{D.1.1}$$

This is the time required for the right edge of the oblique wave to reach the boundary between the two units, i.e.

$$\tau_{dy} = \frac{A_y}{c} \sin\theta, \tag{D.1.2}$$

where A_y and θ represent the length of the periodic structure along y axis and incident angle. c indicates the speed of light in the medium/media placed below the Huygen's surface. As the time increases, the incident wave propagates from the top left to the bottom right (see the middle of the top row in Fig. D.2). At the same time, however, the error (illustrated as the grey colour region in Fig. D.2) propagates from the left to right due to the imperfection of the periodicity.

When the right edge of the wave arrives at the boundary between the two units (i.e. at $t = \tau_{dy}$), the time of the main unit synchronises with that of the sub unit and starts to increase together. With further increase of the time step, the error region approaches the right region and comes to the boundary between the two periodic units. The time required for this propagation τ_{ey} is

$$\tau_{ey} = \frac{A_y}{c}. \tag{D.1.3}$$

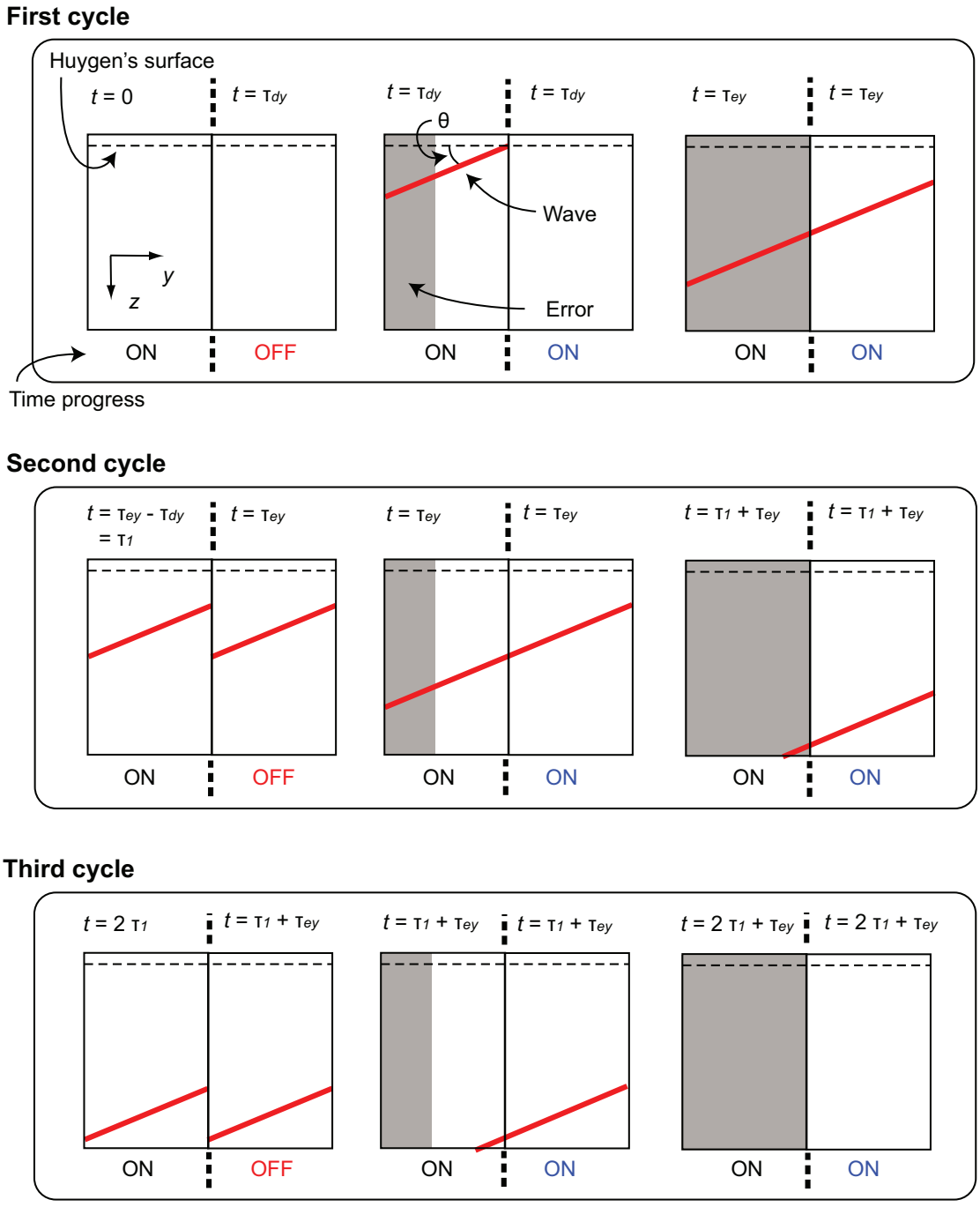

Figure D.2: Voltage copy process. In each time the left and right spaces represent the sub periodic unit and main periodic unit.

At this point, there is no error in the main unit. Therefore, by copying the electromagnetic fields (i.e. all the voltages used in TLM unit cells) in the main unit to those in the left unit, all the error can be removed from the whole simulation space. Since the copy process means reversing the time of the sub periodic unit

by τ_{dy}, the time in the left region is returned to

$$t = \tau_{ey} - \tau_{dy}. \tag{D.1.4}$$

The series of these processes indicates that the correct fields can be obtained in the main periodic unit during

$$\tau_{dy} < t < \tau_{ey}. \tag{D.1.5}$$

As described in the second and third rows of Fig. D.2, this process is repeated for as many times as required so that, maintaining the periodicity, the oblique wave propagates in the main periodic unit without contamination by errors. According to [150], the use of 20 cell width of the auxiliary space can ensure this.

D.1.2 Implementation in the TLM Algorithm

The implementation to the actual TLM programme code requires some modifications. Firstly, the condition of eq. (D.1.5) is described by the time step instead of the time as follows:

$$N_{dy} < N_t < N_{ey}, \tag{D.1.6}$$

where N_t, N_{dy} and N_{ey} are all integers and correspond to t, τ_{dy} and τ_{ey}, respectively. One point for the derivation of eq. (D.1.6) is that the oblique wave must cross the periodic unit width A_y by an integer, i.e.

$$\begin{aligned} \tau_{dy} &= N_{dy}\Delta t, \\ \Delta t &= \frac{\tau_{dy}}{N_{dy}} \end{aligned} \tag{D.1.7}$$

where Δt is the time step. This condition ensures that, when the time step in the sub region (including the auxiliary space) is returned for the copy process (i.e. the removal of the error), the time step corresponds to one of the times used in the past. In this way the time of the sub region can be synchronised

with that in the main unit later again.

Also, since in the TLM method the characteristic impedance of the TLM unit cells must be equal to or larger than zero [85] (also refer eqs. (2.1.15) and (2.1.16)), the next condition is imposed:

$$\Delta t \leq \frac{\Delta l}{2c}. \tag{D.1.8}$$

From eqs. (D.1.7) and (D.1.8) the next expression is obtained:

$$N_{dy} \geq \frac{2y_p \sin\theta}{\Delta l}. \tag{D.1.9}$$

Thus, for calculation efficiency N_{dy} is chosen to be the smallest integer among the ones satisfying eq. (D.1.9). Regarding N_{ey} the following condition is required:

$$N_{ey} = \texttt{floor}\left(\frac{\tau_{ey}}{\Delta t}\right), \tag{D.1.10}$$

where `floor` is the function to derive the highest integer among those equal to or less than the content of the bracket. To sum up, the correct electromagnetic fields are obtained in the main periodic unit, as long as the number of the time step is within the range of eq. (D.1.6), whose limits are determined by eqs. (D.1.9) and (D.1.10).

For the periodicity of the right boundary in Fig. D.1, the past incident voltages at the right boundary of the sub periodic unit are stored by the number of the integer N_{ey}. These are also used for the centre boundary between the main and sub units, while the time of the main unit stops. Provided that the oblique wave is excited with the axis notations illustrated in Fig. D.1 and voltage port numbers in Fig. 2.3, the incident voltages at ports 7 and 12 are saved in a buffer by the number of the integer N_{dy}. The voltages stored can be

expressed in the following form:

$$\mathbf{V} = \begin{bmatrix} {}_0V_{(7,\,12)} \\ {}_1V_{(7,\,12)} \\ {}_2V_{(7,\,12)} \\ \vdots \\ {}_{N_{ey}-2}V_{(7,\,12)} \\ {}_{N_{ey}-1}V_{(7,\,12)} \end{bmatrix}, \tag{D.1.11}$$

where the oldest voltage is ${}_0V$ and the latest one is ${}_{N_{ey}-1}V$. While $N_t < N_{dy}$ (i.e. while the time step in the main unit is not increased), the voltages are used from ${}_{N_{dy}-1}V$ to ${}_{N_{ey}-1}V$ for the new incident voltages at the centre boundary (i.e. as the red arrows in Fig. D.1). While the main region is activated (i.e. during $N_{dy} < N_t < N_{ey}$), the voltages stored are used for the right boundary (i.e. as the blue arrows in Fig. D.1). In this case, always ${}_{N_{ey}-1-N_{dy}}V$ is used for the new incident voltages, but at every time step the oldest data is discarded and all the data is shifted to the older positions by one (e.g. ${}_1V$ becomes ${}_0V$). Then, the current incident voltages sampled at the center boundary are stored as the new ${}_{N_{ey}-1}V$.

D.2 Impedance Boundary

The use of the above calculation algorithm can work in the FDTD provided that a good absorbing boundary condition is used such as the perfectly matched layer, the so–called PML. In [150] a convolution PML [151] is adopted to avoid strong reflection from the top and bottom boundaries in Fig. D.1. In the TLM method reflections can be reduced by using impedance boundary instead of matched boundary [152]. In this approach the impedance of the boundary is changed depending on the angle of the incident wave.

The reflection coefficient Γ from the impedance boundary can be calculated

from

$$\Gamma = \frac{Z_x - Z_0}{Z_x + Z_0} \tag{D.2.1}$$

$$= \begin{cases} \dfrac{\dfrac{Z_0}{\cos\theta} - Z_0}{\dfrac{Z_0}{\cos\theta} + Z_0} = \dfrac{1-\cos\theta}{1+\cos\theta} & \text{(for TE wave)} \\ \dfrac{Z_0\cos\theta - Z_0}{Z_0\cos\theta + Z_0} = \dfrac{\cos\theta - 1}{\cos\theta + 1} & \text{(for TM wave),} \end{cases} \tag{D.2.2}$$

where the TE and TM respectively stand for transverse electric field and transverse magnetic field and, as illustrated in Fig. D.3, the electric field and magnetic field are respectively parallel to the impedance boundary. Z_x and Z_0 are the characteristic impedance beyond the impedance boundary and that in the analysis space, where the vacuum is used here as an example. The new incident voltages can be therefore obtained from the reflected voltages multiplied by eq. (D.2.2) (e.g. provided that the configuration of Fig. D.1 and voltage port numbers in Fig. 2.3 are given, ${}_{k+1}V^{i}_{(8,\,9)} = \Gamma\ {}_{k}V^{r}_{(8,\,9)}$). Fig. D.3 also shows the impedances required to obtain no reflection from the boundary in each case.

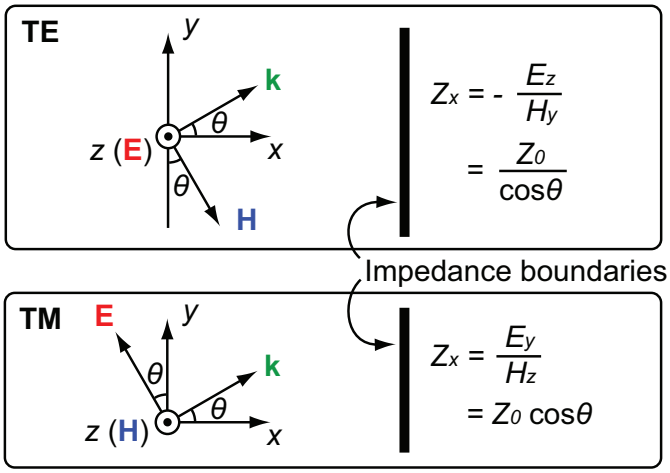

Figure D.3: Use of impedance boundary to reduce reflection of incident wave. The boundary is connected to Z_x of the characteristic impedance so that the reflection of the oblique wave is reduced.

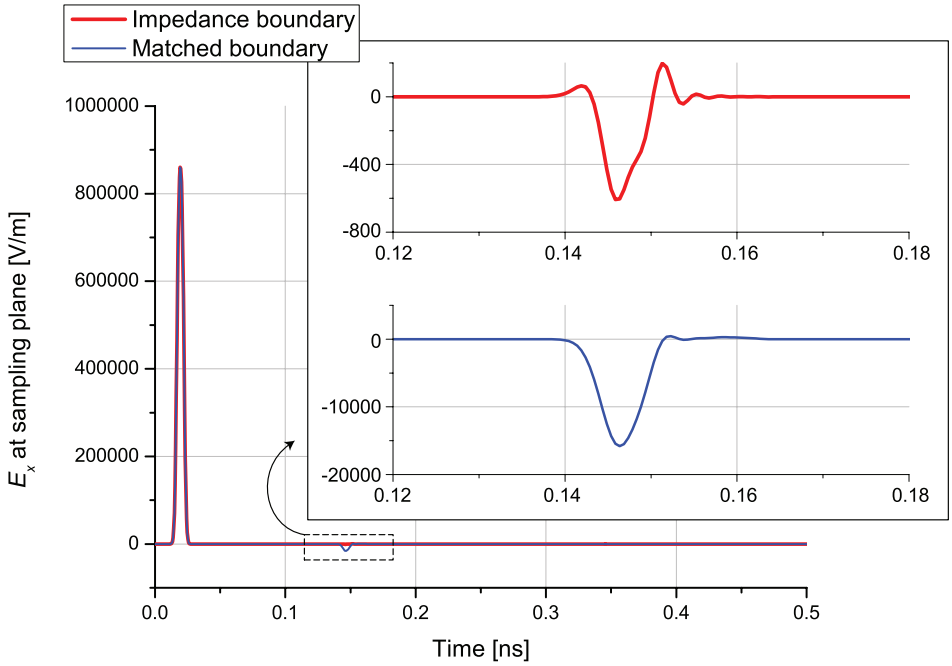

Figure D.4: Performance of impedance boundary and matched boundary for 15 degrees of TE wave. Electric field along x axis was calculated at a sampling plane next to Huygen's surface.

The performance of the impedance boundary can be assessed from Figs. D.4 to D.6. In these figures the electric field in time domain is shown using the impedance boundaries or matched boundaries which were deployed in the top and bottom boundaries (i.e. the xy boundaries) of the analysis space illustrated in Fig. D.1 without any periodic structure. The periodicities along x axis (A_x) and y axis (A_y) are both 21 Δl where $\Delta l = 0.3$ mm. The z axis length of the calculation space was $70\Delta l$. For TE wave and TM wave, the incident electric field and magnetic field were polarised along x axis. The sampling plane was placed next to the Huygen's surface in the main periodic unit (i.e. sixth cells from the top xy boundary).

Ideally the electric field is expected to be zero after the first incidence. However, the use of the matched boundary (see the blue thin curves in Figs. D.4 and D.6) led to unwanted reflection from the top and bottom boundaries. This reflection became more significant, when the incident angle of the TE

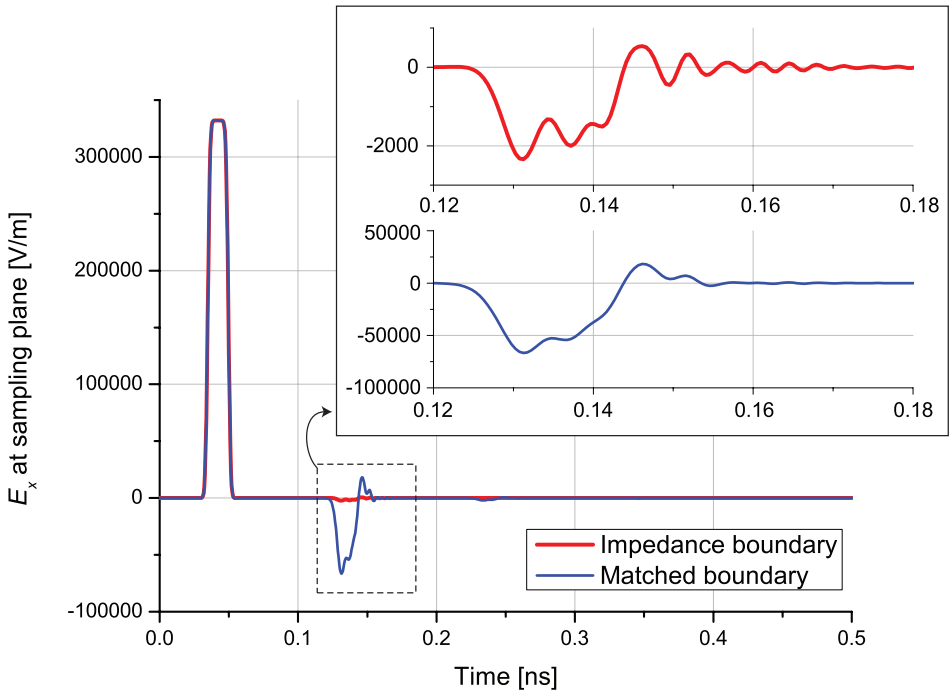

Figure D.5: Performance of impedance boundary and matched boundary for 45 degrees of TE wave. Electric field along x axis was calculated at a sampling plane next to Huygen's surface.

wave was changed from 15 degrees (Fig. D.4) to 45 degrees (Fig. D.5). However, as demonstrated in Figs. D.4 and D.5, using the impedance boundary reduced the unwanted reflection. Fig. D.6 shows that the same performance is obtained for the TM wave.

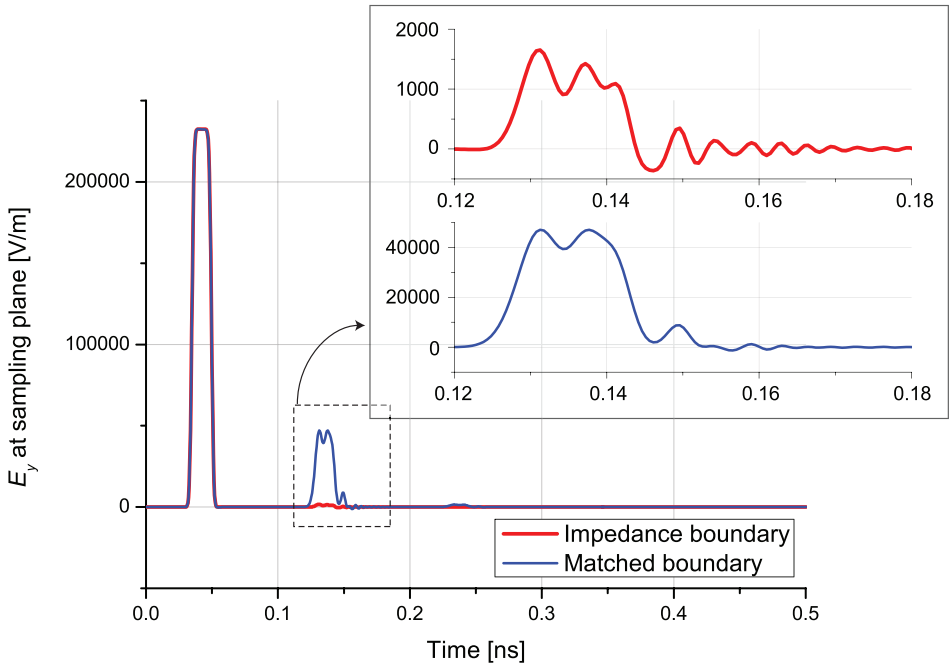

Figure D.6: Performance of impedance boundary and matched boundary for 45 degrees of TM wave. Electric field along x axis was calculated at a sampling plane next to Huygen's surface.

APPENDIX E

Other Publications by the Author

Other publications by the author are written below.

Journals

[1] Hiroki Wakatsuchi, Taiji Sakai, Soichi Watanabe, Masami Kojima, Yoko Yamashiro, Hiroshi Sasaki, Kazuyuki Sasaki, and Osamu Hashimoto, "Application of Reproducible Complex Permittivity Measurements to Crystalline Lens from 500 MHz to 50 GHz," *IEEE Trans. Electromagn. Compat.* (submitted).

[2] Hiroki Wakatsuchi, Taiji Sakai, Soichi Watanabe, Masami Kojima, Yoko Yamashiro, Hiroshi Sasaki, Kazuyuki Sasaki, and Osamu Hashimoto, "Complex permittivity measurements of ocular tissues from 5 GHz to 50 GHz," (in preparation).

[3] Hiroki Wakatsuchi, Taiji Sakai, Soichi Watanabe, and Osamu Hashimoto, "Development of Complex Permittivities Parametric Model Including Dependences on Water–Content Ratio and Temperature in Millimeter Wave Band," (in preparation).

[4] Hiroki Wakatsuchi, M. Hanazawa, S. Watanabe, A. Nishikata, M. Kouzai, M. Kojima, Y. Yamashiro, K. Sasaki, and O. Hashimoto, "The Measurements of the Complex Permittivities of Blood Samples in Quasi–

Millimeter and Millimeter Wave Bands," *IEICE Transactions on Communication*, vol. E90–B, no. 6, pp. 1357–1359, 2007.

Conferences

In English

[1] Taiji Sakai, Masahiro Hanazawa, Hiroki Wakatsuchi, Atsuhiro Nishikata, and Osamu Hashimoto, "Measurements of Dielectric Properties of Biological Tissues in Mm–wave Band by Free–space Reflection Method, Ellipsometry Method and Coaxial Probe Method," *Progress in Electromagnetics Research Symposium (PIERS) 2007*, pp. 45, Prague, Czech Republic, Aug. 2007.

[2] Hiroki Wakatsuchi, Masahiro Hanazawa, Taiji Sakai, Soichi Watanabe, Masami Kojima, Yoko Yamashiro, Kazuyuki Sasaki, and Osamu Hashimoto, "Complex Permittivities Measurements of Ocular Tissues in Quasi-Millimeter and Millimeter Wave Bands," *BEMS The Bioelectromagnetics Society 28th Annual Meeting*, pp. 497–499, Kanazawa, Japan, June 2007.

[3] Hiroki Wakatsuchi, Masahiro Hanazawa, Taiji Sakai, Soichi Watanabe, Masami Kojima, Yoko Yamashiro, Kazuyuki Sasaki, and Osamu Hashimoto, "The Complex Permittivities of Ocular Tissues at Millimeter-Wave Bands," *EBEA 2007 The European Bioelectromagnetics Association*, pp. 56, Bordeaux, France, Apr. 2007.

[4] Hiroki Wakatsuchi, Masahiro Hanazawa, Taiji Sakai, Soichi Watanabe, Masami Kojima, Yoko Yamashiro, Kazuyuki Sasaki, and Osamu Hashimoto, "Complex Permittivities Measurements of Eye Tissues in Quasi-millimeter Wave Band," *2006 KMU Workshop on Ocular changes Induced by Electromagnetic Waves*, Kanazawa, Japan, Dec. 2006.

[5] Hiroki Wakatsuchi, M. Hanazawa, S. Watanabe, M. Kouzai, A. Nishikata, and O. Hashimoto, "Complex Permittivity Measurement of Blood in

Millimeter Wave Band," *Progress in Electromagnetics Research Symposium (PIERS) 2006*, pp. 127, Tokyo, Japan, Aug. 2006.

[6] Masaki Kouzai, Atsuhiro Nishikata, Hiroki Wakatsuchi, Kaori Fukunaga, Masahiro Hanazawa, and Soichi Watanabe, "Complex Permittivity Measurement of Some Biological Materials at 33–50GHz by Dielectric Tube Method," *BEMS 28th Annual Meeting*, pp. 312–316, Cancun, Mexico, June 2006.

[7] Masahiro Hanazawa, Hiroki Wakatsuchi, Soichi Watanabe, Masaki Kouzai, Atsuhiro Nishikata, and Osamu Hashimoto, "Complex Permittivity Measurement of Blood by Probe Method," *BEMS 28th Annual Meeting*, pp. 93–96, Cancun, Mexico, June 2006.

[8] Hiroki Wakatsuchi, Masahiro Hanazawa, Soichi Watanabe, Atsuhiro Nishikata, Masaki Kozai, Masami Kojima, Yoko Yamashiro, Kazuyuki Sasaki, and Osamu Hashimoto, "Complex Permittivity Measurement of Biological Tissues and Numerical Analysis of SAR Distribution in Quasi–Millimeter Wave Band," *2nd Pan-Pacific EMC Joint Meeting PPEMC'06*, Okayama, Japan, May 2006.

In Japanese

[1] Hiroki Wakatsuchi, Taiji Sakai, Soichi Watanabe, and Osamu Hashimoto, "Temperature Dependence to Complex Permittivities of Liquid Biological Tissues from 5 to 50 GHz," *IEICE The Annual Meeting*, vol. B–4–41, pp. 350, Kitakyusyu, Japan, Mar. 2008.

[2] Hiroki Wakatsuchi, Taiji Sakai, Soichi Watanabe, Masami Kojima, Yoko Yamashiro, Kazuyuki Sasaki, and Osamu Hashimoto, "Effect of Storage Conditions after Extracting Tissues on Complex Permittivity Measurement of Ocular Tissues at 5 to 50 GHz," *IEICE Society Conference*, vol. B–4–30, pp. 293, Tottori, Japan, Sep. 2007.

[3] Hiroki Wakatsuchi, Masahiro Hanazawa, Taiji Sakai, Soichi Watanabe, Masami Kojima, Yoko Yamashiro, Kazuyuki Sasaki, and Osamu Hashimoto, "The Complex Permittivities Measurements of Ocular Tissues in Quasi–Millimeterwave Bands and Millimeterwave Bands," *IEICE The Annual Meeting*, vol. B–4–12, pp. 336, Nagoya, Japan, Mar. 2007.

[4] Hiroki Wakatsuchi, Masahiro Hanazawa, Soichi Watanabe, Masami Kojima, Yoko Yamashiro, Kazuyuki Sasaki, and Osamu Hashimoto, "Thermal Analysis of Rabbit Eye Exposed to MMW Considering Uncertainty of Electrical Constants of Eye Tissues and Cooling by Blood Flow," *IEICE Society Conference*, vol. B–4–34, pp. 310, Kanazawa, Japan, Sep. 2006.

[5] Hiroki Wakatsuchi, Masahiro Hanazawa, Soichi Watanabe, Masami Kojima, Yoko Yamashiro, Kazuyuki Sasaki, and Osamu Hashimoto, "Improvement of Reproducibility in Complex Relative Permittivity Measurement of Blood," *IEE The Annual Meeting*, 1–124, vol. 1, pp. 154, Yokohama, Japan, Mar. 2006.

[6] Hiroki Wakatsuchi, Masahiro Hanazawa, Masami Kojima, Yoko Yamashiro, Soichi Watanabe, Osamu Hashimoto, and Kazuyuki Sasaki, "Complex Dielectric Constant Measurement of Blood at Quasi–Millimeter Wave Band," *IEICE Society Conference*, vol. B–4–45, pp. 369, Hokkaido, Japan, Sep. 2005.